Cluster Production in the Matrix Assembly Cluster Source

by

William Terry

A thesis submitted to
The University of Birmingham
for the degree of
DOCTOR OF PHILOSOPHY

Nanoscale Physics Research Laboratory
School of Physics & Astronomy
University of Birmingham
September 2016

Abstract

This thesis focuses on the development of the Matrix Assembly Cluster Source (MACS). There are two major strands to this, the investigation of nanoclusters produced via matrix assembly, and the monitoring of the matrix, during this process. All of the results presented here have been underpinned by the development of new apparatus by the author. The Nanoscale Physics Research Laboratory at Birmingham University is already well known for its fundamental cluster research and the applications of size-selected clusters. The work here represents a significant thrust towards the scaling up of cluster production to small batch industrial work (i.e. grams of clusters per day). More specifically, the thesis describes scaling up production of the original, transmission mode MACS instrument. This has involved the integration of a Time-Of-Flight (TOF) mass filter, including the development of control software. The transmission mode MACS source has achieved a silver nanocluster production rate equivalent to a cluster beam current of 100 nA (previously several nA). Furthermore, an intrinsic size control of the process has been demonstrated in the 1-5 nm range for silver by varying the silver concentration in the matrix.

Furthermore, the matrix assembly technology has been extended to the reflection regime, demonstrating the ability to produce nanoclusters using a planar matrix support surface. Not only does this represent a simpler method for production, but a higher practical conversion rate of incident ions to clusters is achieved, $\sim$1 % compared with $\sim$0.03 % in transmission. The effect of the beam plate geometry is investigated, establishing the optimum incident sputtering and collection angles for cluster production. Based on this proof of principle study, a new high deposition area ($\sim$400 cm^2) reflection mode system (MACS2) has been designed, commissioned

and demonstrated, producing a maximum usable equivalent silver cluster beam current of 170±16 nA (averaged over 4.5 minutes). An average equivalent current of 40 nA has been deposited for a sustained period (45 minutes), without matrix replenishment. The utility of the produced nanoclusters has been demonstrated in a proof of principle biochip study. Patterned nanocluster arrays have been deposited on glass slides using deposition masks. These are then drop cast with florescent dye. The dye demonstrates preferential immobilization on the cluster-coated regions, the primary step towards label-free cluster-based biochips. The MACS2 is capable of depositing a batch of 21 glass slides coated for bio-chips in one hour.

Finally, ion-induced light emission from the matrix has been studied, a by-product of nanocluster production. A simple optical measurement setup has been developed to measure the visible range light emission. Visible range optical measurements demonstrate significant change in the ion-induced light emission spectra with the addition of O_2, N_2, or Ag to the pure argon matrix. Concentrations as low as 0.1% are readily detectable. These measurements demonstrate that, by careful analysis of emission spectra, the thickness, composition and, in certain cases, molecular composition of the matrix can be accessed.

Acknowledgements

I thank the Leverhulme Trust, as well as my supervisor Prof. Richard Palmer, for giving me this opportunity. I especially thank Prof. Palmer for his guidance throughout and placing his trust in me to complete the project. I would also like to thank Lu Cao for introducing me to the MACS and for the many great times working with him; his tireless work ethic and patience are inspiring. I must also thank Lu for his STEM work and the many late nights he has put in to imaging samples for me. Thanks for the pain of imaging my many, many samples must also go to Jian Liu who now must have imaged more samples than any other member of the NPRL. I also thank the many post docs who have all contributed to my work either directly or through their guidance and knowledge: Feng Yin, Simon Plant, Richard Balog, Dimitri Hapiuk, Vitor Oiko, and Shane Murphy. A big thanks to the whole NPRL group for their support, insight and discussions: in particular, to Caroline, Dogan, Lu, Ray and Scott for keeping me sane through the longer days and nights. Finally, thanks go to my family. Without their support and encouragement I would not be here, and thank you to Kate for putting up with and supporting me throughout.

Author's Contribution

The work presented in this thesis was conducted by the author under guidance of my supervisor Prof R. E. Palmer and my co-supervisors Dr. F.Yin and Dr. S. Plant. The first three chapters of this thesis have been proof read for error and grammar by Birmingham Proofreaders. All other contributors to the work are stated in the appropriate chapters.

Author's Publications

Peter R. Ellis, Christopher M. Brown, Peter T. Bishop, Jinlong Yin, Kevin Cooke, William D. Terry, Jian Liu, Feng Yin, Richard E Palmer. *The Cluster Beam route to model catalysis. Faraday Discuss, 188, 39 (2016)*

W. D. Terry, R.Balog, F. Yin, W. Harbich, R. E. Palmer. *Dynamic Ion-induced luminescence in the Matrix Assembly Cluster Source (In Prep)*

L. Cao, W. D. Terry, R. Balog, R. Cai, R. E. Palmer. *The Production of Silver and Gold nanocluster by the Matrix Assembly Cluster Source (In Prep)*

Contents

Chapter 1

Overview and Background

Nanoclusters have attracted a huge amount of attention since the pioneering work of the 1980s. Since the early demonstrations of how matter is arranged down to the atomic level, and the new properties this yields, significant attention has been paid both to the fundamental understanding of clusters and the production of new materials with new and more attractive properties.[1–9] This work has been enabled by the development of a new range of instruments both to produce and characterise[10–15] these nanoscale objects.

1.1 Challenges

Over the past thirty years, significant progress has been made in understanding the behaviour and properties of nanoclusters.[16–24] Several key challenges remain in order to convert the fundamental knowledge into impactful applications. Nanoparticles have gained a significant amount of traction, with more than 1800 consumer products containing nanomaterials,[25] many of which are nanoparticles. The use of precise nanoclusters, however, is very limited. Small nanoclusters have been shown to provide highly desirable properties,[3,26–30] often using a fraction of the material normally required. A significant barrier to commercial usage is the inability to produce large quantities of precise nanoclusters, with specific elemental composition.

For example, size-selected cluster sources, which utilise mass filtering of the cluster beam, produce around 0.1-1 nA of clusters, which equates to around 1 μg of clusters per hour (dependent on cluster size and material). Even for small-batch, fine chemical production or pharmaceuticals, grams or kilograms of catalyst are often required (0.01-10 g of clusters). Furthermore, characterisation of small particles (<5 nm) has proved difficult and time-consuming.

1.2 Thesis Overview

This thesis reports the development of the novel Matrix Assembly Cluster Source (MACS) and investigates the production and deposition of nanoclusters by this unique method. This new technique demonstrates the ability to produce size-controlled nanoclusters in a scalable way. The MACS production method has been investigated in two different modes (geometries): transmission and reflection. The results presented encompasses work carried out on three different Matrix Assembly Cluster Source (MACS) systems. The first is a transmission mode MACS which has been upgraded (chapter 3). The second is a proof of principle reflection mode MACS which is based on the modification of a HREELS preparation chamber (chapter 4), this chamber has also been used for experiments into the light emission of argon matrices under ion bombardment in relation to the transmission mode MACS (chapter 6). The final system is a custom built MACS operating in reflection mode (5).

Chapter 2 provides a context for the work presented in the thesis, giving an overview of state of the art cluster beam technologies, their modes of operation and typical cluster production capabilities. Developments in the burgeoning area of high flux cluster sources are also reported. Finally, two potential impact areas for cluster beam technology are considered. Although there is a myriad of possible applications linked with nanoclusters, the main foci of this section are catalysis and biotechnology, which provide two obvious fields of application for precisely controlled

nanoclusters.

The development of a high flux, transmission geometry MACS is described in chapter 3. The system is designed and built to provide a greater cluster flux compared with the demonstrator prototype and permits systematic investigation of the parameters affecting cluster production. The system is enhanced with the integration of a lateral Time-Of-Flight (TOF) mass filter for real-time analysis of the charged nanocluster fraction of the cluster beam. This is further augmented with full computer control of the TOF mass filter, ion optic lenses, and current, voltage and ion dose measurements.

The two results chapters, 4 and 5 report the proof of principle of a MACS running in reflection geometry, and the development of a system demonstrating high flux and sustained, large area deposition from reflection mode. Several key parameters are measured: dependence of cluster production on incident ion trajectory, the optimal nanocluster ejection angle and the conversion efficiency of ions to nanoclusters. The new source showcases high flux production on large area samples for extended periods. In-situ cluster production rate measurements are demonstrated by the use of a quartz crystal microbalance (QCM). Patterned nanocluster arrays have been produced on glass slides by masked deposition. Drop cast fluorescent dye is shown to be preferentially immobilised on cluster-coated areas after washing. This represents the first step towards the development of a label-free biochip device.

Chapter 6 presents the measurements of the visible wavelength ion-induced light emission, a by-product of the cluster production in the MACS using a simple optical metrology setup is described, that enables the investigation of the composition and state of the matrix based on the analysis of the ion-induced luminescence during cluster production. The effects of matrix thickness, composition and ion dose on light emission are measured. Features relating to argon, silver, nitrogen and oxygen have been identified (in both their molecular and radical forms). In principle, changes in the matrix thickness and composition can be detected by careful analysis and

calibration of the light emission during ion beam bombardment of the matrix.

Throughout the thesis the matrix parameters are given in terms of thickness and concentration an explanation of how these values are calculated based on the measured gas pressure and metal deposition rate is given in appendix A. The principle method of measurement has been aberration corrected High Angle Annular Dark Field (HAADF) STEM, the the nanoparticle density can be measured directly from images. The measurement of cluster size in atoms is done by comparison of integrated HAADF intensities. This method is explained in appendix B.

The remainder of this chapter gives a brief introduction into nanocluster science and technology.

1.3 Background

The use of nanoparticles dates back to antiquity with examples like the Lycurgus cup, whose stained glass has stood the test of time;[31,32] however, the study and understanding of the subject came much later. It is generally agreed that the underlying concepts of nanotechnology began to develop after Richard Feynman's famous lecture "There's Plenty of Room at the Bottom" in 1959. The field of cluster science can be dated to the 1980s with the discovery of "magic number" clusters in alkali metals.[7] At the same time, another significant breakthrough was made with the discovery of fullerenes in 1982.[33] These two major discoveries, mixed with the developing theory of nanoclusters, drew a large amount of scientific interest.[34–39] The timing of these discoveries coincided with new methods of making atomic resolution measurements. Instruments like the STM (Scanning Tunnelling Microscope) were invented in the early 1980s, and the high resolution Transmission Electron Microscope (TEM),[40–42] which was improved repeatedly between the 1950s and the 1970s meant that it was possible to directly image nanoclusters in great detail for the first time.

To give a clearer picture of this subject, a cluster, or nanocluster, is defined as an aggregation of ∼2-200,000 atoms, which puts an upper limit of ∼19 nm on the cluster diameter (assuming a spherical shape). For the purposes of this thesis, the term cluster and nanocluster will be used interchangeably and refer to this size range. Larger particles (>10 nm in diameter) will be referred to as nanoparticles. Understanding the science behind matter that is bridging the gap between atomic and bulk properties is of great intrinsic interest (and is a topic that is not yet fully explored).[43] The initial investigation was led by gas phase studies.[44–48] Several key discoveries of highly desirable properties of clusters on surfaces, however, led to a second boom in the field of clusters.[1,3,49] For example, Haruta demonstrated that gold could be highly catalytically active in nanocluster form.[1]

The reason for the observed change in properties of nanoclusters is twofold. Firstly, there is a significantly increased surface area to bulk ratio, permitting much greater interaction with the surrounding matter, per mass of material. It is worth noting that not only is the amount of surface area changed, but also the form of it, i.e. the number and type of edge, corner or low coordination sites will be changed. These are usually considered to be highly active sites.[50,51] Based on the nanocluster geometry (structure), more or new types of site can be introduced leading to new properties. Secondly, as the size of the particle is shrunk, the electronic band structure observed in bulk materials changes towards a discrete energy level system.[52]

The number of publications published per annum, relating to nanoclusters, cluster-ions or cluster-beams, is presented in Figure 1.1. This shows the number of related publications per year starting from the 1970s up to the present day and gives an indication of the growth of the field.

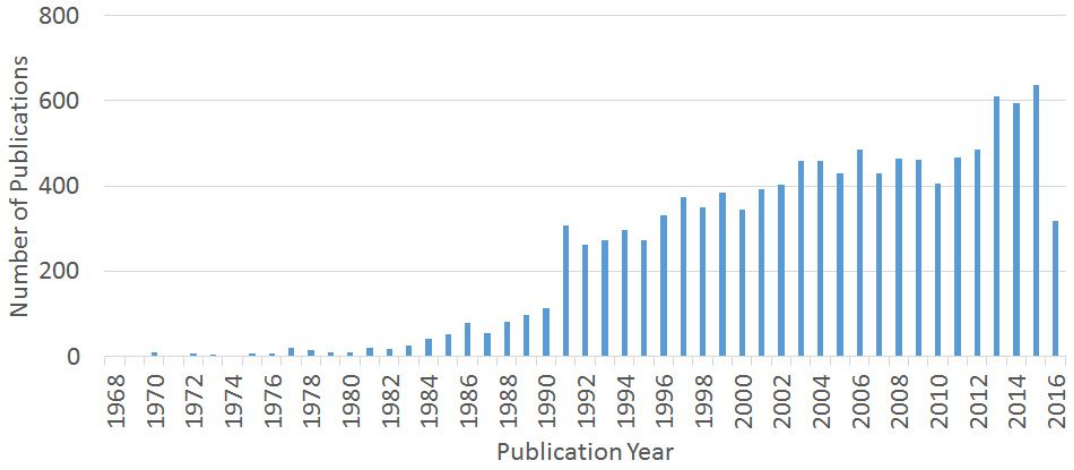

Figure 1.1: The bar chart above shows the number of publications containing the keywords nanocluster, cluster-ion or cluster-beam. The number of publications starts to grow from the early 1980s and increases dramatically in the 1990s. Data is provided by Thomas Reuters, web of science core collection.

These new properties were seen as particularly exciting, potentially ushering in a new era for tuning and optimising material properties, with size acting as a third dimension of the periodic table in terms of material properties.[53] However, this potential impact has not been fully realised, with difficulties arising in the stability, consistency and production of large quantities of highly defined and characterised nanoclusters. This has generally restricted applications to the larger nanoparticles, which mostly possess linearly scaling "modified bulk" properties. More readily available nanoparticles have still found many uses, for example sun cream, catalytic converters and dental resins.[25,51,54] These are generally produced by wet chemical synthesis.[55,56] The clusters are often formed by reducing a salt to form clusters in the presence of a capping ligand or surfactant. The ligands attaching to the cluster prevent its continued aggregation. As such, the ligand concentration provides a level of control over the particle size. Wet chemical methods have been improved

significantly over the last few decades;[57] however, the production and extraction of bare, small-size controlled particles remain an open challenge.

Chapter 2

Review of Cluster Sources and Applications

To establish a context for the work presented in later chapters, this chapter reviews cluster beam technology and examines two of the most attractive fields of application for MACS-produced clusters, i.e. catalysis and biotechnology.

2.1 Cluster Sources

This thesis is concerned with the development of a new type of cluster source, MACS. Prior to discussing the development of the source, it is important to survey existing technologies for cluster production in order to assess the potential impact of this new technology. A wide range of cluster sources have been developed to investigate the different aspects of nanocluster science. There has been a strong demand not only to produce nanoclusters but to produce them from different materials, with increasing control over shape, size and composition. As this thesis focuses on the production of metal clusters via MACS, the production of metal clusters using various cluster sources is examined here. In general, cluster science researchers have favoured the production of nanoclusters through cluster-beam methods, as they provide pristine (i.e. ligand-free) and well-defined clusters with a high degree of monodispersity.

Cluster-beam sources nearly all form clusters in the gas phase from the vaporised cluster material. Essentially, three stages are present in each source: vaporisation of material, nucleation of clusters and growth of clusters. Within each source a wide range of parameters (e.g. material, geometry, flow rates, pressure etc.) contributes to the exact attributes of the clusters produced (size, quantity etc.). The following section describes the general operation and characteristics of different types of cluster sources.

2.1.1 Thermal-Seeded Supersonic Expansion Source

Thermal-Seeded supersonic sources consist of a large crucible or "oven" over which a high pressure (several atm) of inert carrier gas is flowed (e.g. He). The carrier gas and metal vapour mixture pass out of the crucible chamber via a pinhole nozzle, undergoing supersonic expansion. Figure 2.1 gives an example of a typical thermal seeded supersonic expansion source. The large crucible is used for two reasons: firstly, a high metal vapour density is needed to reach supersaturation.[38,58] Secondly, the metal evaporant has low directionality and a small interaction cross section. Therefore, high densities are required to provide adequate material out of the source. As a result, significant amounts of material are deposited on the chamber walls and a large feedstock is necessary to avoid frequent venting.

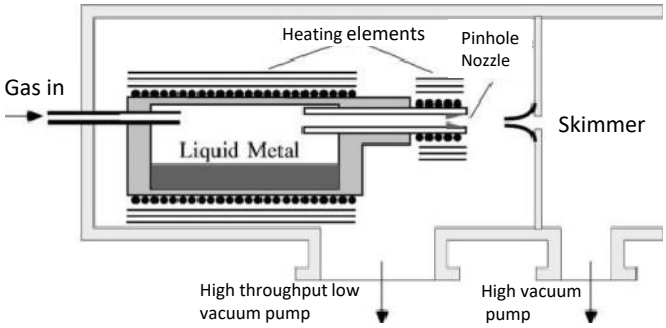

Figure 2.1: Schematic of an oven-type seeded supersonic expansion cluster source. The large surface area of liquid metal exposes a high vapour pressure of metal (several mbar) to the carrier gas (several atm). This is adiabatically expanded through the nozzle to condense clusters. This schematic was reproduced from [59].

Prior to expansion, small metal clusters are formed through three body collisions between two hot metal atoms and a single colder gas atom. The resulting gas-metal mixture undergoes adiabatic expansion, as it passes through the nozzle, cooling to form a supersaturated vapour, which then condenses further.[60] After formation, nanoclusters continue to grow through collisions; however, due to the high temperature of the source it is difficult to stabilise large clusters (e.g. great than a few hundred atoms) as they grow.

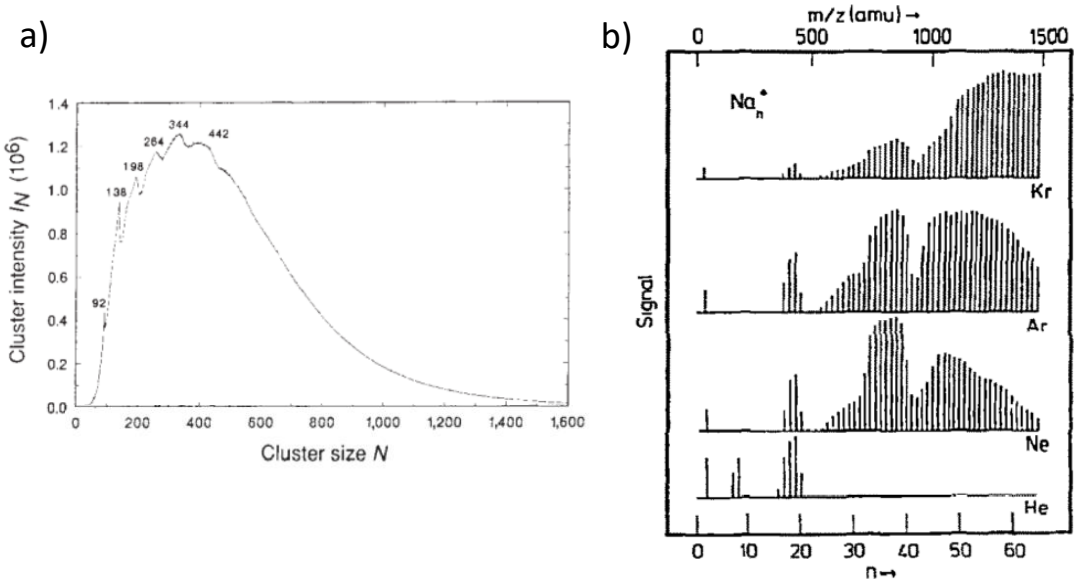

Figure 2.2: Panel a) shows a mass spectrum of large Na clusters produced by seeded supersonic expansion. b) shows the mass spectra of sodium clusters produced using different masses of carrier gases. As the mass increases so to does the resulting mean cluster size. These graphs are reproduced from [61, 62].

Figure 2.2 a) shows a mass spectrum of sodium clusters produced by a thermal-seeded supersonic source, demonstrating the production of large particles by this method (normally limited to <200 atoms[38]). The peak size is 344 atoms, produced with a mass resolution of ∼0.6 (Peak size over FWHM). Figure 2.2 b) illustrates the effect of carrier gas mass on the cluster size produced. As the mass of the carrier gas increases, larger clusters are formed, due to improved cooling, entrainment and slowing of the metal diffusion. As the entire source is heated, evaporation is limited to lower temperature materials with a maximum melting point of around 1300 K.

The main advantage with this type of source is the capability of producing very high neutral nanocluster yields, in the best cases of the order 10^{18}-10^{19} atoms per second.[58,63]

2.1.2 Liquid Metal Ion Source

The principle of the liquid metal ion source is relatively simple: a metal is liquefied and applied to a sharp heated tip. A large voltage (few keV) is applied between the tip and a counter electrode. As the metal proceeds along the tip, the tip narrows increasing the charge density. At a critical point the charge density will be sufficiently high to cause the metal to spray off, similar to electron field emission. This was seen as a possible source for high production as the main limiting step is producing a liquid metal reservoir (multiple tips could even be used if required). The source would even provide ionised particles owing to the ejection method from the tip, significantly removing losses due to ionisation efficiency. An example of such a source is given in Figure 2.3.

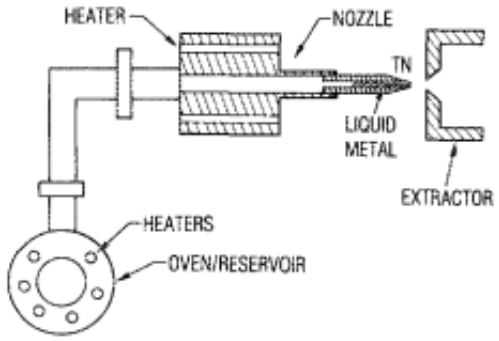

Figure 2.3: Schematic of a liquid metal ion source, reproduced from [64].

Unfortunately, there are several limitations of the nanoclusters produced by this source. Firstly, they have a wide energy spread, due to the formation mechanism,[64] which leads to relatively low resolution mass spectra. Furthermore, the nanoclusters contain very high internal energy, which in the absence of a cooling medium, strongly inhibits the growth of the nanoclusters. The source, however, is an efficient way of

producing low melting point metal ions (singly and multiply charged).[65,66]

2.1.3 Laser Ablation Source

The laser ablation cluster source is somewhat of a hybrid between the gas aggregation source and seeded supersonic source. First developed at the Smalley lab, it employs a laser to vaporise cluster material, which is subsequently expanded through a supersonic nozzle.[67] A schematic of a typical laser ablation cluster source set-up is shown in Figure 2.4. The cluster material feedstock is usually a rod (although almost any shape can be used in principle). This is usually rotatable and translatable, allowing even ablation of the surface. The source material is vaporised by high-power focused laser pulses. This gives great flexibility in cluster material that can be utilised (including semiconductors, refractory metals, etc.). The hot ablated atoms are then subjected to a pulse of cooling carrier gas, promoting nucleation and cluster growth. The mixed gas then expands through a supersonic expansion nozzle (continuous expansion has also been demonstrated).[68]

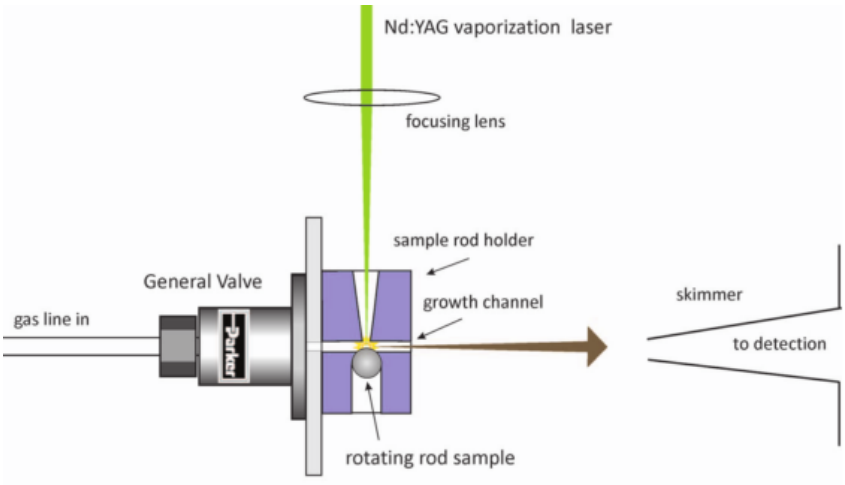

Figure 2.4: Schematic of a laser ablation cluster source, reproduced from [69]

The peak size produced from laser ablation is similar to that of seeded supersonic expansion in most cases (i.e up to a few hundreds of atoms). The caveat is that, as only a small volume is heated, the cooled carrier gas can therefore effectively cool the

sputtered material prior to expansion. As such, larger clusters can be stabilised in principle. The extent of this aggregation is limited due to system geometry. Figure 2.5 shows a mass spectrum of niobium clusters produced by laser ablation. Sizes up to about 1000 atoms are achieved, with a mass resolution of 0.5 (peak size over FWHM).

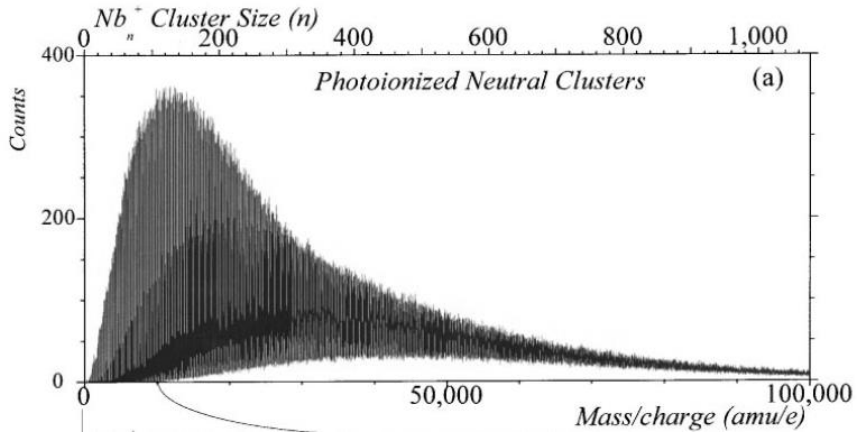

Figure 2.5: Mass spectrum of photoionised Niobium clusters produced by laser ablation with a Nd:YAG laser. The peak cluster size is about 130 atoms. This figure is reproduced from [70].

.

The most significant advantage of this type of source is the range of materials that can be vaporised to form clusters. Complex formations of clusters can be produced by the use of alloy targets or the careful introduction of additives.[71–73] The average flux is generally somewhat lower than gas aggregation and thermal seeded sources due to the pulsing of the laser and loss of nanoclusters in the narrow extraction channel.

2.1.4 Pulsed Arc Discharge Source

Pulse arc discharge works in a very similar way to that of laser vaporisation. Essentially, the laser is replaced with an electrical arc source. An example of such a source is shown in Figure 2.6, where the laser entrance is replaced with a second electrode. A bias is applied between the two to create a discharge (up to tens of kV).

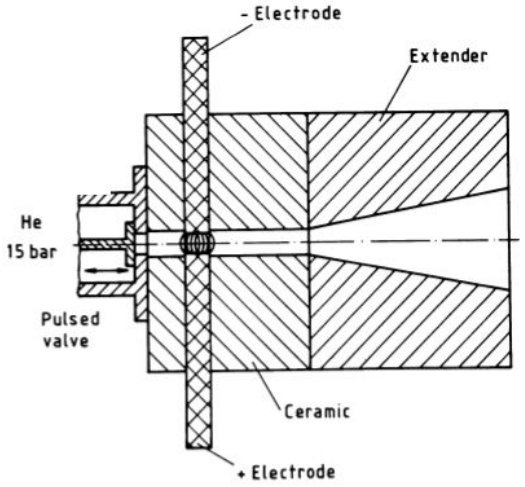

Figure 2.6: Schematic of a Pulsed Arc Ionisation Cluster Source (PAICS), reproduced from [60].

PAICS can discharge more material and permits a faster pulse rate than most lasers (>100 Hz). There are some sacrifices for the improvement in yield. Firstly, the discharge is less consistent in terms of yield, pulse energy and duration. Although not quite as refined as the laser ablation source, high production rates are achievable (deposition rates of up to 2 $\mathring{A}$ per pulse)[74,75] and the ionisation yield is higher ($\sim$ 10 %). An example of a mass spectrum from a pulsed arc cluster source is shown in figure 2.7, giving a peak size and mass resolution of 7 atoms and 0.4 respectively. A significant advantage of the PAICS is the low set-up cost, not requiring a pulsed laser, magnetron, etc.

Both arc and laser ablation methods have been employed in liquids, demonstrating production of large quantities of clusters. The liquid forms a highly effective

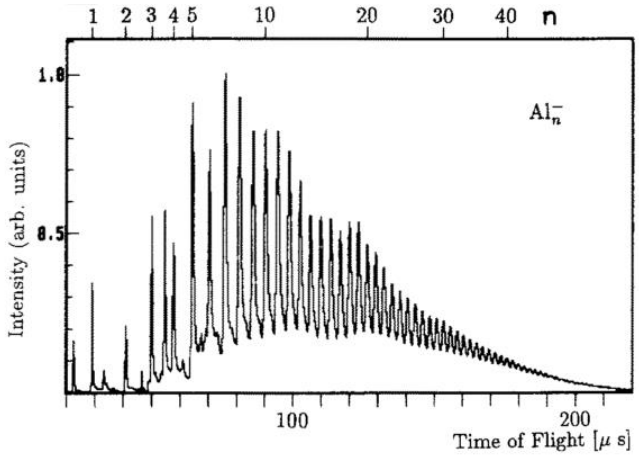

Figure 2.7: An example of Aluminium clusters produced by pulsed arc discharge and using a liquid nitrogen cooled carrier gas. This mass spectrum is reproduced from [75].

cooling medium and allow increased capture of the discharged material.[76–78] The size control, however, is reduced compared to other physical methods described here.

2.1.5 Magnetron Sputtering Gas Aggregation Source

Gas aggregation sources use a vaporisation source to supply cluster material (e.g Knudsen cell, filament, magnetron sputter head). Lower metal vapour pressures are achieved compared with oven type sources; however, the chamber and carrier gas can be cooled (e.g. by liquid nitrogen). This cooled carrier gas is mixed with metal vapour (mbar range) and passes through an expansion nozzle. Dimer clusters are formed in three body collisions, which then subsequently aggregate by adatom-cluster or cluster-cluster collisions.[60,79–81] Growth essentially stops after expansion through the nozzle due to the lower pressure.

An example of an aggregation cluster source is shown in figure 2.8. In this case, a magnetron is used as the vaporisation source. The magnetron provides the additional advantage of being able to evaporate a wide range of materials (using RF and DC modes). Alloy targets and dual magnetron systems provide a route to produce more complex and exotic particles.[82–85] The magnetron source has another

intrinsic advantage, in that ∼30% of the clusters produced are charged due to the plasma.[86]

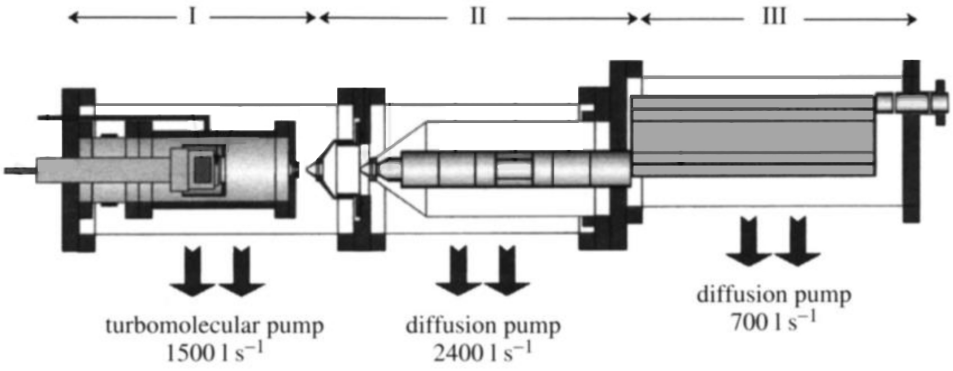

Figure 2.8: Schematic of the magnetron sputtering gas aggregation source at NPRL. Section I shows the source including the magnetron, condensation chamber and expansion nozzle. Sections II and III show the skimmer, ion optics and TOF mass-filter, respectively. This illustration is adapted from [87].

The size distributions of binary clusters produced using a dual magnetron source is shown in figure 2.9. For Pd-Sn clusters, the cluster size obtained peaks at $\sim 6\times10^5$ amu, showing that this method results in the generation of significantly larger clusters than the previously described sources. The mass resolution in this case is 0.7 (peak size over FWHM). Although gas-phase cluster formation is a complex process, significant insight can be gained by the application of classic nucleation theory. To form a liquid droplet from the gas phase, a critical radius is required such that it can grow rather than evaporate. This radius derives from the Gibbs free energy of the droplet,[60]

$$\Delta G = 4\pi r^2\Gamma - \frac{4\pi r^3}{3V}kTln\frac{P_v}{P_s}$$

where r is the droplet radius, Γ the surface tension, V the volume of an atom, k is the Boltzmann constant, and T the temperature. P_v and P_s denote the vapour and saturation pressure at Temperature T, respectively. The maximum of this equation is found when the differential of ΔG with respect to r is zero, i.e.

$$r = \frac{2V\Gamma}{KTln\frac{P_v}{P_s}}$$

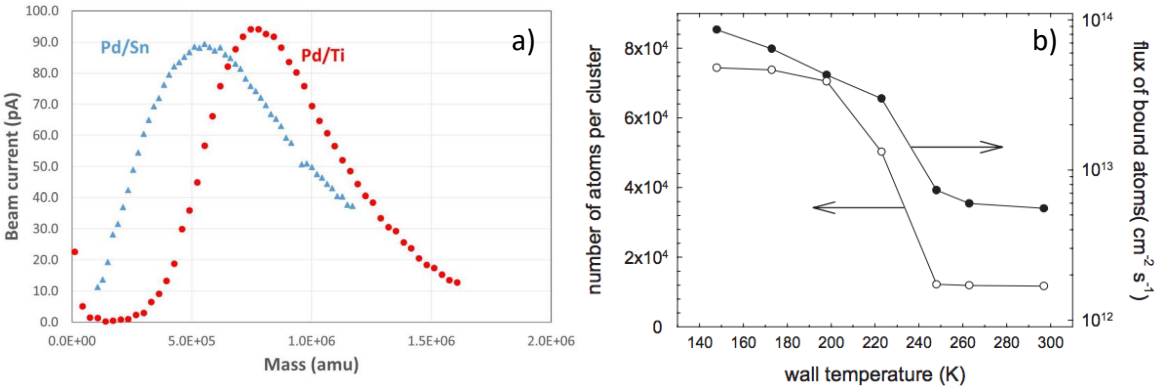

Figure 2.9: The mass spectra of binary Pd/Sn and Pd/Ti clusters produced from a dual magnetron gas aggregation system are shown in a). For Pd/Sn, a peak size of about 6×10^5 amu is observed with a mass resolution of 0.7. b) Illustration of the effect of the argon carrier gas temperature on the size of clusters produced and total amount of atoms deposited. The values are based on AFM measurements of deposited clusters. These graphs have been reproduced from [84, 88].

This is known as the critical radius. Anything larger will sustain growth, whereas anything smaller will eventually decompose. Although both seeded supersonic expansion and gas aggregation can form dimers from three body collisions after passing the critical nucleation point, the seeded source is unable to provide sufficient cooling to stabilise larger clusters. The gas aggregation source, on the other hand, permits the formation of large clusters ($\sim10^5$ atoms) through repeated collisions with cooled carrier gas.[84–87]

There are several limitations of this classical model, as macroscopic surface and volume energy contributions are considered, the fine microscopic structure of the cluster is neglected. This significantly reduces it's validity for small clusters (2 nm and below) where these effects are more pronounced. Even at larger sizes quantitative information is difficult to extract and care must be taken in the temperature, size dependencies.[89] Despite this several qualitative trends in cluster size for experimental can be ascertained from this treatment, these are summarised in Table 2.1. One example of the dependence of cluster size on a preparation parameter is illustrated in figure 2.9 b), where the chamber walls of a magnetron system are cooled

to different temperatures and the resulting mean cluster size analysed by AFM. The cold chamber walls pre-cool the carrier gas, allowing it to more effectively cool the sputtered metal atoms, this results in a larger low temperature region where clusters can be formed and grown, effectively creating a longer condensation length. A recent study indicates that more than just the size can be altered by the formation parameters. The magnetron power and condensation length during formation have also been demonstrated to alter the predominant geometrical structure of the nanoclusters produced.[90]

Table 2.1: The effect of various parameters on the size of nanoclusters produced by gas aggregation. Increases indicate a positive correlation between the variable and size, and reductions a negative one.

Parameter	**Effect on Cluster Size**
Increase in Carrier Gas Pressure	Increases Cluster Size
Increasing Carrier Gas Temperature	Reduces Cluster Size
Increasing Carrier Gas Flow Rate	Reduces Cluster Size
Increasing the Carrier Gas Mass	Increases Cluster Size
Increasing Metal Concentration	Increases Cluster Size
Increasing Aggregation Region Length	Increases Cluster Sizes

An overview of some of the main cluster sources has been provided in the previous section. Table 2.2 summarises the characteristics of these sources. This review demonstrates the wide range of different properties available. For a new source to be viable it must either exceed the current technology in some capacity or target a new niche. The initial investigation of MACS (see 2.3) indicates that both a greater flux of clusters (equivalent to a beam current in the range of mA) and size resolution ($M/\Delta M$ of 1.5) could be achieved.[91]

It is worth noting that in addition to cluster beam methods, a wide range of chemical synthesis methods exists for the production of nanoparticles and nanoclusters.[50,93] These methods have not been discussed here as they lie outside the scope of this work; however, the use of such methods plays a crucial role in the current production of commercial nanoparticles, particularly for catalysis. A common method

Table 2.2: Summary of characteristics of the cluster sources described above. In some cases, the maximum melting point of materials that may be used with a particular source is indicated. Source parameters depend on the precise experimental set up. Therefore, these numbers indicate approximate values under general working conditions. Data taken from numerous sources.[38,58,60,64,69,75,86,92]

Source	**Material**	**Peak Size (Atoms)**	**Charged State**	**TOF Peak Current (nA)**
Seeded Supersonic	<1300 K	<500	Neutral	10 nA
Liquid Metal Ion Source	<1300 K	< 100	Ions	10 nA
Laser Ablation	Any	<500	Neutral	few nA
Pulsed Arc Discharge	Conductors	<500	10 % Ions	few nA
Gas Aggregation	Any	10^5	30 % ions	few nA

is to start with a salt containing the desired cluster material and form a supersaturated salt solution.[50,93] This is then reduced to the cluster material and capped with ligands to prevent continued aggregation. The size, shape and composition of the particles produced can be controlled by varying the experimental parameters. Generally speaking, these processes are able to produce much larger quantities of material and require less costly equipment, making them more economically viable. There are, however, limitations: the nanoclusters produced are capped, precise size selection is not possible, and the processing can lead to the production of undesirable by-products.

2.2 Magic Number Clusters

The interest and origin of cluster physics largely stems from the size-dependent properties of clusters. A key investigation of early sources was understanding the greater abundance of specific masses exhibited in the mass spectra of small clusters.[7,94] This section will provide an overview of the magic number phenomenon in TOF-measured gas phase clusters.

The increased abundance at specific cluster sizes, first observed for supersonic expansion-produced sodium clusters, can also be observed for other alkali metals.

The peaks are observed at N = 8, 20, 40, where N is the number of atoms, as shown in figure 2.10 a). This phenomenon is observed for clusters of other elements, e.g. for Ag^+ peaks are observed at 9, 21 and 41 atoms. The peaks in the abundance are consistent for elements occupying the same group number in the periodic table, indicating that the abundance can be linked to the electronic structure of the element. Further support for this observation is given by measurements of anion and cations of the same material. A shift of two atoms is observed in the high abundance peaks between anions and cations.[95]

The explanation of how the electronic structure causes the preferential formation of specific cluster sizes can be understood using the Jellium model.[38] The model considers that the valence electrons are a free electron gas essentially shared by the whole cluster. These electrons are confined by the uniform spherical field of the core. Once there are enough electrons in the cluster to form a complete shell (based on radial quantum number and angular momentum), further electrons introduced by additional atoms will have to fill a higher energy band. This will have an increased configuration energy cost, lowering stability.

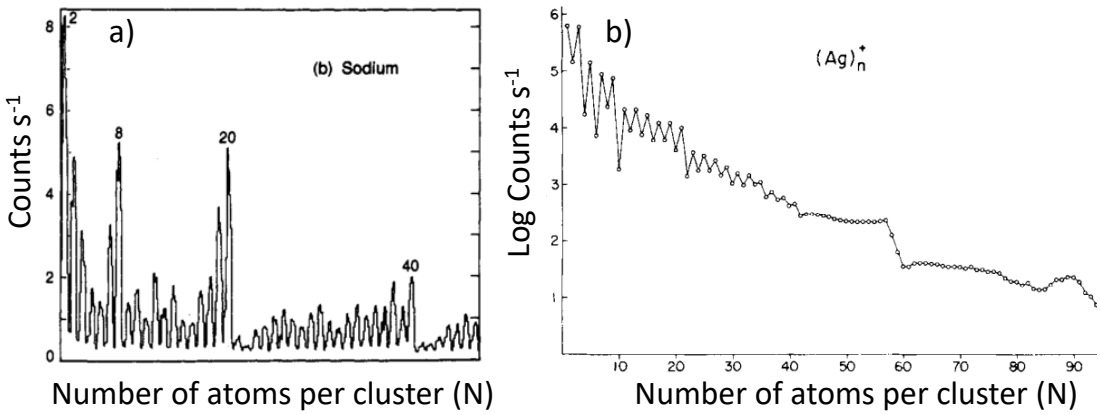

Figure 2.10: a) Shows the measured abundance spectra of sodium clusters, this demonstrates increased abundance at specific sizes. b) shows a similar phenomena in the abundance spectra of silver clusters. These graphs have been reproduced from [94, 95].

There are, however, several discrepancies in experimental results: the fine struc-

ture of abundance peaks between full shells do not match well to those predicted by the Jellium model. Furthermore, at larger sizes, peak abundances with an increasing periodicity were observed. The intermediate peaks were reconciled by the adaptation of the model to include non-spherical (distortions) in the cluster shapes (i.e. distortions to the confining spherical field) for intermediate filling (in accordance with the Jahn-Teller theorem).[96] A comparison of the formation energy predicted by the two models is given in figure 2.11.

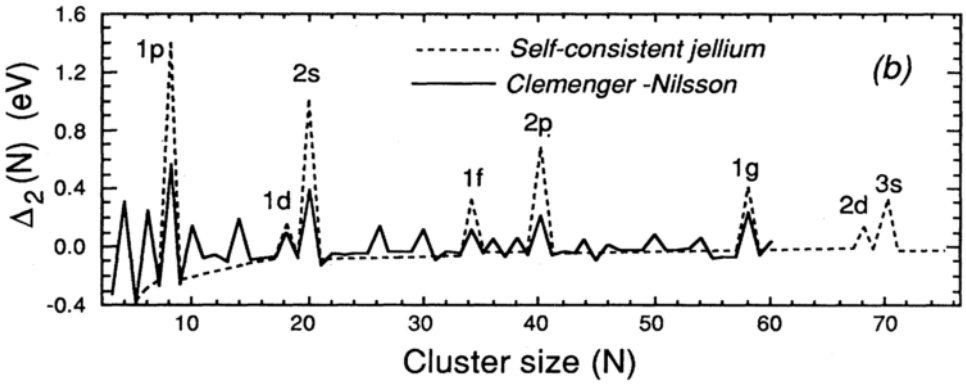

Figure 2.11: A comparison of the Jellium model and Clemenger-Nilsson adaptation. The adaptation allows non-spherical core distortions formation and therefore non-spherical confining potential. This gives rise to a different fine structure in the stability as a function of size predicted based on energy cost. Reproduced from [38].

However the changing periodicity observed presented a more significant challenge, which could no longer be matched to electronic shell filling. By plotting the abundances against $n^{1/3}$, i.e. volume, the period of the peaks becomes constant. The abundance here is dictated not by the electrical shell filling but by geometric shells.[97] The peaks for geometric shell filling can become more complex, as it is possible to form several different structures from the same element requiring a different number of atoms to fill each shell.[98,99]

The crossover between electrical and geometrical shell filling dominance can be seen in the spectra of sodium clusters produced by gas aggregation (see figure 2.12). The crossover point is not defined intrinsically but depends on the experimental parameters. Generally speaking, the geometrical effects become more pronounced

as cluster size increases.[100,101] The elevation of temperature, however, reduces this effect as the structural binding is weakened. The geometrical shell filling abundance has been shown to be removed completely if the energy is sufficient to melt the clusters.[102]

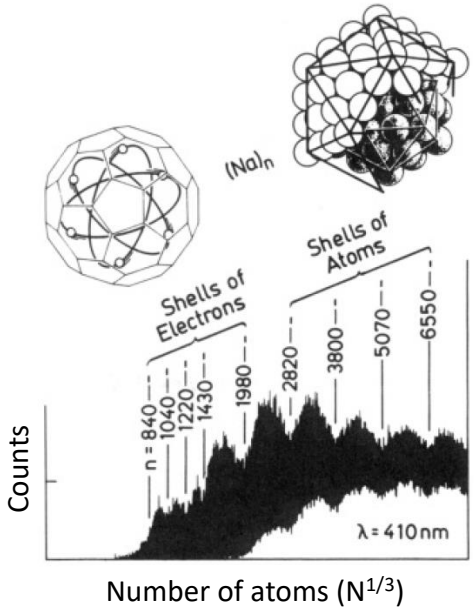

Figure 2.12: Mass spectra of sodium clusters, initial high abundances depend on electronic shell filling. At larger sizes the periodicity becomes dependent on the volume and matches geometric shell filling. Reproduced from [99].

2.3 High Flux Cluster Beam Sources

As the MACS is concerned with the increase of cluster flux towards the industrial R & D or batch production scale, this section aims to contextualise the source within the specific area of high flux nanocluster sources. The cluster beam sources, presented above, have demonstrated numerous improvements, not only in understanding, but also in the control of size, composition (binary materials, core-shell clusters), deposition, purity and even structure.[82,83,90,103–105] However, size-controlled cluster production rates, remain relatively low (<10-100μg/h).[86,106] Interesting developments are taking place currently across several research groups towards attaining

the goal of high nanocluster production rates from cluster beam sources (i.e mg to g).

A pioneer in this field is the Micro Plasma Cluster Source (MPCS).[107–110] Developed in Prof. Paolo Milani's lab, this couples micro plasma vaporisation with supersonic expansion and aerodynamic focusing.[111] A rod of cluster material is used as feedstock, which is sputtered in a pulsed fashion (∼10 Hz) (similar to laser ablation or PAICS). This is performed by injecting a small pulse of gas (normally helium). As the gas reaches the rod, a bias is applied (10^2 V), igniting a plasma and sputtering a localised area.

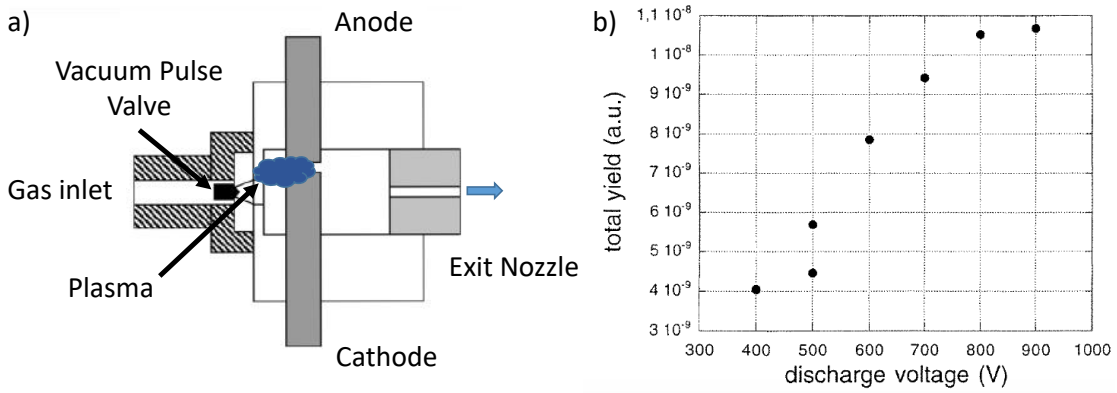

Figure 2.13: a) Schematic of an MPCS. b) Shows the effect of discharge voltage on material yield. Reproduced from [109].

The design of the pulsed micro plasma source is illustrated in figure 2.13 a), alongside the dependence of material yield on bias voltage, which is shown in Fig. 2.13 b). Initially, the increase is linear but diminishing returns are observed at higher voltages. The output can be further enhanced by careful choice of the pulse timings. In figures 2.14 a) and b) the effect of the ratio between the delay from gas pulse to voltage pulse (t^{i-d}) and the gas pulse duration (t_{on}) is investigated. The average size is almost an exact inverse of the yield, which is unexpected compared with the metal concentration in gas aggregation. As such, gas dynamics must have a significant effect on the cluster formation.

Another method of particle size control has been demonstrated by aerodynamic

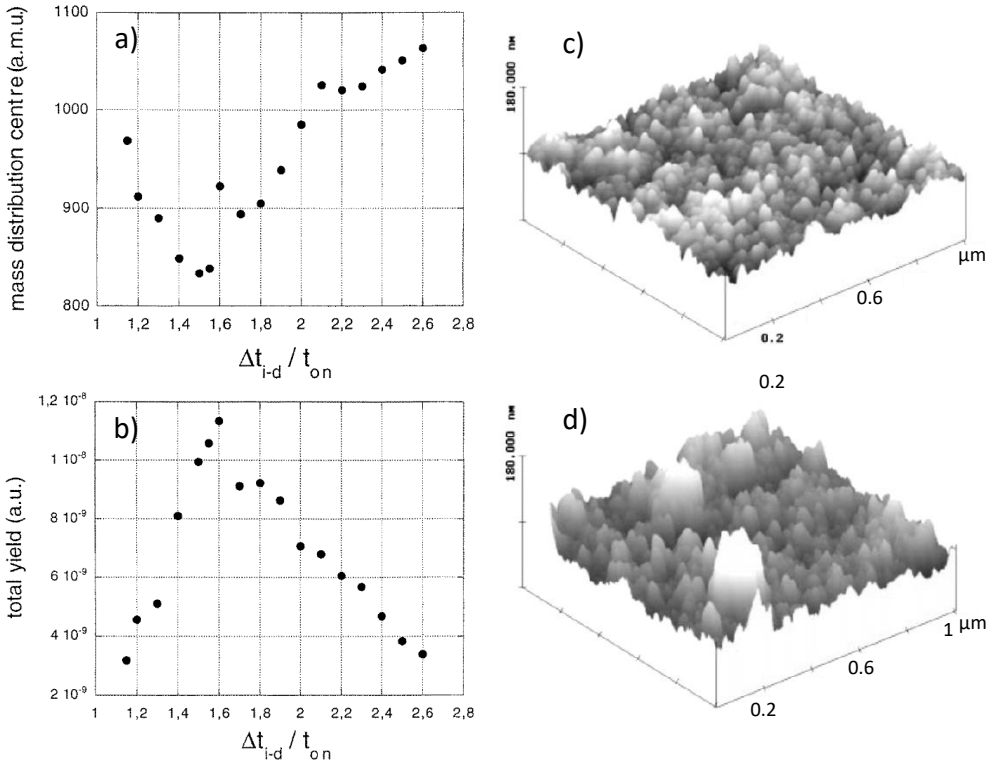

Figure 2.14: The intrinsic control over cluster size a) and yield b) produced is demonstrated by varying the ratio between the gas and voltage pulse delay (Δt_{i-d}) and gas pulse duration (t_{on}). Size can also be selected aerodynamically. Carbon films deposited from aerodynamically separated small c) and large d) nanoclusters show a change in roughness and grain size indicative separation. Images have been reproduced from [108, 109].

filtering.[108] Figures 2.14 c) and d) show the films made by depositing light and heavy clusters, respectively. The effectiveness can be seen in the grain size of the thin films produced (∼8 nm and 15 nm, respectively). Focusing has also been used to control the landing of particles leading to "site selection". The 2D position on the surface can be controlled by the aerodynamics of the source. In the case of soft materials, the velocity can be used to dictate the implantation depth.[112–115]

The MPCS is capable of high-scale production (of the order of 5 nm of material per minute) and relies on aerodynamic focusing and plasma sputtering parameters to provide coarse cluster size selection.[108,111] Since the original studies, a range of materials has been investigated.[113,116–118]

Recently, other high-flux sources have been reported based on different clus-

ter production techniques: a thermal supersonic seeded expansion source,[119] and a dual and tri-magnetron gas aggregation sources.[84,85,120] The thermal supersonic expansion-based source takes this high-flux source and deposits the clusters into a room temperature ionic liquid, providing an effective storage medium that limits aggregation (comparatively). The ionic liquid may provide a way to overcome the size limitation (discussed in section 3.3) as a controllable synthetic medium which both stores and grows the nanoclusters.

The dual magnetron gas aggregation source developed at Teer Coatings Ltd, removes the mass filtering step usually employed in order to gain greater flux. The charged fraction is directly deposited onto the sample achieving beam currents of around 100-200 nA, which compares with cluster beam currents of 0.1-1 nA which are normally realised using mass-filtered sources.[86] The system has two other interesting features, the dual magnetron configuration, which enables the production of binary materials with tunable gas phase material ratios, and the ability to deposit onto catalytic support powders using the novel vibrating cup deposition stage.

The schematic in figure 2.15 shows the configuration of the system. After aggregation, an octopole lens deflects the beam down to deposit on an agitated powder. The beam can also be allowed to pass through the beam deflector in order to reach a mass-filter that is used to take mass spectra of the cluster beam or perform size selected deposition. Binary clusters of PdSn and PdTi have been deposited onto catalytic support powders at weight loadings of $\sim$0.1 %. The catalytic properties of the produced catalyst powders have been compared to similar reference materials made by chemical routes (prepared by Johnson Matthey).

A summary of the results for 1-pentene hydrogenation are given in figure 2.15 b). The results for the chemically prepared samples are indicated by solid symbols, while the cluster beam-deposited samples are indicated by open symbols. The selectivity of the catalyst is plotted against the reactivity, the region of optimum catalyst performance is shaded in yellow (i.e. >80 % selectivity and activity). A large

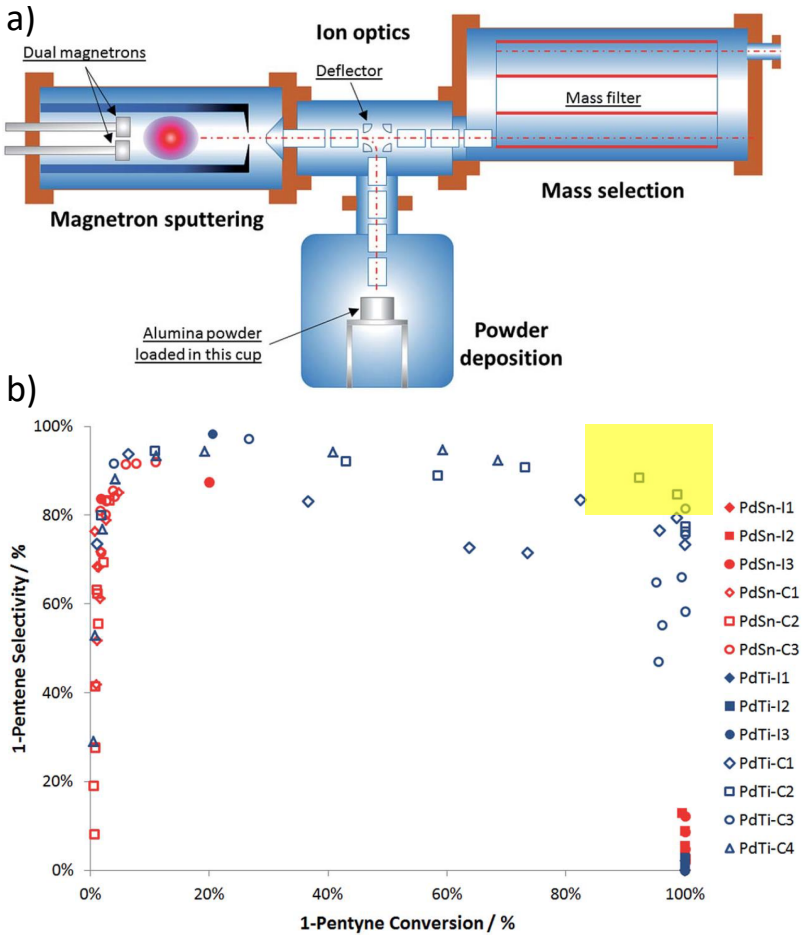

Figure 2.15: a) An illustration of the dual magnetron gas aggregation cluster source developed at Teer Coatings Ltd. This has been designed for deposition onto catalyst support powders. b) shows the comparison of the activity and selectivity of catalysts for 1-pentene hydrogenation. The cluster beam materials (open symbols) are compared with chemically synthesised clusters (solid symbols). Samples have been made with comparable size and stoichiometry. The yellow box indicates the location of ideal catalysts. Images are reproduced from [84].

number of the beam deposited cluster materials are found in or near this region. This is thought to be due to a more monodispersed end product from the cluster beam route i.e. controlled size, cluster surface interaction and no residual active site from production.

The three magnetron gas aggregation system is a commercial system produced by Oxford Instruments. The running parameters (relative magnetron positions, total and relative magnetron gas flows and condensation length) have been investigated in detail by researchers in the Institute of Material Science in Madrid.[121] This

configuration allows better control of the gas flow within the condensation chamber, allowing the extraction of a larger fraction of the formed clusters (growth rate ∼90 nm/min). Furthermore, the three magnetron setup allows the production of ternary materials with a controllable average stoichiometry.[120]

A schematic diagram of the three magnetron source is shown in figure 2.16 a). A second highly interesting property of the source is the ability to produce binary and ternary clusters with ordered shells. This is done by changing the order of the magnetrons (e.g. staggered in vacuum lengths). An example of a CoAu core shell cluster produced in this way is given in Figure 2.16 b). The shell ordering can be reversed by changing the position of the magnetrons and the core-shell ratio modified by the relative magnetron powers. The production of a ternary core-shell-shell particle has also been demonstrated.

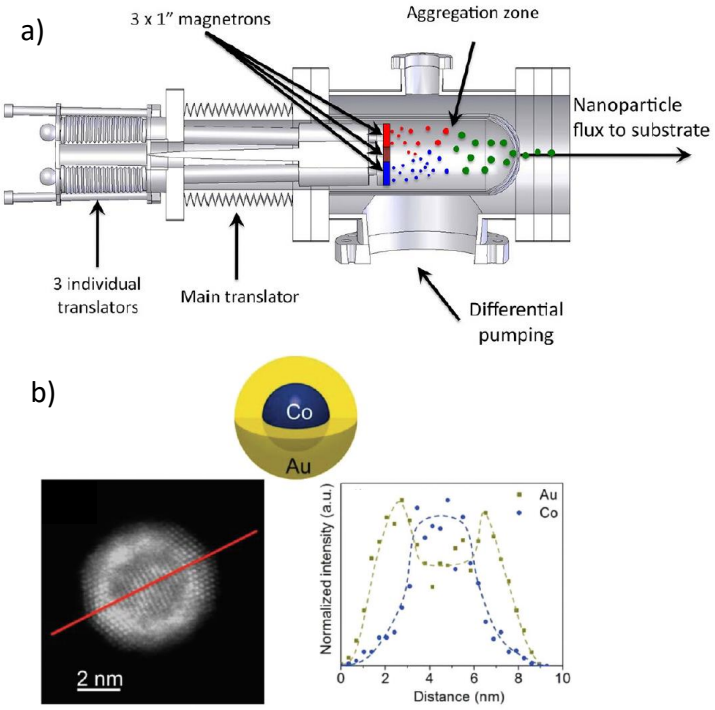

Figure 2.16: a) is a Schematic illustration of the Oxford Instruments three magnetron gas aggregation cluster source (b). An example of a binary core-shell cluster produced from the source. In this case, a CoAu cluster, the shell order and thickness can be controlled via the source parameters. Reproduced from [85, 120].

Each source has a very different specific niche role; however, for a general comparison the amounts of material produced by each system can be roughly compared based on their published numbers. An overview of the amount of material produced by each source is summarised in table 2.3.

Table 2.3: This table summarises the amount of material produced from various high-flux cluster beam sources. The values here are based on published results reviewed in section 2.3. For comparison, the measured films (MPCS, Tri-Magnetron) have been treated as having bulk density. In the case of the MPCS, the true density is known to be 40-60 % of bulk (the corrected number is given in brackets).The dual magnetron average cluster mass is estimated at 7×10^5 amu from reported mass spectra.

Source	**Thickness (nm/min)**	**Area (mm^2)**	**Current (nA)**	**Material (mg/h)**
Thermal Cluster Source	3.3	700	-	1.5
PMCS	120	28	-	46(23)
Dual Magnetron	-	-	200	5
Tri-Magnetron	90	1200	-	90

There is another system that has recently been reported with the potential to deliver a significant scale-up in cluster flux, the MACS, which is the main topic of this thesis. The MACS produces clusters via co-condensing a rare gas and cluster material film on to a mesh, which is then sputtered in transmission geometry to form, ripen and extract clusters.[91] A schematic outline of the MACS system can be seen in figure 2.17.

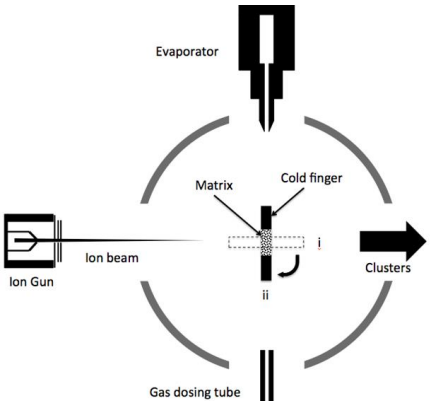

Figure 2.17: Scheme of the MACS1 system, a transmission mode Matrix Assembly Cluster Source (MACS). Reproduced from reference [91].

Figure 2.18 shows how the mean nanocluster size depends on the silver loading in the matrix. As the silver loading changes (1-10% by number of atoms) the mean cluster size varies from <100 to 1000 silver atoms (measured by HAADF STEM). In the best case, an intrinsic size control of ±10 % in the cluster diameter is achieved. This is equivalent to a mass resolution of >1.5 (Peak over FWHM). A 950 eV 70 nA ion beam was incident on the matrix for 60 s to deposit the clusters seen in the STEM image in figure 2.18.

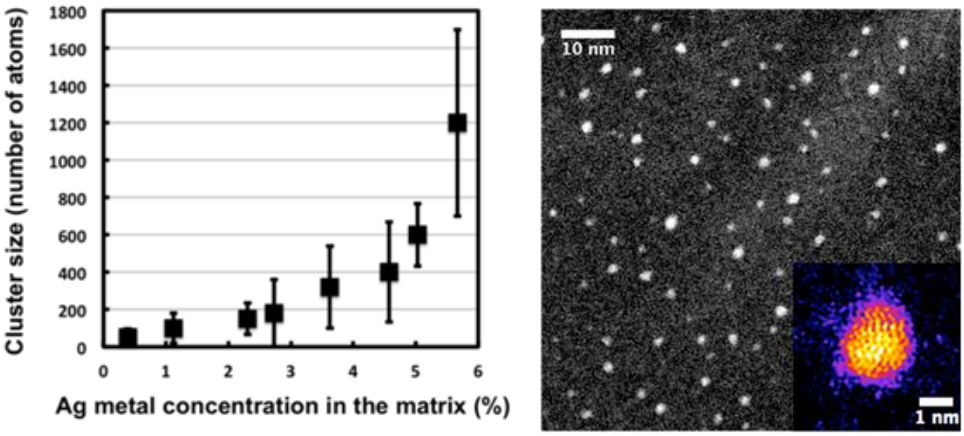

Figure 2.18: The left hand image shows the average size of nanoclusters created by sputtering argon matrices containing different concentrations of silver. The size is obtained by comparing the integrated HAADF intensity of clusters to that of a single atom. The right hand side is an HAADF STEM image of nanoclusters produced from a matrix with a 2.3% loading of silver atoms. Reproduced from [91].

The ultimate aim of the MACS is to increase the production rate of nanoclusters to an industrially meaningful level, i.e. g/h. The conversion efficiency of ions hitting the matrix to clusters is ∼3 % (i.e. excluding ions hitting the support grid). Commercial ion sources producing 1 A of ion current are available. If the process can be effectively scaled this would equate to a nanocluster production rate of ∼1 g/s (assuming a cluster size of Ag_{200}).

2.4 Applications of Nanoclusters

The previous sections demonstrate the significant effort invested in the production and characterisation of size-selected and size-controlled clusters. Fundamentally, nanoclusters bridge the gap between single atoms and bulk media. Understanding how the atoms arrange themselves in these clusters, and how this causes the properties we observe has been a key motivation. Scientific curiosity, however, is not the sole driving force. The novel properties exhibited by clusters have generated much interest.[3,8,59,122,123] These size-dependent properties have led to clusters being exploited in a wide range of applications from optics to theranostics.[113,115,118,124–126] In application terms, the size-dependent properties of these new materials represent a new palette of materials with unique characteristics.[53] The following sections outline two promising fields of application for clusters produced by MACS: nanocluster catalysis and biochips.

2.4.1 Nanocluster Catalysis

The field of cluster science has been strongly linked with catalysis since the seminal studies carried out by Haruta in the 1980s demonstrated the high catalytic activity of small gold nanoclusters.[26,122,127] Gold had previously been considered a relatively inert material due to its macroscopic properties. The results demonstrated that gold is an effective catalyst for CO oxidation even at low temperature. A graph from Haruta's work has been reproduced in figure 2.19, showing the turnover frequency of gold nanoclusters for CO oxidation as a function of diameter. The fact that it is not only a useful catalyst but also exhibits such a strong departure from typical bulk properties, generated a huge interest in the possibilities of nanoclusters as catalysts.

Depending on the reaction and catalyst, a different mechanisms can be responsible for the activity (e.g. low coordination sites, lattice strain, cluster surface interaction, compositional formations[128–132]). With sufficient control of nanocluster pro-

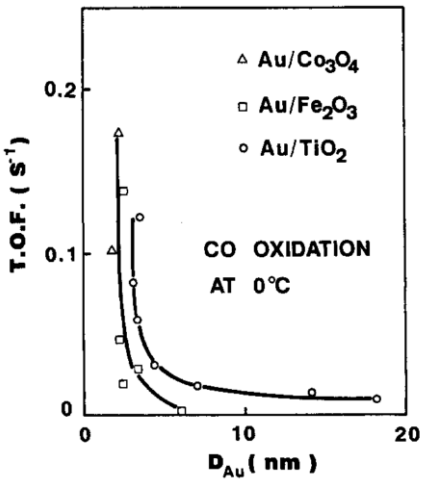

Figure 2.19: The turnover frequency of CO oxidation at 0 °C is compared for different gold particle sizes on a range of supports. The turnover frequency is given relative to the amount of exposed surface. Reproduced from [26].

duction, the active sites can be optimised to produce model catalysts. Ultimately, three main properties are key to a good catalyst: activity, selectivity and stability. The following pages showcase a few examples of small size-controlled nanocluster catalysts, demonstrating the potential of cluster beam produced nanoclusters in catalysis.

CO oxidation has often been used as a benchmark reaction for nanoclusters. A good example is given by Hutchings et al. who studied a series of different gold clusters on FeO_x to isolate the optimal cluster size for catalysing the reaction.[133] In this case, a bilayer of gold was found to be the most active size, questioning previous views that the active site is the cluster surface interface. Interesting work has also been carried out by Heiz and co-workers looking at the nonlinear catalytic properties of very small clusters.[134] This work demonstrates the level of optimisation possible with precise control of one's catalysts.

The high activity of nanoclusters has been demonstrated for other reactions too. For example, MoS_2 clusters have attracted significant interest since they were demonstrated to show high activity for the hydrogen evolution reaction.[131] Measured activity and DFT calculations showed that it sat just below the highly desirable

platinum metals. High activity has also been demonstrated for small clusters Pt (∼1.5 nm) for the oxygen reduction reaction, in this case increasing the effective activity per mass by 6 times compared with industrial standards.[135]

The combination of selectivity and reactivity is required for a good catalyst, in order to avoid unwanted products or catalysing reverse reactions. Selectivity is generally improved by having a more defined, uniform system. Unwanted defects on the surface or different size clusters may either play no role in the reaction or catalyse unwanted products. Thomas et al. demonstrated an example of this,[136] comparing the reactivity of chemically synthesised gold nanoclusters on silicon at a 5 % weight loading to that of the same sample leached with NaCN. Both produced identical activity for benzene alcohol oxidation; however, the leached sample now contained only 0.06 % Au loading. In this case, it appears that the vast majority of the initial material is just a spectator in the reaction.

An example of size-dependent selectivity is shown in figure 2.20 from Heiz et al.[137] Here, Pd_{1-30} clusters deposited on MgO are used to react C_2H_2. Until the cluster size reaches 4 atoms the reaction cannot be catalysed and does not progress to producing C_4H_8 until a cluster size of 7 atoms. In this case, the size restricts the number of units able to bond to the smaller clusters and, therefore, prevents specific reaction pathways. The production method has also been demonstrated to influence selectivity.[84] As shown previously in figure 2.15, similar nanoclusters prepared by cluster beam and impregnation have demonstrated different activity and selectivity. This is attributed to the formation of different active sites. Interestingly, the impregnated samples do not show both high selectivity and activity, which is thought to be due to the wider range of sites available from formation (e.g. ion exchange sites). In these two cases, the cluster beam method has helped to provide a more uniform and controlled catalyst-support system leading to increased selectivity.

There is generally an agreement that nanoclusters can be both highly active and selective catalysts. Small particles, however, are often viewed as unstable and at

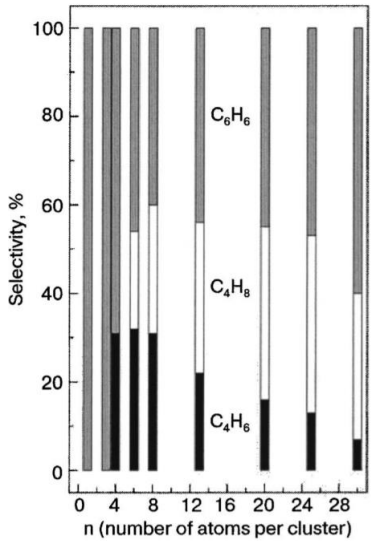

Figure 2.20: The selectivity of Pd clusters to catalyse polymerisation of C_2H_2 for different cluster sizes (1-30 atoms). Size-selected clusters were deposited on defect-rich MgO. Reproduced from [137].

risk of sintering or ripening under reaction conditions. Several studies show that even unprotected nanoclusters below 3 nm can remain relatively unchanged under mild reaction conditions.[138–140]

Figure 2.21 demonstrates two methods to retain cluster size distributions during reaction. Figure 2.21 a)-c) shows a series of STM images of Au_{70} clusters deposited on a graphite surface taken after annealing at different temperatures (room temperature to 643 K). The clusters were deposited with an energy of 1.7 keV to initially pin them to the surface. The initial pinning effect is shown to persist despite significant heating (up to 654 K), wide spread sintering is only observed at 873 K. In figure 2.21 images d)-f) demonstrate sintering resistance through the use of a narrow size distribution suppressing Ostwald ripening. Figure 2.21 d) shows the size of deposited Pt_{68} on SiO_2 before and after the reaction with He + O at 533 K for 5 h. Figure 2.21 e) and f) show Au_{923} deposited on amorphous carbon under heat treatment at 250 °C in He and He + O_2 (0.35 and 0.12 bar respectively). In both cases, the clusters have been soft-landed and it is clear that heating them in the reactive environment does not significantly effect the mean cluster size.

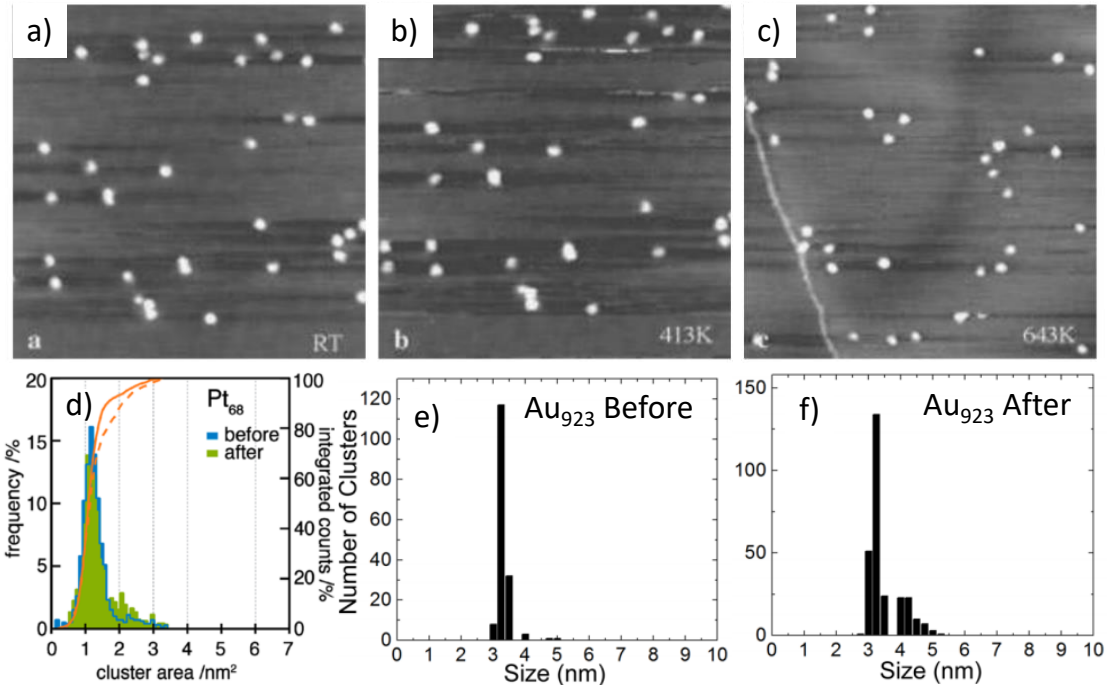

Figure 2.21: a)-c) STM images of Au_{70} clusters pinned on graphite. The clusters have been deposited at high energy (1.7 keV) to pin them to the surface and are then annealed at different temperatures. The pinned clusters remain immobilized on the surface even after annealing at 643 K. d) The size of Pt_{68} clusters soft-landed on SiO_2 (blue). They are then exposed to a hydrogen-oxygen mixture at 533 K for ∼5 h and remeasured (green). e) and f) show the effect of heat treatment on size-selected Au_{923}. e) is subject to 0.35 bar He at 250 °C and f) 0.12 bar He + O_2 at 250 °C. These images are reproduced from [138–140].

The examples presented here highlight the potential of nanoclusters in catalysis and, in particular those produced with a high degree of size and compositional control (like those created by cluster beam methods). In his recent review of precise catalysts, Prof. Stefan Vajda highlights the fact that the field has been hampered by the difficulty in producing significant quantities of size-selected, highly defined and characterised particles.[106] The range of high-flux sources under development discussed in section 2.3 may be able to remove these restrictions!

2.4.2 Biotechnological Applications

Nanotechnology has developed a growing link with biotechnological applications. Nanoclusters and nanoparticles, in particular, have demonstrated a range of uses within the biotechnology sphere, i.e. drug delivery, image markers, radio sensitisers, theranostics and diagnostics.[126,141–148]

Several examples of these are illustrated in figure 2.22. Figure 2.22 a) shows two possible methods of the bio-functionalisation of nanoparticles. In the first case, a protein is bonded non-specifically to the bio-ligand, i.e. to existing common groups. In this case, no modification of the protein is required but orientation is not controlled. The second method employs a specific binding site by modification of the bio-ligand. This allows control over the binding site and, therefore orientation. However, the modification may affect function. The use of antibody-conjugated Au particles has been investigated for cancer detection. The idea is that when mixed with cells, the antibody will lead to a specific attachment to cancerous cells. As such, there will be an increased concentration of Au particles around cancerous cells, which can be detected by light scattering or surface plasmon resonance.[149] Light scattering images of antibody conjugated Au particles mixed with non-cancerous and cancerous cells are shown in figure 2.22 b) and c), respectively.

Radio-sensitising is another application for metal nanoparticles. The idea is that the nanoparticle acts as an absorption centre for radiation allowing a targeted dose of radiative energy to be delivered to localized areas containing nanoparticles. Therefore, tumour regions could be preferentially targeted by the addition of nanoparticles. Tumour growth after radiation therapy with different size implanted Au nanoparticles is shown in figure 2.22 d). Growth at 21 days after radiation therapy was between 40 % and 140 %, compared to ∼300% and ∼500% without Au nanoparticles and without any radiation respectively.

One specific application of MACS-produced clusters is in label-free biochips. Biochips can take several different forms depending on the measurement require-

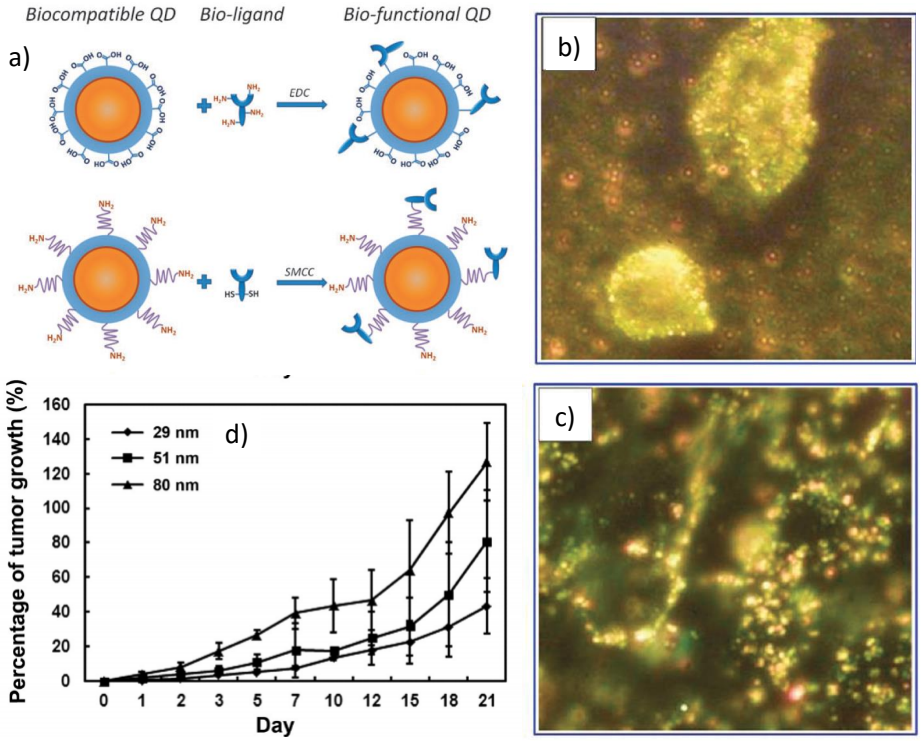

Figure 2.22: Nanoparticles have many potential biotechnological applications. A few examples are given here: a) shows two possible methods of bio-functionalization of nanoparticles by specific and non-specific attachment. b) and c) are light scattering images of cancerous and non-cancerous cells, respectively, mixed with antibody conjugated gold nanoclusters. Lastly, d) shows the use of nanoparticles as radio-sensitisers, comparing the growth of tumours after radiation therapy using different size nanoparticle radio-sensitisers. These images are reproduced from [126,142,149].

ments. The main types are antibody/antigen array, functional array and capture array.[150] Simple antibody arrays are designed to detect a specific protein, functional arrays are designed to investigate protein interactions, and capture chips retain molecules that interact with a specific protein.[150] Antibody arrays will be the focus for the remainder of this section. This type of system relies on the use of a protein with a specific binding site only accessible to the target protein, e.g. an antibody antigen pair. An array of such proteins is immobilised on a surface presenting the specific binding site away from the surface. As a solution is passed over this surface, if it contains the matching partner, it will bind to the specific site. The final requirement is that this binding must effect a measurable change to report the capture and, therefore, presence of the specific protein.

Two difficulties when making biochip systems are effectively immobilising the capture protein in the desired orientation without modifying its biological function,[150–152] and measuring an observable response from binding. Several methods exist to generate an oriented layer of proteins. When depositing across an entire surface, however, a significant difficulty is non-specific binding (the binding of unknown or undesired materials).[150] This can be mediated by the use of additional blockers; however, this introduces cost and complexity into the system.

A common method employed to observe if a protein has bonded to the capture molecule when studying the role and processes of proteins is the labelling of the target proteins with an optical dye or reporter.[153–155] This is not ideal, when working with an unknown solution, as is the case for antigen detection. As such, it is preferable if the capturing system can provide the response to binding; this is known as a label-free biochip.[156] Both charge transfer to the supporting substrate and dye capture/modification have been demonstrated as methods of reporting the attachment in particular cases.[157–159]

Figure 2.23 shows the scheme of a capture system, employing a fluorescent dye (rhodamine) as the reporter. The dye initially starts bound close to the biochip surface (before capture). The close proximity with the gold surface quenches the fluorescence. After the introduction of an additional DNA chain, the dye is displaced away from the surface enhancing the optical signal (after capture). The graph in figure 2.23 b) shows the optical emission after excitation in three different states: the bare surface (trace a and d), the immobilised capture protein (trace b and e), and after capturing an additional DNA strand (trace c and f). After capture, a significant increase in light emission is observed.

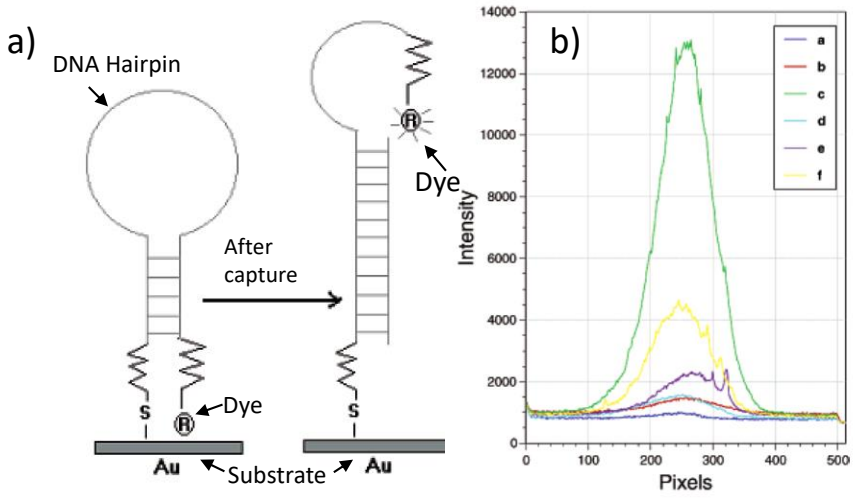

Figure 2.23: a) gives the scheme of a capture response based increase of optical emission due to dye displacement. Initially, the fluorescent dye (rhodamine) is close to the gold surface quenching its optical emission. After capture of an additional DNA strand the dye is displaced away from the surface causing greater light emission. b) shows a series of plots of the light emission from the system for the control (trace a and c), pre-capture (trace b and d) and post-capture cases (trace c and f). These images are adapted from [157].

Multi-functional nanoclusters may be able to provide the solution to both oriented immobilisation and reporting antibody capture. Small metallic nanoclusters are known to bind strongly to thiol groups.[160] Furthermore, nanoclusters produced by cluster beam methods can be immobilised on a wide range of surfaces if given sufficient energy to be pinned.[103] By first immobilising the cluster by deposition at appropriate pinning energies and then the anchoring of the capture protein by cluster-thiol bonding, the entire capture system can be fixed on the surface.[161,162] Figure 2.24 demonstrates the immobilisation of proteins on the surface by size-selected clusters (measured by tapping mode AFM).[162,163] In a) desmoplakin molecules tagged with cysteine molecules have been deposited on a clean HOPG substrate, whereas in b) the HOPG, surface is first decorated with size-selected Au clusters (147 atoms deposited with 23 eV per atom). After scanning with the AFM, the molecules in a) are displaced away from the area. In the size-selected cluster case, the area remains decorated due to the anchoring between the cluster and molecule. In figure 2.24

c) and d) two different proteins, human oncostatin M and green fluorescent protein (GFP) respectively, are deposited onto size-selected clusters. The GFP is unable to attach due to the inaccessibility of the binding site.

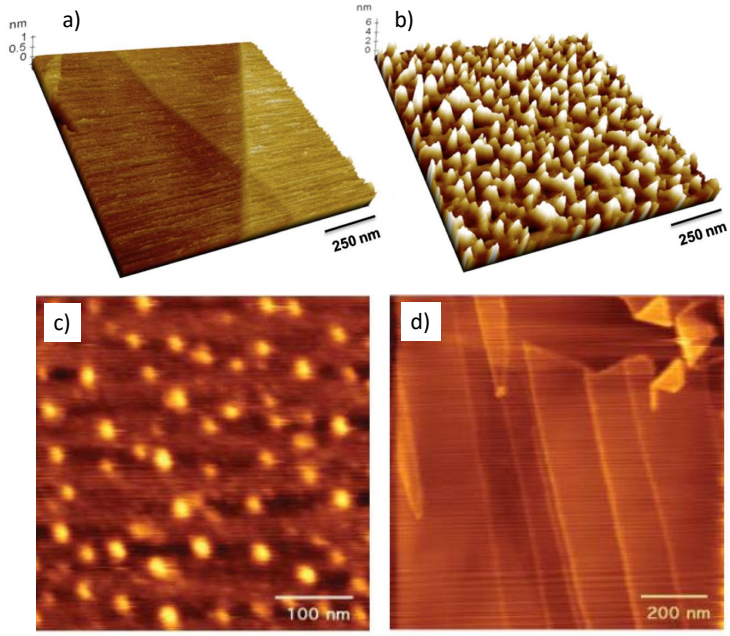

Figure 2.24: a) and b) are liquid phase tapping mode AFM images of desmoplakin molecules deposited on a HOPG surface. a) shows the surface after deposition of desmoplakin onto a bare HOPG surface, the proteins can't attach and are cleared from the surface after one scan. In b) the surface has been covered with pinned Au_{147} clusters before the protein was added. c) and d) show human oncostatin M and green fluorescent protein(GFP) deposited onto HOPG with size-select Au_{40} clusters. The oncostatin c) binds to the cluster and is immobilised. Furthermore, due to accessibility of the binding site a preferential orientation is observed. The GPF does not bind to the clusters due to a lack of site accessibility and is removed by scanning, as seen in d). These images are reproduced from [162, 163].

Even more critically, if multiple binding sites are available but of different accessibility the predominant orientation of the protein binding can be fixed leading to a predominant orientation of the protein on the surface.[163] This is observed in the human oncostatin M shown in figure 2.24 c), based on the height measurement of the attached proteins. Further to this, by modifying the cluster size one can control the number and, to an extent, the type of available binding sites.[162, 164]

To address the needs of biochips, the cluster must not only immobilise the capture protein but also provide a method of measuring the antigen capture. A way

to do this could be through optical response. Simulations indicate that small silver clusters coupled with peptides can enhance the optical absorption properties of the peptide.[165,166] Figure 2.25 a) and b) show the simulated absorption of hybrid cluster-bio system (tryptophan dipeptide and tripeptide).[167] It can be seen that the light absorption of the system with the addition of the silver clusters is greatly enhanced. This is also significantly different from spectra of silver without the attached peptide (peak at 310-320 nm). Figure 2.25 c) shows an example of Tryptophan with Ag_3. In this case, experimental (red), theoretical (black) and Lorentzian broadened theoretical results (blue) are presented.[166] Again, the bare cluster is distinguishable from the cluster bound to the tryptophan. These calculations have also been extended to clusters supported on a surface.[167]

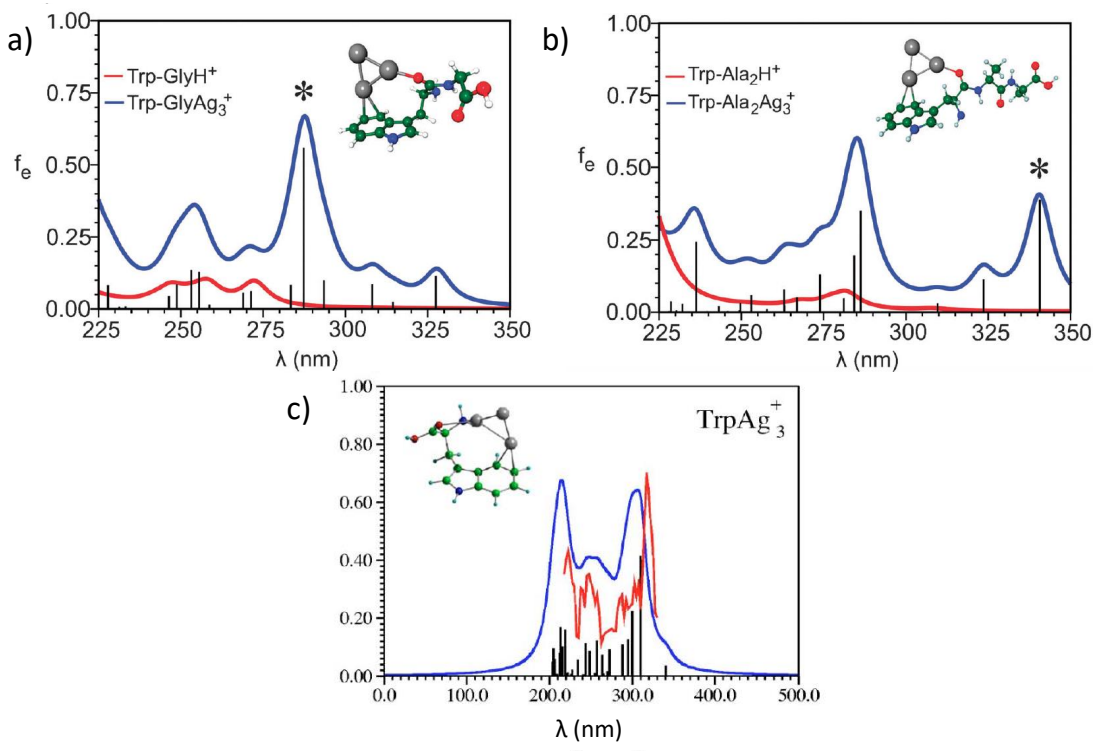

Figure 2.25: a) and b) show the simulated absorption spectra of hybrid cluster-bio system (tryptophan dipeptide and tripeptide). Enhanced absorption is observed in the silver containing systems. c) gives a similar example however, here experimental (red), theoretical (black) and Lorentzian broadened theoretical results (blue) are available. These images are reproduced from [166, 167].

These studies demonstrate that, by careful choice of system, small metal nan-

oclusters can provide a specific binding site to arrange proteins on the surface. The presence of the nanocluster can also lead to an enhancement of the visible range optical absorption properties of the system. These two attributes of small metal nanoclusters make them an ideal candidate to investigate the formation of a label-free biochip. The initial step of surface immobilisation is demonstrated with non size-selected MACS clusters in section 5.6.

Chapter 3

Scaling up The Transmission Mode MACS

This chapter covers the work relating to scaling up cluster production in the MACS (as outlined in section 2.3). Firstly, the chapter further examines the MACS concept and explains developments made in upgrading the source. Results obtained for the production of silver nanoclusters from this source are presented demonstrating the development of the source into a robust high-flux system. This work has been carried out by the author and Dr. Lu Cao. All STEM measurements have been taken by Dr. Cao. Finally, the system has been further improved by the integration of a fully computer-controlled TOF mass-filter, for which the author was primarily responsible.

3.1 Introduction

The new method of cluster production via matrix assembly has been briefly introduced in chapter 2.3. A more detailed examination will be provided here. The MACS produces clusters through ion bombardment of an inert rare gas matrix loaded with cluster material, i.e. Ag or Au. In order to produce a solid rare gas film the matrix support is cooled to <20 K. The matrix is then co-condensed from an atomic vapour

of cluster material atoms and the rare gas. The matrix is grown to a thickness up to hundreds of nanometers before sputtering. The matrix is then bombarded by argon ions with a few keV energy to produce clusters. The conceptual idea is that this method can provide two advantages compared with gas phase aggregation methods: firstly, the collision cross-section of metal atoms should be increased due to the higher density of the materials, and secondly, the solid rare gas matrix provides better cooling during three-body collisions. This should lead to increased cluster formation through larger numbers of initial collisions.

3.2 MACS in Transmission Mode

In this thesis, it is demonstrated that the MACS can run in two distinct modes: transmission and reflection. The difference is the type of support employed for matrix formation. In the case of reflection, a flat copper matrix support plate is used and clusters are collected as they are ejected out of the plane of the support (i.e. the surface normal $\pm$ 90 °). The transmission mode uses a high density holey membrane, i.e. TEM grid or quantifoil.[168] The matrix is then formed from material deposited onto the bars in a layer-by-layer type growth (unpublished work conducted at NPRL). The ion beam is incident normal to the surface of the support, i.e. in the case of the mesh support the ions will be incident at a glancing angle to the sides of the holes in the mesh. To have the best efficiency in terms of cluster production per incoming-ion, a high transmission mesh is required and complete coverage of the holes with a matrix. High hole density membranes with small pores (< 5 μm), such as quantifoil, provide the best balance between transmission and coverage. The principle of transmission mode MACS is given in Figure 3.1.

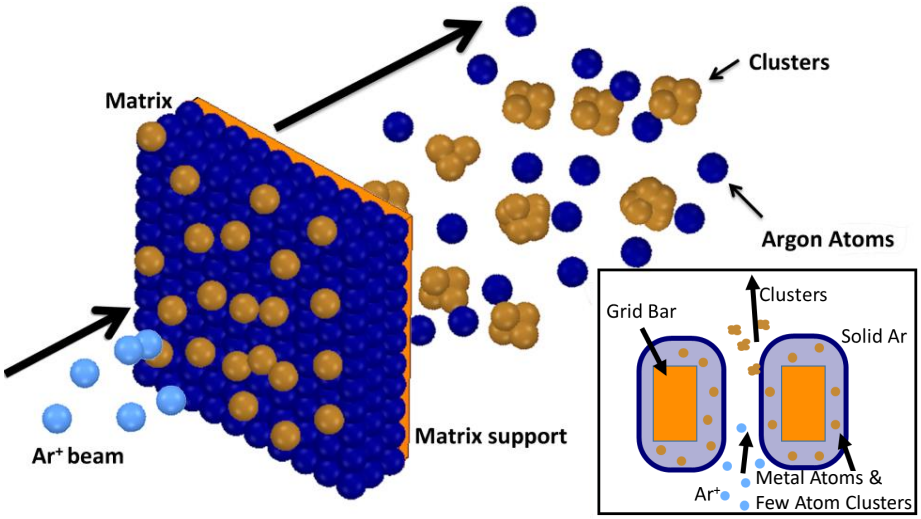

Figure 3.1: Transmission mode MACS produces clusters by sputtering rare gas and metal films co-condensed on a mesh support (depicted above). In reality the mesh holes are not fully covered as show for ease of concept geometry. The insert shows a more realistic example of the sputtering of a single frame as viewed from above.

3.3 Cluster Formation Mechanisms

There are two main mechanisms considered for metal cluster formation in the MACS: near instantaneous formation of metal clusters upon condensation and relaxation, and cluster aggregation through ion beam bombardment. The former has been found true for metals in rare gas matrices in previous studies.[169,170] As the matrix condenses, metal clusters form, driven by the strong local potential to minimise energy. This process is fast (tens of ps) and short-range (several Å). Therefore, the clusters formed are highly dependent on the concentration of metal in the matrix. These small spontaneously formed clusters will be referred to as the preformed clusters, denoting their presence prior to ion beam bombardment.

The second formation mechanism is mediated by ion beam bombardment. Upon impact of the ion with the matrix significant energy is transferred to the system causing diffusion and the ejection of material. The increased mobility causes the metal atoms within the matrix to diffuse and aggregate. Through subsequent ion impacts the clusters are ripened through the diffusion of metal atoms and clusters. These clusters are ejected through the collision cascade and thermal spike regimes

present during ion bombardment. The collision cascade is based on a series of single atom collisions and recoils. Although the first impact will start a collision cascade, where the ion is large and energetic enough many collisions can happen in close proximity. These knock-on effects are no longer isolated events but part of a many-body system.[171,172] This overlap of events leads to what is known as the thermal spike regime, where due to the locality of collision the vast majority of local atoms are part of the dynamic process. The thermal spike regime can be treated somewhat like a fluid, with re-condensing around the cooled sides and material flowing out from the centre of the spike.[171] This is the primary route for cluster extraction. The thermal spike regime correctly predicts the non-linear increase in sputtering yield of rare gas ices with increasing ion energy (keV range).[173] Despite neglecting charge the molecular dynamics approach provides a good description of sputtering yield and process in the few keV range, however when increasing energy to several tens of keV or even MeV the electronic sputtering contribution greatly increases, reducing the validity of such techniques.[174,175] A visualisation of the spike regime in solid Ar from the impact of 1 keV Ar atom can be seen in Figure 3.2, reproduced from [172]. The images are part of a simulation showing the impact of 1 keV Ar atom into an amorphous argon matrix. The time refers to the time after impact. Further discussion on cluster formation and growth will be made alongside the experimental results.

3.4 Scaling Up

One of the most exciting elements of the MACS technology is that it presents a truly scalable method of cluster production. The technologies of all the components used in the proof of principle exist in much larger scale versions. It is possible to provide ion sources producing 6-7 orders more current, as well as evaporators delivering 6-7 orders more material. It is even possible to get cryo-coolers with a cooling

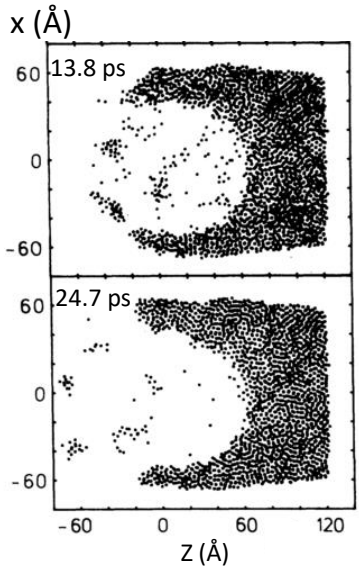

Figure 3.2: Snapshots of amorphous Ar after the impact of a 1 keV Ar atom. Time after impact is indicated at the top left. Adapted from [172].

power in the kW range at 4 K. This indicates that even without optimisation of the process within the MACS, components based on current technologies could provide equivalent cluster beam currents of >milli-amps (six to seven orders of magnitude above present size-selected cluster beam production levels). The difficultly comes from trying to maintain or improve the level of control over the produced particles while converting from a scientific research level technology to a sustained batch production technology. In order to achieve this, both a better level of control and a greater understanding of the system is required. The state of the system prior to the work of the author is given in a recent publication[91] (see figure 2.17).

In order to increase cluster production from an equivalent beam current of ∼2 nA to a target of 100 nA, the MACS1 has been redesigned to incorporate a new evaporator (Createc High Temperature Effusion cell), ion gun (Tectra GenII) and closed cycle cryo-cooler (Sumitomo CH204) with a large area matrix. Furthermore, the chamber has been modified so that the evaporator, ion beam and gas dosing are positioned facing towards the matrix from the same side, permitting cluster production with simultaneous matrix replenishment. This creates a continuous mode

of operation. A schematic of the final system with a corresponding photo is shown in figures 3.3 a) and b) respectively.

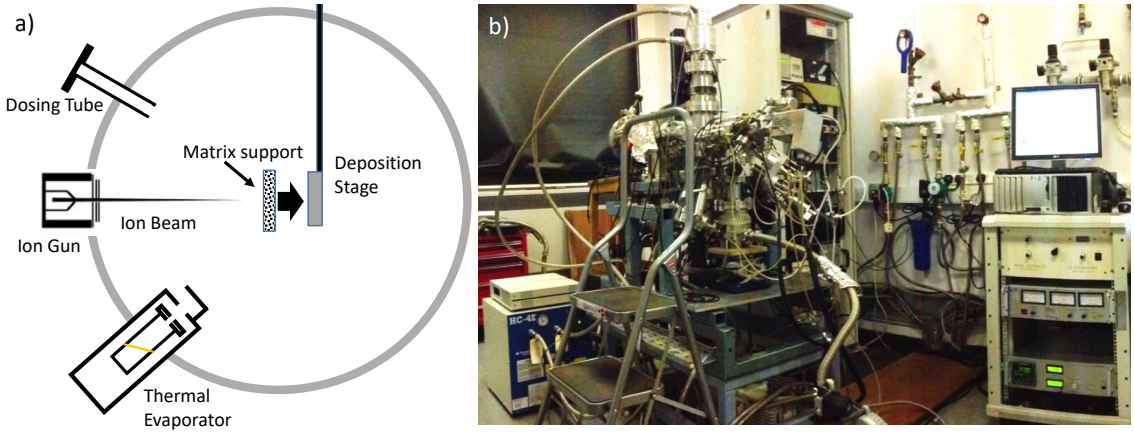

Figure 3.3: a) Schematic of the upgraded MACS transmission mode source, with gas and metal dosing mounted at 45° with respect to the matrix, support surface normal and 45° out of plane (not visible on diagram). The ion beam is aligned in plane parallel to the surface normal. b) is a picture of the system to give an idea of scale.

3.4.1 Evaporation

The new evaporator is a Createc High Temperature Effusion cell capable of reaching temperatures up to 2000 °C. The crucible is a 10 cc Al_2O_3 crucible. This is heated to temperature by radiation from surrounding filaments. The exact temperature is controlled by a programmable PID controller, which gives a temperature variation of 0.1 °C after settling. Stable metal deposition rates of >2 $\AA$/s are achievable using materials such as silver and gold. The large crucible of 10 cc reduces the frequency of replenishment cycles and system exposure to air. Figure 3.4 a) gives the profile of silver deposition rate with position measured by QCM, at a throw distance of ∼10 cm (i.e. the matrix position). The dependence of the deposition rate on temperature can be seen in figure 3.4 b).

Effective thermal shielding of the substrate is provided by the addition of a tantalum cap with a small aperture clipped over the water-cooled jacket (cylindrical water-cooled radiation shield). The additional screening significantly reduces the

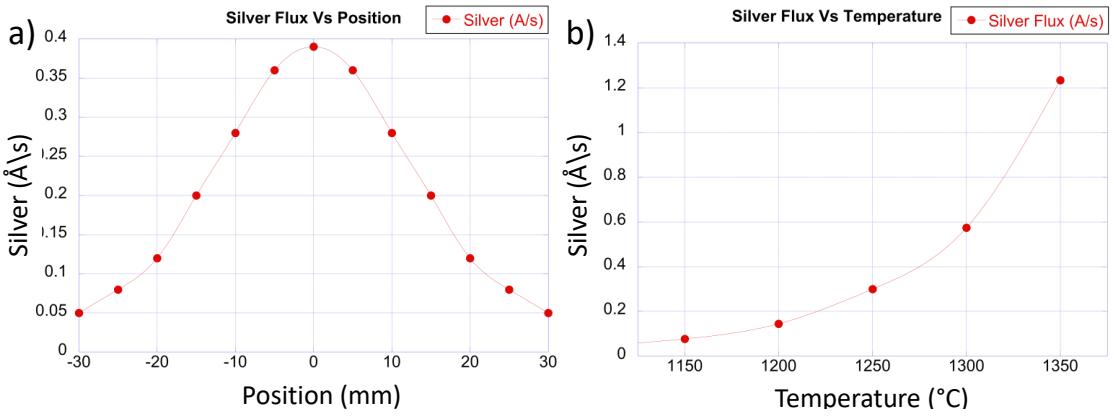

Figure 3.4: a) Profile of silver deposition from the Createc High Temperature Effusion cell. b) Silver deposition rate vs evaporator temperature.

thermal load on the substrate permitting evaporation temperatures up to ∼1600 °C, while maintaining a matrix support temperature below 20 K. The previous system used a home-built direct current heating evaporator with a tantalum crucible. Evaporation rate was set by the current applied, without control feedback. Due to the small boat and the resistance change with heating, the evaporation rate variation was significantly higher.

3.4.2 Cryo-cooler

The MACS uses a Sumitumo CH204 cryo-cooler, with a HC-4E1 helium compressor. This works by compressing and water-cooling helium, which is then transferred to the cold head and expanded. The expansion inside the cold head cools the helium to liquid temperatures. This, in turn, cools the end of the cold head. The warmer helium gas is returned to the compressor and the process is repeated. The cooler is able to reach a base temperature of 10 K and gives ∼7 W of cooling power at 20 K. The system takes about 1.5 h to cool down from room temperature. A schematic of the CH204 and matrix support is given in Figure 3.5. The matrix support is increased from a 3 mm diameter to a 25 mm by 25 mm square of copper 1000 mesh (10 μm hole 15 μm bar), which is clamped in place with a copper frame. The sample stage connects to a mounting block which houses the temperature sensor.

The matrix temperature is measured by a silicon diode temperature sensor (Lake Shore DT-670-CU). This is calibrated with a three-point measurement: ice water, liquid nitrogen and liquid helium. A sapphire washer with two gold-coated faces is used to give electrical isolation permitting direct measurement of the ion beam current on the matrix (Keithley 6485 picoammeter). Connecting faces are gold-coated or use a sandwiched gold foil to improve thermal conduction.

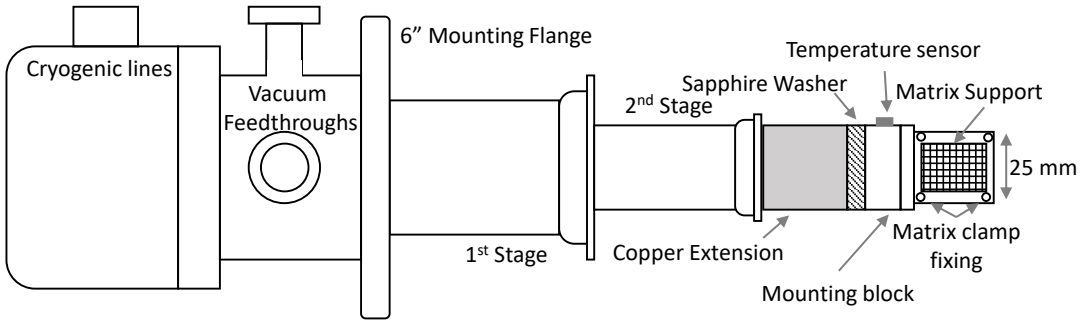

Figure 3.5: Schematic of the Sumitomo CH204 cryo-cooler with custom matrix support mounting. The 25 mm × 25 mm 1000 mesh matrix support.

3.4.3 Ion Gun

The final key part to the scale-up is the high-flux ion gun. The Tectra IonEtch sputter gun provides a total ion current of up to 4 mA with an ion energy of 1-5 keV. Increasing the sputtering rate is the main route to higher nanocluster flux. As discussed, in the cluster formation the ion bombardment controls the nanocluster extraction rates and nanocluster growth (section 3.3). Assuming that there is sufficient fresh matrix and enough time for the matrix to relax between successive local ion impacts, it would be reasonable to assume that the number of nanoclusters produced should increase linearly with the number of ions impinging on the matrix. If all 4 mA of ions were incident on the 25 mm × 25 mm matrix, there would be 10^{16} ions impinging per second. Given reasonable relaxation times (100 ns) and impact areas (25 nm × 25 nm), 10^{19} sites are available per second. Therefore, each ion impact can still be treated as a separate isolated event.

Although a high ion flux is generated to improve focusing and therefore current on the matrix, custom optics have been designed. The lens geometry and voltages have been simulated using SIMION 7.0 to determine the optimal configuration. In order to optimise the system, several parameters have to be considered, for example ion mass, ion energy, divergence, lens geometry, and lens voltage. All parameters can be assigned programmatically and varied in simulation batches. A short overview of parameter choices and examples of the effects are given below.

In SIMION 7.0, the system geometry can be defined in two ways: by directly drawing in system components in a manner similar to CAD software, or procedurally using lua code. The latter method is preferable for designing lens systems as this allows for lens heights, widths, spacings and positions to be defined by variables, which can then be updated or edited procedurally while running a batch of simulations. Due to the large number of variables, running batches of simulations is highly useful for finding optimum conditions. In this way, a geometry file (.gem) and batch simulation file (.lua) can be combined to test multiple parameters in a batch, e.g. lens sizes, positions, shapes and initial ion trajectories. The results are in the form of image and data files, which can be produced after each set of ions is tested. The results are then analysed to find the best configuration (in this case by MATLAB script). Prior to simulating ion flights, the geometry is refined, which essentially means that the software pre-solves the equations for the fields derived for a set of voltages and the solution can then be quickly recalibrated based on new voltages and the properties of the travelling ions.

The voltage of each lens can also be changed manually or automatically to run through a series of voltages. Both static voltage lenses (between simulations) or time-dependent lens voltages (e.g. mass-filter voltage pulses during flight) can be simulated. Due to the available power supplies and safety considerations, only voltages below 10 kV have been considered in the simulations presented here. Where possible, voltages have been minimised to below 5 kV. Initial coarse voltage steps

are used to find good areas, which are fine-tuned to optimise the values. Three examples of different lens voltages in an einzel lens system are given in figure 3.6. In each case, the ion divergence, mass and energy are the same (5 ° half angle, 100 amu and 200 eV respectively). The outer lens voltage is set to 50 V and the inner to -200 V, -300 V and -400 V in i), ii) and iii) respectively.

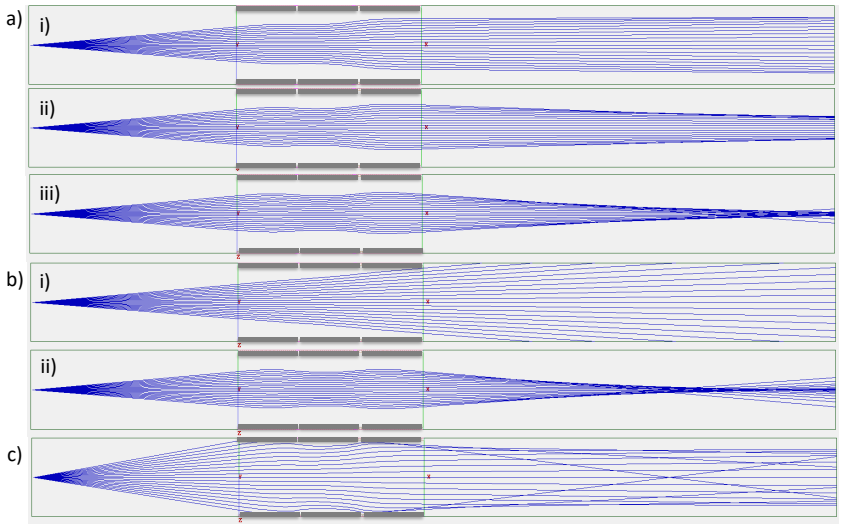

Figure 3.6: Several examples of different ion beam simulations are shown to illustrate the effect of different parameters. Unless stated otherwise, the ions are singly charged with a mass of 100 amu, the ion kinetic energy is 200 eV and the half divergence of the initial beam is 5 °. a) i), ii) and iii) show three different static lens voltages. In all cases, the two outer lenses remain at 50 V, while the middle lens is set to -200, -300 and -400 V respectively. b) i) and ii) employ two different ion kinetic energies: 2 keV and 100 eV respectively. c) illustrates the effect of a wider initial divergence angle (10 ° half angle).

The ion mass, divergence and energy have been set from experimental parameters and measurements (2 and 5 keV have been simulated). For the purpose of illustrating the effect of energy and divergence, however, they have been changed for examples b) and c) in figure 3.6.Figure 3.6 b) i) and ii) illustrates the effect of ion energy, having ion energies of 2 keV and 100 eV respectively. Everything else is the same as Figure 3.6 a) i). Figure 3.6 c) shows the effect of beam divergence, which has been increased from a 5 ° half angle to 10 °, other parameters remain unchanged.

The simulation outputs a trace of each ion's trajectory until it either hits a

defined object or leaves the simulation area. Data from each simulation is output in the form of a log file, which contains information about specific ions (e.g. mass, energy, velocity, position etc.) at particular events (e.g. creation, termination, upon intersecting a plane etc.). The efficiency of the ion-optic lens system and the beam profile of the ions has been assessed by considering the number of ions reaching the matrix support plate and their position (analysed by MATLAB script). The optimal case is chosen based on two parameters: the lens system transmission ratio and the percentage of ions hitting the matrix. A visualisation of the optimised case is shown in figure 3.7. A greater than 90 % transmission efficiency was achieved within the optics, while 85 % of ions also reached the matrix.

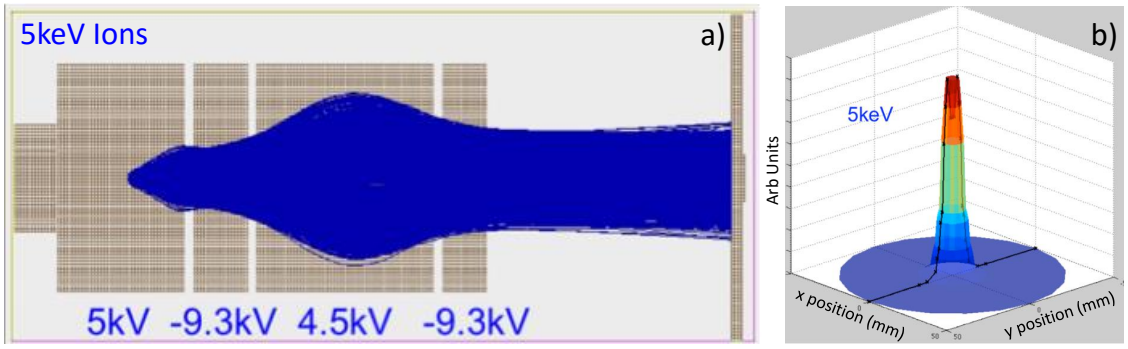

Figure 3.7: a) shows a cut-through of a single run SIMION simulation for the Tectra IonEtch Sputter Gun ion-optics. 5 keV argon ions, with a half angle divergence of 15 ∘ are travelling from left to right. The voltages shown are the optimum found for these lenses, ion mass, divergence and energy (with an upper limit of 10 kV). b) is a projection of ions passing through the plate set on the right-hand side of image a). The x and y axes denote the point on the plane, and the height is the ion density.

Using the custom-designed ion optics, a current of >1 mA is achievable (25 mm by 25 mm sample plate, 100 mm working distance). Prior to this, the maximum current was ∼400 μA using a high voltage bias (-1 keV) on the matrix support. The original and post-lens installation resulting ion beam profiles are shown in figure 3.8.

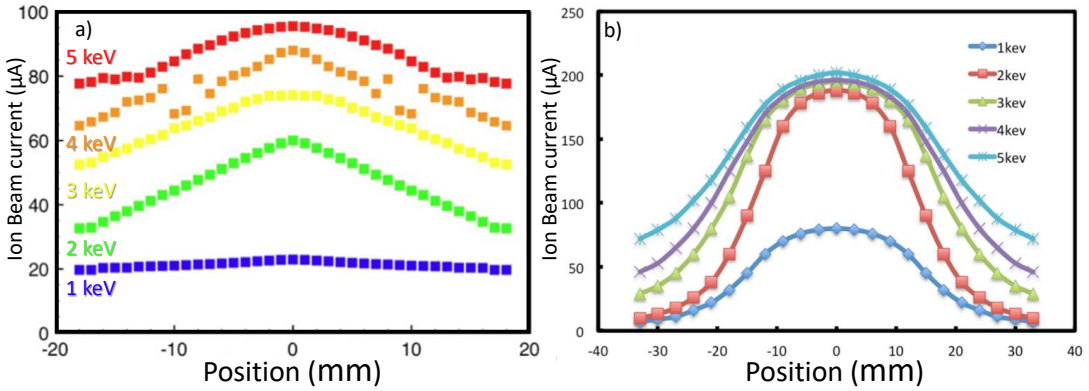

Figure 3.8: Ion beam profiles measured: a) prior to installation of ion optics, b) after installation. The profile is measured using the side of the matrix support holder 3 mm × 30 mm plate. Data for b) provided by Lu Cao.[176]

3.4.4 Deposition Stages

Two different deposition stages are employed, one for large area deposition and the other for sequential deposition (from the original MACS system). Both can be seen in Figure 3.9. The large area deposition stage in figure 3.9 b) is designed to measure the total number of clusters produced. TEM grids can be placed to probe the entire profile of the cluster beam (low cluster beam divergence has previously been observed). The deposition stage is a rectangular plate which mounts perpendicularly to the cluster beam, two lines of TEM grids positioned in a cross shape to cover a 30 mm by 30 mm measurement area. The cluster densities measured on the grids can then be extrapolated to the immediate surrounding area in order to calculate nanocluster coverage across the entire sample plate. Figure 3.9 a) shows the sequential deposition stage, which holds six TEM grid samples, with a rotatable aperture to expose a single grid at a time. This mounts parallel to the direction of the cluster beam.

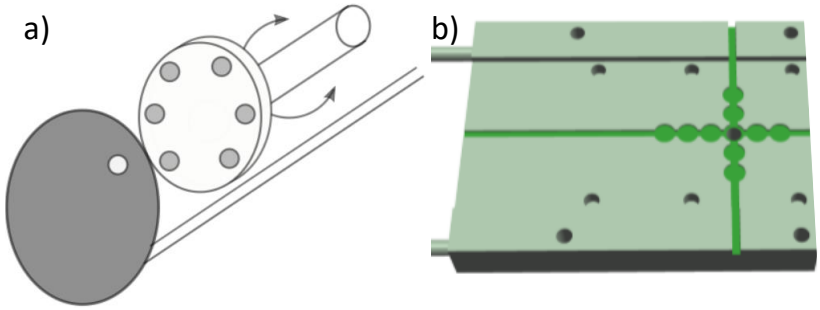

Figure 3.9: a) shows the original MACS sample holder designed for taking single sequential samples. b) is the schematic of the new sample holder to map the spatial profile of cluster deposition. Two additional plates are fitted over the holder, one to fix the grids in place and the other as an aperture for biasing.

3.4.5 Pumping and Venting

The vacuum is maintained using a turbo molecular pump backed by a rotary vane oil pump, giving a base pressure of $<5\times10^{-8}$ mbar. A foreline trap and speedivalve are placed between the two pumps to prevent back streaming of impurities and permit isolation for the two pumps. The gas supply line is pumped using an oil-free scroll pump, with a base pressure of low 10^{-2} mbar. Prior to use, the line is first pumped down to the 10^{-2} mbar range and the line is then filled with approximately 0.5 bar over pressure of argon which is then pumped away. This is repeated three times before an experiment is conducted to reduce impurities and contamination. In order to pump the chamber down, first the pumps are isolated by the speedivalve, the rotary vane pump is started and allowed to warm up, the speedivalve is then opened pumping down the chamber, and when the pressure reaches the $10-2$ mbar range the turbo pump is started. In order to vent, the turbo and rotary are isolated and stopped. After spinning down ($\sim$10-15 minutes), the chamber is vented using liquid nitrogen boil-off.

3.4.6 Sample Preparation

MACS produces clusters via ion beam bombardment of metal doped rare gas matrices. First, the evaporator is warmed to the evaporation temperature to measure the

metal deposition rate on the matrix (measured by QCM). The correct background gas pressure for a specific concentration can then be calculated (or evaporation temperature adjusted). The evaporator temperature is then reduced to below the melting point and the matrix is cooled to below 20 K. A matrix is co-condensed by introducing argon via a precision leak valve at a specific pressure. The evaporator shutter is then opened to deposit metal simultaneously. The pure argon is dosed for a short time before introducing the metal to provide a protecting buffer layer on the support mesh. After deposition of the desired matrix thickness, the shutter and leak valve are closed simultaneously. The sputtering process is started by setting the ion optics lenses voltages and introducing argon gas through a leak valve into the ion gun ($\sim 1 \times 10^{-5}$ mbar), which is then ignited to form a plasma and start sputtering. Deposition is performed by translating the sample stage into the cluster beam or exposing the sample by aligning the aperture. During deposition, the matrix current is monitored to give the ion dose on the matrix.

3.5 High Flux

Replacing the ion source capable of 10-20 μA of sputter current on the matrix with one capable of achieving 400 μA should allow production of thirty times more nanoclusters per unit of time (around 10^{11}-10^{12} clusters per second). To test the highest flux that can be produced, a $\sim$130 nm thick argon matrix was prepared with a 2.2 % silver concentration and sputtered with a 5 keV, $\sim$400 μA Ar^+ beam for 15 s. The maximum ion energy of 5 keV is used, as this gives the highest currents on the matrix. The higher energy will also increase the sputter yield of each ion. To further improve the focusing, the matrix has been biased to -1000 V. The deposition stage has also been biased to ensure a field-free region between it and the matrix. Figures 3.10 a), b) and c) show a series of images taken from TEM grids positioned on the sample plate, with the number of clusters in each image given below. Figure

3.10 d) gives the layout of the sample plate and the positions from where the STEM images were taken.

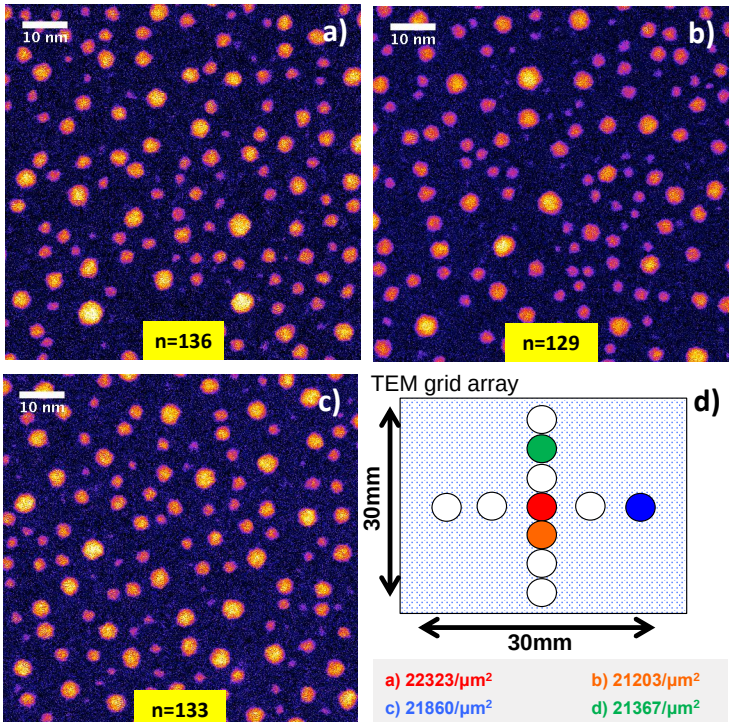

Figure 3.10: Parts a), b) and c) show HAADF STEM images of nanoclusters deposited onto TEM grids positioned over a large deposition area 30 mm × 30 mm (red, orange and blue positions respectively). The number of clusters in each image is indicated in the yellow box. d) is a schematic of the array of TEM grids used to collect the nanoclusters and the respective nanocluster density on each grid (colour coded). The nanoclusters are produced from a ∼130 nm thick matrix with a 2.2 % silver loading. The matrix is biased at -1000 V and sputtered with a 400 μA, 5 keV Ar^+ beam for 20 s.

To calculate the average density of nanoclusters on a single TEM grid, relatively low magnification (78 nm × 78 nm) images were taken at five different positions across the grid (nominally up, down, left, right and middle). A minimum of ten images (two from each position) were then used in the analysis. The images chosen are based on the quality of the image, i.e. those in focus, with a good signal-to-noise ratio and low drift for example. Between 15-20 images are typically used to obtain the average nanocluster density on a single grid. Nanocluster density on the grid is then calculated as nanoclusters per unit area. Most conventional cluster sources deposit just the charged fraction of nanoclusters and, therefore, cluster deposition

rates are often stated in the form of a cluster beam current. As such, it is useful to convert the measured nanocluster flux to an equivalent beam current for the purpose of comparison. An equivalent current value is generated from the number of nanoclusters deposited, divided by time. This treats each cluster as a single charge. In reality, this is not the case, as only 10-15 % of the cluster are charged.[176] The total nanocluster current is written as:

$$Equivalent\ Cluster\ Beam\ Current = \frac{eN_c}{T} = \frac{e}{T} N_i \frac{A_d}{A_i}$$

where e is elementary charge, N_c is the total number of nanoclusters deposited, T is time, N_i is the average number of nanoclusters per image, A_d is the total deposition area and A_i is the area of one image. The cluster density measured across all grid is used average cluster density across the whole plate (30 mm × 30 mm). This calculation yields an average equivalent cluster current of 93±6 nA for a 20 s deposition. The deposition rate increase compared to current size-selected cluster beam sources is between two and three orders of magnitude. The rate is similar to non size-selected gas aggregation magnetron sources, which produce around 100 nA (although magnetron sources normally deposit a larger and broader particle size). This is an increase on the previous generation of MACS by around 60 times, which is about twice as much as anticipated based on the ion beam current alone. This is due to several factors, which in order of contribution are: the higher energy of the ion beam, the increased solid collection angle and the improved metal dosing uniformity.

3.6 Metal Loading

Control over metal dosing has been improved by using a more stable and higher flux evaporator. This allows faster and more controlled matrix formation. To ensure that the level of size control is maintained when using higher current ion density beams to

sputter the matrix, the effect of metal concentration in the matrix has been re-tested. Nanoclusters were prepared from argon matrices with silver concentrations ranging from 0.6 % to 4.8 %. All other parameters were kept the same, i.e. a matrix thickness of ∼60 nm, 14-16 K matrix temperature, 1.5 keV beam energy, ∼300 μA beam current, matrix bias of -1000 V and a 30 s deposition. The HAADF STEM images from these samples can be seen in figure 3.11. The size is measured by comparing the integrated HAADF intensities of the nanoclusters in these images with that of single atoms. The nanocluster size distribution for each metal concentration is shown in figure 3.11.

The results present a similar trend to the one observed in the proof of principle experiments recently published.[91] The average cluster size increases with metal loading, while the total number of clusters deposited reduces. This can be seen quantitatively in figure 3.12, where equivalent cluster current is plotted compared with cluster size and concentration. It can be seen that the current reduction mirrors the increase in size. This is expected, as when sputtering power is constant the total material available for cluster production is fixed.

Furthermore, the total amount of metal deposited appears to reduce, based on the summation of all the atoms contained within the observed nanoclusters. This could partially be due to the reduced contrast between the background and small nanoclusters when large clusters are present in the image. This, however, does not make up for the discrepancy observed. This can be explained by considering the binding of the system. It is well known that, as a Van der Waals ice, the Ar-Ar bond has a much lower binding energy than that of the Ag-Ag, and is also lower than the Ar-Ag binding energy.[172,177] Put simply, as the amount of metal increases more Ar-Ag and Ag-Ag bonds need to be broken and thus the sputtering yield drops, reducing the total amount of metal deposited in the cluster beam. Furthermore, as the size of the clusters embedded in the matrix grows, more atoms need to be vaporised in order to release it and more energy is required to extract it. It is worth

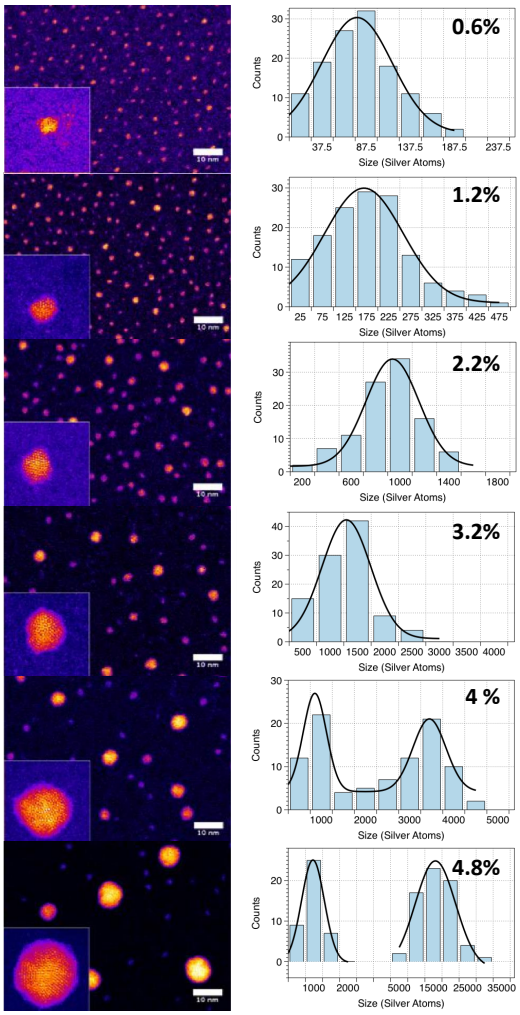

Figure 3.11: HAADF STEM images of silver nanoclusters produced by the MACS using different silver concentrations in the argon matrix (0.6 % to 4.8 %), alongside the corresponding size distributions, measured by integrated HAADF intensity. All samples are prepared from ∼60 nm thick argon-silver matrices at 14-16 K. Samples are deposited for 30 s with a ∼300 μA, 1.5 keV ion beam and matrix bias -1000 V.

noting that the cluster does not need to be vaporised itself but simply the argon binding it to the matrix. This is supported by the observation of large nanoclusters, which could not be formed from the number of atoms sputtered from a single impact alone.[173]

Seed clusters are formed through two processes: the almost immediate aggregation of nearest neighbour metals[178] and the coalescence of single and small groups of metal atoms through thermal spike assisted diffusion. These cluster seeds are then ripened through subsequent ion impacts providing energy for them and other metal

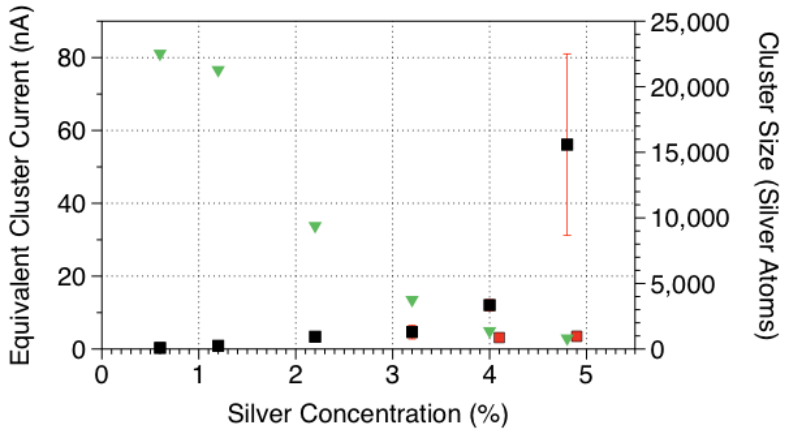

Figure 3.12: Equivalent cluster current (green, left axis) and Peak cluster size (black, right) are plotted against metal concentration. The smaller peaks of the bimodal distributions are plotted offset to avoid clashing(red)

atoms to diffuse and aggregate. Ultimately, these clusters are also extracted by the ion bombardment. As the global concentration of metal goes up so will the local concentration and, therefore, the nanocluster size will increase as more metal atoms are readily available to grow the seeds. The results for the high metal concentration matrices present a biomodal size distribution, which is likely due to the divergence of these two production mechanisms.

3.7 Continuous Production

To form a useful technology, sustained cluster production is needed. An important feature of the new MACS1 system is the mounting of the ion source and evaporator from the same side (see Figure 3.3). This geometry allows for the simultaneous replenishment of the matrix, whereas before the matrix had to be rotated between dosing (i.e. matrix formation) and sputtering. Before ion bombardment, a buffer layer of matrix is deposited to prevent the damaging of the matrix support during initial bombardment. The buffer layer is 25 nm thick with a Ag loading of 5 %. This is then sputtered while being simultaneously replenished. The sputtering and dosing parameters were a 10 μA beam current, 2 keV beam energy, 8×10^{-6} argon

gas dosing pressure, 0.4 Å/s metal deposition rate and 14-16 K matrix temperature. During sputtering, the sample stage shown in figure 3.9 a) was used to prepare six TEM samples sequentially over a period of 500 s. Clusters were deposited onto each TEM grid for 15 s. Figure 3.13 shows the extrapolated number of nanoclusters on each TEM sample. After an initial reduction in the number of nanoclusters deposited, the production rate stabilises having only a slight downward trend. The significantly higher flux observed for the first few seconds of sputtering is likely due to a large burst of ions when the gun is ignited, but could also be due to the initial extended surface area of the pristine matrix. The continuing decline with sputtering time is suspected to be caused by non-even depletion of the matrix. The global amount of material is maintained; however, the Ar^+, argon gas and silver deposition profiles do not match exactly, leading to saturation and depletion regions. This matrix condition extends into the microscopic regime. Initially, only small nearest neighbour formed nanoclusters are present in the matrix, but as the ion dose increases so does the population of larger retained nanoclusters, thus altering the target composition.

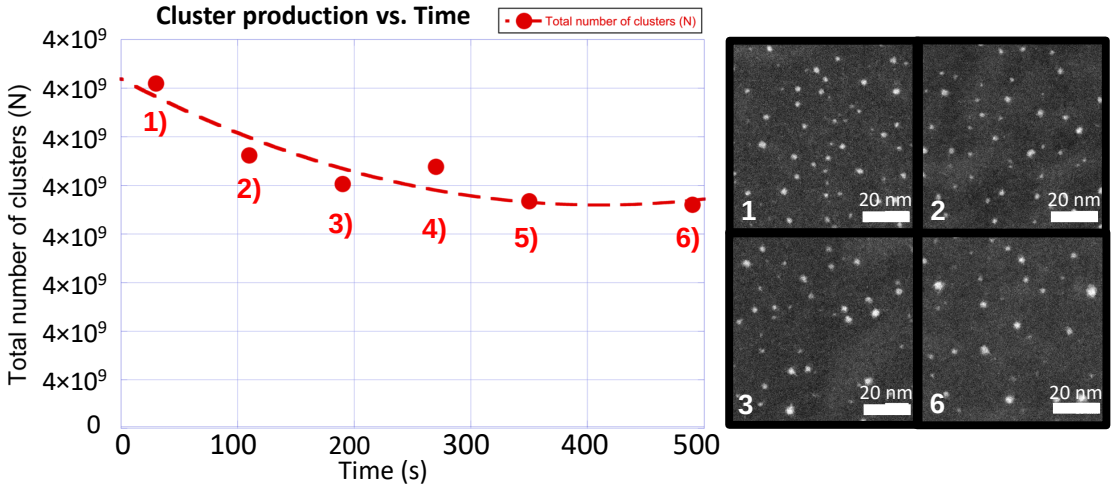

Figure 3.13: The number of nanoclusters deposited over a 15 s deposition period, at six different times during continuous production of nanoclusters for 500 s period. The dotted line provides an eye guide to the cluster production trend. The cluster density has been calculated from HAADF STEM images, examples of which are shown on the right for sample 1, 2, 3 and 6.

3.8 Mass-Filter Installation, Control and Commissioning

Considering the results so far, it is possible to question whether the nanoclusters produced are truly formed inside the matrix or, rather, by surface aggregation of atoms or small groups of atoms after deposition on the sample surface. The work presented in this section aims to answer that question through consideration of cluster size at different deposition times and measurement of TOF mass spectra.

3.8.1 Deposition Time

If the nanoclusters were formed by nucleation and aggregation on the sample surface, rather than arriving preformed from the gas phase, several different phenomena would be observed. Firstly, the size of the clusters would be dependent on the coverage of material put onto the surface and to an extent the time allowed for aggregation. Secondly, larger nanoclusters or islands (> 10 nm) should be relatively flat in nature if able to wet the surface. To test this, a series of 4 samples have been deposited for different deposition times. The results from this can be seen in figure 3.14. These images show that there is no significant change in the size of clusters produced, only the number of clusters deposited. This can be seen even more clearly from the size distribution data presented under the images. Only a minimal increase is observed in the mean nanocluster size, which would be expected as when the numbers of nanoclusters deposited increase there is a greater chance of cluster aggregation via landing on already deposited clusters.

This provides strong evidence that the nanoclusters are formed prior to landing on the surface. However, instability in cluster production rate with time, makes it difficult truly to decouple coverage and deposition rate, which is important for surface nucleations.[179,180] This is illustrated by figure 3.15, it shows four samples deposited for different deposition times. In each case a fresh 130 nm thick 2.2 %

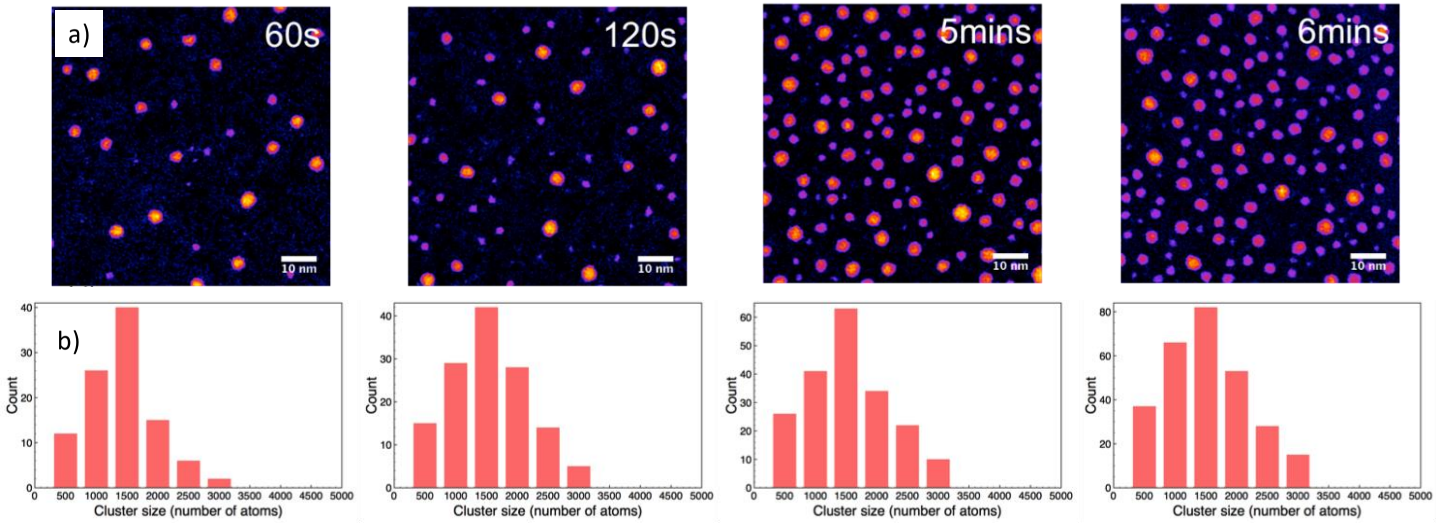

Figure 3.14: a) shows a series of images for samples prepared with different deposition times. In each case, the silver concentration in the matrix was 3.2 %. The corresponding size distributions are shown in b). Samples were deposited from a ∼128 nm matrix pre-prepared at 14-16 K, using a 50 μA, 1 keV ion beam.

silver matrix is prepared on a clean matrix support and is sputtered with a 0.4 mA 5 keV argon ion beam. After an initial increase, as deposition time increases the average flux of clusters produced reduces likely due to depletion of the matrix.

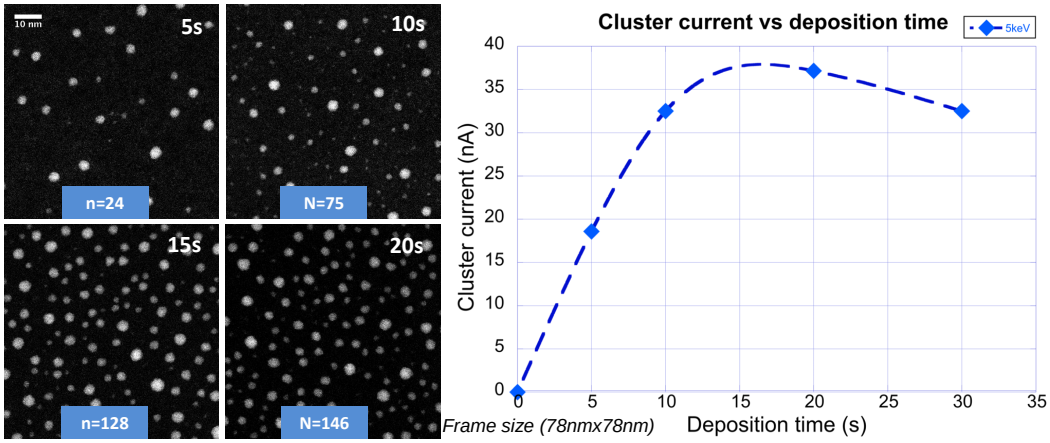

Figure 3.15: The average equivalent nancluster current measured for samples prepared with different deposition times (5,10,15,20 s). Corresponding STEM images are given to the left. The average current increases with deposition time up to 15 s before reducing. This is likely due to matrix depletion or aggregation of the metal within the matrix. Samples are produced from a matrix with 2.2% silver concentration using a 0.4 mA, 5 keV argon ion beam (with -1000 V matrix bias).

3.8.2 Time-of-Flight Mass Filter

To prove conclusively that the nanoclusters are formed before landing on the surface, TOF mass spectrometry can be used to compare with previous results. To do this, a TOF mass-filter has first been simulated and then integrated into the transmission mode MACS1 system. The mass-filter chosen was developed at the University of Birmingham by von Issendorff and Palmer.[181] A schematic of it can be seen in figure 3.16. This uses three separate field regions: an acceleration region, a field-free region and a deceleration region. The charged clusters are focused into the acceleration region of the mass-filter via ion optics. A short positive pulse (typically μs - ms) is applied to the bottom plate, accelerating the clusters into the field free region. The velocity of each cluster is determined by its charge-to-mass ratio (i.e. the higher the charge-to-mass ratio the greater the particle's vertical velocity). The clusters then

enter the field-free region, progressing through at a constant velocity. Therefore, each charge-to-mass ratio will reach the deceleration region after a different time duration. An identical pulse is then applied to the top plate of the TOF cancelling the cluster's vertical kinetic energy, leaving it travelling along its original axis. By changing the time delay between the acceleration and deceleration pulses different size clusters will be displaced sufficiently to align with the exit aperture. This process is illustrated in figure 3.16.

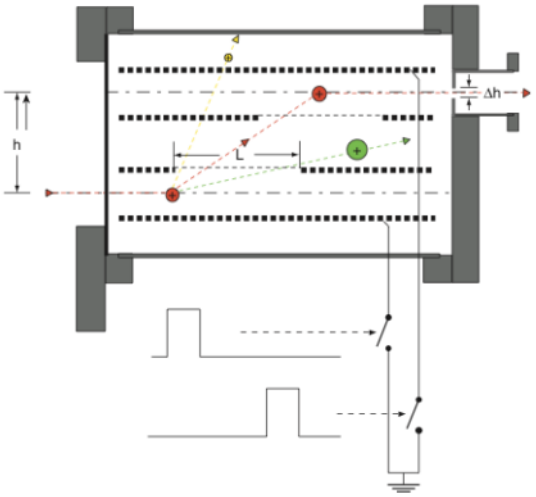

Figure 3.16: Schematic of the Von Issendorff-Palmer mass-filter reproduced from reference.[181] There are three electrically screened regions, acceleration (lower), field-free (middle) and deceleration (upper). For full explanation see text.

The charge-to-mass ratio passed by the filter is given by:

$$m = \frac{eU_a}{d_1 h}\frac{\alpha}{f^2}$$

where e is the elementary charge, U_a the pulse voltage, d_1 the width of acceleration and deceleration regions, h the displacement distance between the entrance and exit apertures, α the pulse duty cycle and f^2 the pulse frequency. Hence, all parameters are fixed after construction besides the pulse voltage, frequency and duty cycle. If perfectly focused, the resolution of the filter reduces to a ratio of the dis-

placement distance and the width of the final aperture (essentially the probe size). The resolution can be written as:

$$R = \frac{M}{\Delta M} = \frac{h}{\Delta h}$$

where M is mass, ΔM is the width of the mass peak, h is the lateral displacement distance and Δh the FWHM of the convolution of the aperture and ion beam. Although the absolute time required between pulses can be calculated for given charge-to-mass ratios and plate voltages, it is more accurate to calibrate with a real source. This has been carried out using a beam of argon ions. Although it is possible to use many different combinations of plate voltage and pulse frequency for greater transmission, a high voltage should be used, giving a high deflection angle that reduces loss of clusters (or argon ions) through the field-free region. The optimal value is highly dependent on the initial particle velocity. Again, for the greatest transmission efficiency, the delay between acceleration pulses should be set such that the acceleration region is "filled" before a subsequent pulse, assuming this is after the deceleration pulse for the previous cycle. In addition to these filtering pulses, a third pulse is employed, called the clearing pulse. This is applied sideways after each deceleration to prevent clusters with integer fractions of the charge-to-mass ratio progressing through after multiple cycles.

3.8.3 Focusing Ion Optics

A key part of integrating the mass-filter with the MACS source is the ion optics. In order to achieve a high signal and resolution, effective extraction and focusing of the nanoclusters is required. When designing ion optics many parameters contribute to the efficiency of the system. In order to find the optimal lens geometry, configuration, position and voltages, SIMON 7.1 was employed as introduced in

the ion source section (3.4.3). The exact divergence and energy spread of the nanoclusters produced in MACS1 is unknown so several different reasonable values are considered. Experimental data indicates that the divergence of the nanoclusters is low. When additional TEM grids are placed to the side of the initial grid (e.g. 3-5 mm off the central axis), few or no clusters are observed. Likewise, the nanocluster energy range can be narrowed by deduction. The incoming ion energy is usually 1.5 keV, which produces a sputtering yield of ∼600 atoms, while even more atoms are involved in the complete sputtering event (e.g. atoms that are excited or displaced but not removed from the matrix). In addition, it has been reported that the mean energy of argon atoms ejected from the matrix is low, in the hundreds of meV range.[172] As such, an energy of more than a few eV per atom is unreasonable even for small clusters. Therefore, an energy range of 1 - 100 eV per nanocluster is chosen with a divergence half angle of 5-10 °. Furthermore, the nanocluster size is intentionally varied. Small (10s of atoms) and large (1000s of atoms) nanocluster sizes have been simulated to ensure an effective lens system across the produced size range.

The final design of the ion optic system in MACS1 was based on the simulation results and is shown in figure 3.17. This gives the entire setup for the system prior to upgrading the ion source (i.e. using the omicron ISE-5 ion gun). The only difference with the upgraded system is the addition of the ion source optics shown in 3.7 a).

3.8.4 Control

In addition to the design and installation of new lenses and the TOF, the implementation of new control software was required. This would enable a single user to control easily the entire system without the assistance of a second person, which was not possible up to now. Further, functionality is also incorporated, such as mass spectra sweeps and a dose monitor. This would have been either much more time-consuming or impossible to carry out manually. To provide full control of the

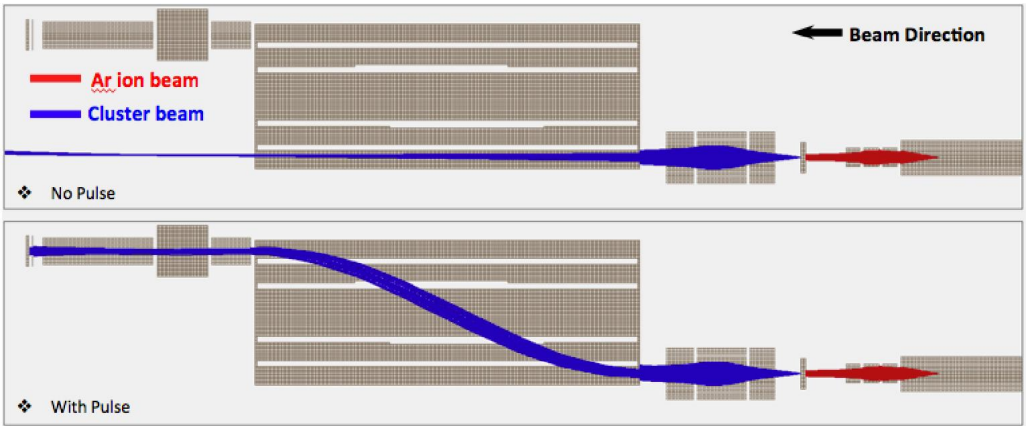

Figure 3.17: Schematic of the final ion optic setup for coupling the MACS source and the Von Issendorff-Palmer TOF mass-filter. The beam direction of travel is from right to left, the initial spread of the ions (red) is based on manual from the ISE-5 ion gun. The nanocluster initial trajectories are based on experimental data from the MACS1 running in transmission mode. The upper image shows direct focusing of the nanoclusters into the TOF spectrometer while all plates are grounded. The lower image is with the pulses switched on.

mass-filter and ion optics, several different instruments required controlling. A flow diagram of the communication is shown in figure 3.18. The control software itself is written entirely in LabVIEW 2012 and incorporates elements of commercial control software supplied with instruments (i.e. LabVIEW VIs for the Glassman and Wienner power supplies), as well as software written entirely by the author (e.g. picoammeter and pulse generator command controls and all additional functionalities). A brief overview of the user interface and functionality is given in the next few pages.

3.8.5 Tuning and Mass Filtering

The section of the interface shown in figure 3.19 presents all the settings and commands needed to tune up the ion optics to improve the focus and, therefore, the mass-filter transmission efficiency and quality of the cluster beam produced (e.g. size, shape etc.). Furthermore, the mass-filter is also controlled here allowing the pulses to be turned on and off, and the parameters set for filtering a specific size. The ion optics have sixteen channels over two modules, which can all be controlled

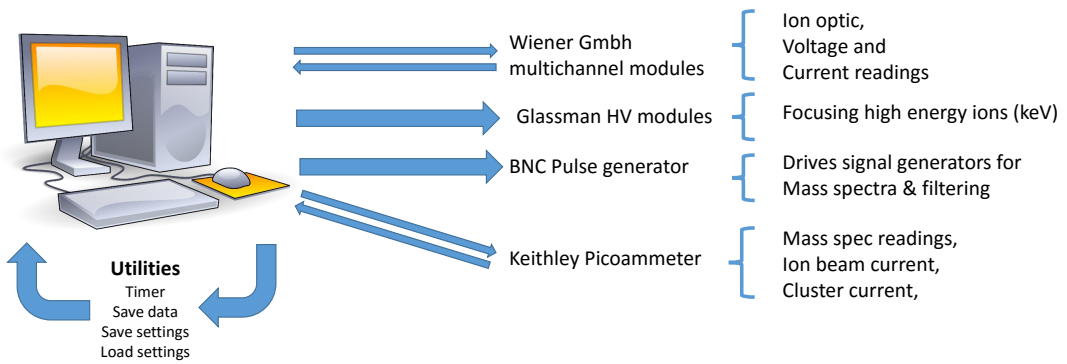

Figure 3.18: Communication or data flow diagram of the computer controlled elements of the MACS1 system. This setup provides complete control of TOF mass filtering, mass spectra measurements, ion optics and current measurements (ion beam or charged clusters). Additional utilities are also provided in the user interface, save/load data and settings, timer and dose display (integrated current) and dose limit warning. Computer image from [182]

here. The channels can either be set individually to specific voltages or to the same voltage (right-hand purple box). A reading of the set and output voltage is fed back to the interface, as well as the current drawn by each channel. The settings of the mass-filter calculate a specific pulse frequency for filtering the desired size (central purple box) based on the calibrated frequency (Ar_1 peak frequency). The main graph displays current readings taken from the picoammeter against time. This current is used to tune up ion optics or to provide a dose level for cluster or ion deposition. A set limit for dose can be provided, after which an indicator is given that the required level is reached (LED illuminates). The tuning, mass filtering and current readings can all be carried out simultaneously. Commands required for all of these operations (e.g. on/off, reset etc.) are highlighted with a green box. Finally, the red highlighted LED indicators provide information on the state of the system and the processes it is running. The upper five indicators report the completion or state of tasks, e.g. if the instrument ID is confirmed, the lower four report different possible errors based on the breakdown of communication within the system.

The most common cause of instrument communication errors is incorrect instrument configuration rather than a real-time failure. The setting for each instrument

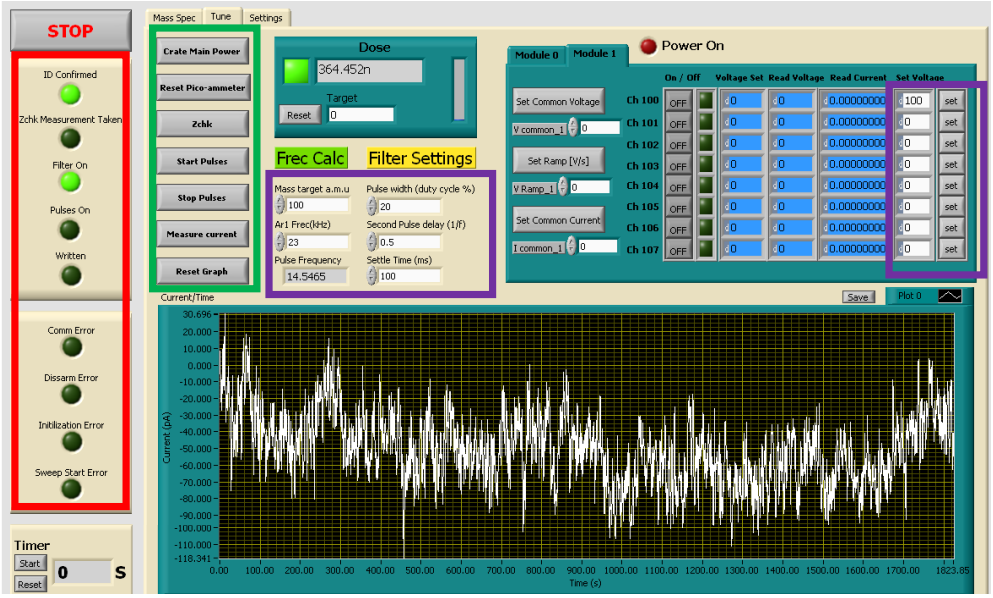

Figure 3.19: The user interface for tuning the ion optics and filtering with the TOF mass-filter is shown above. The purple boxes indicate settings for the ion optics and mass-filter (e.g. voltages, pulse frequency etc.), the green box highlights commands to perform set actions and the red box contains indicators of complete, in-progress or error status. The graph displays the measured current from the picoammeter with an integrated dose indicator above.

can be edited in the "Settings" tab (with the exception of the high voltage power supplies discussed later). A screen shot of this tab is presented in figure 3.20. The instrument communication and device settings are highlighted in purple boxes and the measurement settings in green. The measurement settings provide different measurement parameters for the picoammeter. This allows the user to specify the measurement range and number of measurements taken per data point, as well as how they are averaged. This provides the ability to increase measurement accuracy greatly or to manipulate measurement time to capture more dynamic processes.

3.8.6 Mass Spectra

The control required for the acquisition of mass spectra is more sophisticated, requiring several instruments to carry out actions in the correct sequence and timing. The user interface panel is given in figure 3.21. The filter settings for the acquisition of mass spectra and the commands used to carry out measurements are highlighted

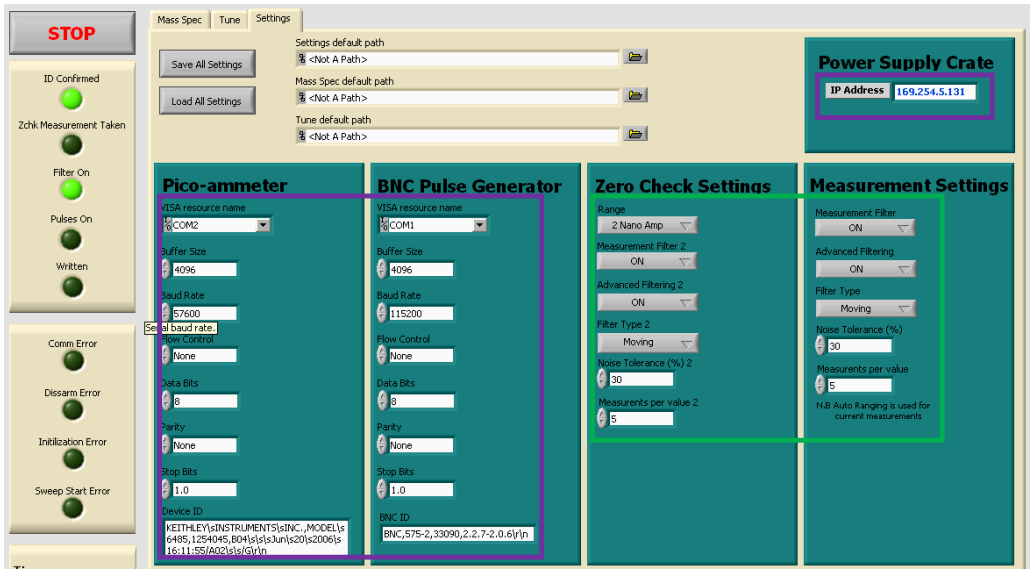

Figure 3.20: The settings user interface permits the communication (purple) and measurement parameters (green) to be edited. The latter allows the range and number of samples taken by the picoammeter to be set, as well as whether they are averaged from repeated measurements or use a moving average.

by purple and green boxes respectively. The general overview of the communication is as follows: first, a look-up table is generated of all required time periods based on the frequency range, step size and calibration settings. The communication to the BNC pulse generator and picoammeter is configured and an ID check performed. Once confirmed, the parameters for the zero-check measurement are sent to the picoammeter and the zero-check is performed. Following confirmation, the running parameters of the picoammeter are transmitted and the first frequency for the sweep is sent to the BNC pulse generator. The pulse generator is then armed, starting the pulses. This is followed by a short delay (settle time) and then a measurement request to the picoammeter is made. Once the measurement is confirmed, the data is requested, received and uploaded to the data set. Subsequent steps just repeat this process, e.g. set new pulse frequency, settle, request data and upload until the end of the sweep range is reached. At the end of the process, the pulse generator is disarmed, channels switched off and then the communication channels are closed. The data is retained after this and can be saved at any time. Only resetting or

starting a new sweep will remove the data from the memory. During this process, it is possible to change ion-optic voltages and run utilities (timer, save etc.) as these are controlled by separate parallel threads.

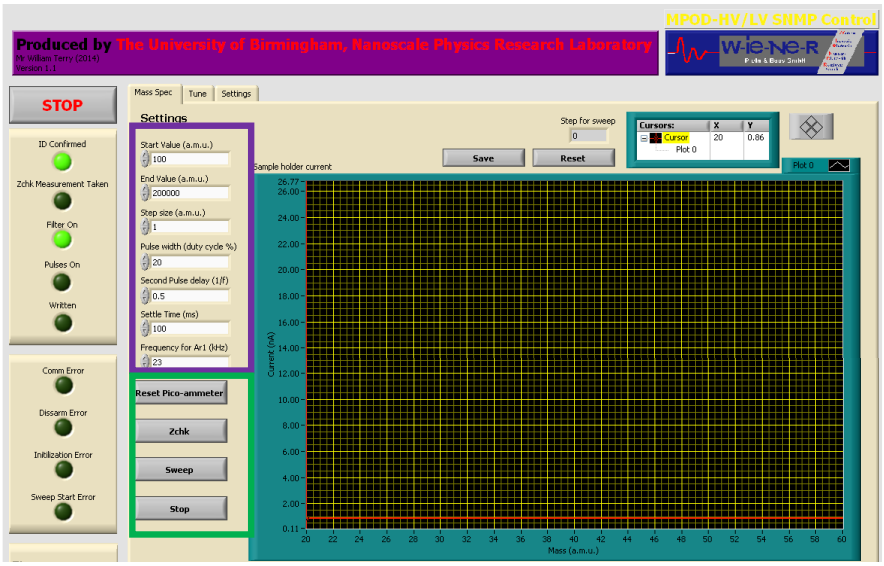

Figure 3.21: The "Mass Spec" tab is displayed above. Here, all the settings for taking mass spectra can be controlled, e.g. start/end position, step size and calibration frequency are set by values highlighted by the purple box. The green box indicates the commands to prime the picoammeter and run the mass spectra, e.g. zero-check, sweep etc.

3.8.7 Utilities

In addition to the main functionality already presented, there are other more minor utilities incorporated into the software, such as the timer, save and reset data from the graphs, and save or load all settings within the interface. These can be seen in figures 3.19 and 3.20. A couple of the more important extra features are present in Figure 3.22, i.e. the combination of controls for the Glassman high voltage power supplies and error reporting: a) and b) respectively. The Glassman software has combined the single channel control software provided to allow control of the channels separately and to manage the communication ports in parallel. Part b) presents three error feeds providing additional feedback from the BNC pulse generator and

picoammeter. The first two are standard error reporters for RS232 ports; the third, however, is a custom feed that will provide more insight into error in the system, similar to the LED indicators (e.g. the number of communication errors and last successful process). This platform can be improved upon for further error tracking; however, given the proposed design of the system easy error location is currently achievable for a familiar user.

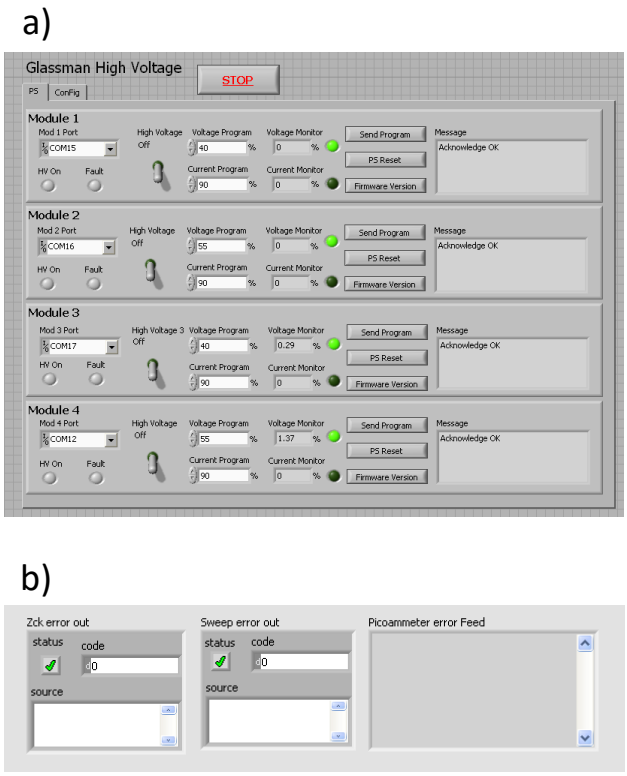

Figure 3.22: The front panel for the incorporated Glassman high voltage power supply control a), and error reporting b). This gives control of several single high voltage channels in parallel (adapted from series control) and additional support in tracking down communication errors respectively.

3.8.8 Commissioning

After installation, the first step is to calibrate the mass-filter using a known charge-to-mass ratio ion. In this case the argon ion source provides a perfect tool, being well defined in mass, charge state, beam energy and having a large signal (micro-amps at one specific size). The lens voltages were set to the optimum voltages

determined from the simulations and then tuned to increase the white beam (i.e. the beam passing through the mass-filter without the mass selecting pulses on). The resulting mass spectrum is shown in figure 3.23. The frequency where the peak is found is then fed back into the calculations to calibrate the filter. The insert shows calibrated mass spectra taken while sputtering the matrix support. Peaks for Ag_1 and Cu_1 are visible. The signal of the size-selected Ar^+ beam is very low compared with the white beam signal ($< 0.001\%$). The transmission ratio of $\sim$50 % is typical for this type of filter (depending on system parameters); therefore, the transmission efficiency has been investigated further.

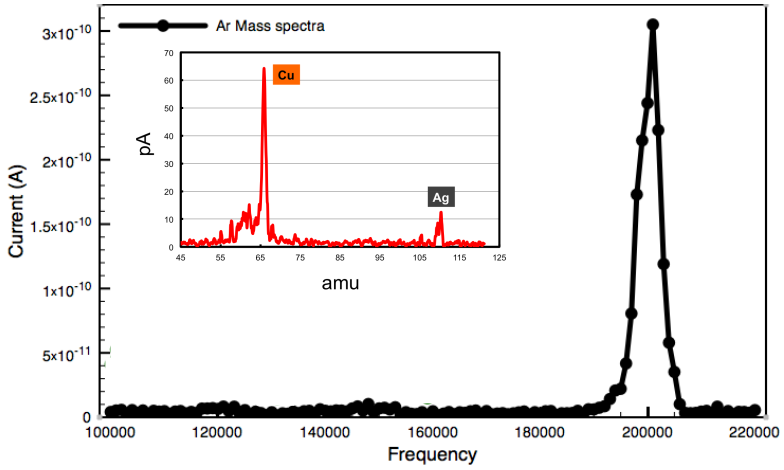

Figure 3.23: The mass spectrum of the argon ion beam is plotted in black and is the average of ten spectra. This gives a clear peak for the calibration of the filter, which can then be used to measure charge-to-mass ratios. The insert is of a calibrated spectrum taken while sputtering the matrix support (e.g. Cu and Ag) with an argon ion beam. This insert is provided by Lu Cao

Due to the higher kinetic energy of the argon ions (keV) compared with nanoclusters(eV), it is possible that the beam does not get displaced vertically before reaching the end of the chamber. To test this, the pulse voltage has been increased to provide greater deflection. The results are given in Figure 3.24. As the pulse voltage is increased so is the transmitted current due to the increased angle of the ion trajectory. There is, however, a limit to this. If the trajectory becomes too steep, extra ions will hit the plate before the first opening or exit of the filter; refer

to Figure 3.16 for a schematic of the mass-filter. In addition, the higher voltage results in a greater pulse frequency, which means that eventually the ions do not completely "fill" the acceleration region before the next pulse; however, the same number of atoms will still hit the first plate reducing the filter efficiency. The ideal case for maximum transmission would be to optimise with a combination of both frequency and plate voltage. From this, it follows that if nanocluster velocity is dependent on it's size, the measured size distribution can be somewhat skewed by different transmission efficiencies, however this can be accounted for experimentally.

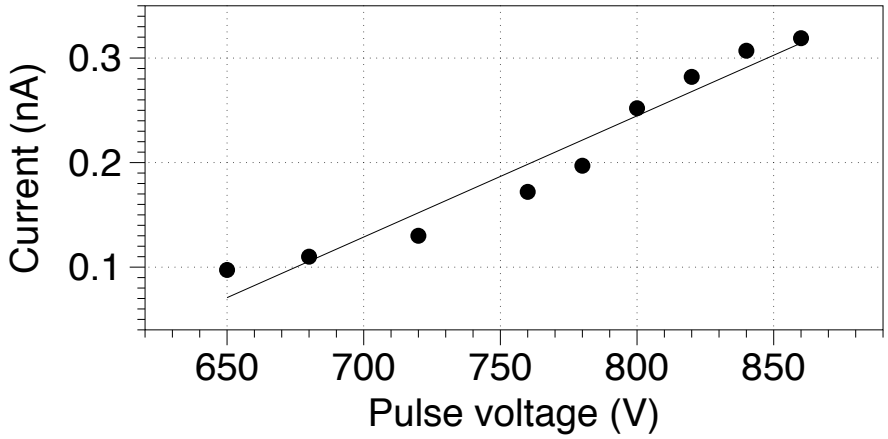

Figure 3.24: The peak current measured in mass spectra of the argon ion beam is plotted against the pulse voltage used. As the voltage increases so does the transmission of the ion beam. The linear trend is used as an eye guide.

One further step was taken to improve the transmission efficiency: the entrance and exit apertures were replaced with expanded letter box apertures (from 3 mm diameter to 5 mm $\times$ 10 mm) and the post TOF lenses were realigned. These two changes were able to increase the transmission ratio of the filter from $\sim$0.03 % to $\sim$2 %. Reducing the ion energy from 1.5 keV to 0.5 keV gave an even more dramatic increase in transmission efficiency of up to 70 %! This clearly demonstrates that the loss of Ar^+s is mainly due to insufficient voltage to displace them before reaching the end of the chamber.

The final validation of the installation and software development can be seen in Figure 3.25, which shows mass spectra of silver clusters produced by the MACS

using different matrix loadings (1, 1.5 and 2.5 %). These results have been provided by Lu Cao.[176]

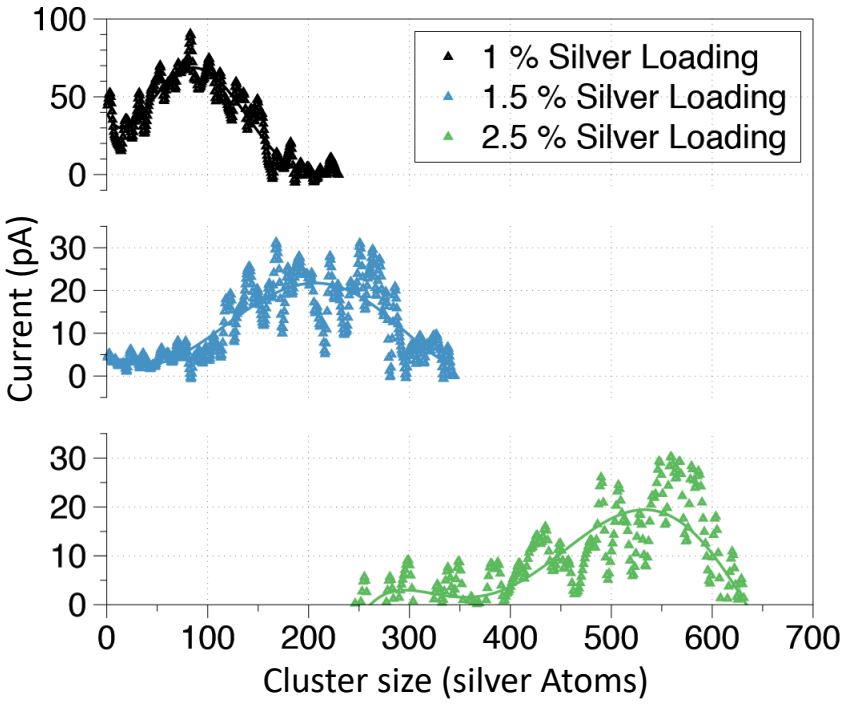

Figure 3.25: The mass spectra of clusters using MACS in reflection mode. Three different silver loadings in have been used in the matrix: 1 %, 1.5 % and 2.5 % (black, blue and green respectively). A simple polynomial fit has been added to each spectrum as an eye guide. Data provided by Lu Cao.

3.9 Conclusion

To conclude, in this chapter the MACS1 has been designed and built to scale up production of size-controlled nanoclusters. The source has been improved, by introducing improvements to both the system geometry and components. High-flux cluster production of size-controlled nanoclusters has been demonstrated, achieving an equivalent cluster current of nearly 100 nA (equivalent to ~100 μg/h). Clusters have been produced across a range of sizes, while maintaining size control (from hundreds to thousands of atoms per cluster). Furthermore, the source has been demonstrated to run in a continuous mode via real-time replenishment of the ma-

trix. The Von Issendorff-Palmer TOF has been simulated for optimum coupling with the source and subsequently commissioned and the transmission efficiency optimised. Bespoke software has been developed to control the TOF, ion optics and current measurements, allowing the measurement of MACS produced clusters in the gas phase. These results demonstrate that clusters are preformed before landing on the surface.

Chapter 4

Proof of Principle of Reflection Mode MACS

This chapter presents the first results from the MACS used in a reflection geometry. The effect of sputtering and collection angle is investigated as well as the total cluster yield of the system. For demonstration and comparison with previous MACS results, all work is carried out with silver clusters. This work has been carried out by the author, Dr Feng Yin and Jian Liu. The cluster production was conducted by the author and Dr. Yin, all the STEM imaging was carried out by Jian Liu. Sample analysis was completed by Jian Liu and the author, independently, and then compared.

4.1 MACS in Reflection Mode

A significant level of complexity when using the MACS in transmission mode comes from the matrix support. The most effective grids have been found to be those with small holes(1.2 μm hole 1.3 μm bar), which provide better matrix coverage of the holes.[176] The best commercial grids for cluster production yield were found to be Quantifoil.[168] Quantifoil is a carbon film with an ordered array of micron ($\sim$1 μm) size holes, which is supported on a standard copper TEM grid (3 mm diameter).

To use this effectively careful grid handling and mounting protocols are required. Furthermore, it is necessary to deposit a thin buffer layer of argon onto the grids prior to experiments to protect the very thin (∼10 nm) carbon film from damage during sputtering. Replenishment must be carefully controlled to maintain "filled" holes maximising the useful area, without excess dosing, which can block the holes completely and prevent cluster production.

Moving to larger areas (> 10 cm^2) this type of support becomes very difficult to work with, and uniform cooling also becomes a problem. As the grid is thin and can only realistically be supported on the outer edges, the thermal path from the cold head becomes much longer and the thermal conduction becomes bottlenecked by the thickness of the mesh and the lower thermal conductivity of the carbon film.

Layer-by-layer growth of argon has been observed on bare copper grids in experiments carried out in the department. This demonstrates that the holes will fill in uniformly from the edges. If the holes were to be fully covered during cluster formation they would become blocked due to the thick film (10's μm). As such, during the cluster production process in transmission mode MACS most of the sputtering must take place in a grazing regime (figure 4.1 a), rather than direct transmission through the matrix as originally envisaged (figure 4.1 b)). The available surfaces for sputtering using a mesh support are the inside of the holes/bars. This prompted the hypothesis that a single flat plate placed at an angle can provide a greater usable area. Adopting a plate support would also remove the need for complex grid handling and buffer layer protection of the support. Moreover, thermal conduction would be improved (thicker support) and the parts can be easily sourced or produced in-house.

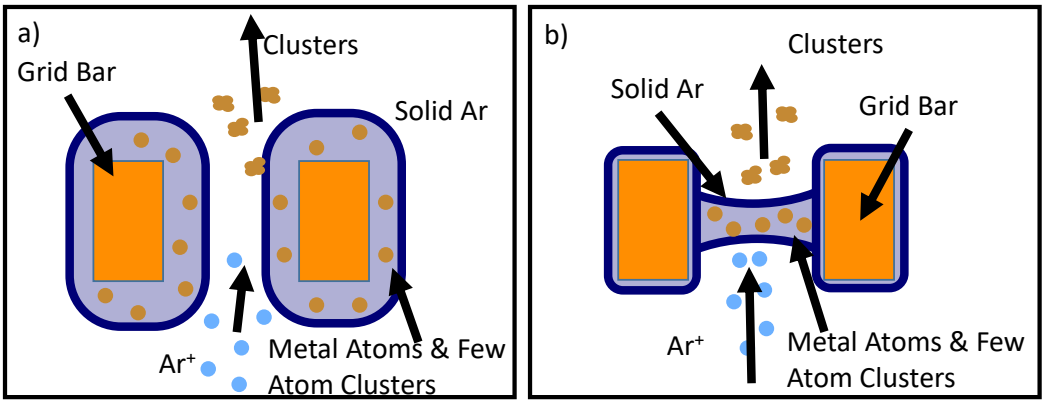

Figure 4.1: Top down cross-sectional representation of the sputtering regime in a single mesh hole in the transmission geometry. a) depicts the sputtering regime predicted based on layer-by-layer growth observed in as yet unpublished experiments at the University of Birmingham. b) illustrates the previous concept of transmission sputtering of the matrix. This change has a significant impact on the available sputtering area in the transmission geometry.

The proposed principle of the reflection mode operation can be seen in figure 4.2. This arrangement provides much greater access for dosing, sputtering and collecting clusters. There is also increased flexibility in support geometry. As this is no longer a transmission technique confined by the mesh geometry the optimum angle for sputtering and collection must be explored. This open geometry allows a wide range of sputtering and collection angles to be tested in order to optimise performance.

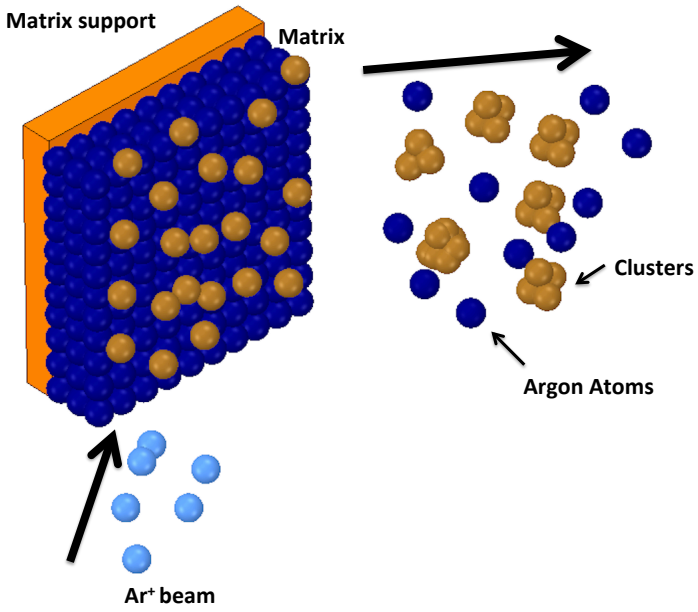

Figure 4.2: The principle of reflection mode in the MACS is shown in the concept image above. An argon ion beam is impinged onto a cryogenically cooled matrix of co-condensed metal and rare gas atoms. Nanoclusters are formed, ripened and extracted by successive ion impacts. This arrangement offers greater freedom in the system geometry, and convenience in matrix support handling.

4.2 Experimental Setup

The MACS system described in this chapter was a proof of principle instrument that is based around the chamber of an LK High Resolution Electron Energy Loss Spectrometer (HREELS). Figure 4.3 a) shows a picture of the entire system, however, the top chamber was put to use for MACS research, the full chamber drawing is shown in Figure 4.3 b). No substantial modifications were carried out on the underlying system. A Pfeiffer 250 L/s turbo-molecular pump and gamma vacuum 100 L/s ion pump are mounted on port 1 and an ion gauge, is mounted on port 2, details shown in Figure 4.3 b). View ports are also kept on ports 7 and 8. The remaining labelled ports are new introductions and are considered in the next section. This base system has been used for both these proof of principle measurements and the ion-induced light emission described in Chapter 6, the wide range of ports provides the flexibility required for these experimental investigations.

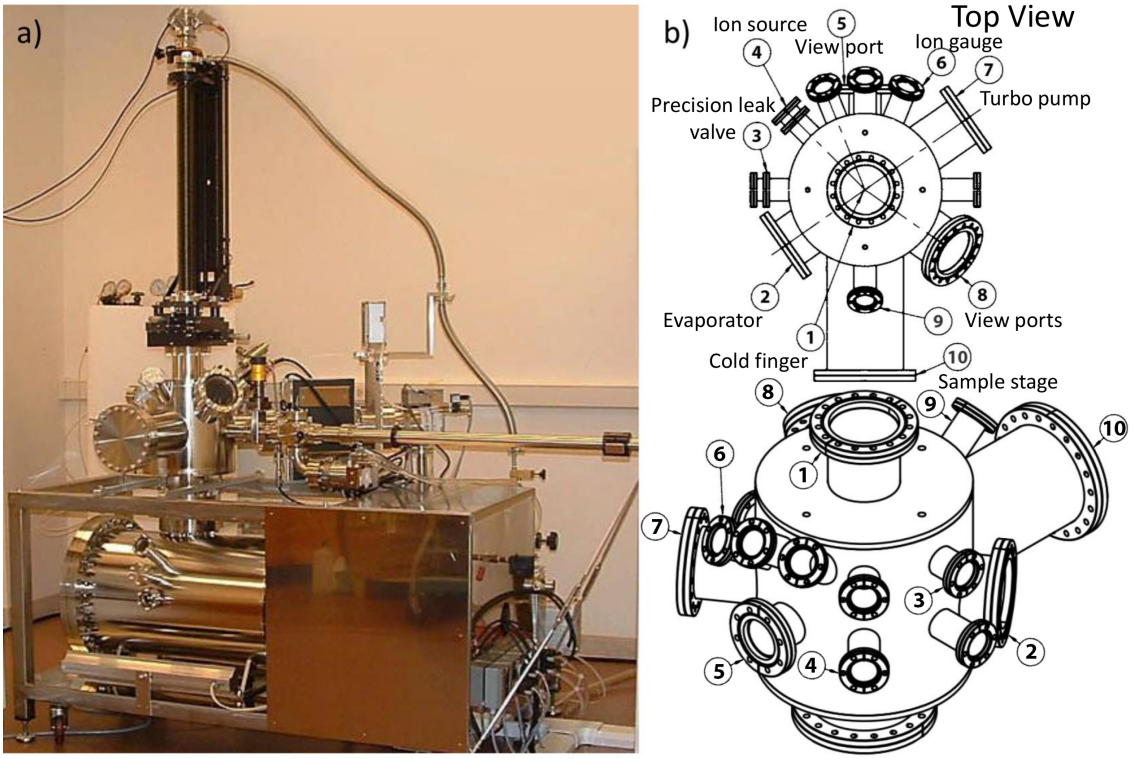

Figure 4.3: a) presents an image of the entire HREELS system as new, prior to modification for use as a MACS system, reproduced from [183]. b) is the technical drawing of the upper chamber labelled as used for the production of nanocluster via reflection mode matrix assembly.

4.2.1 System Modification

As shown in Figure 4.2 the reflection mode allows variation in sputtering angle (α) and cluster collection angle (β). To take advantage of this a system permitting manipulation of the sputtering angle and the ability to make angle-resolved measurements of the produced nanoclusters is required. To implement, this there are four main changes to the upper chamber shown in figure 4.3, the ion source, evaporator, cryogenically cooled matrix support and sample holder, which are each described in brief here. A simplified schematic of the entire system is shown in figure 4.4.

The matrix is cooled to below 20 K by a continuous flow of liquid helium through the cold finger. A diagram of the cooling lines can be seen in Figure 4.5. To avoid

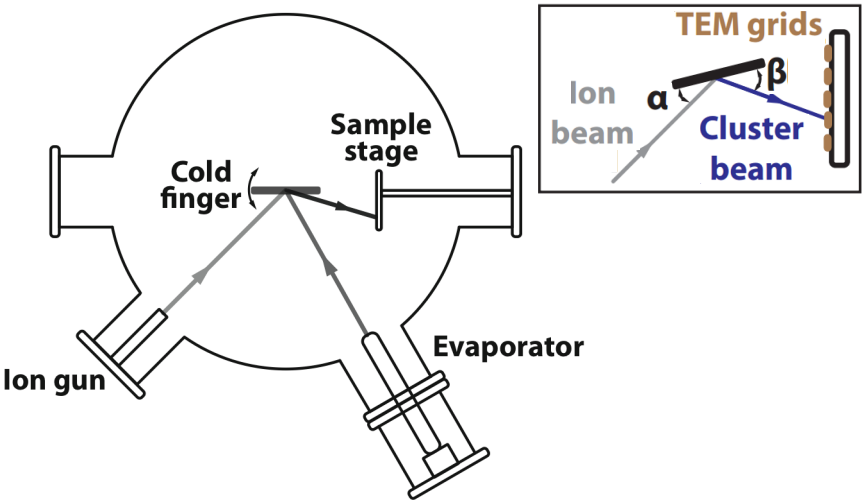

Figure 4.4: Schematic of the proof of principle reflection mode MACS system (based on the LK HREELS chamber). The insert shows a close up of the matrix support and defines the sputtering (ion bombardment) and collection (cluster deposition) angles α and β respectively. The rotation of the cold finger allows the sputtering and collection angles to be changed. Additional ports have been left out for simplicity.

blockage from frozen water vapour, the lines are first pumped out and then cycled with warm helium gas from the top of the dewar before cooling (∼10 minutes), the transfer line is then slowly inserted into the liquid helium. The flow to the tip (red line in figure 4.5) is restricted initially to speed up the cooling of the shield (blue line in figure 4.5). Once the radiation shield is sufficiently cooled this is then reversed , i.e. restricting flow to the shield and increasing flow the tip, in order to provide greater cooling at the tip. The ultimate temperature is reached after 1.5-2 h of cooling, without additional thermal load this is 9-10 K. The temperature is measured by a four pin 27 Ω Rhodium-Iron resistive sensor from Oxford Instruments. This is housed in the support block (see figure 4.6)

To load and sputter the matrix the Createc HTC thermal effusion cell evaporator and Omicron ISE-5 ion gun have been installed on ports 6 and 5. The effusion cell is fitted with 10 cc Al_2O_3 crucible, to permit horizontal mounting this is used with a 5 cc boat inserted into the crucible, which prevents melted evaporants flowing out. To investigate different sputtering angles the sample stage is mounted on a rotary drive

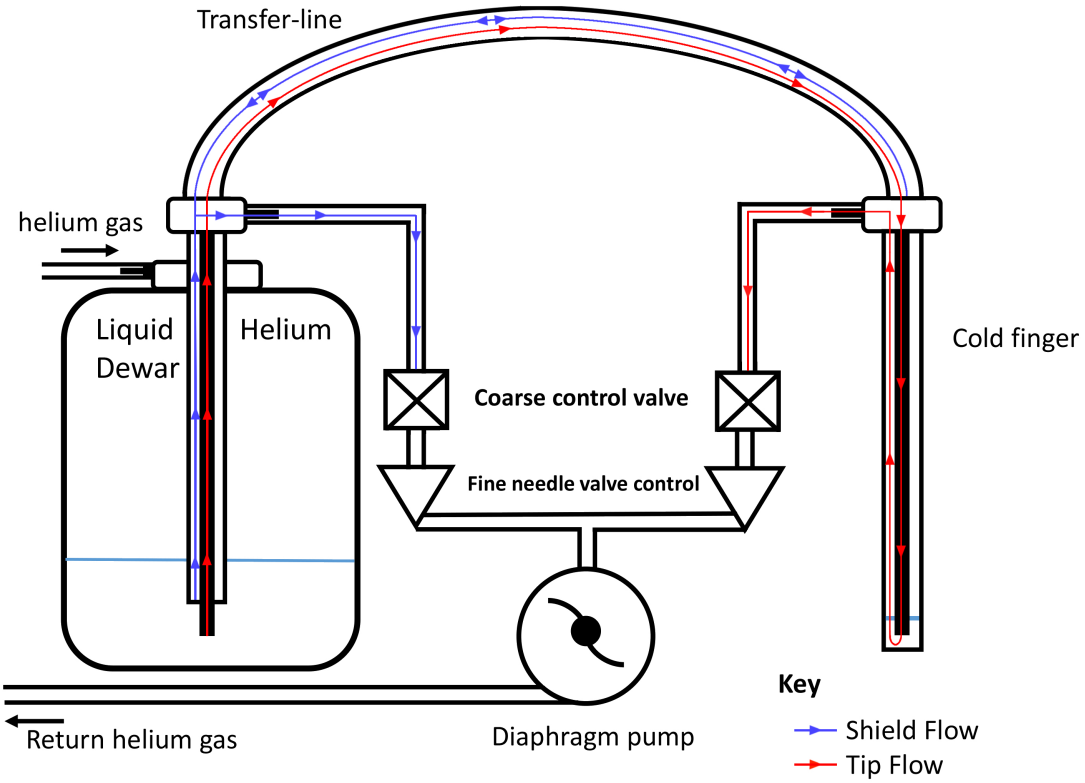

Figure 4.5: Scheme of cryogenic cooling lines, transferring liquid helium to the cold finger. The shield line (blue) within the transfer-line acts like a cryostat, while the tip (red) delivers liquid helium to the end plate of the cold finger.

and manipulator. This set-up allows rotation of the matrix support through 360° as well as x, y, z manipulation, as such the support can be carefully aligned to the beam and sample stage. The matrix support plate itself is shown in Figure 4.6, the mounting block after the sapphire isolation houses the Rhodium-Iron temperature sensor and fixing point for biasing the support. This is electrically isolated from the main body of the cold finger by a sapphire spacer and ceramic washers on the screw mountings. The sapphire faces are coated in gold to improve thermal contact. The main support plate is a simple copper plate chosen to be smaller than the ion beam (plate 15 mm $\times$ 30 mm) to give a near uniform current density.

The sample stage holds an array of up to 12 TEM grids, the array is mounted horizontally i.e. permitting azimuthal angle-resolved measurements (β in figure

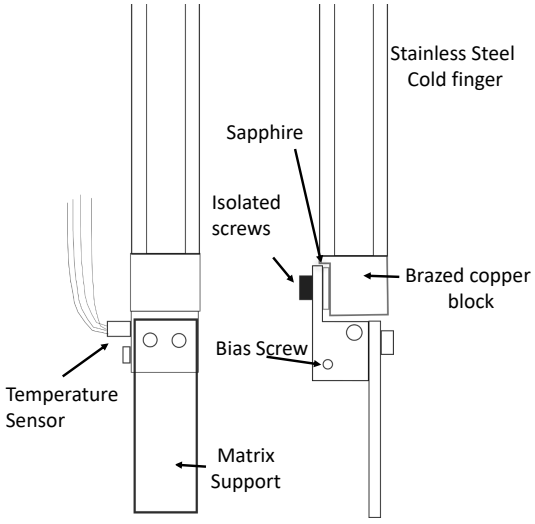

Figure 4.6: Schematic diagram of the cold finger. The matrix support is formed by the copper plate (15mm × 40 mm × 2 mm). The support is electrically isolated from the cold finger by a sapphire spacer that is used to provide electrical isolation. The two faces of the spacer are coated in gold to increase thermal contact. The system is capable of reaching a base temperature of 9 K.

4.4). This array is fixed to a stainless steel rod which is then mounted on a linear translator (see figure 4.7). The spacing between the 12 TEM grid holders increases along the holder to give more even angular increments from the centre of the cold finger. The samples are isolated from the linear drive by a PTFE mounting block, so that they can be biased for deposition. However, all experiments were performed with the stage grounded to avoid any charging by cluster deposition or stray ion beam. A foil is mounted on a second rod, which is used as a simple shutter to avoid undesired depositions. The schematic of this stage can be seen in Figure 4.7.

4.2.2 Sample Preparation

In this system, nanocluster production performed in a two stage process. First, the matrix is deposited onto the cooled matrix support, which is aligned perpendicularly to the thermal evaporator. Argon is deposited by backfilling the chamber to a pre-selected pressure via a precision leak valve. The metal concentration is varied by changing the evaporator temperature, and deposition rate is measured by QCM.

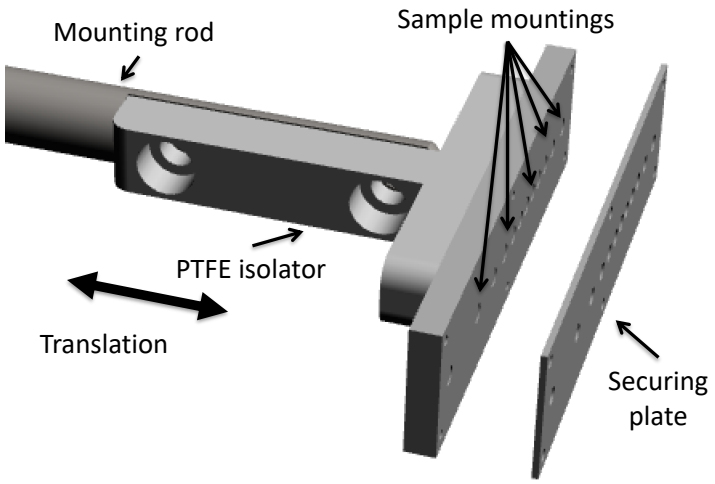

Figure 4.7: Schematic of the deposition stage for reflection mode MACS. A total of 12 TEM grids can be mounted. Samples are spaced to give an even angular spread from the centre of the cold finger. A securing plate is used to fix the TEM grids in place. A grounding wire is also fixed to one of these screw to avoid charging.

During formation matrix temperature remained between 15-18 K. Examples of the change in silver deposition rate with evaporation temperature and the deposition profile of the evaporator are shown in Figure 4.8 a) and b), respectively. The dependence of deposition rate on temperature has been carried out in both heating and cooling directions. These results are averaged to negate the influence of the ramp direction. The rate in terms of $\mathring{A}$/s is too low to be measured by the QCM in real-time, therefore it is calculated based on the thickness deposited over an extended duration, two hundred seconds per point for the temperature dependence and sixty seconds per point for the deposition profile. The deposition profile is measured by translating the QCM along the line of the matrix position. The profile appears to be relatively flat at the centre of the chamber and across the matrix surface. During preparation of the matrix the sample stage is covered with a shutter to prevent contamination.

After matrix formation the matrix is sputtered to produce clusters. First the matrix rotation is set to the desired sputtering angle. The deposition stage is moved in until it is <0.5 cm from the matrix support the alignment is carried out before

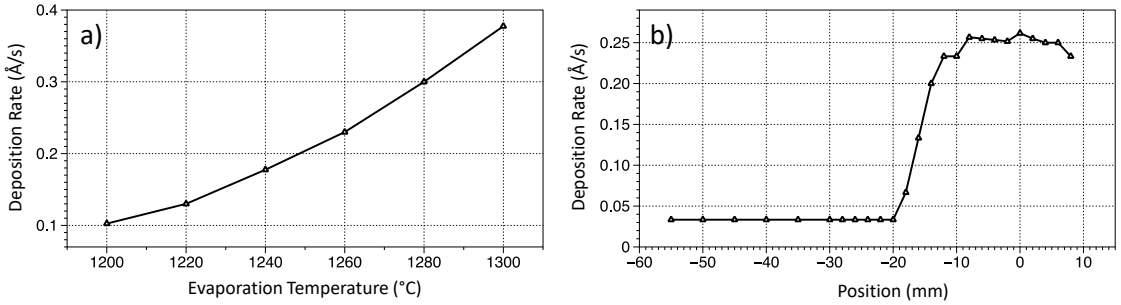

Figure 4.8: The effect of both evaporator temperature and substrate position has been calibrated. Graph a) shows the effect of evaporator temperature on the deposition rate of silver. b) is the profile of the evaporant beam, the central position has been set by the observed peak and the matrix support positioned accordingly. The temperature dependence measurements were carried out at the peak position for maximum signal.

cooling). The alignment is made such that the edge of the matrix support always meets the sample position on the sample stage (see figure 4.15). This will cause the centre of the support to be slight offset from the centre of the chamber (<1 ° change to sputtering angle). Based on the alignment position the angle between the matrix support and each sample can then be calculated. The matrix is then sputtered using a 2.5 keV argon ion beam, with a current of approximately 6 μA (argon gas pressure 9×10^{-7} Torr). To improve the accuracy of the ion dose, the current is measured in real-time using labview and a picoammeter, the current is integrated during the deposition to give an ion dose value. Once a set dose level is reached the ion gun is switched off (the same ion dose has been used in each experiment). The dose is chosen such that the matrix is not depleted, based on previous experimental results. Collected samples are then removed from vacuum and transferred to the microscope or a vacuum box (1×10^{-2} to $\times10^{-3}$ mbar) for imaging and interim storage, respectively. Nanocluster densities are measured by counting the number of clusters per frame, from five different areas across the TEM grid with a minimum of two images from each area. Nanocluster size is assessed using HAADF intensity analysis as illustrated in appendix B.2.

4.3 Dependence of Nanocluster Production on Sputtering Angle

To reproduce the glancing incidence geometry found in the transmission mode a low sputtering angle with a collection close to in-line with the matrix surface was investigated. The sputtering angle (α) was set to 10 ° from parallel to the matrix surface and the collection angle (β) varied from 8 ° to 110 °. A total of eight samples were collected over that range. A ∼100 nm argon matrix is formed with 1.1 % silver loading. This has then been sputtered for 30 seconds using a 3 μA, 2.5 keV argon ion beam. Sample images of the resulting clusters from three of these positions can be seen in Figure 4.9.

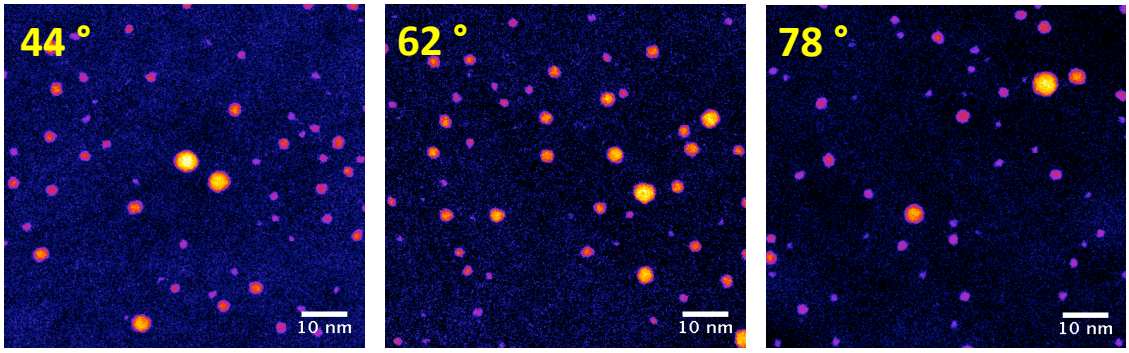

Figure 4.9: HAADF STEM images of silver clusters produced in reflection mode with a sputtering angle (α) of 10°. Each image is take from a TEM grid placed at a different collection angle (β), indicated in the top left of each image. The argon matrix thickness was ∼100 nm with a 1.1 % silver loading. The matrix temperature during formation was 15-18 K. This has been sputtered for 30 seconds using a 3 μA Ar^+ beam at 2.5 keV.

The nanocluster density at each angle is shown in figure 4.10 a), the profile is fitted with a Gaussian. The peak flux is observed at a collection angle 59°, which is not expected from previous transmission mode results. The previous transmission mode demonstrated a narrow low-divergence beam exiting from the matrix area, i.e. almost parallel to the surface. This is probably due to the channel nature of the mesh holes. The average size distribution of the produced nanoclusters across all collection angles is presented in Figure 4.10 b).

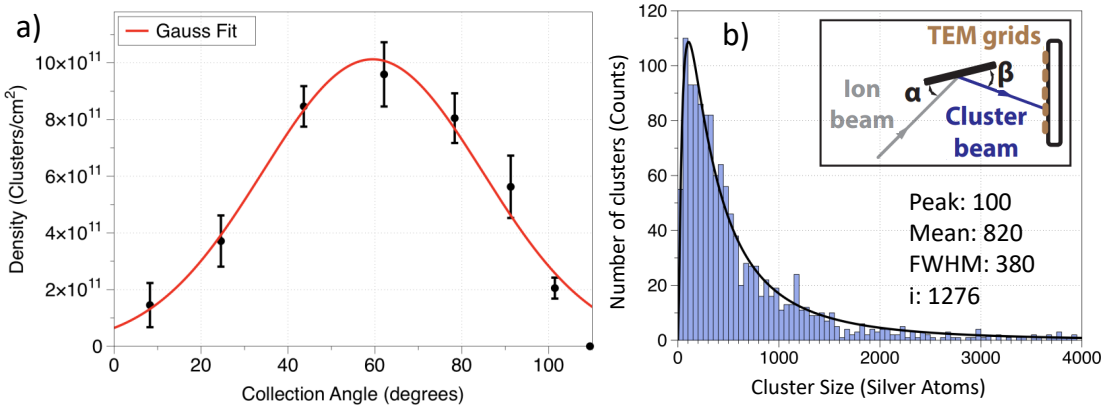

Figure 4.10: The cluster density as measured on each TEM grid is given in a). The Gaussian fit (red) gives a peak density at around 59 °. The average size distribution of nanoclusters deposited across all grids is shown in b). A peak value is observed at 100 silver atoms with a mean of 820. The FWHM is 380 silver atoms. The bin width is fifty silver atoms. The insert provides a reminder of the geometry with α being sputtering angle and β cluster collection angle. i denotes the total number of clusters measured.

The peak size is ∼100 silver atoms with a Full Width Half Maximum (FWHM) of about 380 silver atoms. Throughout this chapter peak values and FWHM values of cluster size distributions are calculated based from fitting the size distribution histogram with a lognormal function. The majority of clusters are small with only a minor fraction $< 5\%$ of large outlier nanoclusters > 2000 silver atoms. A more detailed view of the size distribution is given in Figure 4.11, the size distribution of nanoclusters imaged at each collection angle is depicted separately. Each sample is imaged in 5 regions (four quadrants and the centre) taking a minimum of 25 images per sample, a minimum of ten images are analysed to provide a good statistical representation. Although, samples with lower density ($\sim 1 \times 10^{11}$) will have fewer particles to analyse, the total number of particles is given in each figure denoted by i. Samples generally show consistent particle density and size distributions across all areas imaged.

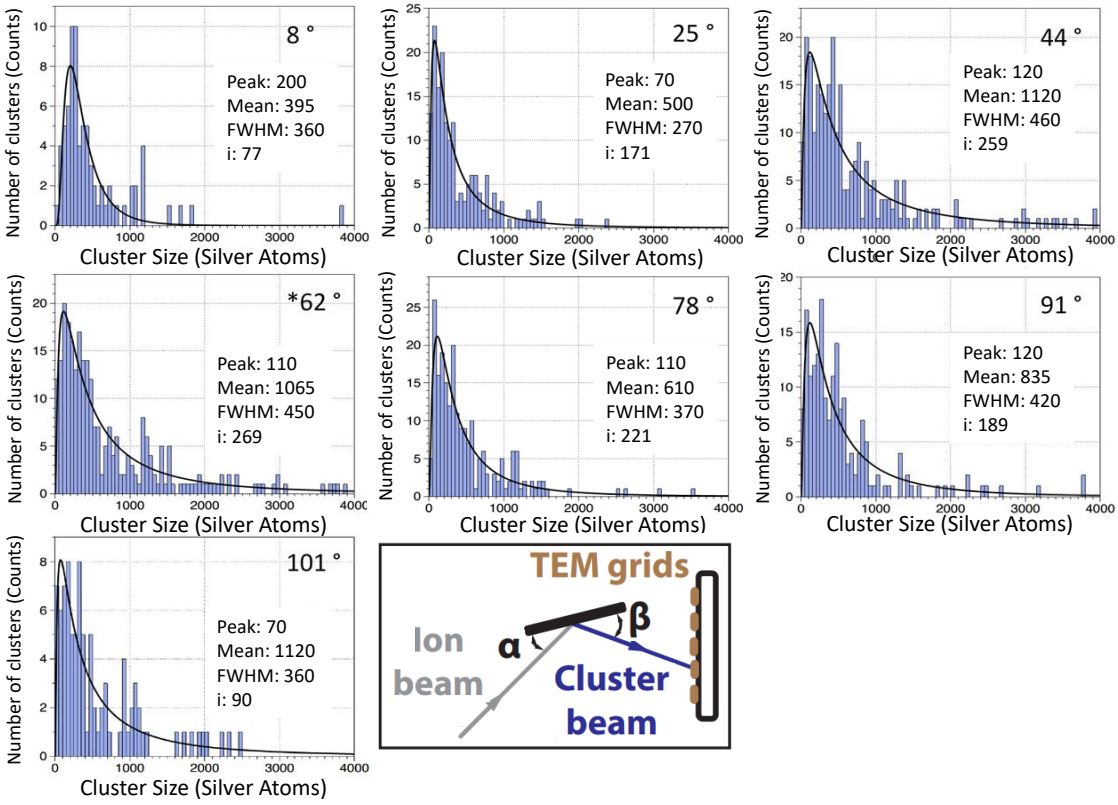

Figure 4.11: The size distribution of the nanoclusters observed at each collection angle is plotted in a histogram. In all cases the sputtering angle (α) is ten degrees, the collection angle (β) is displayed in the top right of each graph. The insert in the bottom middle indicates the geometry. The bin width is 50 silver atoms. The peak and mean cluster size is shown for each distribution, as well as the FWHM and number of particles imaged (i).
** indicates the peak flux position.*

4.4 Cluster Yield

In terms of viability as a cluster source the amount and deposition area of clusters produced is a key parameter. The cluster beam is observed to be broad, with clusters produced across an 80 ° arc. This is unexpected compared with the low divergence of clusters in transmission mode. However, this is generally observed when sputtering ices.[184–186] This maybe due to the grid shape channelling both the incoming ions and outgoing cluster confining the beam. If ejected nanoclusters are recaptured, further ion impacts would be required to release the cluster (a minimum of one). Furthermore, in transmission mode a large portion of the argon ions will be wasted

as they hit the face of the matrix and sputter material out in the opposing direction of the impinging ions (i.e. conventional sputtering). Therefore, the efficiency of reflection mode (ion to cluster conversion ratio) is expected to be higher. The yield is calculated based on the number of nanoclusters deposited divided by the number of ions impinging on the matrix. Which in turn is calculated from the measured drain current between the electrically isolated matrix and ground. Thus, the exact value should be treated with some caution as it is not a true measurement of the ions incident on the matrix but the sum of incoming ions as well as the contribution of outgoing electrons and ions. Current measurements performed on different surfaces as well as single point Faraday cup measurements seem consistent with typical matrix current measurements so the discrepancy is considered to be small.

The yield achieved in high flux experiments with transmission mode is <0.03 % using a copper 1000 mesh matrix support. STEM measurements of the deposited TEM grids are used to calculate the average cluster density over the total deposition area. The total number of clusters can then be calculated and compared with the number of impinging ions during deposition (calculated from real time current measurement).

In order to calculate the yield in reflection mode the profile of nanoclusters collected in 1D has to be extrapolated to a surface, based on the target geometry (40×15 mm rectangle). Using the surface extrapolation the total number of nanoclusters produced can be calculated and hence the yield. The beam hits the entire plate with a near uniform current density of argon ions (due to defocusing). The azimuthal angular cluster density has been measured by HAADF STEM of TEM grids (figure 4.10), relative to the centre of the matrix support. Therefore, just the vertical extrapolation is needed to give total cluster flux. A linear fall off of cluster flux in the z-direction is used as an approximation. This is pinned to 50 % at the extremes of the matrix support (i.e. top and bottom of the plate). The 50 % at the edge is

based on the fact the cluster flux measured at the centre is the sum of contributions form the entire plate above and below (which are equal). As such, at the top there is no contribution from the plate above (as there is none). The extended distance below is neglected as the contribution will become smaller with distance.

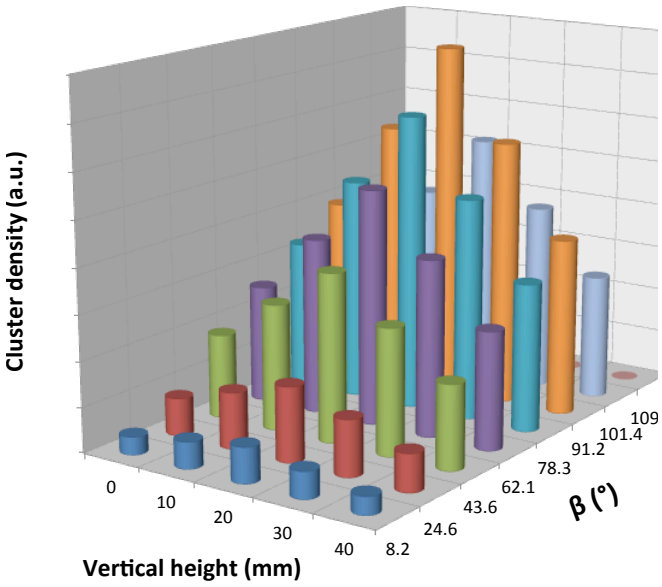

Figure 4.12: A representation of the cluster beam shape based on measured azimuthal angular distribution (β) showing a skewed Gaussian shape and assumed linear fall off vertically across the matrix support (z direction). Such a profile can be used to estimate total cluster production and obtain the argon ion-to-nanocluster yield.

The profile of produced cluster flux has been extrapolated from the 10 ° sputtering angle data shown in figure 4.10. The resulting cluster beam shape can be seen in 4.12. The extrapolation covers all measured angles and the full height of the plate (40 mm). This calculation should be a lower limit as in reality the beam profile should extend below and above the plate to some degree. After integration of the entire beam the equivalent cluster current is 28 nA over the deposition ($\sim$ 30 s). The average ion beam current measured over this time was 3 μA giving a conversion of 0.0093 (almost 1 %). In comparison, the yield observed in transmission mode for high flux measurements using a copper 1000 mesh is of the order of 0.03 % (Chapter 3). The $\sim$1 %, observed in reflection provides a much more efficient

method of cluster production. This is primarily due to the much greater area used in reflection mode (i.e. 100% of the surface).

4.4.1 Incident Angle Dependence

To investigate the effect of incident angle on nanocluster production, further measurements have been made for sputtering angles ranging from 10° to 45 °. All other parameters remain unchanged (i.e. energy, matrix thickness and metal concentration, as well as matrix temperature). Due to experimental constraints the absolute ion dose measured at the matrix support varied between successive experiments due to the build-up of a metal film on the insulated surfaces of the coldfinger supporting the matrix. This introduces a degree of uncertainty in the measured sputter current dose, except for the initial 10° case. In the worst case, the error in the ion dose value, introduced by this experimental artefact, is of the order of 50 % . As such the absolute flux is not a reliable result for all other sputtering angles, however the distribution can still be considered. The nanocluster density versus collection angle and as a function of incident sputtering angle can be seen in figure 4.13 a). This shows the nanocluster density measured by STEM. The peak collection angle for cluster ejection changes with the incident sputtering angle. Figure 4.13 b) is obtained after factoring in the solid angle of the grid projection relative to the centre of the matrix support plate. This produces an asymmetric distribution reducing the contribution of the low-angle samples, as they are very close to the matrix support. Factoring in the solid angle projection adds more weight to samples covering small solid angles (i.e. high collection angles), which in turn have lower cluster densities.

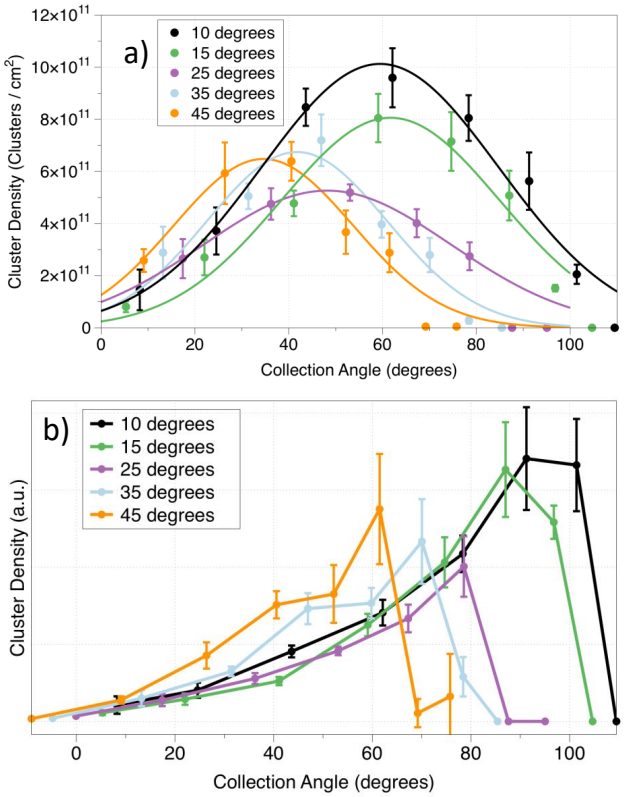

Figure 4.13: The measured nanocluster density is plotted against the collection angle for incident ion beam angles (sputtering angle). a) plots the "as measured" cluster density for different collection angles, sputtering angle is given in the top left corner. Peak trends are given by gaussian fits b) presents the data after solid angle compensation for the relative angle and distance of each TEM grid compared with the centre of the matrix. The solid angle consideration skews the originally Gaussian distributions (lines are used as eye guides).

Considering not only the collection angle but the combination of both sputtering angle and collection angle, further information can be extracted about the effect of sputtering angle on the production of nanoclusters. Figure 4.14 plots the sputtering angle against the angle with the highest observed nanocluster flux, for both the as measured density and solid angle corrected values i.e. the optimum collection angle (β) for a particular incident ion angle (α). In both cases a near linear trend is observable. In the case of the solid angle correction, a near direct correlation is observed (gradient of 0.85 and 0.6 for the solid angle corrected and raw values respectively). A gradient of 1 would indicate a constant value for the sum of the sputtering and peak collection angle and would mean the peak nanocluster produc-

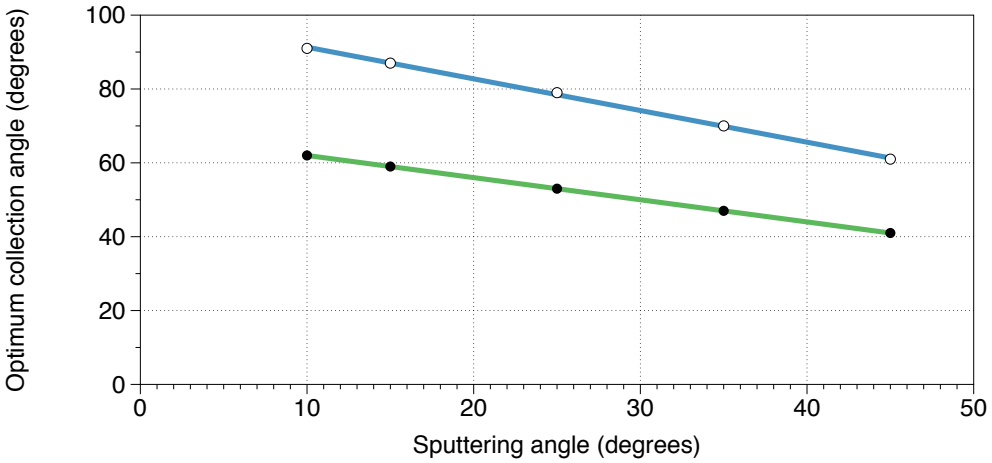

Figure 4.14: The collection angle of the maximum cluster density is plotted against the sputtering angle, for both the "as measured" (green) and after solid angle corrections (blue). In each case a linear trend is observed with gradients of 0.6 and 0.85 respectively.

tion is independent from the surface orientation. The average sum of sputtering and collection angle over the 15-45 ° sputtering angle range is 104±3 ° for the solid angle corrected maxima, and 78±6 ° for the raw data maximum cluster flux. The error values here are based on standard deviations of the sum of the sputtering and collection angles.

The shift to larger collection angles for smaller incident sputtering angles (α) can be linked to the system geometry. As the alignment of the sample plate is made relative to the edge of the matrix support, this point is fixed and as the incident sputtering angle is changed this point effectively becomes a pivot (see figure 4.15). When the sputtering angle α is reduced, the ion density will increase in position i) relative to position iii), positions shown in figure 4.15. Similarly the distance between the support and samples reduces at the edge nearest to the ion source, the distance from i) to ii) in figure 4.15, while the distance from points iii) to iv) remains unchanged. These two effects will lead to the increase in the cluster density observed at high collection angles when α is reduced. Therefore, the peak collection angle will shift towards larger angles.

The size distribution of clusters produced at each sputtering angle has also been

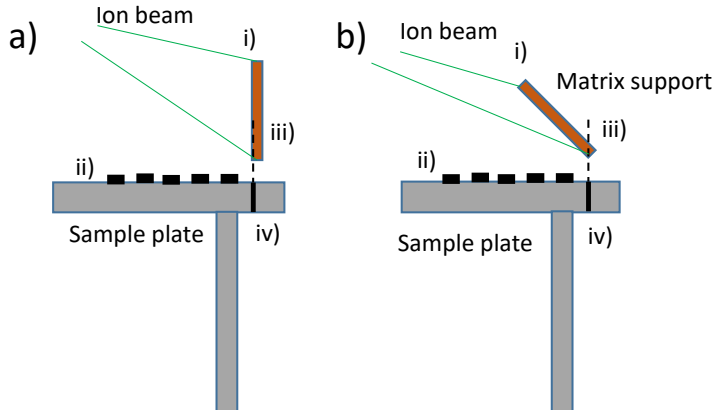

Figure 4.15: Illustration demonstrating the effect of changes in the incident angle α on the ion density gradient across the matrix support and the throw distance. a) shows a high sputtering angle (α) and b) a low sputtering angle. As the sputtering angle decreases, points i) and ii) become closer together. Due to the alignment method, points iii) and iv) always have the same separation. Reducing alpha also increases the ion density a point i) relative to point iii).

measured. The average size distribution across all collection angles as a function of sputtering angle is given in figure 4.16. In each case the peak, mean size and FWHM of the distribution is given.

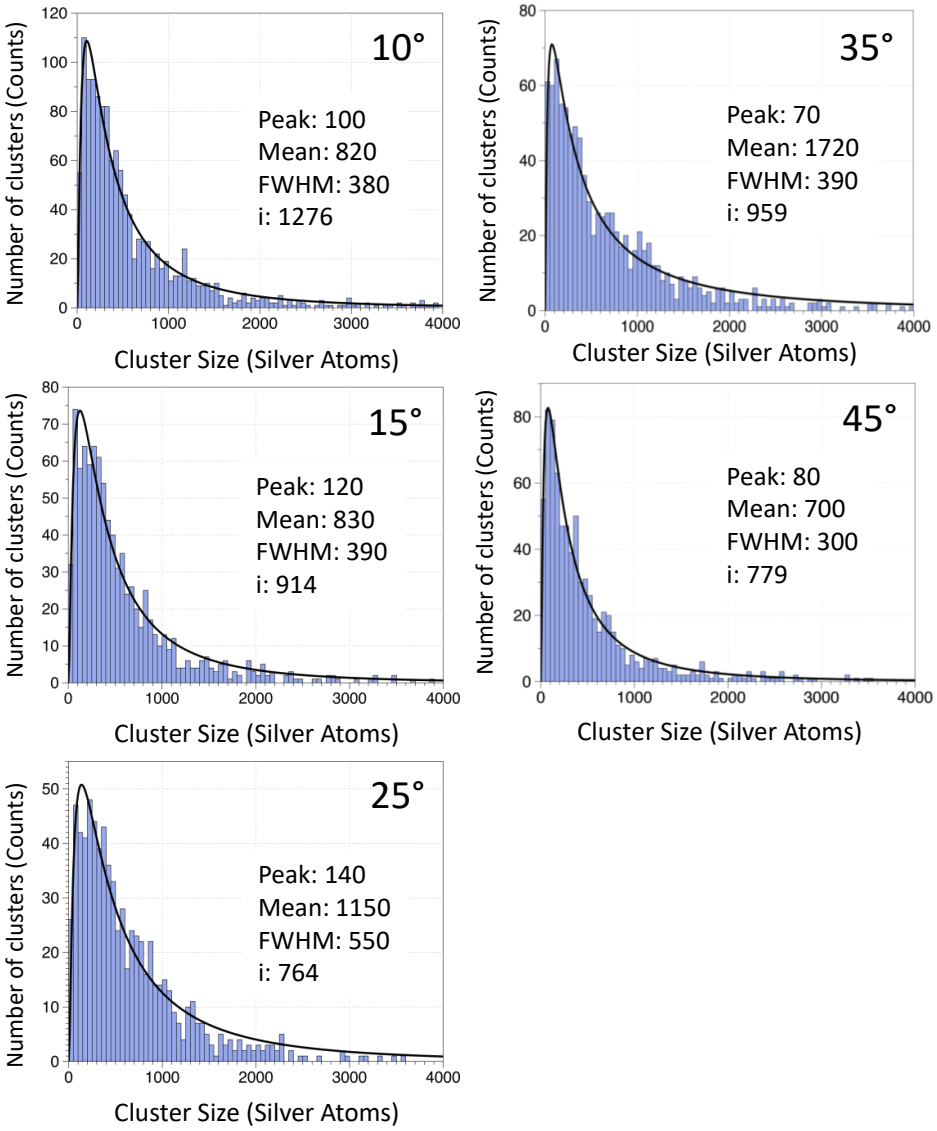

Figure 4.16: The average size distribution of deposited nanoclusters is shown for different sputtering angles (shown top right). In all cases a lognormal distribution is observed. There is no significant trend observed as a result of the sputtering angle.

A similar lognormal size distribution is seen across all sputtering angles, the peak nanocluster size remains between 70 and 140 silver atoms. The number of large clusters (>2000 silver atoms) also remains within the experimental error of 3-7 % for all sputtering angles. The size distributions appear unchanged by sputtering angle with just experimental fluctuation. This consistent peak size at higher sputtering angles is some what surprising given that this generally results in high sputtering yields. However, it does indicate limited surface aggregation in the resulting nanoclusters

due to ejected atoms. The limited effect of sputtering angle of size relaxes system geometry constraints.

4.5 Conclusion

This chapter has reported the use of the matrix assembly technique in a reflection geometry. This simplifies the existing technology both for maintenance and day-to-day running, providing a more reliable and consistent source. Low angle sputtering (10 °) has been employed as this is likely the same process that takes place in the transmission geometry based on argon growth mode studies. The method was shown to produce a wide beam of nanoclusters with the FWHM of the beam giving a half angle of $\sim$30°. Further to this, the practical efficiency increased from <0.03% of ions being converted into nanoclusters in high flux transmission mode, to 1 % in reflection mode, a dramatic improvement largely due to the more accessible geometry. The peak ejection angle was found to be dependent on sputtering angle with a linear relation between the sputtering and collection angles. The average angle between incident and peak ejection angle in this geometrical configuration was found to be $\sim$86°.

Furthermore, the size distribution appears to be largely independent of the sputtering or collection angle, with mean nanocluster size being $\sim$ 100 atoms. An average of 60% of the nanoclusters produced are small containing <500 silver atoms. The number of large outlier nanoclusters is also similar for all angles at between 3-7 %. The invariance of the size away from the peak where there is much less material deposited is an indication that surface aggregation does not play a significant role in the resulting cluster size.

With this ion-to-nanocluster conversion rate, current commercial ion beam sources of 1 A could be used to achieve a equivalent nanocluster beam current of 10mA, which is about 4-5 orders more in terms of the number of clusters than current

unfiltered high flux cluster beam technology! This would bring the production level to grams of nanoclusters per hour. This exploratory work forms the basis for a new practical source scaling up cluster production. The results demonstrate such a source could not only increase the rate of production but also deposit clusters with relatively uniform density over large areas (with appropriate choice of geometries). The development of the first such source is the focus of the following chapter and is the start of a new strand of research within the MACS technology.

Chapter 5

Development and Demonstration of a MACS for Routine Nanocluster Deposition

The work presented in this chapter covers the design, construction and commissioning of the new reflection mode MACS2. These experiments have all been conducted with silver clusters which provides a good comparison to previous results. The author, who lead the work, was supported at times by both Thibaut Mathieu and Dr. Vitor Oiko in constructing and commissioning the source. Again all STEM was conducted by Jian Liu and Fluorescence Microscopy of nanoclusters deposited onto glass was carried out by Timothy Poon. Any other contributions are stated clearly in the appropriate section.

5.1 Concept and Development

The success of the initial reflection mode experiments provided a strong case for further investigation and adoption of this new geometry, specifically the increased ion to nanocluster conversion ratio observed in Chapter 4) compared with that in transmission (see Chapter 3). The new cluster source is built based on reflection

mode cluster production for routine deposition. The key criteria of this source are; to produce large quantities of nanoclusters (equivalent to hundreds of nA), to deposit nanoclusters over large area substrates (10s of cm^2), to establish a robust system for routine nanocluster production by non-experts. The resulting system takes the role of a sample production instrument for size-controlled nanoclusters for model catalysts, biochips and colloids.

5.2 Design and Construction

As the instrument should deposit large numbers of clusters over an extended area (e.g. for biochip production), the starting point for the design is to decide on a deposition stage that permits the production of such samples.

5.2.1 Deposition Stage

To provide a means for large-area deposition a previously purchased deposition chamber for coating glass slides has been employed. This provides a mounting for 21 glass slides, an area of about 400 cm^2, which can all be deposited onto without the need to break vacuum. This was supplied by Inanovate, the full assembly drawing can be seen in figure 5.1 and the technical drawing in figure 5.3 a).

To maintain a high flux a large fraction of the nanoclusters produced must be collected. This can be achieved either by bringing the deposition stage close to the generation position to capture a large solid angle, or by focusing the nanoclusters onto the deposition stage (e.g. electrostatically). Previous results have shown that 10-15 % of the nanoclusters are produced either positive or negative,[176] limiting the cluster collection possible from ion-optic extraction and focusing. Furthermore, the effect on the ion beam from the addition of such extraction optics would need to be considered. Figure 5.2 shows the percentage of nanoclusters collected for a given distance between the matrix and deposition stage. The size of the deposition area

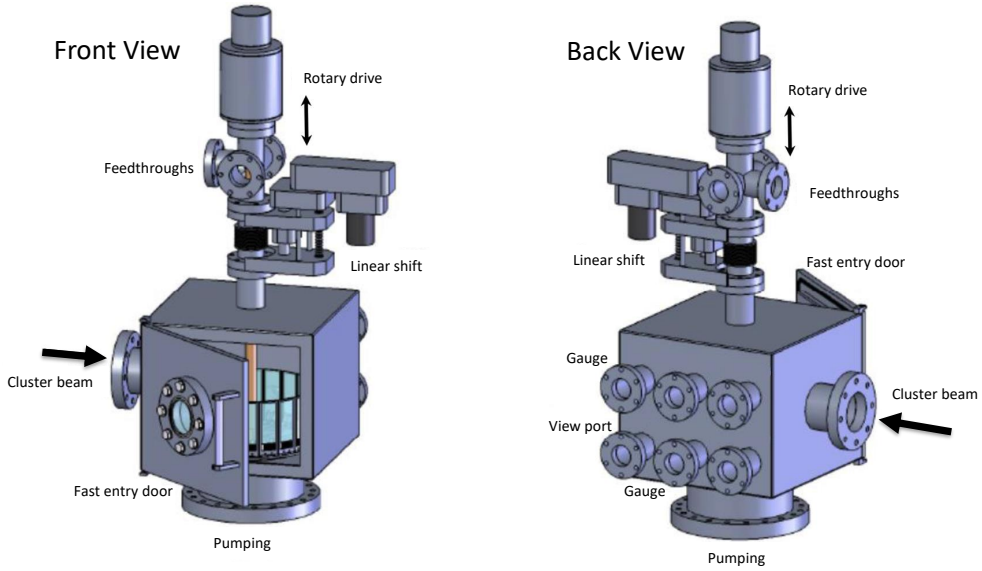

Figure 5.1: Drawing of the fully assembled deposition chamber supplied by Teer Coatings Limited. Inside the carousel can be seen which is driven by two drives mounted on top of the chamber (one for height and the other for rotation).

is set to a single glass slide (75 × 25 mm). These results are based on the angular spread of produced nanoclusters observed in chapter 4. The fraction captured is first considered for the 1D case of a 75 mm (blue) and 25 mm (green) plate. These are then combined for the 2D case, to give the fraction of nanoclusters collected as a function of distance. The spread of the cluster flux is then based on the fit of the cluster density from angle resolved cluster deposition (chapter 4). In this calculation, production is considered to be symmetrical in the horizontal and vertical planes (i.e. lower estimate compared with expected vertical production profile). The insert in figure 5.2 provides an illustration of the process with a support at two different locations a) and b) with respect to the matrix. In each case a different fraction of the cluster beam (orange) is collected. Based on these considerations, as long as a deposition distance of 10 cm or less is used a greater fraction can be collected by direct deposition onto a glass sized substrate than through ion extraction methods.

To achieve a shorter distance between the matrix deposition stage, the chamber requires modification to introduce the beam both perpendicular and close to the deposition surface. The modifications can be seen in figure 5.3 b). This design has

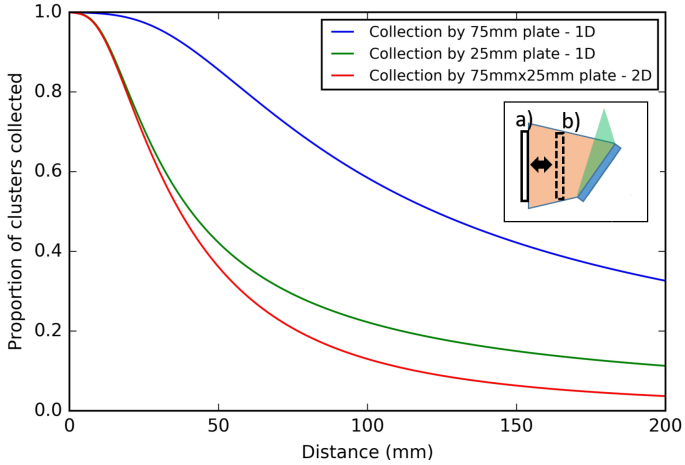

Figure 5.2: The fall off of collected nanocluster percentage with distance, based on the azimuthal nanocluster divergence measured in chapter 4. The 1D case for a 75 mm and 25 mm plate are indicated by the blue and green lines, respectively. The combined collection percentage in 2D is indicated by the red line, considering a 75 $\times$ 25 mm substrate (i.e. MACS2 substrate). The insert provides an illustration of the substrate at two different positions a) and b). The MACS 2 uses a matrix to deposition stage distance of $\sim$8cm.

a distance of $\sim$ 8 cm between the matrix and deposition stage, which corresponds to an expected collection of $\sim$15-20 % of the produced nanoclusters. The ISE-5 ion source can produce a maximum of ion current of 80 μA, which should yield a maximum equivalent nanocluster current of 120-160 nA. This is based on the 1 % conversion demonstrated previously and the 15-20 % collection efficiency.

The decision to integrate the ion source into the deposition chamber restricts the system to a two stage cluster production process i.e. matrix formation followed by sputtering, due to the limited space for evaporation sources. There are two advantages to splitting the process, firstly the matrix formation chamber can be made very flexible to incorporate additional evaporation sources or metrology tools, etc. Secondly the formation and deposition stages can be completely isolated from each other by means of a gate valve without the introduction of further distance between the sputtering position and the deposition stage. The advantage here is two-fold, the deposition stage is completely removed from cross contamination sources during matrix formation and the cold finger can be retracted from the deposition stage and

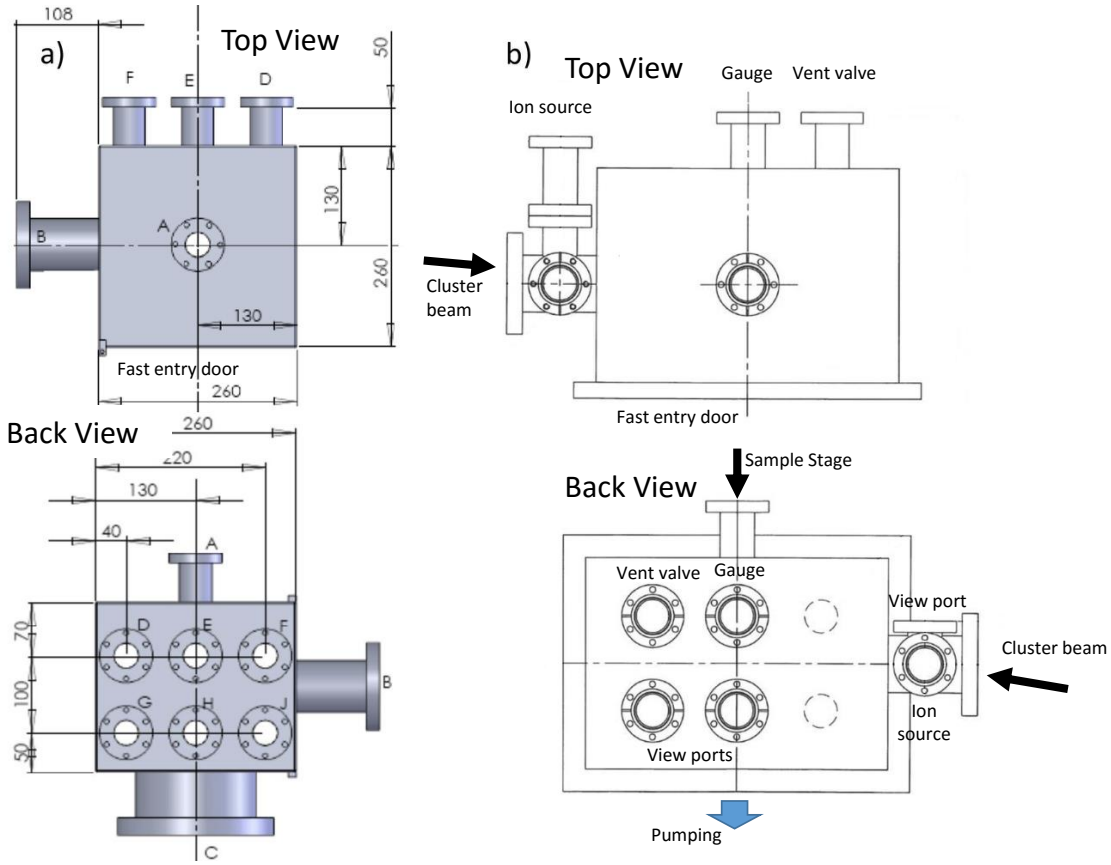

Figure 5.3: Technical drawings of the carousel deposition chamber; a) presents the drawing of the as supplied box chamber for housing the carousel. b) shows the modified chamber, with this configuration the ion gun can be mounted from the back, close to the carousel deposition surface (∼8 cm). The ports are used as follows A is a sample stage, B cluster beam inlet, C pumping port, D vent valve, E gauge, G and H are view ports, F and J have been removed in modification. The removal of the two back ports gives space for a larger ion source to be mounted in future configurations. The additional top port can be used for either a Faraday cup or view port.

closed off after deposition. The deposition chamber can then be vented, the samples removed and replaced without the need to warm up the cold finger. With sufficient pumping multiple depositions could be completed in one day, under the current conditions this allows subsequent day depositions (which would be impossible if the cold finger is warmed up between depositions ∼6 hours).

To provide a clear view of the how the entire system is setup, an image of the final system is given in Figure 5.4. A greater level of detail can be seen in the concept diagram, which is shown in figure 5.5. The system comprises two main parts, the

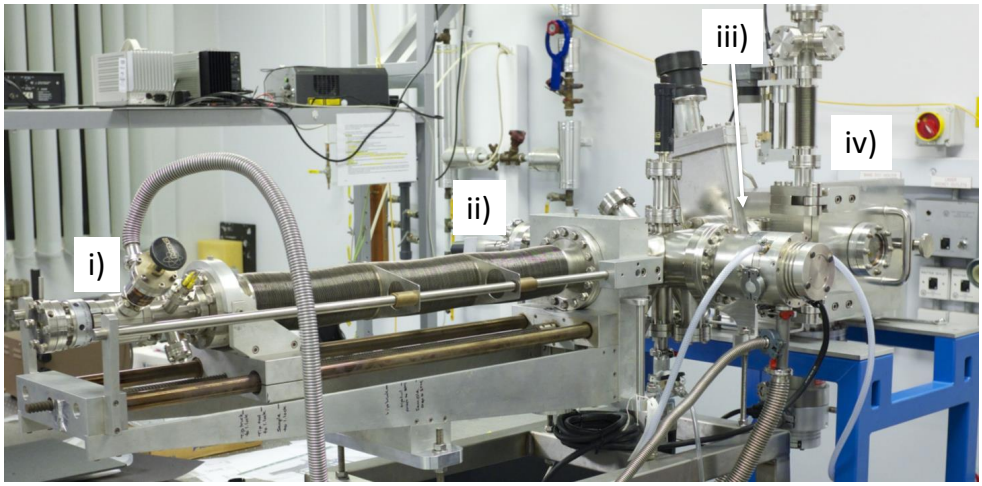

Figure 5.4: Photograph of the fully assembled MACS2 instrument. i), ii) ,iii) and iv) denote, a translatable horizontal cold finger, matrix generation(dosing) chamber, ion gun & sputtering position and the deposition chamber, respectively. The whole system is mounted on a custom welded stainless-steel frame.

matrix formation chamber and the deposition chamber. The first is where the matrix is condensed in preparation for cluster production. This houses the cold finger, metal source, gas dosing and deposition monitor (QCM). Metal deposition is performed by a Createc high temperature thermal effusion cell, argon gas is leaked into the system via a precision leak valve and is balanced with the metal evaporation rate to obtain the desired matrix composition. The second chamber is the deposition chamber, which is isolated from the generation chamber by a gate valve. The matrix is translated into the deposition chamber and is sputtered with keV argon ions, to form, ripen and extract clusters which are deposited onto the deposition stage; a carousel containing 21 glass slides. The three main components in the deposition chamber are the ion source, deposition stage and fast entry door for sample removal. The concept drawing has been slightly simplified for ease of viewing (e.g. the deposition turbo pump which would be coming up from below the carousel has been removed), the exact system is as shown in Figure 5.4. Individual components will be discussed in more detail in the following sections. The full pumping diagram of the system is shown in a later section (figure 5.10).

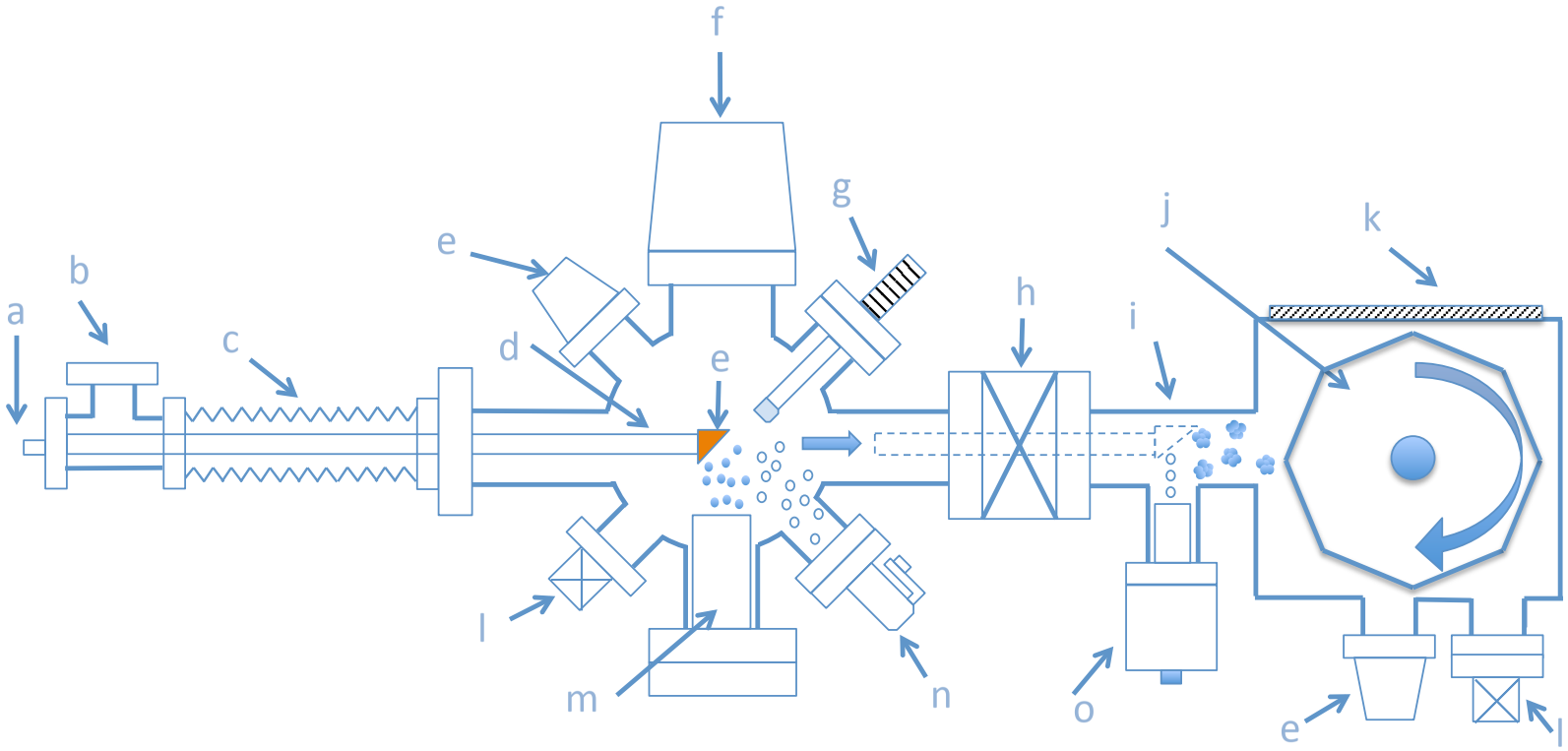

Figure 5.5: Concept drawing of MACS2 system. The key components are labelled (in the case of duplicates the same letter is used). a) Cryogenic inlet for matrix cooling, b) electrical feedthroughs for matrix current and temperature sensor measurement, c) Linear translator with xy alignment , d) Cryogenically cooled cold finger, e) electrically isolated matrix support plate containing a Rhodium-Iron resistance base temperature sensor , f) turbomolecular pump, g) quartz crystal microbalance mounted on a screw drive, h) gate valve, i) Sputtering position of the coldfinger, j) carousel deposition stage, k) fast entry door,l) vent valve, m) high temperature effusion cell, n) Precision leak valve, o) ion souce.

5.2.2 Matrix Support

The MACS2 system requires a new matrix support to provide an angled target for sputtering, while mounted on a horizontal cold finger. The cryogenic cooling system itself is the same continuous flow helium cooling system explained in detail in the previous chapter (see figure 4.5). There are several important considerations for the design of the matrix support; the surface area, volume and joints for cooling and the shape and angle for cluster production. As the ion source produces a radially symmetric Gaussian beam and the produced nanoclusters exit into the deposition chamber via a circular DN63 port, a support plate with a circular projection in both directions was chosen. As the matrix support angle was shown to have a relatively small effect on the peak production compared to the collection angle, a sputtering angle of 45° was adopted as this is the largest sputtering angle previously tested (shown in Chapter 4) and thus provides the largest projected size to the ion gun per surface area of matrix support plate. The increased target size increases the accessible ion current and reduces the radiation heat load per area of usable target. Therefore the final matrix support is ellipsoidal as can be seen in the 3D drawings shown in figure 5.6 a) and b). Finally a gold coated sapphire spacer connects the cold head and the matrix plate electrically isolating the support. The ion beam current impinging on the matrix support can then be measured directly. Figure 5.6 c) - e), shows a second matrix support plate that was designed for use with higher melting temperature metals by reducing the surface area and therefore heat the load from the evaporator and background radiation. This reduces the heat load by about 40-50 % (depending on experimental conditions). In addition, the volume and number of joints is reduced compared with previous systems by incorporating the temperature sensor into the matrix support rather than an additional spacer block. The key features remain the same in both versions, however the projection of the matrix support to the beam is reduced from a 28 mm diameter circle to 22 mm.

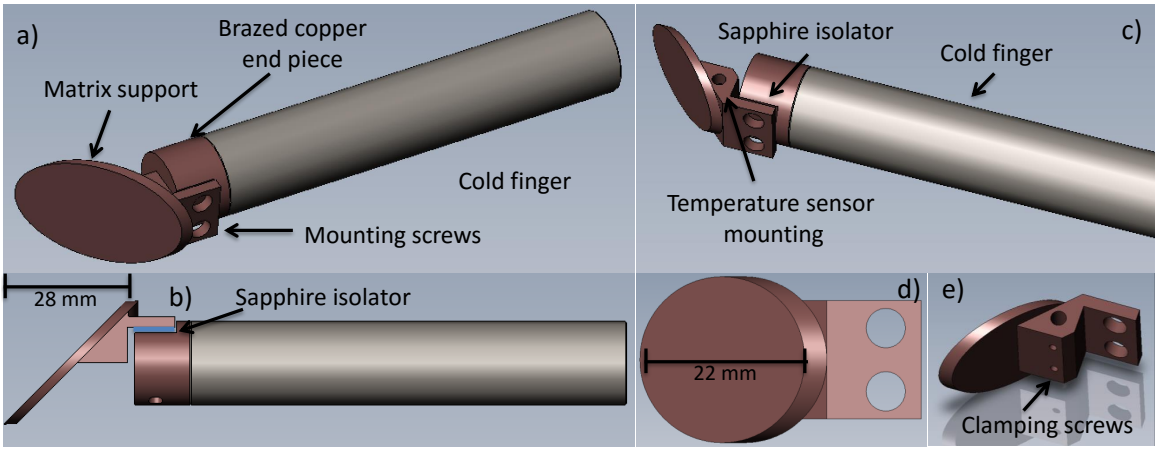

Figure 5.6: a) and b) show CAD drawings of the end of the cold finger and matrix support plate. c), d) and e) is a reduced size plate used for high melting point materials to reduce heat load and maintain sub 25 K temperatures. In both cases the support is a 45 ° angled ellipse which projects as a circle both parallel and perpendicularly to the cold finger. The diameter of the projected circle is 28 mm and 22 mm, for the standard and reduced size plate respectively. A temperature sensor is clamped inside the back of the plate. The entire plate is electrically isolated by a sapphire spacer, the front and back faces are coated in gold to improve thermal conduction. Ceramic washers prevent electrical contact through the fixing screws.

5.2.3 Evaporation

The source of the cluster material is a Createc high temperature effusion cell, which is mounted vertically from the bottom of the matrix formation chamber. This orientation requires the rotation of the matrix support to face the bottom of the chamber before deposition of a matrix. The cold finger is mounted on a differentially pumped rotary feedthrough to permit rotation for metal deposition, the evaporated metal impinges at 45° to the surface normal of the matrix support. The need for rotation could be removed by mounting the evaporator horizontally. However, this would require the addition of a boat within the evaporator crucible to prevent liquid metal flowing out of the evaporator. The inclusion of the boat increases the evaporation temperature required and in turn the heat load on the cryogenic system. Therefore this setup is only feasible for low melting temperature materials (<1000 °C).

Material impinging on to the matrix is measured using a quartz crystal micro balance (QCM). The micro-balance is mounted on a screw drive which is used to measure the deposition rate at different positions. When the matrix support is inserted for matrix formation, the QCM is positioned along side the matrix to measure material deposition in real time, the quantity of metal deposited onto the matrix support can be calculated from the rate measured by the QCM in the offset position, compared to that measured at the matrix position. Figure 5.7 a) is the measured evaporation rate with respect to matrix position and 5.7b) an example of the metal deposition observed during the formation of a matrix for cluster production. Graph 5.7a) is fitted with a Gaussian to show the extended profile, during deposition the QCM is positioned at ∼15 mm offset from the matrix centre.

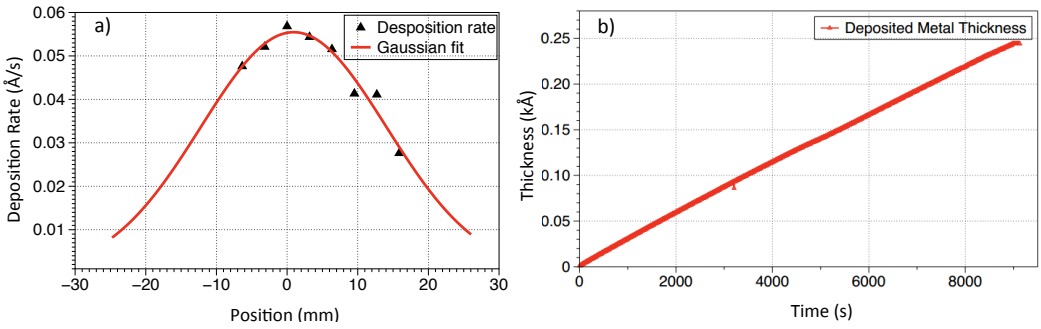

Figure 5.7: The evaporation profile is mapped by QCM measurement, the resulting profile is shown in a). A Gaussian is fitted to the measured points to provide a guide to the extended evaporation profile. b) gives a typical measurement of silver deposition from the QCM during matrix formation. This is positioned along side the matrix and the profile is used to calibrate the readings to values on the matrix.

5.2.4 Ion Source

The ion beam source is the Omicron ISE-5 ion gun, used in the reflection mode experiments presented earlier (Chapter 4). The ion beam profile and operating conditions are well known. An ion beam profile for different energies is given in figure 5.8. An ion beam energy of 1.5 keV has been adopted for these experiments as it gives the most uniform profile across the entire width of the matrix. Reducing the energy further increases the uniformity but greatly reduces the sputter current.

In real time, the beam size and rough profile can be checked by looking at the light emission from the matrix, which is visible to the eye. In-situ measurements of the beam can be performed via the top flange (see figure 5.3 b) however, a view port for visual confirmation of matrix alignment is generally used.

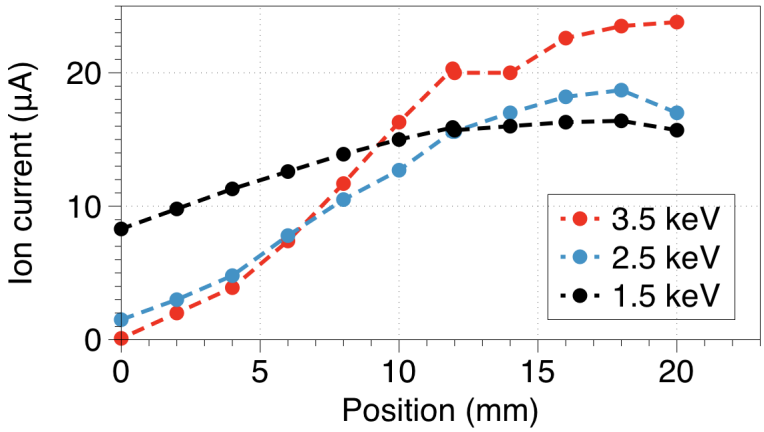

Figure 5.8: Beam profiles of the Omicron (ISE-5), for different ion beam energies. Increased energy provides a more focused beam but at the cost of uniformity across the matrix. As such 1.5 keV was adopted for the experiments.

Regular maintenance of the ion gun is required to ensure reliable performance (about every operational 20 hours). Primarily this is due to sputtering of the carbon apertures inside the source, which leads to build up of carbon on the isolating ceramics, which requires cleaning to prevent arcing and shorting. This involves removing all ceramic parts and cleaning off the sputtered carbon to return maximum isolation (>50 GΩ). In addition to cleaning the lens pieces can also be realigned in the event of misalignment (a specific alignment jig is used to perform this).

5.2.5 Pumping and Venting

The system is pumped with two Leybold TMP 151, 6", CF flange-mounted 145L/s turbomolecular pumps, one on each chamber, backed by a large three phase Edwards 28 oil-sealed rotary pump. To evacuate the chamber the rotary pump is first used to rough out the chambers to 10^{-2} mbar, before starting the turbomolecular pumps. A typical pumping time of the system is shown in Figure 5.9, such records are

kept to check for increased base pressure, introduction of contamination or early leak detection. The base pressure of both chambers is in the mid 10^{-8} mbar range without baking.

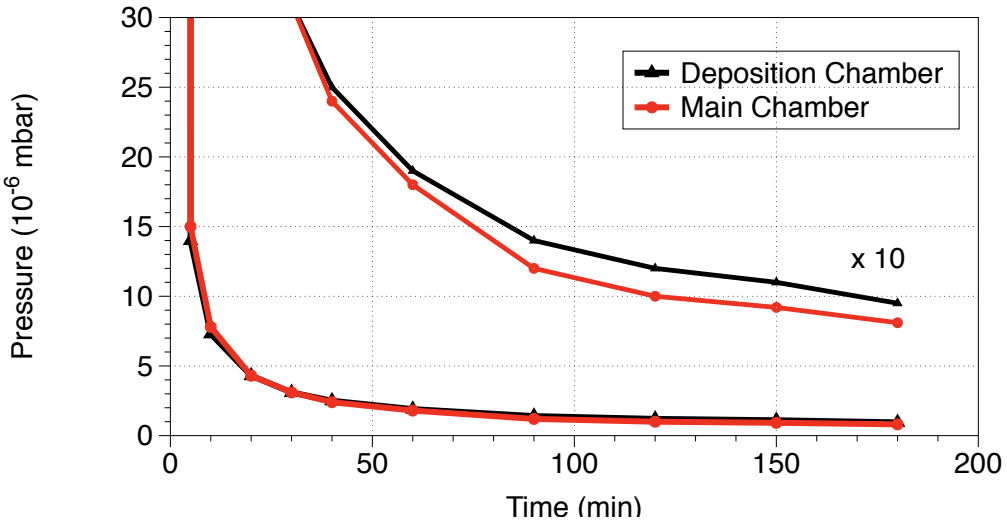

Figure 5.9: A typical pump down cycle for turbo pumps after roughing(1×10^{-2}), pressure for the main (matrix formation) and deposition chambers are shown in red and, black respectively. The two upper lines show a $\times10$ zoom of the latter part of the curves.

Both the formation and deposition chambers are connected to a nitrogen line for venting, as shown in the full pumping diagram (Figure 5.10). To vent, the turbomolecular pumps are isolated from the rotary pump using a speedivalve and then stopped (the rotary pump can also be stopped at this time). After the turbo pumps have come to a stop (spun down), nitrogen gas is slowly added to the chamber to vent it. A regulator is attached to the nitrogen inflow line to prevent significant over pressuring of the system.

The rotary pump is also used to pump the gas line before dosing, reaching a base pressure of 4×10^{-3}. To further ensure the quality of the gas supply the gas line is flushed three times before each experiment. To flush the gas line it is filled with 0.5 bar over-pressure of argon. This is allowed a short time to equilibrate and is then pumped out again. This process is used to purge out any air or contaminants, which may have leaked into the gas line over time. When filled for dosing the gas

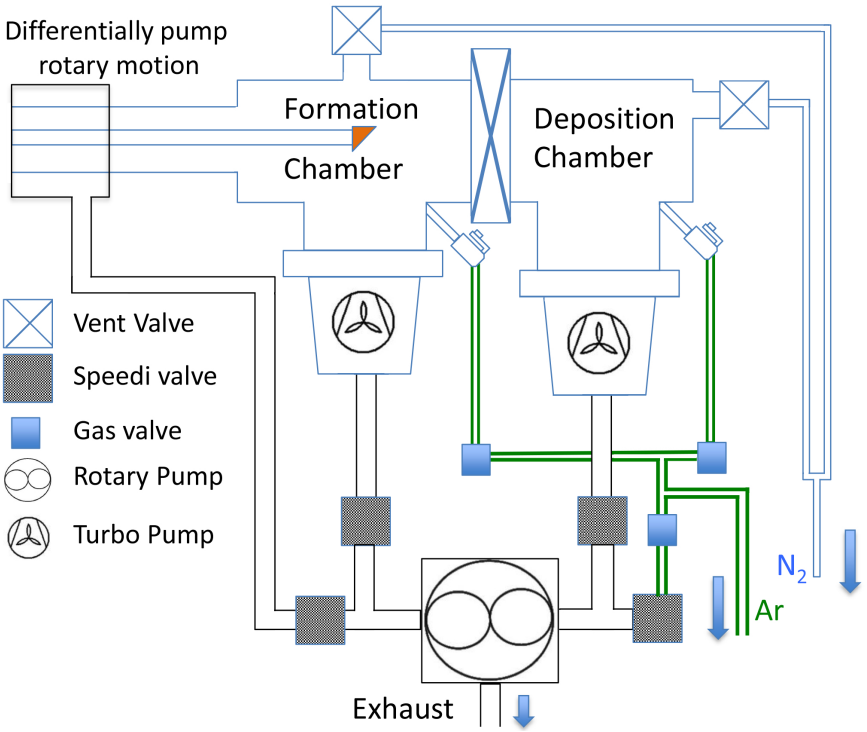

Figure 5.10: Pumping diagram of the MACS2 system. The vacuum is maintained by two turbomolecular pumps backed by shared a rotary pump. This vacuum fore line is shown in black. In addition to backing the turbo pumps the rotary pump also differentially pumps a rotary stage fitted to the cold finger. The venting and dosing lines are shown in blue and green respectively. The dosing line is also purged by the rotary pump to remove impurities before use. The blue arrows indicate the location of the gas source or in the case of the vacuum line the exhaust.

line is at an over-pressure of approximately 0.5 bar, given the base pressure of the gas line (5×10^{-3} mbar) this gives $\sim$5 orders of magnitude between the desired gas and contaminations in the line. This is comparable to the purity of the gas source (i.e. gas bottle) .

5.2.6 First Samples

Results from the first tests of the system can be seen in figure 5.11. The panels a), b) and c) show the cluster size distribution, the raw HAADF STEM image and an enhanced contrast image, respectively. The cluster intensities are measured using the two circle method discussed in appendix B. Based on previously calibrated intensities this would give a peak cluster size of 40-50 silver atoms, which is consistent

with mean diameters of the clusters in the STEM images. The silver nanoclusters were produced using a 120 nm thick matrix with a 1.3 % silver concentration, deposited at 12 K. The matrix was sputtered for 600 s with an estimated ion beam current of 6 μA and an ion energy of 1.5 keV. For the initial samples the sapphire had been removed to achieve the lowest possible matrix temperatures, therefore the current is estimated based on measurements under similar conditions. The average nanocluster density was 200±60 nanoclusters/per frame (3.2×10^{12} per cm^2). The size distribution is shown to have a lognormal distribution. This provides the first proof that the system functions, the remaining sections will give a detailed account of the MACS2 source in use. These demonstrations will focus on sustained high flux cluster production deposited onto large area supports.

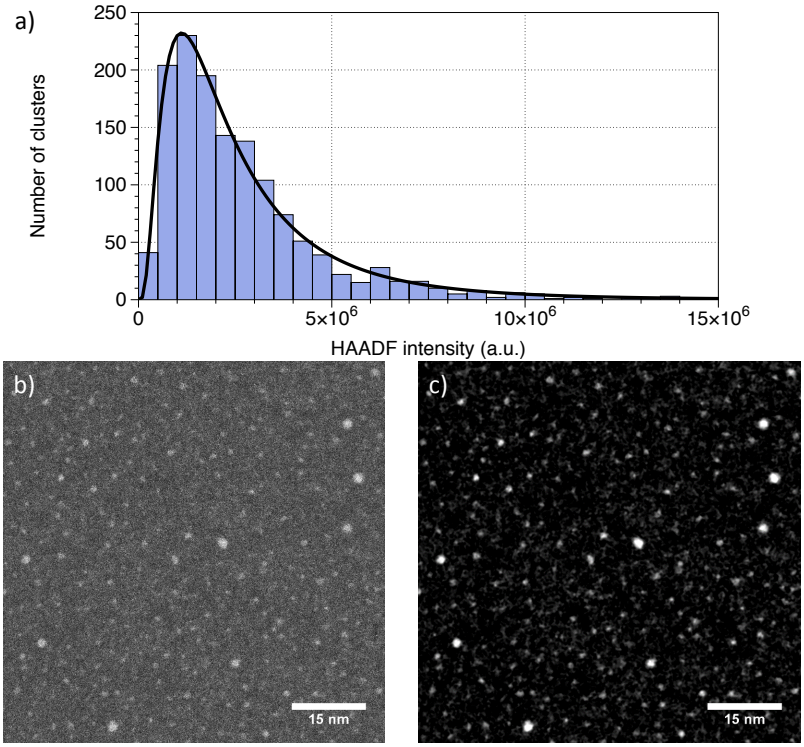

Figure 5.11: The first silver nanocluster sample produced from MACS 2 using a 3 % silver concentration, silver-argon matrix. The samples were deposited for ten minutes with a beam energy of 1.5 keV and an estimated ion current of 6 μA. a) shows the size distribution of the measured nanoclusters based on their HAADF intensities. b) and c) present examples of raw and enhanced contrast HAADF STEM images, of the kind used for size and density analysis.

5.3 High Flux Production

An important specification of the source is the quantity of nanoclusters it can produce. To establish the amount of nanoclusters produced both the density and the spatial spread of the nanoclusters is required. To achieve this two different calibration measurements have been employed. The cluster density has been mapped in a cross pattern. An example of the average number of clusters per frame at different positions on the substrate is given in Figure 5.12.

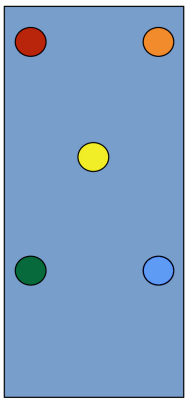

Grid positions on sample

Sample position	Deposition 1 Clusters per frame (x10)	Deposition 2 Clusters per frame (x10)
	13±2	20±3
	9±2	18±4
	14±2	22±3
	11±2	17±2
	7±3	15±2
Average	**11±2**	**18±3**
Ratio between average and center flux values	0.8	0.85
Equivalent current	**28±6nA**	**50±7nA**

Figure 5.12: The number of nanoclusters deposited per 78.7 nm × 78.7 nm STEM image (frame) is shown for different positions on the substrate (colour coded). An illustration of the substrate is given on the left. The results from two different depositions are given as an example. The equivalent cluster beam current deposited on these samples is given. Finally the ratio between the average number of nanoclusters per frame and the number of nanoclusters per frame on the centre grid is given (value used for equivalent current calculation).

As the source is designed for high volume production (∼400 cm^2 equivalent to twenty one slides per deposition run) , it is not feasible to map the full spatial distribution by STEM measurements on every sample produced, it would be both too expensive and time intensive. However, both the nanocluster density and size at different positions across the sample can be inferred from the analysis of a single

TEM grid. This is based on previously measured relations of the density and size in a given place relative to that measured at the centre. To provide the most accurate measurement the centre position was chosen as in principle this has the highest signal. The density of nanoclusters in the centre has been measured and compared to the average nanocluster density in all five positions. To verify the behaviour this has been repeated for different deposition conditions (time, current and metal concentration e.t.c), no significant variation was observed. The ratio between the average of the centre point remains similar for each repeat with the average ratio between the centre density and total area density across all samples being 81±6 %. This scale factor allows estimation of the average density across a wide area by measuring the density on a single grid, providing a good estimate of collected cluster flux. To calculate the total nanocluster flux produced, rather than just the flux deposited on to the sample, extrapolation beyond the collection area is required, which requires further analysis.

The production rate is limited by the incident ion current, to demonstrate high flux nanocluster production the maximum uniform ion beam current of 30 μA at 1.5 keV is impinged on a 1 μm thick, 2.4 % silver loading argon-silver matrix. Higher currents can be produced but require a more focused beam leading to significant inhomogeneity in the beam across the matrix. Three consecutive samples have been deposited for 90 s each. The average of the equivalent currents measured across all three samples is 80 nA ± 5 nA. The average equivalent cluster beam current deposited onto each sample is plotted in Figure 5.13.

The size of the deposited nanoclusters has also been measured by the atom counting technique. The intensity of a single atoms is used to weigh the nanoclusters by comparison of the integrated intensities. The cluster size distribution once again shows a lognormal tendency as often observed for diffusing particles growing by the addition of adatoms or coagulation.[187] Figure 5.14 shows the size distribution of the nanoclusters produced across all samples. The peak size is 48 silver atoms, with a

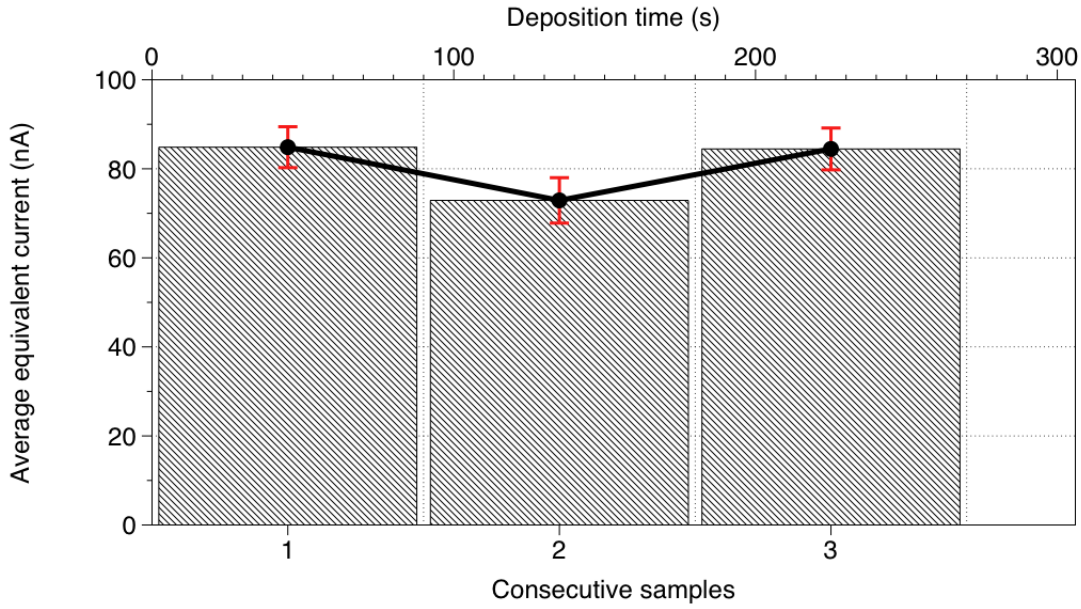

Figure 5.13: The average equivalent nanocluster current of three MACS2 nanocluster samples deposited consecutively each for 90 s. Deposition is carried out using an ion beam current and energy of 30 μA and 1.5 keV respectively. The matrix was prepared with a thickness of $\sim$1 μm and silver concentration of 2.4 %. The error is derived from the variation in the number of clusters in each image.

half width variation of 25 atoms. Based on the mean cluster size across all three samples (61 silver atoms), the MACS2 would deposit $\sim$20 μg of nanoclusters per hour. Figure 5.15 considers each sample individually, a), b), and c) are the size distribution of each, of the three samples, d) provides the average nanocluster size(black squares), peak nanocluster size(white triangles), and variance(error bars). The peak cluster size of the deposited nanoclusters are 49 silver atoms, 47 silver atoms and 48 silver atoms respectively (calculated from the lognormal fit parameters). There is no significant change in nanocluster size with time (ion dose), the stability of the source will be investigated further using long deposition times and ion doses. Considering the size distribution of each sample separately, it is apparent that they are consistent with each other.

As stated in the design section both the ion source and matrix support plate have a radial symmetry (at least in projection), therefore a reasonable assumption is that the cluster profile maps to that of the incident ion beam. This hypothesis

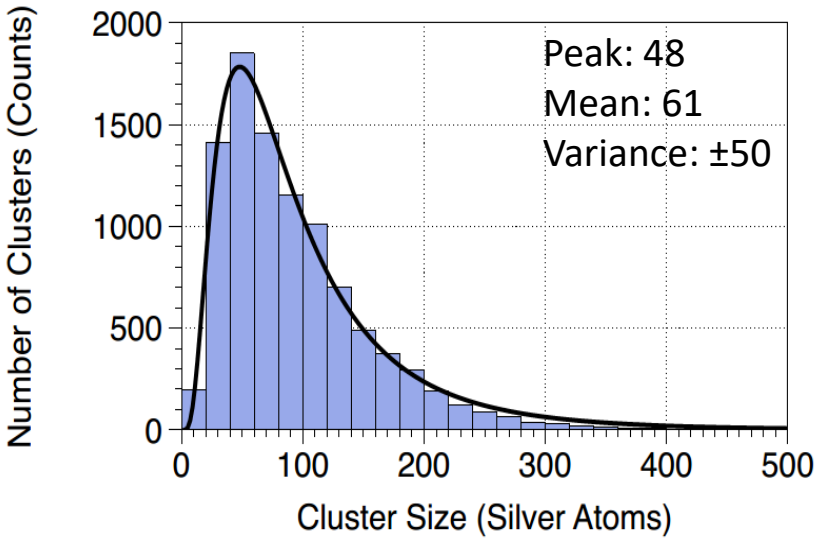

Figure 5.14: The histogram plots the size distribution of nanoclusters deposited across all three high flux samples. The histogram is then fitted with a lognormal distribution which gives an average and peak cluster size of 61 silver atoms and 48 silver atoms, respectively. The variance is calculated to be 50 silver atoms. The bin width used is twenty silver atoms.

is supported by the radial falloff in nanocluster flux observed on the substrate. In the discussion of the proof of principle reflection mode data a skewed Gaussian is observed in the azimuthal plane. The skewing is likely due to the angle of the plate i.e. inhomogeneous current density. If correct, the vertical (polar) direction would have a normal Gaussian distribution of nanocluster flux, due to the fact it sits perpendicular to the beam. To confirm the vertical nanocluster distribution, nanocluster density has been measured across an array of five TEM grids with 1 cm spacing between centre of each ($\sim$30 $^\circ$ arc). The results are presented in figure 5.16, a shallow curve is observed. This is consistent with beam profile considerations. The black line is the "as-measured" nanocluster density of the samples and the red line indicates the density after factoring in solid angle.

By considering both the polar and azimuthal distributions of cluster flux measured, the total produced cluster flux can be mapped. In each case, the as-measured distribution has been fitted with a Gaussian, which is then normalized. Each fit is measured over the same range, as such the two profiles can be multiplied together to

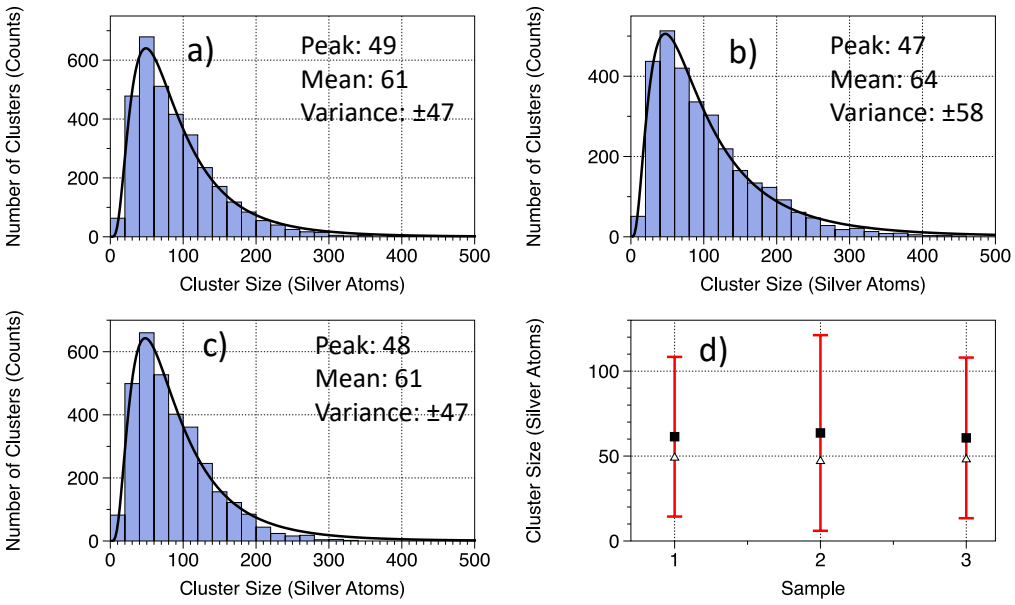

Figure 5.15: The first three graphs a), b) and c) present the size distribution of nanoclusters deposited onto three consecutive samples from the same matrix. The final graph d) gives a summary of the distributions showing the average (black squares), peak (white triangles) and variance (error bars) of the cluster size in all three samples. Over this short time frame no significant changes are observed in the size distributions

form a square matrix of the normalized cluster density. This profile of the emitted nanocluster density is given in figure 5.17 a). This normalized flux can be equated to an actual value of produced clusters by scaling the entire mesh from the position measured. Applying this gives the total equivalent cluster current produced over the entire 80 ° arc. The total equivalent current produced for the high flux samples is 350±50 nA (Averaged across the three samples). This is over four times greater than the portion of the cluster beam that is deposited on a single glass slide (81±5 nA) as shown in figure 5.13. However, based on the geometry of the tube housing the matrix (DN63 flange) a 75 mm × 75 mm circle is about the largest substrate that can be used at an 8 cm working distance. Therefore the maximum usable flux produced by the source, is calculated by truncating the previous cluster profile as shown in figure 5.17 b). In the case of the three high flux depositions demonstrated above, the average usable equivalent cluster current from the source was 170±16 nA. This will be referred to as the "produced" equivalent current of the instrument

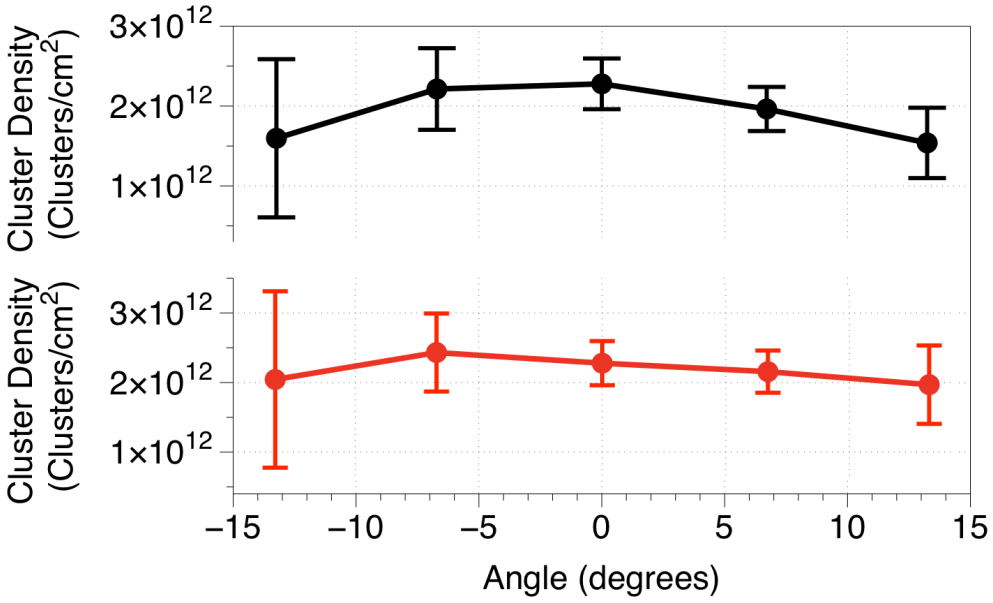

Figure 5.16: The nanocluster density of five different samples positioned along a vertical line in the centre of the sample. The separation between each sample is 1cm, in total covering approximately a 30 ° arc from the centre of the matrix support. The upper graph displays the cluster density as measured from STEM images and the lower after factoring in solid angle projection of the grids.

compared with the "collected" equivalent current (i.e. the fraction that is deposited onto the sample).

5.4 Large Area Sustained Production

The increased production rate alone is not sufficient to make a case for the development of a new technology, the source needs to maintain stable and consistent production. To investigate this, a 45 minute long deposition has been conducted onto 15 glass slide size samples (three minutes each). As real time replenishment of the metal is not possible here, a thick matrix has been used (3.6 μm). The matrix is prepared at 25 K with a silver concentration of 1.8 %. This is then sputtered with a 15 μA, 1.5 keV argon ion beam, for the duration of the deposition.

The lower current is used as this permits better defocusing of the beam, which provides a more uniform profile and therefore more homogeneous depletion across the matrix. Homogeneous depletion is preferred in order to maximize the use of the

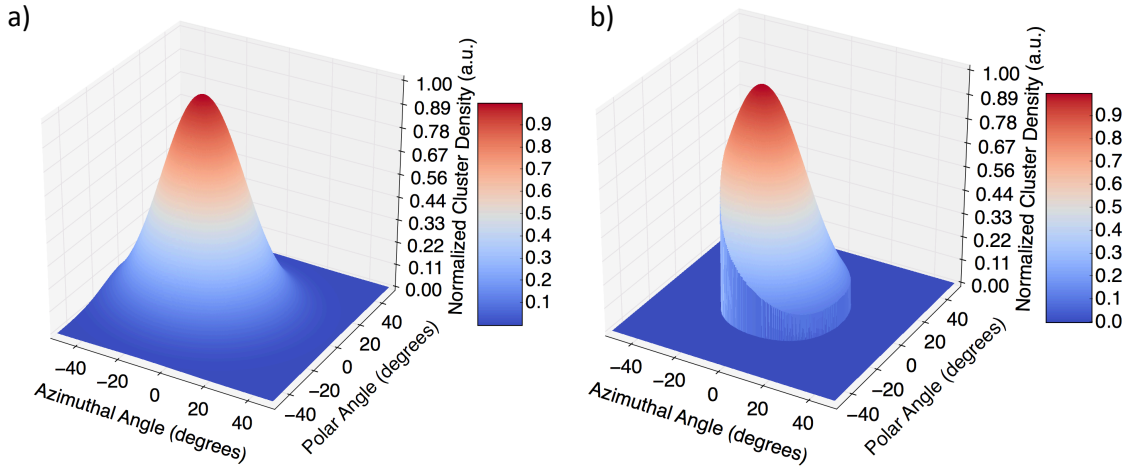

Figure 5.17: Two 3D plots of the cluster beam profile produced by MACS2.This has been extrapolated from the gaussian profile of azimuthal and polar cluster densities measured by HAADF STEM. a) Gives a profile of the entire beam, the zero angle is perpendicular to the ion source (i.e. 45 ° from the surface normal of the matrix support. b) Shows the beam truncated to the maximum collectable solid angle (based on chamber geometry).

matrix, thereby reducing waste and extending the matrix lifetime. In this case, it will also reduce the risk of sputtering through the matrix into the support, which would result in a reduced flux and the introduction of contamination. TEM grids are mounted on the 1^{st}, 3^{rd}, 5^{th}, 10^{th}, 15^{th} positions in the rotatable sample carousel to provide information on the deposition rate and nanocluster size at different sputtering times. Glass slides are mounted in the other deposition positions. Figure 5.18 shows the equivalent collected cluster current obtained during sustained deposition.

The results show significant longevity in the production with an average equivalent collected nanocluster current of 40±14 nA. Moreover the rate takes thirty minutes to drop ∼50 % and looks to continue to drop off at a reducing rate, giving a "halflife" of around thirty minutes without any replenishment. If the flux was related purely to the total amount of material available to sputter (i.e. depletes homogeneously and formation is unaffected by rearrangement), while the thickness is significantly greater than the penetration depth of the argon ions (tens of nm) there would be a constant production rate. This is not observed so a more detailed consideration of what is going on inside the matrix during sputtering is required.

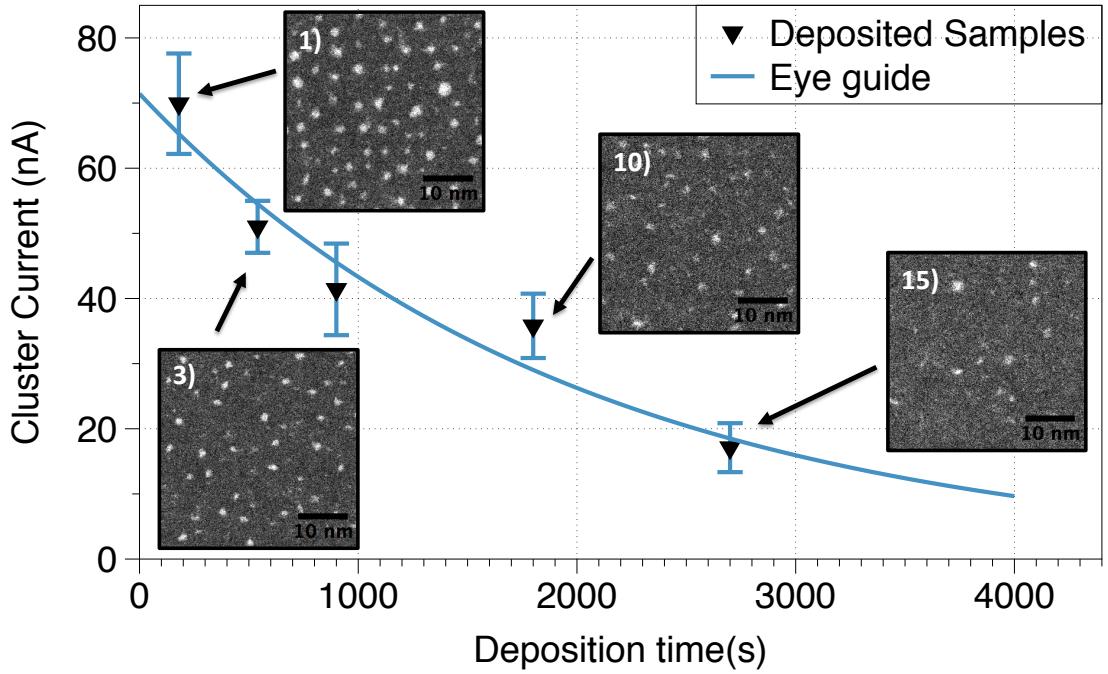

Figure 5.18: The sustained cluster deposition, shows a steadily deceasing production yield with time (ion dose). The STEM images show examples of nanoclusters deposited in samples 1,3,10 and 15. The average collected equivalent cluster current is 40±13 nA. Error bars come from the standard deviation from the number of clusters recorded per image.

There are two other major factors that are ion dose dependent and impact upon the sputtering process and therefore the number and size of clusters produced, namely the metal concentration and the arrangement within the matrix.

Assuming arrangement of the metal is the primary variable changing the yield. This is due to the fact that metal atoms or groups of atoms involved in a collision spike will either be extracted or given sufficient energy to cause some diffusion of the clusters and surrounding atoms. For clusters that remain in the matrix each subsequent impact affords the cluster an additional chance to grow by acquiring further metal atoms. Therefore with time clusters are either grown or extracted leading to a reduced population but larger clusters inside the matrix.

Considering the matrix concentration there are again two possible causes of compositional change, excess dosing of argon and preferential sputtering of the weakly bound argon.[186] The excess dosing and re-condensation is more significant at low

concentrations (the region considered here), the chance of direct collision is relatively low. Furthermore, the smaller silver clusters can be extract within the argon ejection spike without the need to break many metal bonds. In high concentrations systems, preferential sputtering becomes more prominent as metal 'frame works' form within the argon matrix significantly reducing sputtering yields. To form the ion beam a gas pressure of 9×10^{-7} mbar is required, which will also deposit argon onto the matrix during sputtering, thereby reducing metal concentration, and causing metal free layers, leading to fewer smaller clusters. This pressure is between 10-25 % of the original dosing pressure ($\sim$ 0.2 ML/s). .

To confirm if the decrease in yield is primarily due to the aggregation of silver clusters and atoms to form larger clusters, or the dilution of the matrix, the cluster size for each sample has been measured. Figure 5.19 presents the size distributions of deposited nanoclusters obtained by comparing the measured intensity of single atoms with that of the clusters. The resulting histograms have been fitted with a lognormal distribution (black line). Over the duration of the deposition a slight reduction in peak nanocluster size can be observed, which is consistent with a slight reduction in metal concentration expected.

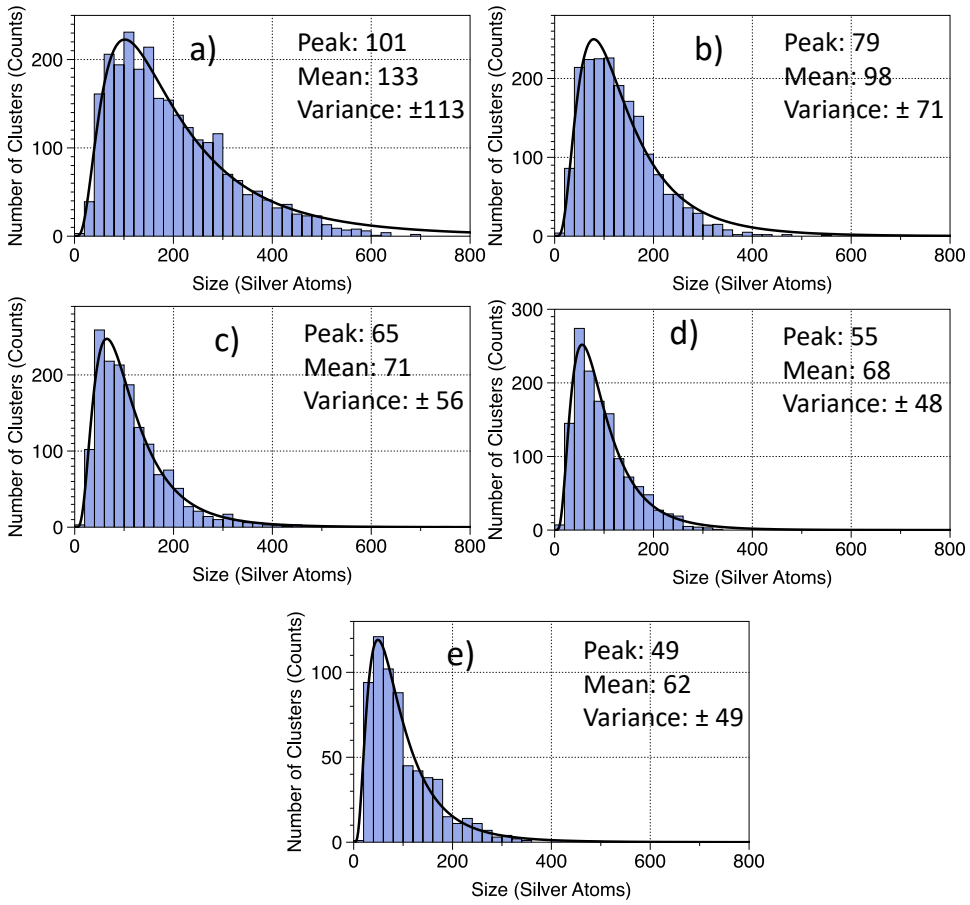

Figure 5.19: The graph sequence shows the size distribution of nanoclusters deposited at different intervals throughout a 45 minute long nanocluster deposition. The entire deposition is completed using a single matrix. Each sample has been deposited for 3 minutes a), b), c), d), and e) show results from samples 1, 3, 5, 10, and 15 respectively. Each plot is fitted with a lognormal distribution (black line), the key parameters of the resulting fit are shown on the right hand side of each graph. Both the peak nanocluster size and distribution width reduces with increasing deposition time. The bin width used is twenty silver atoms.

A more surprising feature is that the size distribution narrows with sputtering time, both in absolute and relative terms (i.e. peak size over variance decreases). The effect can be seen more clearly by plotting the cluster size and size variation with respect to sputtering time (Figure 5.20). The black squares represent the average cluster size, the triangles the peak nanocluster size, and the error bars the variance of the measured particle size (these values are calculated based on lognormal fit parameters). From this plot, a clear trend of reducing size and polydispersity is visible with longer deposition times. To extract further information a complete

description of what is occurring inside the matrix at a microscopic level is required. This is currently under investigation via molecular dynamic simulations.

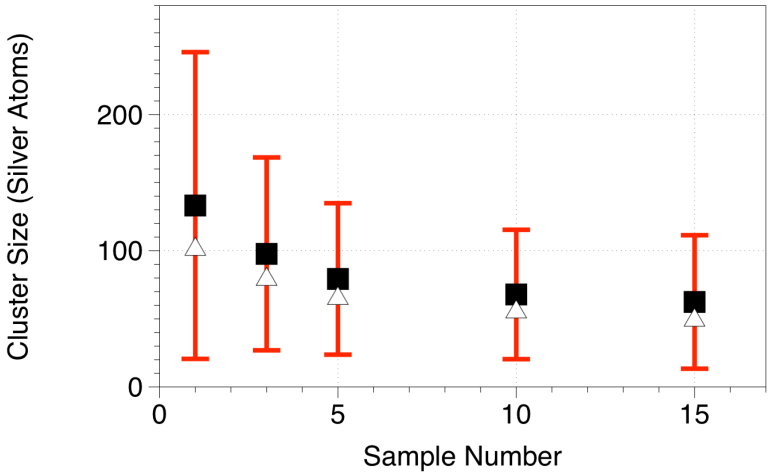

Figure 5.20: The nanocluster peak (triangles) and average size (black squares) are plotted against sample (i.e. sputtering time). The variance in size is shown by the red error bars. Every sample is deposited for three minutes, the cluster sizes are calculated based on the cluster intensity compared to the intensity of a single atom. These are compiled into histograms and fitted with log-normal to get the values shown.

To quantify the amount of nanoclusters collected over this period, the mass can be calculated. Given the size and number of the nanoclusters deposited, in total as $\sim$10$\pm$4 μg, have been deposited. The total mass of clusters produced by the source can be extrapolated as described previously to arrive at a value of $\sim$21 μg. An average deposited cluster density of 2.5×10^{12} clusters/cm^2 is deposited over a 280cm^2 area in 45 minutes. This concentration, permits a full batch of twenty one slides to be coated for use, e.g. as bio-chips, in one hour.

5.5 In-situ Cluster Flux Measurement

Full exploitation of high flux nanocluster production is not possible without the tools to characterise the samples produced. Although STEM provides detailed insight and characterisation, it is very time intensive and requires the production of specific samples. Implementation of a high throughput or real time technique for

characterisation and quality control is key to further development. One of the possibilities is the direct measurement of the mass of deposited nanoclusters using a QCM inserted into the nanocluster deposition beam. To trial this method a new QCM holder plate has been fabricated to allow mounting of 1-3 small 6 MHz quartz oscillator crystals to the deposition stage. These crystals are driven using an STM-2 controller which both drives oscillation and measures the oscillation frequency of the crystal. As mass is deposited the oscillation frequency reduces which allows determination of the deposited thickness if the deposition material and area is known (within a working linear region). Before use the crystal is calibrated against either another dedicated QCM monitor or by co-depositing onto a flat substrate e.g. silicon or mica and measuring the deposited thickness with a line profiler. This can either be performed by shadow deposition or scratching the surface after deposition and measuring the depth. Unlike dedicated UHV QCMs these are not water cooled so if measuring in the line of sight of an evaporation source they should be allowed to cool before recording the reading, however in the case of cluster deposition radiative heating will be small and the total heat capacity of the clusters is small compared with the macroscopic size of the crystal.

A demonstration experiment directly measuring cluster deposition using a QCM is presented in Figure 5.21. The trace shows two depositions initiated at following points a) and c), with a break between them where the ion gun and gas dosing is stopped b). Finally at d) the ion gun is switched off leaving the gas dosing on. The black trace is a background measurement taken directly following the experiment. During the ∼40 minute deposition the QCM records a thickness increase of 1 Å, this means a mass equivalent to 1 Å of bulk density silver has been deposited across the QCM (i.e. 0.105 μg/cm^2). The deposition is carried out with a 15 μA, 1.5 keV argon ion beam, impinging on a 0.7 μm thick matrix with a silver concentration of 1.9 %. This matrix has been sputtered under the same conditions for three minutes prior to this measurement. The amount of material deposited across the plate during

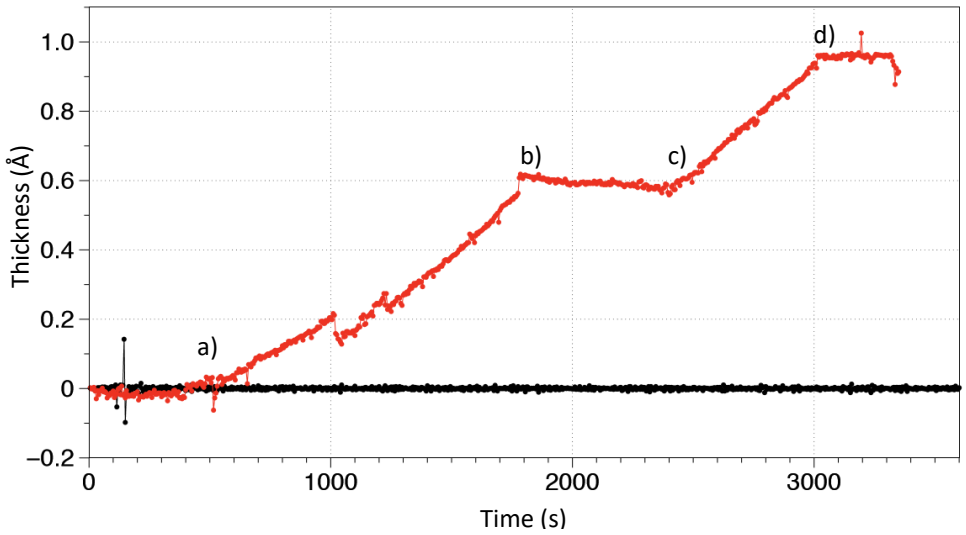

Figure 5.21: Raw data taken from QCM measurement during nanocluster deposition. Several distinct features are visible a) the ion beam is switched on starting cluster deposition, b) the ion source and gas flow are switched off, c) ion beam and gas dosing are switched on and d) the ion gun is switched off. A steady increase in the mass measured by the QCM is observed during deposition. The black trace is a background measurement zeroed and taken directly after deposition for reference.

deposition is $\sim$2 μg. After deposition the mass on the QCM remains constant (point d)) proving this is not simply temporarily adsorbed material.

This type of measurement provides an excellent way to obtain real time information on the amount of cluster material being deposited. For applications such as catalysis. Where the catalyst loading is a key parameter, such measurements could be sufficient for batch quality control, using known tested matrix parameters. To complete a rigorous quality control more methods like TOF or STEM measurement are necessary.

5.6 Bio-sensing Proof of Principle

The principle of a bio-chip is to detect the presence of a particular protein in a solution (i.e. antigen). This is achieved by using a paired capture protein (e.g. antibody to a specific antigen). This capture protein needs to be anchored in place to prevent removal into solution and be provided with a means to "report" the

capture. This can be carried out by using a linking protein to fix the antibody to the surface and connect a reporting dye. This dye can be optically probed and is chosen such that the response to the optical probe changes with the attachment of the antigen to the antibody. The scheme of a bio-chip system is shown in the left image of figure 5.22. There are several draw backs to this system. Firstly it is possible for other unknown species within the test sample to bind to the dye, also causing an optical response. Furthermore, unless the surface is fully saturated, species from the sample may attach directly to the surface altering the system. Blockers can be employed to prevent attachment to these sites but this requires significantly more cost and introduces another layer of complexity into the device.

Small clusters have previously been demonstrated to be good immobilizers of proteins[161,163] and also work as light emitters and absorbers.[166,167,188,189] As such multifunctional clusters could be used to provide both the pinning function, and a reporting response (e.g. an optical response to an antigen). This type of technique is often referred to as a label free biochip.[190–192] This is desirable as it removes the need for reporter dyes, which often need to be tailored for each protein detected due to interaction with the system. Additionally, this could extend the lifetime of a bio-chip system as the clusters would not experience photo-bleaching unlike most dyes (the degradation of light emission through excitation and exposure to light). The principle of a cluster based bio-chip is shown in the right hand side of Figure 5.22. Furthermore, in principle the number and properties of the binding sites can be controlled, eliminating the need for blocker molecules.[162]

To explore this avenue, the optical absorption and immobilization of small silver nanoclusters has been investigated. Silver nanoclusters were deposited onto glass slides (with a peak diameter of 1-2 nm based on previous results) to measure their optical absorption. Silver nanoclusters were chosen as they are a well known plasmonic particles and bind strongly to thiol terminated ligands such as linker proteins. The first step was to ensure that the nanoclusters themselves remain on the glass in

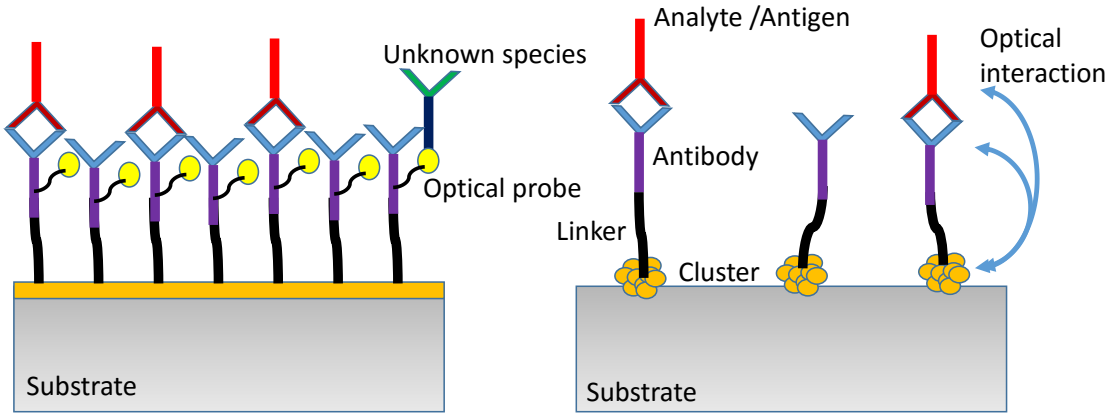

Figure 5.22: Bio-Chip schemes for standard configuration (left) and multifunctional cluster based system (right). The standard configuration anchors directly to the surface and employs a linker to connect both an antibody and an optical dye to the surface. The attachment of the antigen to the antibody is measured through a modification of the optical emission of the dye due to the dye and antigen interaction (electron transfer, additional fluorophore contribution from the antigen). The cluster method proposes to link directly to the antibody, relying on an optical interaction between the cluster and the captured antigen.

sufficient quantity to provide a measurable optical signal. This was performed by preparing a high coverage sample and comparing the optical absorption spectra of glass slides with silver nanoclusters to blank glass slides.

A 1 μm argon matrix containing a silver concentration of 2 % was prepared for cluster deposition. The clusters were then deposited onto the slide for 30 minutes using a 20 μA Ar^+ beam with an energy of 1.5 keV. The average estimated cluster density across the slides is 1.4×10^{13} cm^{-2} equivalent to $\sim$1.5 ML of silver atoms. The absorption spectra measured from this slide are presented in figure 5.23. Each of the five traces gives the absorption from a different position on the nanocluster coated slide (colour coded). The background subtraction has been performed using the absorption averaged from several glass slides (see insert). All spectra have been taken using the Cary50 UV-VIS absorption spectrometer, which can be seen in Figure 5.24.

The nanocluster coated slides show an additional peak after background subtrac-

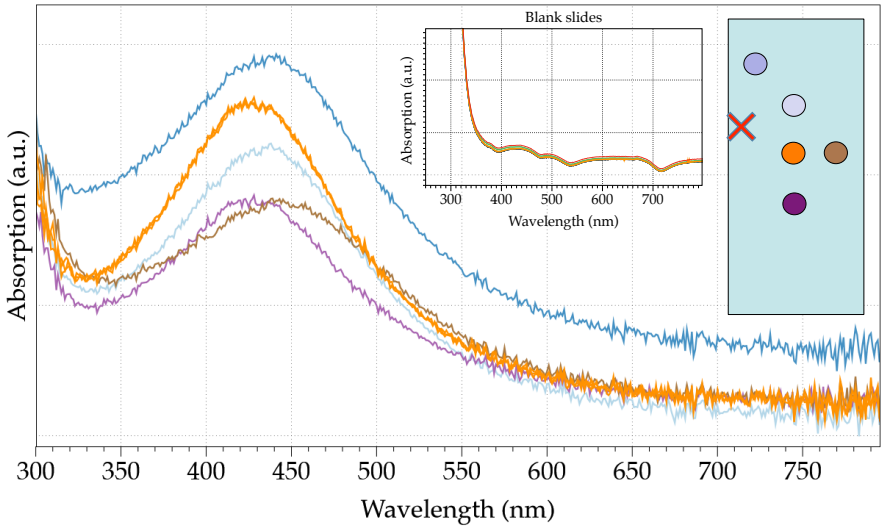

Figure 5.23: Absorption spectra taken with the Cary 50 UV-VIS absorption spectrometer. The absorption traces are measured from different parts of the same sample, marked in matching colours on the insert (far right). The absorption intensity falls as the position moves away from the centre of the nanocluster beam (rough position marked with cross). The background is given by the average of five blank slides these can be seen in the left hand insert.

tion, between 430-450 nm, this is consistent with the absorption of plasmonic silver nanoparticles, although determination of exact size is not possible without knowing the exact shape and surface interaction.[155,194,195] It is that likely the particles remain in the 1-10 nm range,[196–198] however for typical colloidal solutions this wavelength would signify much larger particles. Further evidence of nanoclusters being the source of the absorption is the reduction in intensity in the outer positions, as shown previously the nanocluster flux reduces with distance from the centre. The absorption shown here demonstrates that particles can be produced and deposited in sufficient quantities to achieve measurable UV-VIS signals.

The next step is to test immobilization of a thiol terminated molecule using the clusters. In this case a boron-dipyrromethene dye (DODIPY FL L-cystine) is chosen to be the attaching molecule, this gives access to the location of the protein via laser fluorescence microscopy. To confirm the dye is attached to the cluster and not just the glass slide between, the slide is patterned with cluster arrays. These are formed by mask deposition using the mesh mask (nickel 100mesh). If the

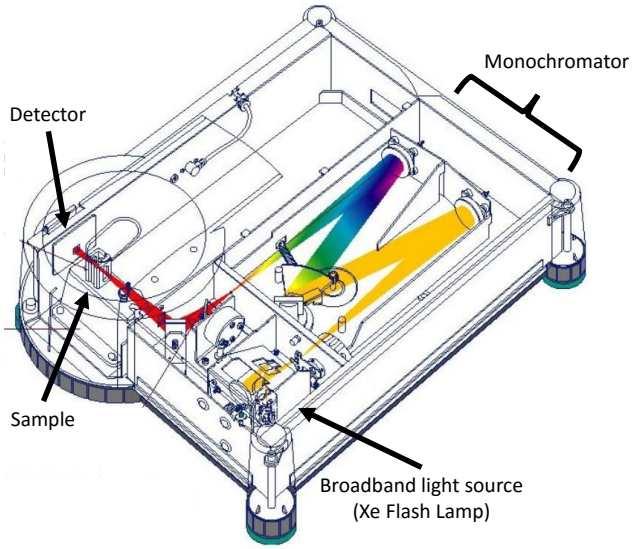

Figure 5.24: Schematic of the Carry 50 UV VIS spectrometer, including the light pathway. This image has been reproduced from the system manual and is labelled by the author[193]

dye preferentially attaches to the clusters a contrast will be observed between the cluster coated regions, the bare glass sections. The experimental procedure is shown in Figure 5.25.

Briefly, nanoclusters are deposited in an array of squares across a glass slide (10^{12} cluster/cm^2), the dye solution is drop cast onto the slide and left for 24 h at room temperature. The dye solution is 500 μl in total, 450 μl TCEP (tris(2-carboxyethyl)phosphine) at 10 mM and 50 μl of BODIPY FL L-cystine at 1 mg/ml. The excess dye solution is then washed off with ethanol, and the slide is dried with N_2 gas. Finally the glass slide is imaged using fluorescence microscopy.

Fluorescence microscopy works by using a short wavelength to excite a sample to emit (fluoresce) at a longer wavelength (lower energy). The results present in figure 5.26 were taken using a Nikon A1R Inverted Confocal Total Internal Reflection Florescence Microscope (TIRFM). Excitation was performed with a 488 nm source using 50 % of the laser power to avoid significant photo bleaching of the dye. Images were taken with a 40× dry lens and exposure time of 31 ms, using a 44.7 μm pinhole. The PMT was biased to 135 V and a dark current offset of -80. All images were

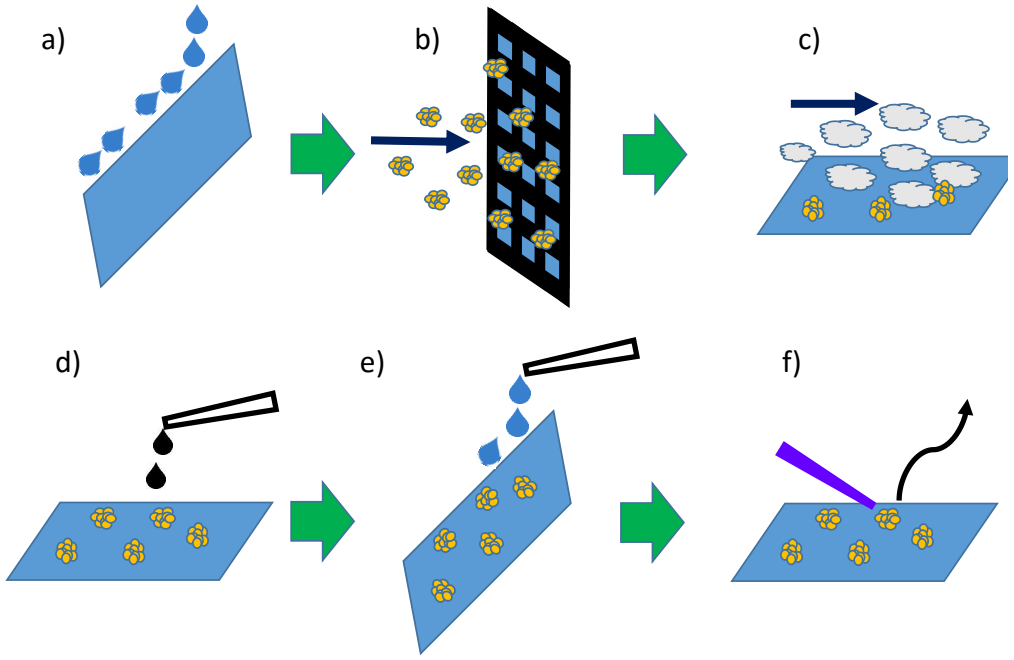

Figure 5.25: In order to achieve consistent results a systematic method is required for processing slides into biochip demonstration samples. The procedure is as follows a) slides are cleaned with isopropanol and dried in air, b) the slides are mounted in vacuum and nanoclusters are deposited onto the surface through mesh grids, c) samples are stored in closed tin foil lined boxes prior to use and blown with N_2 to removed any dust etc. before processing, d) a solution of the dye and reducing agent is drop cast onto the slide and left for 24 h, e) excess dye solution is removed by washing with ethanol and dried with N_2 gas, f) finally the slide is placed in the confocal microscope for florescence analysis.

taken at a resolution of 512 pixels by 512 pixels.

Images of dye-coated cluster arrays deposited through two different meshes (One a nickel mesh with a bar width of ~110 μm and a 220 μm pitch, and the other a copper grid with 19 μm holes and 6 μm bars) are shown in Figure 5.26. It is clear that more dye is observed in the nanocluster coated areas of images a) and b). The average pixel intensity in the cluster coated regions is 5-7 times greater than that for the darker uncoated regions. Panel d) shows an image of a partially washed slide (after a single rinsing cycle), where significant residue remains on both cluster coated and blank regions. In images a) and b), taken after several rinsing cycles the uncoated areas become darker and the contrast more pronounced. This demonstrates that the rinsing process is able to remove the dye from the cluster free

regions but not the coated areas. As such, the dye must be more strongly fixed in the cluster coated regions.

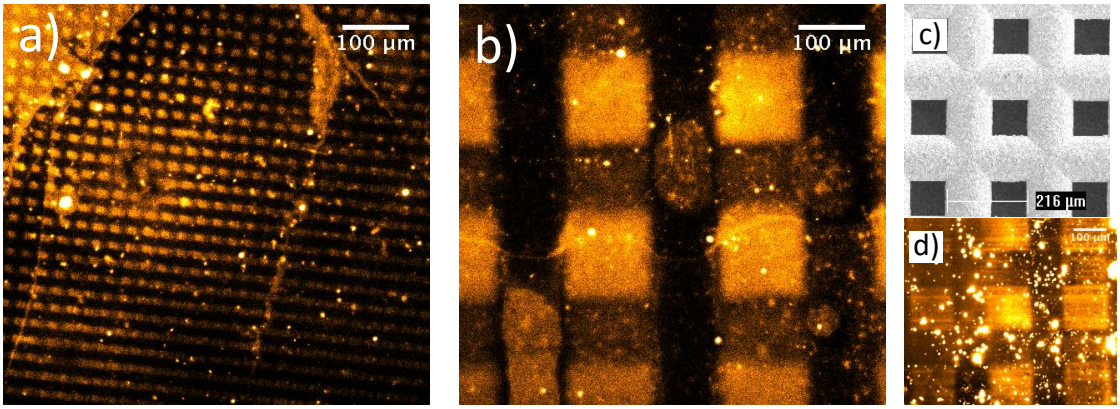

Figure 5.26: Fluorescence microscopy images showing position of the optically active dye (BODIPY FL L-cystine) on the substrate. The dye preferentially "sticks" to the nanoclusters, so that the nanocluster coated regions appear bright. a) and b) show the florescence microscope images of nanoclusters deposited through two different mesh size grids 19 μm and $\approx$ 110μm holes respectively and then drop cast with dye. c) is an SEM image taken of the larger mesh grid and d) an example of how the dye lays across the surface if excess dye is not washed off.

These results demonstrate the first step towards the development of label free biochips based on multifunctional clusters. Silver nanoclusters have been proven to act as an anchor providing a "site" for proteins to be immobilized. Furthermore, the absorption of a single layer of silver clusters is measurable from a standard UV-VIS spectrometer providing a possible high throughput measurement technique for measuring the optical response to surface modifications.

5.7 Conclusion

This chapter has presented the design and demonstration of a reflection mode MACS system. The level of production has been increased to a usable equivalent current of 170 nA (80 nA deposited) from a 30 μA ion source. This represents a significant step forward for MACS technology, improving on the number of clusters produced by approximately a factor of two compared with the previous transmission mode source, and with less than a tenth the ion beam current. Furthermore, this is an

increase by over a factor hundred compared with conventional size selected cluster beam sources (∼0.1-1 nA)[86] and comparable with an unfiltered magnetron source (∼100 nA).[84] Although, significantly less in terms of deposited mass due to the size of clusters produced. This level of increase in such a short time is very encouraging for the technology. Furthermore, this technology has been demonstrated to work in a sustained fashion without real-time replenishment, depositing an average nanocluster equivalent current of 40 nA over a 45 minute period. During the course of the deposition the cluster peak size decreases due to unintended argon dosing from the ion source. The use of a QCM to measure the real-time in-situ deposition rate has been demonstrated and proven to be a viable technique for real-time measurement of the cluster deposition rate. Finally, an example of the utility of the nanoclusters themselves can be seen in the conceptual biochip system, demonstrating the functionality of Ag clusters deposited by MACS as an anchor for the reporter dye, with multifunctional potential as an intrinsic reporter based on the enhancement of absorption properties.[166] An additional advantage of using small nanoclusters is that the particle can be tuned to give different attachment sites providing a method of potentially controlling which proteins immobilize and to an extent which orientations are permitted.[162] Furthermore, the detailed knowledge of the number and type of sites presented can be used to prevent unwanted attachments through saturation.

Chapter 6

Ion-Induced Light Emission from Argon Matrices

This chapter reports results from optical metrology of the ion-induced luminescence, observed as a by-product of cluster production in the MACS operating in transmission mode. Optical metrology can probe a wide range of properties from chemical composition and bonding to material thickness.[4,199–202] This investigation aims to provide insight into the processes taking place within the matrix under ion bombardment and ultimately develop a tool capable of real-time monitoring of the state of the matrix. This work was conducted in collaboration with my co-supervisor Dr. Feng Yin, and Dr. Richard Balog.

6.1 Introduction

In the MACS process sputtering of the matrix induces a strong luminescence (visible to the naked eye) from the argon matrix. This by-product of the nanocluster formation and extraction via ion beam bombardment, is of acute interest for two main reasons; firstly, the luminescence could provide information on the mechanisms and processes taking place inside the matrix and secondly, it could report real-time information on the composition and condition of the matrix. This would

be highly advantageous from a system feedback control view point. Sputtering and light emission of frozen rare gases has been studied quite extensively in the past.[18,173–175,203–207] There have also been extensive studies of frozen ices in conjunction with matrix isolation spectroscopy used to study molecules and clusters in pseudo-gas-phase conditions.[123,170,208–212]

The initial work comes primarily from trying to develop an understanding of molecular crystals, considering the rare gases as a "simple" model starting case due to their limited interaction and inert behaviour. This initial thrust drove towards developing a complete description of the molecular crystals and focuses on the crystal forces, formation, growth, band structure and lattice dynamics. A good overview of this work can be found in reference 213. Sputtering of rare gases has found significant scientific interest as it deviates from sputtering yields predicted by linear collision cascades. The collision cascade description breaks down due to the large number or particles in motion within a local volume and the fact some particles undergo multiple collisions.[175] This is replaced with the thermal spike model, where the vast majority of local atoms are in motion and given more energy than the binding energy. The thermal spike process is active for a much longer time scale (10^{-12}-10^{-10} s) than the initial cascade (10^{-13}-10^{-12} s) as the sputter region continues to emit atoms while cooling.[214] The behaviour can be well described by a liquid or high-pressure gas region around the initial impact.[172,173] This effect can cause a locally lowered binding energy which coupled with the low energy of thermally "evaporated" atoms, leads to most emitted atoms having low kinetic energy.[175] It has also been shown that for high sputtering energies (tens of keV or more) the small amounts of the electronic energy deposited can couple into lateral motion having a noticeable effect on sputtering yields.[175,215]

There has been limited interest in the visible range spectra of Ar as this is largely suppressed in the solid phase (compared with gases) however a rich and highly efficient UV range spectra is observed. This is largely due to the large ionization

energy (∼16 eV), after ionization it effectively couples to an excimer emission (9.8 eV from Ar_2^*).[216,217] This large band gap also causes solid argon to be transparent into the UV range which makes argon and rare gases in general a useful support for optical absorption or photo-excitation studies of isolated particles (matrix isolation spectroscopy). Also, due to the weak support interaction of rare gas matrices this allows pseudo gas phase cluster properties to be probed while permitting accumulation of a large number or density of particles prior to measurement (unlike in-flight measurement). Studies have demonstrated that clusters and atoms can be deposited into matrices.[218–221] Through these studies the limits and properties of matrices containing different levels of metal have been well established, in the regime examined with the matrix formation in the MACS (<10 %) limited homogeneous aggregation of atoms is expected (clusters of a few atoms only).[218] Furthermore it has been possible to observe the absorption and emission spectra of small silver particles in or impinging on matrices.[220,221]

Despite this extensive study, the case of keV bombardment of metal containing matrices does not appear to have been studied, this is likely due to the significant effort generally made to ensure limited structural change of the matrix during optical measurement, which is completely at odds with the experimental conditions in the MACS. In the MACS there is both, significant modification of the matrix, and a large excess of energy deposited into the local regions, which results in a highly dynamic system.

6.1.1 System Set-up

The optical metrology set-up is given in Figure 6.1. This is a modification of the proof of principle reflection mode MACS system (described in chapter 4). There are two main parts to the system, the transmission MACS section and the optical measurement section. The light emission from the matrix exits the vacuum chamber via a standard DN40 borosilicate view port which is coupled to the optical measurement

system, which is located inside a black-out box. Inside, the light is focused into a Triax 190 monochromator, using a convex glass lens (with a focal length of 20 cm). The transmitted light is then directed into a photomultiplier to give a photocurrent, which is measured by a picoammeter (Keithley 485) and recorded with Labview software. In the case of total photocurrent measurements, the monochromator is replaced and the photomultiplier is used directly.

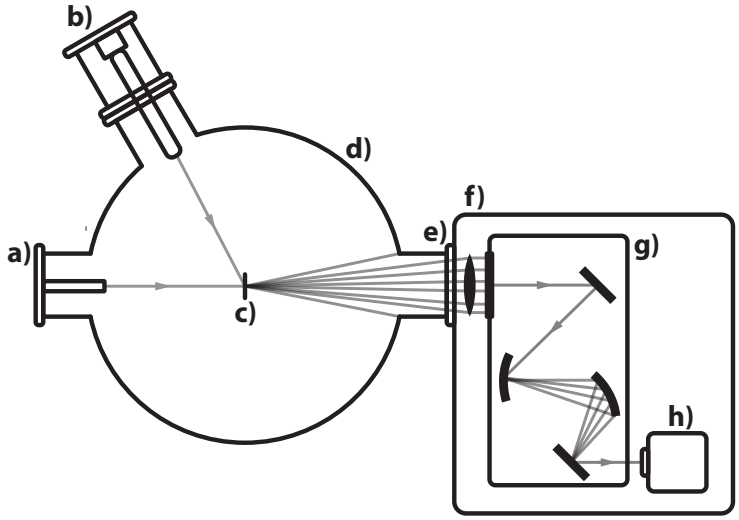

Figure 6.1: Experimental set-up of the modified HREELS system for use in optical measurements. a) ISE-5 ion gun, b) Createc thermal evaporator, c) matrix support (copper 1000 mesh), d) UHV vacuum chamber, e) optical window, f) optical blackout box, g) monochromator and h) photomultiplier.

The vacuum is maintained with turbo molecular pumps backed by rotary vane pumps. A base pressure in the low 10^{-8} mbar region can be achieved with this set-up. To reach the ultimate pressure for luminescence experiments the chamber undergoes a short baking cycle (24-48 h), during which time the chamber temperature is maintained between 100°C and 120°C. Once the chamber pressure has reached below 2.5×10^{-8} mbar still while warm, the bakeout is stopped and the system cooled. An example of the before and after gas compositions can be seen in table 6.1. Post baking the pressure is maintained using a Gamma Vacuum ion pump and reaches values in the high 10^{-10} mbar region. Experiments carried out before section 6.3.4 are conducted without baking.

Table 6.1: This table shows the residual gas measurements made before and after the system bakeout. A significant decrease is observed in the overall pressure as well as in the partial pressures of specific residual gases e.g. water and nitrogen. All pressures are given in mbar.

a.m.u.	**1**	**2**	**16**	**17**	**18**	**20**
Before Baking	9×10^{-10}	9×10^{-10}	1.9×10^{-10}	5.3×10^{-10}	1.6×10^{-9}	1.4×10^{-10}
After Baking	2.4×10^{-10}	1.9×10^{-10}	0.4×10^{-10}	1.2×10^{-10}	4.4×10^{-10}	0.5×10^{-10}
a.m.u.	**28**	**32**	**40**	**Total**		
Before Baking	5.7×10^{-10}	0.4×10^{-10}	1.4×10^{-10}	$\mathbf{4.4\times10^{-9}}$		
After Baking	1.9×10^{-10}	0.1×10^{-10}	0.5×10^{-10}	$\mathbf{1.5\times10^{-9}}$		

The system schematic in figure 6.1 shows the geometry of the transmission mode MACS system: the matrix support is a copper 1000 mesh grid (25 × 25 mm diameter) mounted on the end a copper cold finger. The cold finger is cooled by a continuous flow liquid helium cryostat (see figure 6.2 for details). Both the Omicron ISE-5 ion gun a) and the Createc high-temperature effusion cell b) are mounted on the same side of the matrix support c), which allows continuous replenishment during sputtering. However, to prevent stray light from these sources, they are situated out of line of sight of the matrix and the collection view port (i.e. offset above and left for the ion gun and evaporator, respectively). Argon gas is supplied to the ion gun by a dedicated precision leak valve. An additional precision leak valve is used to provide the matrix dosing pressure inside the chamber. The gas line comprises 1/4" stainless steel tubing connected with Swagelok tube fittings, that is pumped with a small turbo molecular pump, backed by a rotary vane pump. A schematic of the gas line is shown in Figure 6.3.

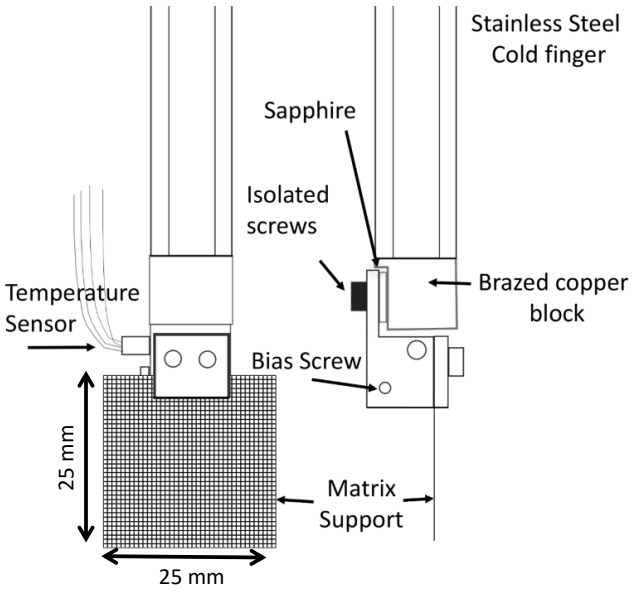

Figure 6.2: Schematic diagram of the cold finger. The top edge of the matrix support is clamped between two copper plates (gold foils are used for improved thermal contact). The only other connection between the brazed copper block and the matrix support is formed by a sapphire washer used to provide electrical isolation. Both faces of the washer are coated with a gold film in order to increase thermal contact. The base temperature obtainable in the absence of an external heat load is 9 K.

6.1.2 Matrix Preparation

The first stage is to cool the matrix to below 20 K, to achieve this liquid helium is flown through the cold finger. The cooling system here is identical to that used in chapter 4, a diagram of the system is shown in figure 4.5. The base temperature of the set-up with this matrix support is 9-10 K. This is reached after about 2 h of cooling in this manner.

To purge the gas line of impurities it is filled with argon gas to a pressure of approximately 1 bar (absolute), which is slowly released into the gas line turbo to be pumped away, this process is repeated three times. The gas line is then filled with the desired gas or gas mixture to run the experiment, to ensure the correct doping level of oxygen or nitrogen in the argon matrix the composition is checked using an RGA. Once the cold finger reaches temperature the gas is backfilled into the chamber to provide the desired dosing pressure, the matrix is grown for a specific time to

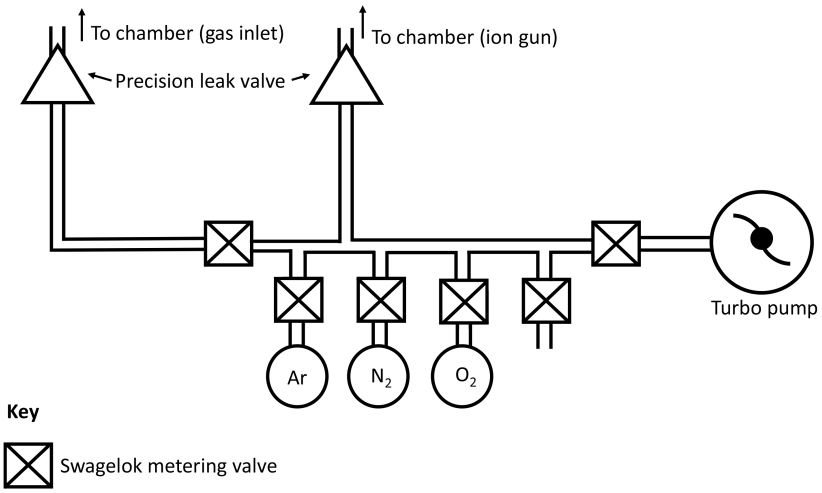

Figure 6.3: Schematic of the gas dosing lines for matrix formation and sputtering. This permits the mixing of gases for doping matrix and isolation of the argon ion gun gas supply

produce a known matrix thickness on the support. The method for calculation of the matrix thickness is outlined in appendix A. Sufficient mixed gas can be stored in the isolated line for the duration of the experiment. The rest of the gas line is purged and argon gas is introduced into the ion gun to produce the ion beam for sputtering, the beam is defocused to give a near uniform current density across the matrix. During the initial 3-4 minutes of sputtering the ion gun warms up, to maintain a constant current on the matrix the focus is adjusted slightly, until it stabilizes. When studying the equilibrium state of the matrix under bombardment the dosing gas pressure is maintained, the level chosen is based on experimental measurement of the dosing pressure required to maintain a stable luminescence.

6.2 Photocurrent Measurements from Argon Matrices During Depletion

The bombardment of a frozen Argon matrices with keV Argon ions leads to the production of thermal spikes where many atoms are given energy and move simul-

taneously. Assuming that visible range light emission does not occur as a result of a specific decay of a single high energy interaction, it is logical to assume that each ion can cause multiple light emission events. If this is the case, the greater the interaction the region available to the ion, the more light will be emitted. To investigate this, two different parameters have been tested, the matrix thickness and ion beam energy. In solid Argon keV ions can penetrate up to tens of nm.[171] By increasing the argon matrix thickness, more energy should be delivered into the matrix itself, rather than reaching the support, leading to greater light emission. Naturally, energy deposited directly into the metal support will not contribute to the argon luminescence. Neither will energy deposited near the support surface due to quenching.[220,222,223] Secondly, by increasing the energy of the impinging ions more energy is delivered in to the matrix, covering a larger volume,[172,173,175,216] which would be expected to increase light emission. The total visible light emission of a pure argon matrix during ion beam bombardment has been measured directly using a PMT. Figure 6.4 shows the change in photocurrent produced by sputtering different thickness matrices (53 nm, 106 nm, 159 nm and 265 nm) with the same ion beam current and energy (6 μA and 1.5 keV, respectively). It can be seen that the thicker the matrix the higher the initial light emission intensity. As the argon becomes sputtered away by the ion beam the light emission reduces. This agrees with the hypothesis that the light intensity is directly proportional to the concentration of argon atoms, which are the light emission centres. The matrix is not replenished so the sputtered area not only reduces light emission by having fewer emission centers, but also, by reducing the chance of the ions hitting the matrix. As such, the drop in rate will be of a greater than linear power dependence. When matrix becomes thick (significantly thicker than the ion penetration depths) the light emission should remain constant, this saturation can start to be observed in peaks emission seen when sputtering the 159 nm and 265 nm-thick matrices (shown in figure 6.4).

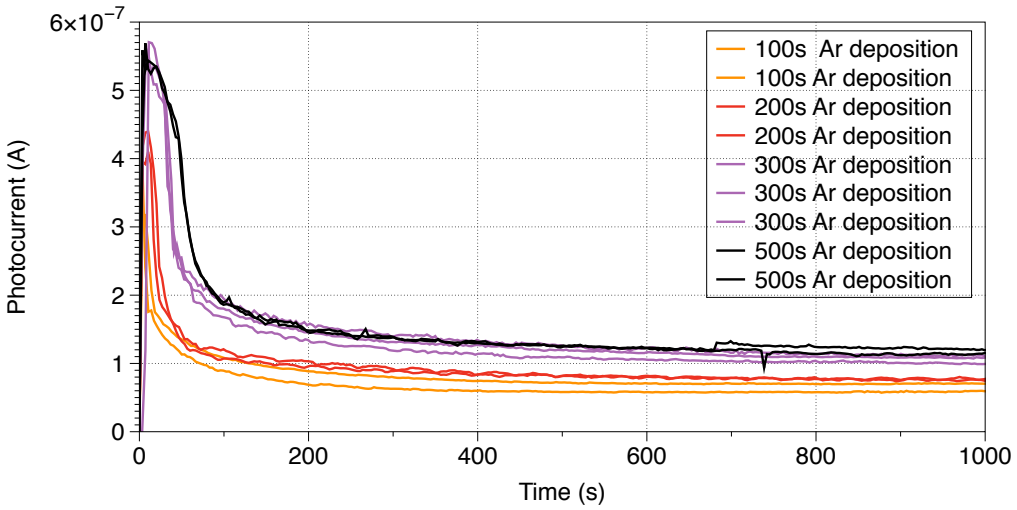

Figure 6.4: Metal free matrices have been prepared by dosing for different lengths of time in an argon pressure of 4×10^{-6} Torr (resulting in a matrix thickness of 53 nm, 106 nm, 159 nm and 265 nm, respectively). Light emission has been induced via ion bombardment with a 6 μA, 1.5 keV Ar^+ beam. Total light emission is collected with a PMT and plotted versus sputtering time.

The dependence of luminescence intensity on the incident ion energy has also been measured, the results can be seen in Figure 6.5. The green line plots photocurrent against incident ion energy (upper panel), while the black line plots sputtering yield as a function of ion energy (lower panel). The values for the sputtering yield have been reproduced from the work of Urbassek et al.[173] The increased ion energy is known not just to transfer energy to just a single atom, but quite effectively into the local matrix area.[172,173,224] As the ion energy increases so to does the light emission, this can be attributed to the increased volume of interaction, resulting in a greater number of light emission centres. This correlates well with the trend in sputter yield at higher incident ion energies. Similar findings have been reported in previous work.[216] These results indicate that it is unlikely that the emission route or mechanism within the matrix undergoes significant change as the incident ion energy increases. However, as there are many other possible routes to remove the energy non-radiatively or even radiatively in different energy ranges, spectroscopic measurements would be required to confirm this.

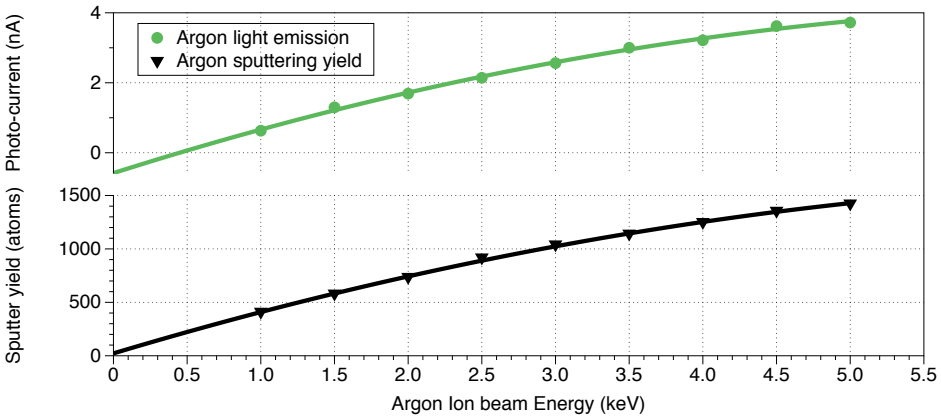

Figure 6.5: The intensity of the initial peak in light emission from a ∼125 nm thick argon matrix (green) is measured under argon ion bombardment at different ion energies (1-5 keV). Light emission increases with ion energy. The dependence of the sputter yield on the incident energy is shown by the lower black graph. The latter data has been reproduced from Urbassek's work.[173]

6.3 Spectroscopic Measurements

To probe composition and emission mechanisms spectroscopic measurement has been applied. To provide wavelength resolved spectra, the Triax 180 monochromator has been placed before the PMT. The measurements are calibrated by measuring the spectrum of a red laser pointer, which is given in figure 6.6, and has been used to measure the resolution and wavelength correction required. The calibration has been confirmed with a multi-peak lamp to ensure there are no scaling errors. The experimental resolution is the FWHM observed in the laser spectrum, in this case 6 nm. However, using the matrix as a source will increase this for several reasons; spectrometers are designed to work optimally with collimated light sources. Therefore with light coming in at different angles (due to the large light source of 25 mm × 25 mm) there will be broadening in the spot size and therefore the spectral resolution. Furthermore, as this set-up probes excitations from a solid phase, further broadening will arise due to the band structure changes from nearest-neighbour interactions.[218]

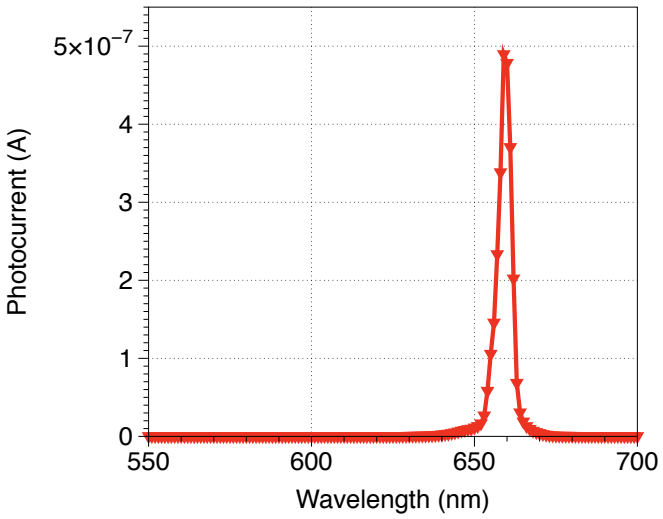

Figure 6.6: Light emission spectrum of a red laser pointer passing through the optical set-up. This measurement of a known wavelength laser is used to calibrate the system, giving both resolution(FWHM ∼6 nm) and wavelength position for correction (also confirmed with a multiple peak lamp).

6.3.1 Light Emission During Growth and Depletion of Argon Matrices

In order to distinguish changes in light emission arising from compositional changes in the matrix rather than it's depletion or growth a stable light emission signal is required on the time scale of the spectroscopic measurements i.e. minutes. As demonstrated previously both the thickness and depletion of the matrix leads to a change in light emission intensity. This has been investigated further to find an equilibrium replenishment rate and confirm that the emission mechanism is not affected by the matrix thickness or incident ion energy. Firstly, to demonstrate that the light emission increases are due to the thickness of the matrix rather than a compositional or mechanistic change, wavelength resolved measurements have been taken at high argon dosing rates. A dosing pressure of argon (5×10^{-6} Torr) was used while sputtering with a reduced ion beam current (4 μA), to ensure net growth of the argon matrix. Figure 6.7 shows repeated scans taken under these conditions. An increase in the luminescence signal is observed with each scan, without spectral

modification. The scan time is about three minutes for all experiments unless stated otherwise.

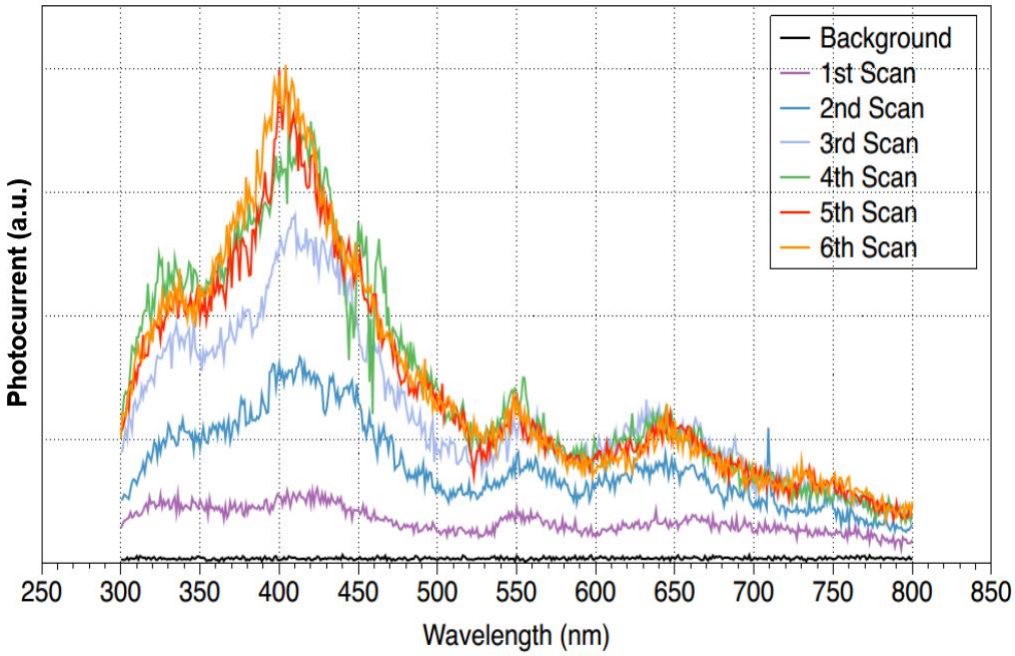

Figure 6.7: Ion-induced luminescence of argon with a high background chamber pressure (5×10^{-6} Torr). This causes growth of the matrix with time despite the ion beam sputtering (4μA at 5 keV), increasing the observed luminescence signal. Each scan duration is $\sim$3 minutes.

For each of the specific set of ion beam parameters a different equilibrium Argon pressure is required due to the different total sputter yields and the ion gun gas leakage. Figure 6.8 shows an example of tuning the argon gas dosing to achieve equilibrium where both the growth and depletion of the matrix can be seen. In a) the dosing pressure is too low and the matrix is thinned by the sputtering process. However, in b) the Argon dosing pressure has been increased and net growth of the matrix, with a corresponding increase in the luminescence photocurrent is observed. Experiments following this point will be carried out using the experimentally optimized equilibrium dosing levels, to maintain a constant matrix thickness, unless otherwise stated. Even under these conditions an initial increase is always observed in the first few scans which is attributed to structural rearrangement of the matrix and will be discussed in more detail later.

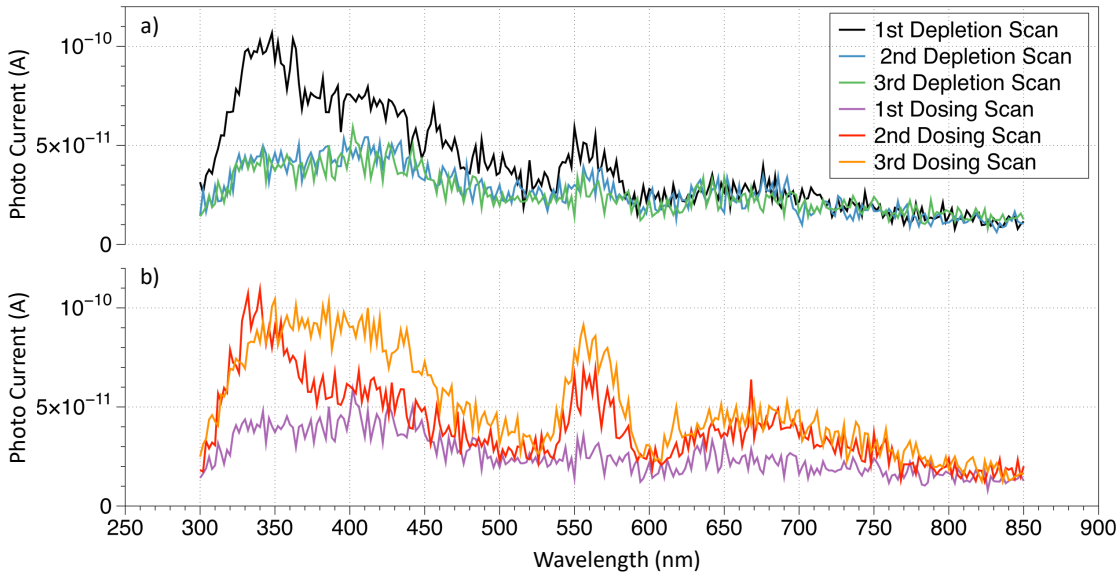

Figure 6.8: The graphs shows the ion-induced luminescence intensity measured while sputtering a matrix under two different chamber pressures a) 2×10^{-6} Torr and b) 6×10^{-6} Torr. Repeated spectra are taken showing the evolution of the light emission with time. The upper graph is indicative of a depletion regime running in the order black, blue, green, while the lower shows matrix growth following the order purple, red, orange. An ion beam current and energy of 4 μA and 5 keV was used in both cases

6.3.2 Light Emission Dependence on Ion Energy

As mentioned in the section 6.2, to confirm that the increase light emission with energy is due to the increase in the number of emission centers, rather than different emission mechanisms, spectroscopic information is required. The spectral signatures of same-thickness Argon matrices under ion bombardment with different incident ion energies are presented in figure 6.9. In each case, the signature remains largely unchanged except for an increase in intensity. This confirms there is not a significant change in the emission mechanism within the matrix, but simply that a greater volume is being involved in the process.

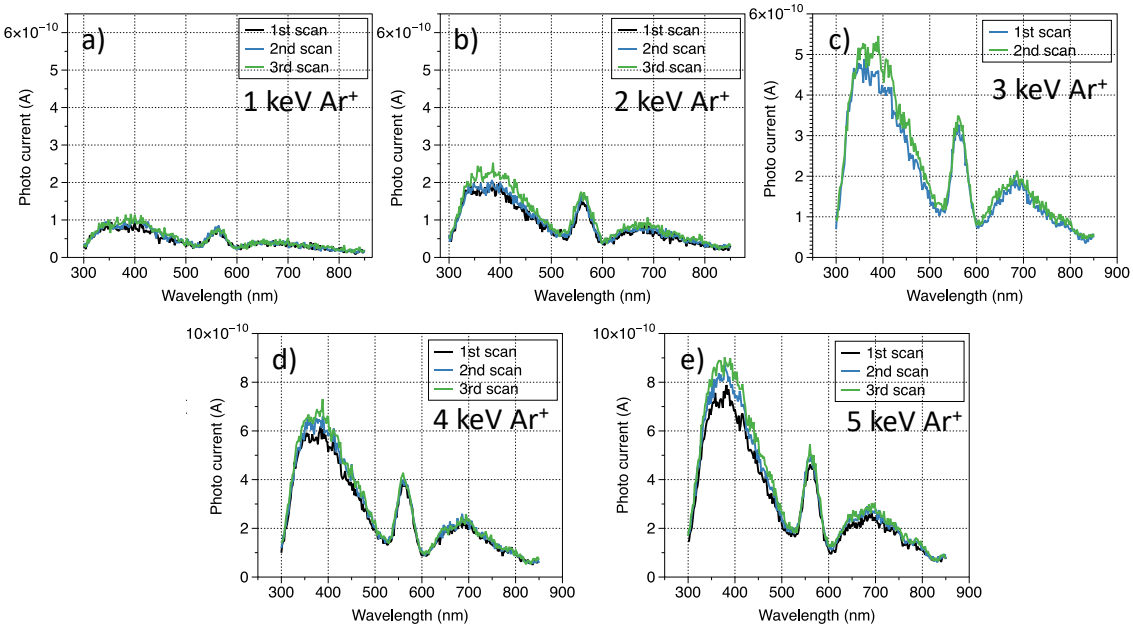

Figure 6.9: Ion-induced luminescence spectra of argon matrices under argon ion bombardment with different incident ion energies between 1 keV and 5 keV. The energy of the incident argon ions is indicated on the right hand side of each graph. Little change is observed within the spectra besides the increasing intensity as the energy of the impinging ion is increased.

6.3.3 Matrix Composition

In the previous sections the basis has been laid to perform stable steady-state measurements without the introduction of artefacts from dosing rates, matrix thickness, beam parameters, and ion energy. In the following experiments the matrices are replenished during bombardment at the equilibrium dosing rate. The following sections are concerned with the identification of the matrix composition from the spectroscopic measurements in real-time. Three main cases are investigated: the light emission of a pure argon matrix, a nitrogen-doped argon matrix and an oxygen-doped argon matrix. The latter two cases not only provide insight into the matrix behaviour in the presence of common contaminants under high vacuum (HV) conditions but also are an interesting route to the production of nitride/oxide clusters through matrix doping.

6.3.4 Pure Argon

The light emission from the pure argon matrix under ion bombardment (6 μA at 1.5 keV) at 12 K presents relatively broad features between 350 and 520 nm, figure 6.10. Immediately, it can be seen that these spectra demonstrate significantly different features to the pre-bakeout spectra (those previously shown). The main peak is at 410 nm although there is also a shoulder to either side at 385 nm and 460 nm. Each spectrum has been taken sequentially (with a scan duration of ~3 min), the light emission intensity stabilizes over several scans, this will be considered in more detail later. This broad emission is attributed to step transitions from the highly excited Ar** (5p-4s), and thought to emit from the hot regions or tracks where the ion has impinged causing the solid to sublimate into a high pressure gas.

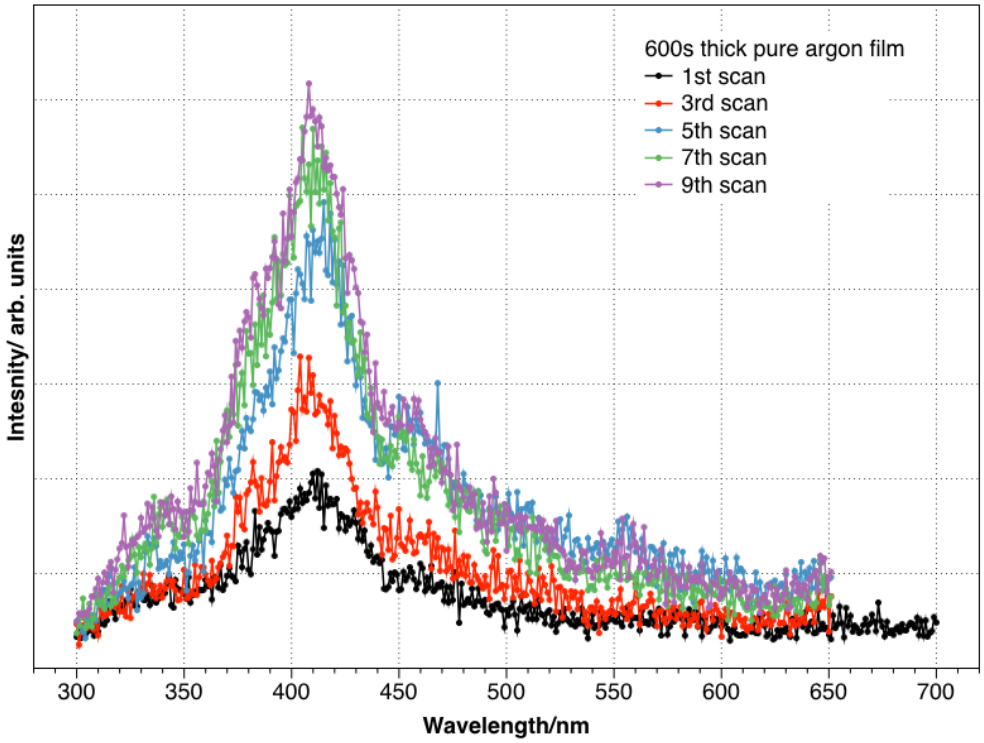

Figure 6.10: Luminescence signal from ~300 nm thick film of argon deposited onto a cryogenically cooled Cu 1000 mesh grid (at 12 K) and irradiated with 1.5 keV Ar+ ions (6 μA). Sputtered argon is replaced by dosing argon at a chamber pressure of 2.5×10^{-6} Torr. Nine consecutive scans are plotted. The signal comprises a broad spectrum between 300 nm and 530 nm with the main feature at 420 nm.

This interpretation is supported by other reported work;[225–229] in most of cases high pressure argon gas is made to emit by applying a high voltage to cause an arch discharge. Although it might not initially appear related in some ways this type of discharge system is remarkably similar to the experimental set-up here; the sputtered solid forms a high pressure gas, due to the recent ion impact a significant fraction of this is ionized and highly excited, furthermore it is possible that electrical arcs can be directly caused within the matrix if the matrix does not fully neutralize the charge of the incoming ions and a significant potential builds up. Potentials of less than 50 V over tens on nm have been observed to destroy matrices due to arc discharge.[220]

This emission has also been observed by Gabla et al when bombarding an argon matrix with keV Ar ions.[225] However, in their experiment only light emission from the sputtered particles is measured. Light directly from the solid is blocked. The spectrum reported shows only a weak signal in this region, which is dominated by other emissions. Due to our experimental setup up it is not possible to determine the contribution of the overall signal that comes from the solid or emitted gas phase atoms. However, this indicates that the emission observed must predominately originate from inside or very close to the solid. As the excitation is primarily populated via decay from ionized argon dimers, the increased abundance of argon either in or near the solid would be expected to increase this emission ($Ar_2^+ + e \rightarrow Ar^{**} + Ar \rightarrow Ar^* + h\nu$). This also agrees with findings of the arc discharge studies where the Ar** emission intensity was found to have a strong dependence on Ar pressure.[226] In addition Gabla et al's experiment only observes sputtered material at a significant distance away from the matrix, it is possible by this point the highly excited state has already decayed due to the short life times for such species.[230,231]

There are two possible reasons for the significant broadening of the features, observed here compared with previous work, the experimental resolution of the system as discussed previously, and the possibility of broadening due to solid phase

emission. Despite the large number of papers on the luminescence of frozen argon this emission does not appear to have been previously reported for the solid phase. There are two main reasons for this, firstly many of the previous results are carried out in the UV range, and secondly, the excitation sources are different (He^+,x-ray, alpha particle, electron, etc.)[230–234] Furthermore, in some cases only the total emission intensity is recorded. There are two experimental observations that hint towards a source within or close to the matrix surface, opposed to purely from the gas phase. The light emission is observed to initially (over the first few spectra) increase with ion dose and with reducing temperature of the matrix, demonstrating a dependence on the matrix state not just the amount of material sputtered. Typically this emission is not possible in the solid phase due to fast non-radiative decay of highly excited species through heating (e.g. $Ar_2^+ \rightarrow Ar_2{}^*$). However, irradiation of the film can lead to amorphization,[235] which in tern significantly reduces the local conductivity,[236] which could be enough to suppress non-radiative channels and allow emission from the solid phase. This is consistent with experimental observations that the emission intensity initially increases with ion dose and that at lower temperatures the emission increases (due to reduced "healing" of the amorphous regions).

6.3.5 Nitrogen Doped Argon

The interest in gas doping the matrix is two-fold; firstly, the addition of a dopant could lead to a route to produce binary material clusters e.g. oxides, nitrides etc. secondly, low levels of such gases can usually be found in the residual gas of the a vacuum system. Therefore it is important to detect the presence of such gases, and for the purpose of feedback control the effect they have on light emission. Argon and nitrogen gas have been pre-mixed and then introduced into the chamber for dosing. The composition is measured using an RGA prior to deposition. Figure 6.11 shows spectra from an argon matrix doped with ∼5 % concentration of nitrogen, the matrix is ∼300 nm thick and sputtered with a 6 μA, 1.5 keV argon ion beam.

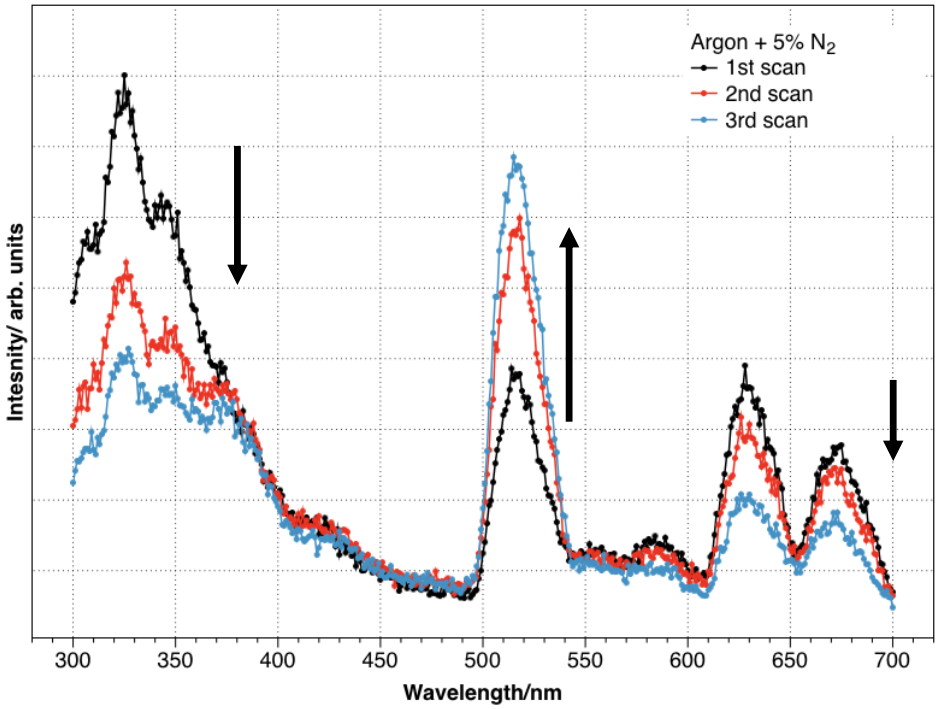

Figure 6.11: The luminescence spectra of three successive scans of a nitrogen doped argon matrix(initially 5 % N_2). The emission signals below 430 nm and above 540 nm are caused by the excited N_2 molecule. These both decrease with sputtering however, the 523 nm peak arising from the nitrogen atom increases in intensity with sputter time. This increase is caused by the generation of nitrogen atoms by cleaving of the N_2 molecules and therefore the reduction of the nitrogen molecule-related peaks.

There are several key features that can be observed; the Vergard Kaplan lines at <430 nm[237,238] , the excited atomic nitrogen state at 523 nm,[237,238] the N_2 vibrational modes in the region above >540 nm.[239] Unlike the pure argon case, with increased dose (sputter time) the shape of the spectra changes, the peaks at <430 nm and >540 nm decrease, while the central peak at 525 nm increases. The decreasing peaks are related to transitions in the N_2 molecule, whereas the 523 nm peak arises from an excitation of the single nitrogen atom. This indicates a change in the nitrogen population contained within the matrix with ion beam dose. During bombardment of the matrix the argon ions can cause dissociation of the N_2 molecules through cleaving, increasing the population of N radicals and reducing the number of N_2 molecules. This causes an increase in the 523 nm peak at the expense of the N_2

molecule, reducing the other two peaks. As the replenished gas dosing contains only N_2 molecules the stock cannot be fully depleted and the emission intensities would eventually equilibrate with the few fresh upper layers containing N_2 molecules. This demonstrates that the technique is sensitive to molecule/atom concentrations within the matrix, which is in turn dependent on ion-exposure.

6.3.6 Oxygen Doped Argon

Oxygen is widely know as an effective scavenger[174] and can have dramatic effects on observed emission spectra even with exceptionally low concentrations. Previously this has led to emission from very low levels of O_2 being assigned to "pure argon".[240] Therefore the distinction between the two is an important test for the sensitivity of the measurement technique and it's usefulness in monitoring the MACS process, which would generally contain trace amounts of O_2. The effect of the addition of 0.1 % oxygen into a pure argon matrix can be seen in figure 6.12. Again gases are pre-mixed and then leaked into the main chamber via a leak valve, the matrix thickness is $\sim$300 nm and sputtered with a 6 μA, 1.5 keV argon ion beam.

Even with such low concentration a dramatic change can be seen the light emission spectra, the main peaks are at 420 nm, 440 nm, and 560 nm (figure 6.12). The broad feature ultimately peaking around 420 nm is assigned to a combination of the 410 nm pure argon peak and the 440 nm Herzberg oxygen emission peak.[241] With prolonged sputtering there is a shift in the feature moving towards the 410 nm argon peak. The 440 nm emission is a well known Herzberg emission of O_2 and as such direct cleaving of the ion beam can split the O_2, reducing the molecular population and increasing the number of oxygen radicals, leading to the argon emission at 410 nm dominating the region. The 560 nm ArO exciplex peak supports this hypothesis as it's intensity increases with sputtering as more radicals become available. These results demonstrate that after baking, any residual oxygen is sufficiently low so as not to influence metrology measurements of the Ar matrix. Furthermore, small levels

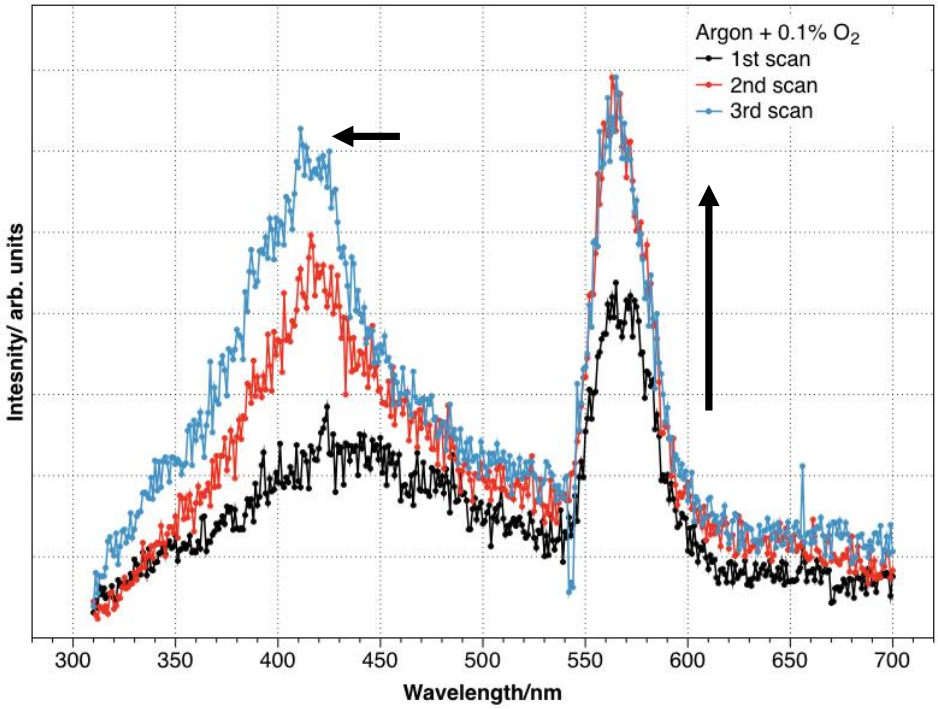

Figure 6.12: The luminescence signal from the three successive scans of an argon matrix doped with 0.1 % O_2 is given above. The first scan shows a broad feature around 440 nm, which then shifts towards 420 nm in consecutive scans (horizontal arrow). Initially the primary origin is the Herzberg emission (440 nm) of O_2. With sputtering the O_2 population reduces and the 410 nm Ar peak starts to dominate the emission. The ArO* excimer is the source of the 563 nm which increases with sputtering due to the higher abundance of O radicals to form the ArO* excimer (vertical arrow).

of O_2 impurities can be observed by this method, with the possibility to distinguish between molecular and atomic species.

6.3.7 Matrix Condition

In the case of the pure argon emission some limited information can be gained as to the condition of the matrix, it is observed that with an equilibrium level of argon replenishment, the light emission initially rises with sputtering. This effect is reproducible and it is consistently found that after several scans the emission stabilizes. The emission is assigned to hot tracks and trapped gas pockets. When sputtered, if a material does not have sufficient energetic freedom to rearrange or reconstruct,

it generally becomes rougher and more irregular. In the case of the cryogenically cooled matrix after impact local rearrangement may occur due to the energy injected by the ion, however long range reconstruction does not take place. This leads to defects, craters, pits and tracks roughening the surface, creating more pockets for trapped gases and significant reduction in the thermal conductivity,[236] thereby lessening the suppression of highly excited species due to faster non-radiative decays. However, the increase in gas "pockets" is sufficient to motivate the observed increase in luminescence intensity alone. Further agreement with this argument can be found by altering the matrix temperature and considering the luminescence intensity. Qualitatively speaking a greater light intensity is observed at lower temperatures, this was also seen by Sieber et al.[242] Lower temperature means a more "fixed" matrix with less "self-healig" of damage induced by sputtering, which is in agreement with the findings so far. However, due to experimental factors this has only been measured over a small range and does not rule out other decay pathways being permitted by the increased temperature.

6.3.8 Initial Investigations With Metal Loaded Matrices

Up to this point only frozen gas matrices have been investigated. In order to provide useful information for control of the MACS precise knowledge of the exact metal concentration within the matrix is vital. As shown earlier (Figure 2.18) the metal concentration affects both the cluster size and the number of clusters produced. Initial studies investigating metal-doped matrices are presented here. It is known that bulk metal surfaces quench light emission in rare gases by dipole interaction.[220,222,243] Argon films deposited on metal surfaces with a thickness less than $\sim$20 nm show no visible light emission . The addition of metal atoms for cluster formation also significantly reduces light emission through quenching, despite the lack of a bulk material. The increased conduction of the matrix due to the presence of these metal atoms has been linked to the quenching of small metal particles in

rare gas. In addition to conduction, the light absorption of the clusters may play some role. The light absorption of silver clusters varies greatly from that of bulk silver. For example, this can be seen in figure 6.13, which is taken from a paper by Harbich et al.[123] In this work the absorption of small silver clusters is investigated through DFT calculations and the measured absorption of ion sputtered silver clusters deposited into rare gas matrices. As the clusters are directly sputtered from a target they are produced with high internal energy and are free to rearrange their shape and structure, considering this only DFT calculations for low energy stable isomers have been used. Larger silver particles also exhibit a surface plasmon, which changes wavelength with particle size,[244,245] as silver aggregates inside the matrix it may be possible to see some change in this contribution with sputtering time from implanted ripening clusters.

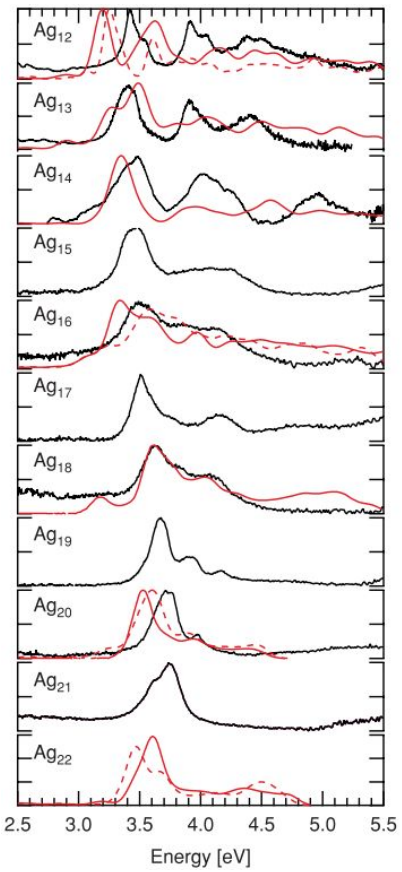

Figure 6.13: The optical absorption of small silver clusters calculated by simulation (red line) and measured experimentally by deposition into argon matrices (black line). This figure is reproduced from Harbich et al's paper [123].

To study the effect of silver doping, argon matrices of the same thickness were prepared with different metal loadings by changing the evaporation temperature. The addition of metal induces significant quenching, which is further enhanced as the concentration of metal, in this case silver, is increased. In the same sense that the thicker matrix increases the number of excitation sites and therefore light-emission sites, increasing the silver loading increases the concentration of quenching sites reducing the total light emission. In figure 6.14, the sequential reduction in light emission can be seen as the metal loading increases.

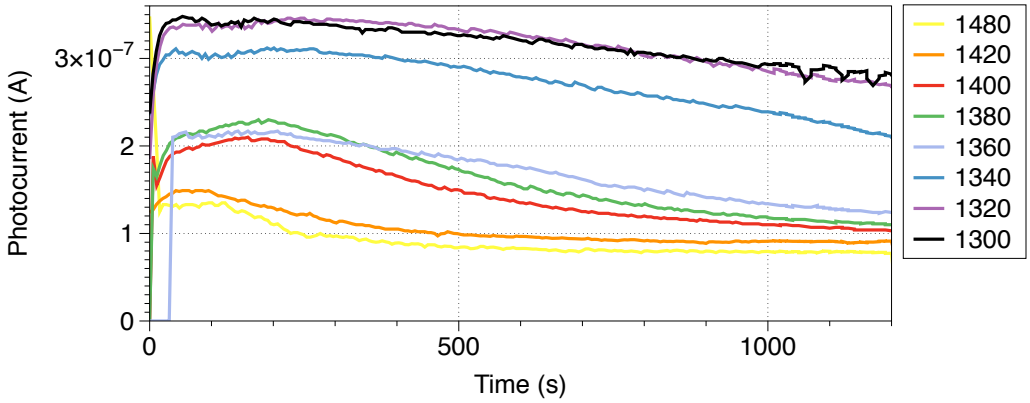

Figure 6.14: Ion-induced luminescence intensity for argon matrices containing different concentrations of silver. The legend denotes the evaporation temperature in degrees Celsius. As metal loading increases the light emission is reduced.

The same result can be seen for gold by comparing the peak initial photocurrent measured when sputtering pure argon matrices and gold doped systems. This has been tested for a range of incident ion energies 1-5 keV as shown in Figure 6.15. In each case, the same thickness matrix was prepared prior to sputtering, the matrix was sputtered without replenishment and the peak current observed in each case is plotted against the ion energy (figure 6.15).

Although concentration dependent quenching increases measurement complexity, the intensity of the emitted light could be a way to determine the metal concentration for a known thickness matrix. With a known matrix thickness it would be possible to de-convolute the quenching and depletion effects and determine the concentration

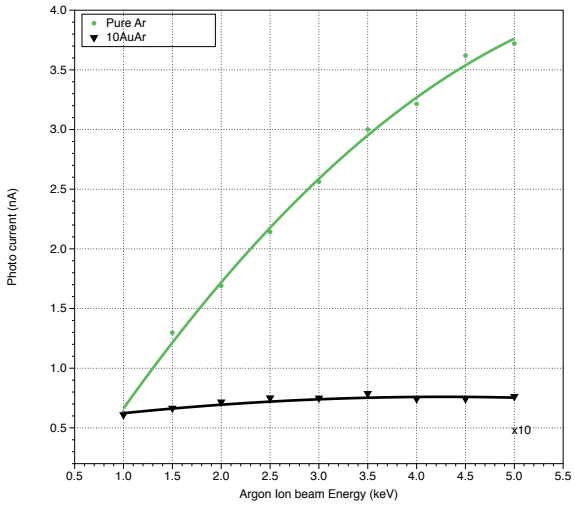

Figure 6.15: The total light emission from a ∼125 nm thick argon matrix (green) measured under different energy argon ion bombardment (1-5keV). Light emission increases with ion energy. The same effect can be seen from a gold doped (9 % concentration) matrix however the emission is much weaker (black). The emission from the gold-doped matrix has been multiplied by a factor of ten before plotting.

of metal. This is somewhat difficult to carry out in practice however. It would be much more advantageous if a specific excitation was quenched or induced by the addition of the metal, the amount of metal could then be calculated independent of the matrix thickness (i.e. by a ratio of excitations). To this end spectroscopic measurements have been performed with the intent to identify specific emission or quenching signatures due to the silver doping. Figure 6.16 shows a series of spectra investigating the effect of metal doping. First a 120 nm thick matrix with 0.2 % Ag concentration is prepared, the spectra in figure 6.16 a) shows the light emission of the matrix while being replenished by both Ag and Ar at an equilibrium level. Figure 6.16 b) shows the light emission when the replenishment of Ag is stopped, so the freshly deposited layers are pure Ar. Finally, figure 6.16 c) presents the effect of reintroducing the Ag replenishment.

In figure 6.16 a) two broad peaks are observed, the 410 nm peak that has been associated with argon emission and a 460 nm peak. Stopping the Ag replenishment will first cause the 460 nm peak to reduce until it is as observed in figure 6.16 b), while the 410 nm Ar emission increases. Once silver replenishment is started again

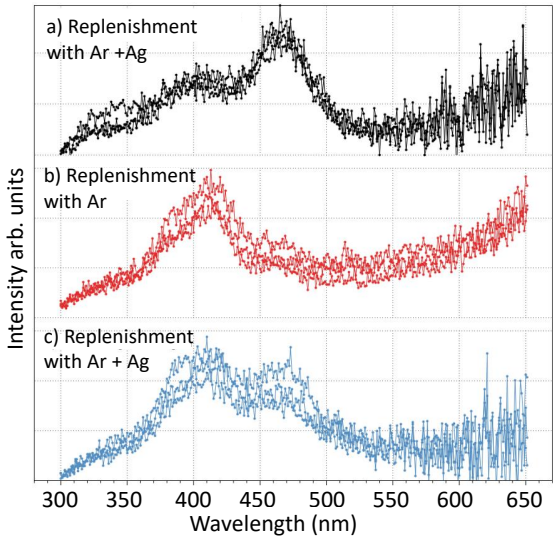

Figure 6.16: A sequence of luminescence signals observed from a 120 nm thick argon silver matrix under different replenishment conditions. The matrix was prepared with a thickness of 120 nm at a 0.2% Ag loading. In each case three successive spectra are plotted. a) luminescence under constant replenishment with Ag and Ar (0.2 % silver concentration), b) luminescence with just argon replenishment and c) return to replenishment with both Ag and Ar. In each case, the matrix is irradiated with a 6 μA 1.5 keV argon ion beam during measurement. In the case of the metal dosing spectra, a background subtraction is performed to account for the light emission of the evaporator.

the 460 nm peak recovers however, the light emission at 410 nm due to pure argon is not as suppressed as before. Experiments conducted by Harbich et al.[220] show luminescence of Ag_1 at 460 nm. This is probably the source of this 460 nm signal. The replacement of the silver with another metal with different absorption and emission wavelengths (e.g. gold) could be employed to further investigate elemental signatures of metal doped matrices. The replacement of argon gas with say krypton or xenon my also provide a more neutral background for experiments over this emission range. This short investigation provides the basis for further investigations of the light emission within the MACS, both for mechanistic insight and system control.

6.4 Conclusion

The fundamental processes within the MACS and a method of feedback control have been investigated via optical metrology of the matrix under ion bombardment. Results show it is possible to measure the thickness of matrices based on the total light emission, assuming that the composition remains consistent. This can be further enhanced by taking wavelength resolved measurements, which can reveal the elemental and molecular composition of the matrix with exceptionally high sensitivity (in some cases < 0.1 %). Furthermore, limited information can also be extracted about the matrix condition under exposure to ion bombardment. Despite these promising results for real-time monitoring and feedback significant challenges remain. Although an advantage in many respects, the high sensitivity to composition is problematic in non-UHV systems. Moreover, the complex interaction between materials and the non additive nature of the light emission from combinations of materials is difficult to analyse for unknown situations. Prior to implementation a comprehensive library or catalogue of emission spectra from all matrix components and mixtures would be required. It is hoped that these measurements will for the basis of such a library.

The nature of ensemble measurements likely limits the use of such a technique to investigating fundamental processes, without a complementary microscopic measurements or simulation. In addition to further investigation of metal containing systems using the methodology presented in this chapter, absorption spectroscopy of the metal containing matrices after different ion beam doses, or low intensity laser irradiation may provide further insight into the state of the matrix.

Chapter 7

Summary and Outlook

This thesis has focused on the development of the matrix assembly method for the production of nanoclusters. The initially conceived transmission mode has been scaled up to produce a cluster flux equivalent to almost 100 nA (previously just several nA). The ability to control the size of produced nanoclusters, from a hundred atoms to several thousand atoms, by changing the metal concentration in the matrix has been demonstrated. The large size achieved confirms that the nanoclusters are not produced and sputtered from a single impact, but are ripened and grown over a number of impacts, before extraction.

Subsequently a new reflection geometry has been investigated, where nanoclusters are produced in a back-sputtering regime, although clusters could be collected from a wide arc ($\sim$80°) the optimum collection angle for peak current was found to be around 86° relative the incident beam. This mode also provides a better conversion yield of ions to nanoclusters with around 1 % of incident ions resulting in a deposited nanocluster. This is largely due to the increased usable surface area for incident ions, but may have also been improved by greater efficiency in cluster extraction due to the open nature of the surface, as compared to the channelling grid holes used in transmission mode.

This new geometry formed the basis for the development of a new cluster source.

The newly constructed source uses a two-step production method to produce nanoclusters, with a deposited peak equivalent flux of 81±5 nA (of a total 350±50 nA produced). Sustained cluster production without matrix replenishment has also been demonstrated, with an average deposited current of 40±14 nA being obtained over a 45 minute deposition.

Ion-induced luminescence, a by-product of the cluster ripening and extraction process, has been studied for both pure and doped matrices (O2, N2 and Ag) with a view to establishing a real-time means of monitoring the matrix composition during cluster deposition. In each case, the doping gases alter the observed luminescence spectra allowing qualitative identification of the matrix composition. Further to this, a sensitivity to molecular and atomic composition is observed. It is hoped that these initial results will form the basis of a real-time quantitative measurement tool for matrix composition and state, via further experimental calibration.

The development of the MACS source opens several avenues for further research, three main routes that could be investigated are; the fundamental mechanisms and processes behind cluster formation in the MACS; alloy and compound nanoclusters; or further scale up of the source.

The nature of matrix assembly itself makes it hard to probe with accuracy and without altering the system due to the microscopic, dynamic and cryogenic nature of the system. However, a combined simulation and experimental approach might be able to provide sufficient insight to identify cluster formation mechanisms. Molecular dynamic simulations using repeated high-energy atom impacts within the same region of interest with different matrix temperatures, incident atom energies and metal concentrations would help provide a dynamic and microscopic picture of cluster formation. If coupled with non-invasive probing methods such as optical absorption and fluorescence spectroscopy of the matrix during matrix formation and as a function of ion dose (for different experimental conditions), the simulation results could be verified. In this fashion, the microscopic mechanisms and formation routes

could be identified and understood in more detail.

The study of different matrix composition on cluster formation, is a particularly interesting route as, using different binding energy, heat capacity/conductivity or reactivity matrices may both provide information of the formation process and prove to be a more efficient medium for cluster formation. Initial experiments have already been conducted using a CO_2 matrix, which shows cluster size has a reduced dependence on the ion energy and metal concentration, compared to similar experiments with argon matrices.[246] This is likely due to the increased binding energy of the system. Systems such as CO_2 or H_2O would provide a significant advantage if viable due to the greatly reduced cooling power and therefore energy required to sustain the matrix. Additionally the use of different incident particles may also prove advantageous for nanocluster formation, for example cluster ions would provide a greater sputtering yield without increasing the penetration depth, bringing a greater number of local atoms into the formation process. Optically heating the matrix would also provide a more precise, controlled method of damaging/modifying the matrix.

A second consideration for the modification of matrix composition is the addition of a second cluster material to the matrix, enabling the formation of more complex and exotic nanoclusters. This could be in the form of another metal (e.g. Au, Pt, Ti) or reactive gas (e.g N_2, O_2, SO_2). Very preliminary experiments have proved that by depositing two materials into the matrix (Ag and Au) mixed alloy nanoclusters can be formed. Further investigation is required to understand the level of control possible on the global and microscopic stoichiometry. The ability to produce core-shell or segregated particles is yet to be investigated but through sequential deposition into the matrix or the use of high and low mobility constituents it might be possible to influence the formation more directly.

Alternatively to studying and developing the matrix assembly process itself, the current level of scale up in the production of size controlled nanoclusters (10

mg/h based on the source presented in chapter 3 used in reflection), opens up the possibility to work on directly developing size controlled nanocluster materials from physical methods for specific applications such as bio-sensing or catalysis at a test tube scale. Using the ultimate scale of ion sources and cryogenic coolers currently available, without improvement of the technique efficiency, the production rate can be scaled up a further three orders of magnitude to tens of grams per hour, through careful engineering.

Bibliography

[1] Masatake Haruta, Tetsuhiko Kobayashi, Hiroshi Sano, and Nobumasa Yamada. Novel gold catalysts for the oxidation of carbon monoxide at a temperature far below 0 C. *Chemistry Letters*, 16(2):405–408, 1987.

[2] M Haruta. Gold catalysts prepared by coprecipitation for low-temperature oxidation of hydrogen and of carbon monoxide. *Journal of Catalysis*, 115(2):301–309, 1989.

[3] A. G. Cullis and L. T. Canham. Visible light emission due to quantum size effects in highly porous crystalline silicon. *Nature*, 353(September):335–338, 1991.

[4] M.M. Alvarez, J.T. Khoury, T.G. Schaaff, M.N. Shafigullin, R.L. Whetten, and I. Vezmar. Optical Absorption Spectra of Nanocrystal Gold Molecules. *The Journal of Physical Chemistry B*, 101(19):3706–3712, 1997.

[5] J P Wilcoxon, J E Martin, F Parsapour, B Wiedenman, and D F Kelley. Photoluminescence from nanosize gold clusters. *The Journal of Chemical Physics*, 108(21):9137, 1998.

[6] M. Schmidt, R. Kusche, B. von Issendorff, and H. Haberland. Irregular variations in the melting point of size-selected atomic clusters. *Nature*, 393:238, 1998.

[7] W. D. Knight, Keith Clemenger, Walt A. De Heer, Winston A. Saunders, M. Y. Chou, and Marvin L. Cohen. Electronic shell structure and abundances of sodium clusters. *Physical Review Letters*, 52(24):2141–2143, 1984.

[8] I M Billas, A Châtelain, and W a de Heer. Magnetism from the atom to the bulk in iron, cobalt, and nickel clusters. *Science*, 265(5179):1682–1684, 1994.

[9] R.H Kodama. Magnetic nanoparticles. *Journal of Magnetism and Magnetic Materials*, 200:359–372, 1999.

[10] G Binnig, H Rohrer, C Gerber, and E Weibel. Surface studies by scanning tunneling microscopy. *Physical Review Letters*, 49(1):57–61, 1982.

[11] D. K. Schweizer and E. K. Eigler. Positioning single atoms with a scanning tunneling microscop, 1990.

[12] G. Binnig and C. F. Quate. Atomic Force Microscope. *Physical Review Letters*, 56(9):930–933, 1986.

[13] P E Batson, N Dellby, and O L Krivanek. Sub-ångstrom resolution using aberration corrected electron optics. *Nature*, 418(6898):617–620, 2002.

[14] Sandra Van Aert, Kees J Batenburg, Marta D Rossell, Rolf Erni, and Gustaaf Van Tendeloo. Three-dimensional atomic imaging of crystalline nanoparticles. *Nature*, 470:374–377, 2011.

[15] M. Bosman, V. J. Keast, J. L. Garcia-Munoz, A. J. D'Alfonso, S. D. Findlay, and L. J. Allen. Two-dimensional mapping of chemical information at atomic resolution. *Physical Review Letters*, 99(8):086102, 2007.

[16] Kenji Koga, Tamio Ikeshoji, and Ko Ichi Sugawara. Size- and Temperature-Dependent Structural Transitions in Gold Nanoparticles. *Physical Review Letters*, 92(11):115507, 2004.

[17] Radha Narayanan and Mostafa A. El-Sayed. Shape-dependent catalytic activity of platinum nanoparticles in colloidal solution. *Nano Letters*, 4(7):1343–1348, 2004.

[18] Trevor E. James, Stephanie L. Hemmingson, and Charles T. Campbell. Energy of Supported Metal Catalysts: From Single Atoms to Large Metal Nanoparticles. *ACS Catalysis*, 5(10):5673–5678, 2015.

[19] Jeppe V. Lauritsen, Jakob Kibsgaard, Henrik Topsøe, Stig Helveg, Bjerne S. Clausen, Erik Laegsgaard, and Flemming Besenbacher. Size-dependent structure of MoS2 nanocrystals. *Nature Nanotechnol.*, 2(1):53–58, 2007.

[20] Eva M. Fernández, José M. Soler, Ignacio L. Garzón, and Luis C. Balbás. Trends in the structure and bonding of noble metal clusters. *Physical Review B*, 70(16):165403, 2004.

[21] J P Wilcoxon and B L Abrams. Synthesis, structure and properties of metal nanoclusters. *Chem. Soc. Rev.*, 35:1162–1194, 2006.

[22] Günter Schmid and Benedetto Corain. Nanoparticulated Gold: Syntheses, Structures, Electronics, and Reactivities. *European Journal of Inorganic Chemistry*, (17):3081–3098, 2003.

[23] K. Nanda, S. Sahu, and S. Behera. Liquid-drop model for the size-dependent melting of low-dimensional systems. *Physical Review A*, 66(1):013208, 2002.

[24] Selim Alayoglu, Anand U. Nilekar, Manos Mavrikakis, and Bryan Eichhorn. RuPt coreshell nanoparticles for preferential oxidation of carbon monoxide in hydrogen. *Nature Materials*, 7(4):333–338, 2008.

[25] Marina E. Vance, Todd Kuiken, Eric P. Vejerano, Sean P. McGinnis, Michael F. Hochella, and David Rejeski Hull. Nanotechnology in the real

world: Redeveloping the nanomaterial consumer products inventory. *Beilstein Journal of Nanotechnology*, 6(1):1769–1780, 2015.

[26] Masatake Haruta. Size-and support-dependency in the catalysis of gold. *Catalysis Today*, 36(1):153–166, 1997.

[27] Geoffrey C Bond and David T Thompson. Catalysis by Gold. *Catalysis Reviews: Science and Engineering*, 41(3):319–388, 1999.

[28] E Roduner. Size matters: why nanomaterials are different. *Chemical Society Reviews*, 35(7):583–592, 2006.

[29] S Abbet, A Sanchez, U Heiz, W.D Schneider, A M Ferrari, G Pacchioni, and N Rosch. Size-effects in the acetylene cyclotrimerization on supported size-selected Pdn clusters (1<n<30). *Surface Science*, 454-456:984–989.

[30] C. Félix, C. Sieber, W. Harbich, J. Buttet, I. Rabin, W. Schulze, and G. Ertl. Fluorescence and excitation spectra of Ag_4 in an argon matrix. *Chemical Physics Letters*, 313(1-2):105–109, 1999.

[31] Ian Freestone, Nigel Meeks, Margaret Sax, and Catherine Higgitt. The Lycurgus Cup A Roman nanotechnology. *Gold Bulletin*, 40(4):270–277, 2007.

[32] M. Faraday. The Bakerian Lecture: Experimental Relations of Gold (and Other Metals) to Light. *Philosophical Transactions of the Royal Society of London*, 147(0):145–181, 1857.

[33] H .W. Kroto, J. R. Heath, S. C. O'Brien, R. F. Curl, and R. E. Smalley. C 60: buckminsterfullerene. *Nature*, 318(14):162–163, 1985.

[34] Martin F Jarrold. Nanosurface Chemistry on Size-Selected Silicon Clusters. *Science*, 252(5009):1085–1092, 1991.

[35] V. E. Bondybey and J. H. English. Laser induced fluorescence of metal clusters produced by laser vaporization: Gas phase spectrum of Pb_2. *The Journal of Chemical Physics*, 74(12):6978–6979, 1981.

[36] SJ La Placa, PA Roland, and JJ Wynne. Boron clusters (Bn, n= 252) produced by laser ablation of hexagonal boron nitride. *Chemical physics letters*, 190(3):163, 1992.

[37] L D Marks. Experimental studies of small particle structures. *Reports on Progress in Physics*, 57(6):603, 1994.

[38] Walt de Heer. The physics of simple metal clusters: experimental aspects and simple models. *Reviews of Modern Physics*, 65(3):611–676, 1993.

[39] W. Ekardt. Dynamical polarizability of small metal particles: Self-consistent spherical jellium background model. *Physical Review Letters*, 52(21):1925–1928, 1984.

[40] Manfred T Reetz, Wolfgang Helbig, Stefan A Quaiser, Ulrich Stimming, Norbert Breuer, and Roland. Vogel. Visualization of surfactants on nanostructured palladium clusters by a combination of STM and high-resolution TEM. *Science*, 267(5196):367–369, 1995.

[41] X Lai, T. P. St. Clair, M Valden, and D.W. Goodman. Scanning tunneling microscopy studies of metal clusters supported on TiO2 (110): Morphology and electronic structure. *Progress in Surface Science*, 59(1-4):25–52, 1998.

[42] C R Henry, C Chapon, C Duriez, and S Giorgio. Growth and morphology on a MgO (100) surface of palladium particles epitaxially deposited. *Surf*, 253:177–189, 1991.

[43] Emil Roduner. *Nanoscopic Materials*. The Royal Society of Chemistry, 2006.

[44] Mark B. Knickelbein. Electronic shell structure in the ionization potentials of copper clusters. *Chemical Physics Letters*, 192(1):129–134, 1992.

[45] A W Castleman and R G Keesee. Gas-phase clusters: spanning the states of matter. *Science*, 241:36–42, 1988.

[46] Patrick Weis, Rainer D. Beck, Gotz Brauchle, and Manfred M. Kappes. Properties of size and composition selected gas phase alkali fulleride clusters. *The Journal of Chemical Physics*, 100(8):5684–5695, 1994.

[47] Manfred M. Kappes. Experimental Studies of Gas-Phase Main-Group Metal Clusters. *Chemical Review*, 88:369, 1988.

[48] George Alameddin, Joanna Hunter, Douglas Cameron, and Manfred M. Kappes. Electronic and geometric structure in silver clusters. *Chemical Physics Letters*, 192(1):122–128, 1992.

[49] Mt Reetz and W Helbig. Size-selective synthesis of nanostructured transition metal clusters. *Journal of the American Chemical Society*, 116:7401–7402, 1994.

[50] Series page. In Roy L. Johnston and J.P. Wilcoxon, editors, *Metal Nanoparticles and Nanoalloys*, volume 3 of *Frontiers of Nanoscience*, pages ii –. Elsevier, 2012.

[51] Adnan Nasir. *Photoprotection in the Era of Nanotechnology*, pages 335–360. Springer International Publishing, Cham, 2016.

[52] Julio A Alonso et al. *Structure and properties of atomic nanoclusters*. World Scientific, 2005.

[53] A. W. Castleman. From elements to clusters: The periodic table revisited. *Journal of Physical Chemistry Letters*, 2(9):1062–1069, 2011.

[54] Jan Kašpar, Paolo Fornasiero, and Neal Hickey. Automotive catalytic converters: Current status and some perspectives. *Catalysis Today*, 77(4):419–449, 2003.

[55] Takuya Tsuzuki. Commercial scale production of inorganic nanoparticles. *International Journal of Nanotechnology*, 6(5/6):567–578, 2009.

[56] Costas a. Charitidis, Pantelitsa Georgiou, Malamatenia a. Koklioti, Aikaterini-Flora Trompeta, and Vasileios Markakis. Manufacturing nanomaterials: from research to industry. *Manufacturing Review*, 1(11), 2014.

[57] Copyright. In Roy L. Johnston and J.P. Wilcoxon, editors, *Metal Nanoparticles and Nanoalloys*, volume 3 of *Frontiers of Nanoscience*, pages iv –. Elsevier, 2012.

[58] Otto F Hagena. Cluster ion sources (invited). *Review of Scientific Instruments*, 63(4):2374–2379, 1992.

[59] C. Binns. Nanoclusters deposited on surfaces. *Surface Science Reports*, 44(1-2):1–49, oct 2001.

[60] H Haberland. *Clusters of atoms and molecules*. Springer series in chemical physics. Springer-Verlag Berlin, 1994.

[61] J. Pedersen, S. Bjørnholm, J. Borggreen, K. Hansen, T. P. Martin, and H. D. Rasmussen. Observation of quantum supershells in clusters of sodium atoms. *Nature*, 353(6346):733–735, 1991.

[62] Manfred M Kappes, Roland W Kunz, and Ernst Schumacher. Production of large sodium clusters (Nx<65) by seeded beam expansions. *Chemical Physics Letters*, 91(6):413–418, 1982.

[63] L Bewig, U Buck, Ch Mehlmann, and M Winter. Seeded supersonic alkali cluster beam source with refilling system. *Review of Scientific Instruments*, 63(8):3936–3938, 1992.

[64] N. D. Bhaskar, C. M. Klimcak, and R. P. Frueholz. Liquid metal ion source for cluster ions of metals and alloys: design and characteristics. *Review of Scientific Instruments*, 61(1):366, 1990.

[65] N. Davies, D.E. Weibel, P. Blenkinsopp, N. Lockyer, R. Hill, and J.C. Vickerman. Development and experimental application of a gold liquid metal ion source. *Applied Surface Science*, 203-204:223–227, jan 2003.

[66] G L R Mair. Review Liquid metal ion sources and their applications. *International Journal of Mass Spectrometry and Ion Processes*, 114(1-2):1–21, 1992.

[67] T. G. Dietz, M. a. Duncan, D. E. Powers, and R. E. Smalley. Laser production of supersonic metal cluster beams. *The Journal of Chemical Physics*, 74(11):6511–6512, 1981.

[68] E K Parks, T D Klots, B J Winter, and S J Riley. Reactions of cobalt clusters with water and ammonia: Implications for cluster structure. *The Journal of Chemical Physics*, 99(8):5831–5839, 1993.

[69] Michael a Duncan. Invited review article: laser vaporization cluster sources. *The Review of scientific instruments*, 83(4):041101, apr 2012.

[70] Naoaki Saito, Kazuyoshi Koyama, and Mitsumori Tanimoto. Cluster generation by laser ablation. *Applied Surface Science*, 169-170:380–386, 2001.

[71] Michael A Duncan. Invited Review Article: Laser vaporization cluster sources, 2012.

[72] Eric F Rexer, Mukesh P Joshi, Robert L. DeLeon, Paras N Prasad, and James F Garvey. A reactive laser ablation source for the production of thin films. *Review of Scientific Instruments*, 69(8):3028, 1998.

[73] Michael A Duncan. Spectroscopy of Metal Ion Complexes: Gas-Phase Models for Solvation. *Annu. Rev. Phys. Chem.*, 48(1):69–93, 1997.

[74] Wenyun Lu, Rongbin Huang, Junqi Ding, and Shihe Yang. Generation of fullerenes and metalcarbon clusters in a pulsed arc cluster ion source (PACIS). *The Journal of Chemical Physics*, 104(17):6577, 1996.

[75] H. R. Siekmann, Ch Luder, J. Faehrmann, H. O. Lutz, and K. H. Meiwes-Broer. The pulsed arc cluster ion source (PACIS). *Z. Phys. D -Atoms, Molecules and Clusters*, 20(1):417–420, 1991.

[76] Mikihiro Kobayashi, Shu-Man Liu, Seiichi Sato, Hiroshi Yao, and Keisaku Kimura. Optical Evaluation of Silicon Nanoparticles Prepared by Arc Discharge Method in Liquid Nitrogen. *Japanese Journal of Applied Physics*, 45(8A):6146–6152, aug 2006.

[77] N Parkansky, B Alterkop, R L Boxman, S Goldsmith, Z Barkay, and Y Lereah. Pulsed discharge production of nano- and microparticles in ethanol and their characterization. *Powder Technology*, 150(1):36–41, 2005.

[78] Sayyar A Shah and Shen Cui. Preparation of silicon nanomaterials by arc discharge. *Materials Science in Semiconductor Processing*, 40:491–500, 2015.

[79] J.M. Soler, N. Garcia, O. Echt, K. Sattler, and E. Recknagel. Microcluster growth: Transition from Successive Monomer Addition to Coagulation. *Phys Rev Lett*, 49(25):1857, 1982.

[80] Takehiko Hihara and Kenji Sumiyama. Formation and size control of a Ni cluster by plasma gas condensation. *Journal of Applied Physics*, 84(9):5270, 1998.

[81] C G Granqvist and R A Buhrman. Ultrafine metal particles. *Journal of Applied Physics*, 47(5):2200–2219, 1976.

[82] Feng Yin, Zhi Wei Wang, and Richard E Palmer. Controlled formation of mass-selected Cu-Au core-shell cluster beams. *J. Am. Chem. Soc.*, 133(27):10325–7, jul 2011.

[83] Martin J Cuddy, Kenton P Arkill, Zhi Wei Wang, Hannu-Pekka Komsa, Arkady V Krasheninnikov, and Richard E Palmer. Fabrication and atomic structure of size-selected, layered MoS2 clusters for catalysis. *Nanoscale*, 6(21):12463–9, 2014.

[84] Peter Ellis, Christopher M Brown, Peter Trenton Bishop, Jinlong Yin, Kevin Cooke, William David Terry, Jeng Liu, Feng Yin, and R E Palmer. The cluster beam route to model catalysts and beyond. *Faraday Discuss.*, 188:39–56, 2016.

[85] D Llamosa, M Ruano, L Martínez, A Mayoral, E Roman, M García-Hernández, and Y Huttel. The ultimate step towards a tailored engineering of core-shell and core-shell-shell nanoparticles. *Nanoscale*, 6(22):3–6, 2014.

[86] S. Pratontep, S. J. Carroll, C. Xirouchaki, M. Streun, and R. E. Palmer. Size-selected cluster beam source based on radio frequency magnetron plasma sputtering and gas condensation. *Review of Scientific Instruments*, 76(4):045103, 2005.

[87] C Xirouchaki and R E Palmer. Deposition of size-selected metal clusters generated by magnetron sputtering and gas condensation: a progress review. *Philosophical transactions. Series A, Mathematical, physical, and engineering sciences*, 362:117–124, 2004.

[88] Ibrahimkutty Shyjumon, Manesh Gopinadhan, Christiane A Helm, Boris M Smirnov, and Rainer Hippler. Deposition of titanium/titanium oxide clusters produced by magnetron sputtering. *Thin Solid Films*, 500(1-2):41–51, 2006.

[89] O. F. Hagena. Condensation in free jets: Comparison of rare gases and metals. *Zeitschrift fur Physik D Atoms, Molecules and Clusters*, 4(3):291–299, 1987.

[90] Simon R. Plant, Lu Cao, and Richard E. Palmer. Atomic structure control of size-selected gold nanoclusters during formation. *Journal of the American Chemical Society*, 136(21):7559–7562, 2014.

[91] R. E. Palmer, L. Cao, and F. Yin. Note: Proof of principle of a new type of cluster beam source with potential for scale-up. *Review of Scientific Instruments*, 87(4):046103, 2016.

[92] K M Mchugh, H W Sarkas, and J G Eaton. The smoke ion source : a device for the generation of cluster ions via inert gas condensation. *Zeitschrift fur Physik D Atoms, Molecules and Clusters*, 12(1):3–6, 1989.

[93] Graham J. Hutchings and Jennifer K. Edwards. Chapter 6 - application of gold nanoparticles in catalysis. In Roy L. Johnston and J.P. Wilcoxon, editors, *Metal Nanoparticles and Nanoalloys*, volume 3 of *Frontiers of Nanoscience*, pages 249 – 293. Elsevier, 2012.

[94] ML Cohen, MY Chou, W. D. Knight, and Walt A. De Heer. Physics of metal clusters. *J. Phys Chem.*, 91(12):3141–3149, 1987.

[95] I Katakuse, T Ichihara, Y Fujita, T Matsuo, T Sakurai, and H Matsuda. Mass distributions of copper, silver and gold clusters and electronic shell structure. *International Journal of Mass Spectrometry and Ion Processes*, 67(2):229–236, 1985.

[96] W D Knight, Walt A. De Heer, Winston A Saunders, Keith Clemenger, M Y Chou, and Marvin L Cohen. Alkali metal clusters and the jellium model. *Chemical Physics Letters*, 134(1):1–5, 1987.

[97] T. P Martin, T. Bergmann, H. Goehlich, and T. Lange. Shell structure of clusters. *The Journal of Physical Chemistry*, 95(17):6421, 1991.

[98] T. P. Martin. Shells of atoms. *Physics Report*, 273(4):199–241, 1996.

[99] T. P. Martin. From atoms to solids. *Solid State Ionics*, 131(1):3–12, 2000.

[100] T. P. Martin, T. Bergmann, H. Gohlich, and T. Lange. Evidence for icosahedral shell structure in large magnesium clusters. *Chemical Physics Letters*, 176(3-4):343–347, 1991.

[101] T. P. Martin, T. Bergmann, H. Gohlich, and T. Lange. Observation of electronic shells and shells of atoms in large Na clusters. *Chemical Physics Letters*, 172(3-4):209–213, 1990.

[102] T. P. Martin, U. Näher, H. Schaber, and U. Zimmermann. Evidence for a size-dependent melting of sodium clusters. *J. Chem. Phys.*, 100(1994):2322, 1994.

[103] R E Palmer, S Pratontep, and H-G Boyen. Nanostructured surfaces from size-selected clusters. *Nature Materials*, 2(7):443–8, 2003.

[104] U Heiz, A Vayloyan, and E Schumacher. A new cluster source for the generation of binary metal clusters. *Review of Scientific Instruments*, 68(1997):3718, 1997.

[105] Dawn M. Wells, Giulia Rossi, Riccardo Ferrando, and Richard E. Palmer. Metastability of the atomic structures of size-selected gold nanoparticles. *Nanoscale*, 7(15):6498–6503, 2015.

[106] Eric C. Tyo and Stefan Vajda. Catalysis by clusters with precise numbers of atoms. *Nature Nanotechnology*, 10(7):577–588, 2015.

[107] P. Piseri, a. Podesta, E. Barborini, and P. Milani. Production and characterization of highly intense and collimated cluster beams by inertial focusing in supersonic expansions. *Review of Scientific Instruments*, 72(5):2261, 2001.

[108] P Milani, A Podesta, P Piseri, E Barborini, C Lenardi, and C Castelnovo. Cluster assembling of nanostructured carbon films. *Diamond and Related Materials*, 10(2):240–247, 2001.

[109] E Barborini, P Piseri, and P Milani. A pulsed microplasma source of high intensity supersonic carbon cluster beams. *Journal of Physics D: Applied Physics*, 32(21):L105–L109, 1999.

[110] L Ravagnan, F Siviero, C Lenardi, P Piseri, E Barborini, P Milani, C. S. Casari, A. Li Bassi, and C. E. Bottani. Cluster-Beam Deposition and in situ Characterization of Carbyne-Rich Carbon Films. *Physical Review Letters*, 89(28):285506, 2002.

[111] H. Vahedi Tafreshi, G. Benedek, P. Piseri, S. Vinati, E. Barborini, and P. Milani. A Simple Nozzle Configuration for the Production of Low Divergence Supersonic Cluster Beam by Aerodynamic Focusing. *Aerosol Science and Technology*, 36(5):593–606, may 2002.

[112] E Barborini, P Piseri, A. Podesta', and P Milani. Cluster beam microfabrication of patterns of three-dimensional nanostructured objects. *Applied Physics Letters*, 77(7):1059, 2000.

[113] Cristian Ghisleri, Mirko Siano, Luca Ravagnan, Marco Alberto Carlo Potenza, and Paolo Milani. Nanocomposite-based stretchable optics. *Laser and Photonics Reviews*, 7(6):1020–1026, 2013.

[114] F Borghi, C Melis, C Ghisleri, A Podestà, L Ravagnan, L Colombo, and P Milani. Stretchable nanocomposite electrodes with tunable mechanical properties by supersonic cluster beam implantation in elastomers. *Applied Physics Letters*, 106(12):4–9, 2015.

[115] Francesca Soavi, Luca Giacomo Bettini, Paolo Piseri, Paolo Milani, Carlo Santoro, Plamen Atanassov, and Catia Arbizzani. Miniaturized supercapacitors: key materials and structures towards autonomous and sustainable devices and systems. *Journal of Power Sources*, 326:717–725, 2016.

[116] E Barborini, I N Kholmanov, A M Conti, P Piseri, S Vinati, P Milani, and C Ducati. Supersonic cluster beam deposition of nanostructured titania. In *European Physical Journal D*, volume 24, pages 277–282, 2003.

[117] Alessandro Podestà, Francesca Borghi, Marco Indrieri, Simone Bovio, Claudio Piazzoni, and Paolo Milani. Nanomanufacturing of titania interfaces with controlled structural and functional properties by supersonic cluster beam deposition. *Journal of Applied Physics*, 118(23), 2015.

[118] Mattia Marelli, Giorgio Divitini, Cristian Collini, Luca Ravagnan, Gabriele Corbelli, Cristian Ghisleri, Antonella Gianfelice, Cristina Lenardi, Paolo Milani, and Leandro Lorenzelli. Flexible and biocompatible microelectrode arrays fabricated by supersonic cluster beam deposition on SU-8. *Journal of Micromechanics and Microengineering*, 21(4):045013, apr 2011.

[119] David Christopher Engemann, Stefanie Roese, and Heinz Hövel. Preformed 2 nm Ag Clusters Deposited into Ionic Liquids: Stabilization by CationCluster Interaction. *The Journal of Physical Chemistry C*, 120(11):6239–6245, 2016.

[120] L. Martinez, M. Diaz, E. Roman, M Ruano, P. D. Llamosa, and Y Huttel. Generation of nanoparticles with adjustable size and controlled stoichiometry: Recent advances. *Langmuir*, 28(30):11241–11249, 2012.

[121] Manuel Ruano, Lidia Martínez, and Yves Huttel. Investigation of the Working Parameters of a Single Magnetron of a Multiple Ion Cluster Source : Determination of the Relative Nanoparticles. *Dataset Papers in Science*, 2013:597023, 2013.

[122] Masatake Haruta. Gold as a novel catalyst in the 21st century: Preparation, working mechanism and applications. *Gold Bulletin*, 37(1-2):27–36, mar 2004.

[123] M. Harb, F. Rabilloud, D. Simon, a. Rydlo, S. Lecoultre, F. Conus, V. Rodrigues, and C. Félix. Optical absorption of small silver clusters: Agn, (n=4-22). *Journal of Chemical Physics*, 129(2008):0–9, 2008.

[124] A Sanchez, S Abbet, U. Heiz, W.-D. Schneider, Hakkinen. H, R. N. Barnett, and Uzi Landman. When gold is not noble: Nanoscale gold catalysts. *J. Phys. Chem A*, 103:9573–9578, 1999.

[125] Libing Zhang and Erkang Wang. Metal nanoclusters: New fluorescent probes for sensors and bioimaging. *Nano Today*, 9(1):132–157, 2014.

[126] Yi Yang, Lu Zhang, Jiali Cai, Xiao Li, Dengfeng Cheng, Huilan Su, Jianping Zhang, Shiyuan Liu, Hongcheng Shi, Yingjian Zhang, and Chunfu Zhang. Tumor Angiogenesis Targeted Radiosensitization Therapy Using Gold Nanoprobes Guided by MRI/SPECT Imaging. *ACS Applied Materials and Interfaces*, 8(3):1718–1732, 2016.

[127] Masatake Haruta. When gold is not noble: Catalysis by nanoparticles. *Chemical Record*, 3(2):75–87, 2003.

[128] A. Stephen K Hashmi and Graham J. Hutchings. Gold Catalysis. *Angew. Chem. Int. Ed.*, 45(47):7896–7936, 2006.

[129] Beatriz Roldan Cuenya. Synthesis and catalytic properties of metal nanoparticles: Size, shape, support, composition, and oxidation state effects, 2010.

[130] Patricia Hernandez-Fernandez, Federico Masini, David N. McCarthy, Christian E. Strebel, Daniel Friebel, Davide Deiana, Paolo Malacrida, Anders Nierhoff, Anders Bodin, Anna M. Wise, Jane H. Nielsen, Thomas W. Hansen, Anders Nilsson, Ifan E. L. Stephens, and Ib Chorkendorff. Mass-selected nanoparticles of PtxY as model catalysts for oxygen electroreduction. *Nature Chemistry*, 6(8):732–738, 2014.

[131] Thomas F Jaramillo, Kristina P Jørgensen, Jacob Bonde, Jane H Nielsen, Sebastian Horch, and Ib Chorkendorff. Identification of active edge sites for electrochemical H2 evolution from MoS2 nanocatalysts. *Science*, 317(5834):100–102, 2007.

[132] N. Lopez, T. V W Janssens, B. S. Clausen, Y. Xu, M. Mavrikakis, T. Bligaard, and J. K. Nørskov. On the origin of the catalytic activity of gold nanoparticles for low-temperature CO oxidation. *Journal of Catalysis*, 223(1):232–235, 2004.

[133] Andrew a Herzing, C. J. Kiely, A. F. Carley, P. Landon, and G. J. Hutchings. Identification of Active Gold Nanoclusters on Iron Oxide Supports for CO Oxidation. *Science*, 321(5894):1331–1335, 2008.

[134] U. Heiz, A. Sanchez, S. Abbet, and W. D. Schneider. Tuning the oxidation of carbon monoxide using nanoassembled model catalysts. *Chemical Physics*, 262(1):189–200, 2000.

[135] Markus Nesselberger, Melanie Roefzaad, R. Fayçal Hamou, P. Ulrich Biedermann, Florian F. Schweinberger, Sebastian Kunz, Katrin Schloegl, Gustav K. H. Wiberg, Sean Ashton, Ueli Heiz, Karl J. J. Mayrhofer, and Matthias Arenz. The effect of particle proximity on the oxygen reduction rate of size-selected platinum clusters. *Nature. Mater.*, 12(10):919–924, 2013.

[136] Adrian Thomas, Qian He, and Jennifer K. Edwards. Preparation of ultra low loaded Au catalysts for oxidation reactions. *Faraday Discussions*, 152:381, 2011.

[137] S. Gilb, M. Arenz, and U. Heiz. The polymerization of acetylene on supported metal clusters. *Low Temperature Physics*, 32(11):1441–1448, 2006.

[138] Feng Yin, Chrisa Xirouchaki, Quanmin Guo, and Richard E. Palmer. High-temperature stability of size-selected gold nanoclusters pinned on graphite. *Advanced Materials*, 17(6):731–734, 2005.

[139] Kristina Wettergren, Florian F. Schweinberger, Davide Deiana, Claron J. Ridge, Andrew S. Crampton, Marian D. Rötzer, Thomas W. Hansen, Vladimir P. Zhdanov, Ueli Heiz, and Christoph Langhammer. High sintering resistance of size-selected platinum cluster catalysts by suppressed Ostwald ripening. *Nano Letters*, 14(10):5803–5809, 2014.

[140] Kuo Juei Hu, Simon R. Plant, Peter R. Ellis, Christopher M. Brown, Peter T. Bishop, and Richard E. Palmer. Atomic Resolution Observation of a Size-Dependent Change in the Ripening Modes of Mass-Selected Au Nanoclusters Involved in CO Oxidation. *Journal of the American Chemical Society*, 137(48):15161–15168, 2015.

[141] Christine E. Probst, Pavel Zrazhevskiy, Vaishali Bagalkot, and Xiaohu Gao. Quantum dots as a platform for nanoparticle drug delivery vehicle design. *Advanced Drug Delivery Reviews*, 65(5):703–718, 2013.

[142] Pavel Zrazhevskiy, Mark Sena, and Xiaohu Gao. Designing multifunctional quantum dots for bioimaging, detection, and drug delivery. *Chemical Society reviews*, 39(11):4326–54, 2010.

[143] Hélder A Santos and Jouni Hirvonen. Nanostructured porous silicon materials: potential candidates for improving drug delivery. *Nanomedicine*, 7(9):1281–4, 2012.

[144] Jingjing Li, Jun Jie Zhu, and Kai Xu. Fluorescent metal nanoclusters: From synthesis to applications. *Trends in Analytical Chemistry*, 58:90–98, 2014.

[145] Kenton P. Arkill, Judith M. Mantell, Simon R. Plant, Paul Verkade, and Richard E. Palmer. Using size-selected gold clusters on graphene oxide films to aid cryo-transmission electron tomography alignment. *Scientific Reports*, 5:9234, 2015.

[146] Mohammad Babaei and Maryam Ganjalikhani. The potential effectiveness of nanoparticles as radio sensitizers for radiotherapy. *BioImpacts*, 4(1):15–20, 2014.

[147] Lev Dykman and Nikolai Khlebtsov. Gold nanoparticles in biomedical applications: recent advances and perspectives. *Chemical Society Reviews*, 41(6):2256–2282, 2012.

[148] Nathaniel L Rosi and Chad a Mirkin. Nanostructures in biodiagnostics. *Chemical Reviews*, 105(4):1547–62, apr 2005.

[149] Ivan H. El-Sayed, Xiaohua Huang, and Mostafa A. El-Sayed. Surface plasmon resonance scattering and absorption of anti-EGFR antibody conjugated gold nanoparticles in cancer diagnostics: Applications in oral cancer. *Nano Letters*, 5(5):829–834, 2005.

[150] Ju Huangxian Zhang, Xueji and Joseph Wang. *Electrochemical Sensors, Biosensors and their Biomedical Applications.* Burlington, US: Academic Press, 2011.

[151] Anja Watzke, Maja Kohn, Marta Gutierrez-Rodriguez, Ron Wacker, Hendrik Schroder, Rolf Breinbauer, Jurgen Kuhlmann, Kirill Alexandrov, Christof M. Niemeyer, Roger S. Goody, and Herbert Waldmann. Site-selective protein immobilization by Staudinger ligation. *Angew. Chem. Int. Ed.. Chem. Int. Ed.*, 45(9):1408–1412, 2006.

[152] Ramakrishnan Ganesan, Karl Kratz, and Andreas Lendlein. Multicomponent protein patterning of material surfaces. *Journal of Materials Chemistry*, 20(35):7322, 2010.

[153] Yang Liu, Deng Zhang, Evangelyn C. Alocilja, and Shantanu Chakrabartty. Biomolecules detection using a silver-enhanced gold nanoparticle-based biochip. *Nanoscale Research Letters*, 5(3):533–538, 2010.

[154] Yen Ting Tung, Cheng Chung Chang, Yi Ling Lin, Shie Liang Hsieh, and Gou Jen Wang. Development of double-generation gold nanoparticle chip-based dengue virus detection system combining fluorescence turn-on probes. *Biosensors and Bioelectronics*, 77:90–98, 2016.

[155] Jeffrey N Anker, W Paige Hall, Olga Lyandres, Nilam C Shah, Jing Zhao, and Richard P Van Duyne. Biosensing with plasmonic nanosensors. *Nature Materials*, 7(6):442–453, 2008.

[156] Amir Syahir, Kenji Usui, Kin-ya Tomizaki, Kotaro Kajikawa, and Hisakazu Mihara. Label and Label-Free Detection Techniques for Protein Microarrays. *Microarrays*, 4(2):228–244, 2015.

[157] Hui Du, Matthew D. Disney, Benjamin L. Miller, and Todd D. Krauss. Hybridization-based unquenching of DNA hairpins on Au surfaces: Prototypical "molecular beacon" biosensors. *Journal of the American Chemical Society*, 125(14):4012–4013, 2003.

[158] Dai, Zhou, Khan, Huck, and Kaminski. Direct Visualization of Reversible Switching of Micropatterned Polyelectrolyte Brushes on Gold Surfaces Using Laser Scanning Confocal Microscopy. *Langmuir*, 24(22):13182–13185, 2008.

[159] Yaron Ram, Tal Yoetz-Kopelman, Yael Dror, Amihay Freeman, and Yosi Shacham-Diamand. Impact of Molecular Surface Charge on Biosensing by Electrochemical Impedance Spectroscopy. *Electrochimica Acta*, 200:161–167, 2016.

[160] Soo Youn Lee, Chi Young Ahn, Jiho Lee, Jin Hyung Lee, and Jeong Ho Chang. Rapid and selective separation for mixed proteins with thiol functionalized magnetic nanoparticles. *Nanoscale Research Letters*, 7(1):279, 2012.

[161] J. A. Collins, C. Xirouchaki, R. E. Palmer, J. K. Heath, and C. H. Jones. Clusters for biology: Immobilization of proteins by size-selected metal clusters. *Applied Surface Science*, 226(1-3 SPEC. ISS.):197–208, 2004.

[162] Umberto Prisco, Carl Leung, Chrisa Xirouchaki, Celine H Jones, John K Heath, and Richard E Palmer. Residue-specific immobilization of protein molecules by size-selected clusters. *Journal of the Royal Society, Interface*, 2(3):169–75, 2005.

[163] P Rodrigeuz-Zamora, J Barreto, F Yin, and E Palmer, R. Non-covalent Immobilization of Desmoplakin Plakin Domain Molecules by Size-Selected Clusters for AFM Imaging. *BioNanoSci*, 4:97–103, 2014.

[164] Wolfgang Fritzsche and T Andrew Taton. Metal nanoparticles as labels for heterogeneous, chip-based DNA detection. *Nanotechnology*, 14(12):R63–R73, 2003.

[165] Thibault Tabarin, Alexander Kulesza, Rodolphe Antoine, Roland Mitric, Michel Broyer, Philippe Dugourd, and Vlasta Bonacic-Koutecky. Absorption

enhancement and conformational control of peptides by small silver clusters. *Physical Review Letters*, 101(21):213001, 2008.

[166] Isabelle Compagnon, Thibault Tabarin, Rodolphe Antoine, Michel Broyer, Philippe Dugourd, Roland Mitric, Jens Petersen, and Vlasta Bonacic-Koutecky. Spectroscopy of isolated, mass-selected tryptophan-Ag3 complexes: A model for photoabsorption enhancement in nanoparticle-biomolecule hybrid systems. *Journal of Chemical Physics*, 125(16):1–6, 2006.

[167] Vlasta Bonačić-Koutecký, Alexander Kulesza, Lars Gell, Roland Mitrić, Rodolphe Antoine, Franck Bertorelle, Ramzi Hamouda, Driss Rayane, Michel Broyer, Thibault Tabarin, and Philippe Dugourd. Silver clusterbiomolecule hybrids: from basics towards sensors. *Physical Chemistry Chemical Physics*, 14(26):9282, 2012.

[168] Quantifoil Micro Tools. http://www.quantifoil.com/index.php?name=home. viewed 17/09/2016.

[169] T. Irawan, D. Boecker, F. Ghaleh, C. Yin, B. von Issendorff, and H. Hövel. Metal clusters on rare gas layers growth and spectrscopy. *Appl. Phys. A*, 86:81–86, 2006.

[170] I Rabin, W Schulze, G Ertl, I Rabin, W Schulze, and G Ertl. Light emission during the agglomeration of silver clusters in noble gas matrices Light emission during the agglomeration of silver clusters in noble gas matrices. *Journal of Chemical Physics*, 108(12):5137–5142, 1998.

[171] Donald E. David, Thomas F. Magnera, Rujiang Tian, Dusan Stulik, and Josef Michl. Cluster ions from keV-energy ion and atom bombardment of frozen gases. *Nuclear Instruments and Methods in Physics Research Section B: Beam Interactions with Materials and Atoms*, 14(4-6):378–391, apr 1986.

[172] Herbert M. Urbassek and K. Thomas Waldeer. Spikes in condensed rare gases induced by keV-atom bombardment. *Physical Review Letters*, 67(1):105–108, 1991.

[173] V Balaji, DE David, T.F Magnera, J Michl, and H M Urbassek. Sputtering Yields Of Condensed Rare Gases. *Nuclear Instrument and Methods in Physics Research*, 46:435–440, 1990.

[174] CT Reimann, WL Brown, and RE Johnson. electronically stimulated sputtering and luminescence from solid argon. *Physical Review B*, 37(4), 1988.

[175] W. L. Brown and R E Johnson. Sputtering of ices: a review. *Nuclear Inst. and Methods in Physics Research, B*, 13(1-3):295–303, 1986.

[176] Lu Cao. *Deposition of Size-Selected Nanoclusters*. PhD thesis, University of Birmingham, 2015.

[177] Julius Jellinek Sudha SriniVas, Umesh A. Salian. *Metal-Ligand Interactions in Physics and Biology*. kluwer Academic Publishers.

[178] Lanquing Xu. Unpublished Molecular Dynamics Simulations. 2014.

[179] Yuh Lang Lee and Jer Ru Maa. Nucleation and growth of condensate clusters on solid surfaces. *Journal of Materials Science*, 26(22):6068–6072, 1991.

[180] Khanna S. N. Castleman, A. W. *Quantum phenomena in clusters and nanostructures*. Springer series in cluster physics. New York ; London : Springer, 2003.

[181] B. von Issendorff and R. E. Palmer. A new high transmission infinite range mass selector for cluster and nanoparticle beams. *Review of Scientific Instruments*, 70(12):4497, 1999.

[182] Clipartkid. http://www.clipartkid.com/desktop-computer-clip-art-at-clker-com-vector-clip-art-online-7ezktd-clipart/. confirmed 20/09/2016.

[183] LK Technologies. Hreels operation manual.

[184] Donald E David and Josef Michl. Sputtering of Condensed Gases by Nuclear Stopping: Chemical Aspects. *Prog. Solid St. Chem.*, 19(4):283–328, 1989.

[185] Peter Sigmund. Elements of Sputtering Theory. *PSP Review Volume*, 2011.

[186] R. Behrisch and W. Eckstein. *Sputtering by Particle Bombardment: Experiments and Computer Calculations from Threshold to MeV Energies*. Topics in Applied Physics. Springer Berlin Heidelberg, 2007.

[187] J Soderlund, L. B Kiss, G. A. Niklasson, and C. G. Granqvist. Lognormal Size Distributions in Particle Growth Processes Without Coagulation. *Phys. Rev. Lett.*, 80(11):2386–2388, 1998.

[188] W. Harbich, S. Fedrigo, J. Buttet, and D. M. Lindsay. Optical spectroscopy on size selected gold clusters deposited in rare gas matrices. *Z. Phys. D -Atoms, Molecules and Clusters*, 19(4):157–159, 1991.

[189] C Félix, C Sieber, W Harbich, and J Buttet. Ag_8 fluorescence in argon. *Physical Review Letters*, 86(14):2992–2995, 2001.

[190] Gergely Lautner, Zsófia Balogh, Viola Bardóczy, Tamás Mészáros, and Róbert E Gyurcsányi. Aptamer-based biochips for label-free detection of plant virus coat proteins by SPR imaging. *The Analyst*, 135:918–926, 2010.

[191] Tatsuro Endo, Kagan Kerman, Naoki Nagatani, and Eiichi Tamiya. Excitation of localized surface plasmon resonance using a coreshell structured nanoparticle layer substrate and its application for label-free detection of biomolecular interactions. *Journal of Physics: Condensed Matter*, 19(21):215201, may 2007.

[192] Ann E. Grow, Laurie L. Wood, Johanna L. Claycomb, and Peggy A. Thompson. New biochip technology for label-free detection of pathogens and their toxins. *Journal of Microbiological Methods*, 53(2):221–233, 2003.

[193] Inc. Agilent Technologies. *Measuring baseline corrected spectra on a Cary 50 Dual Beam Spectrophotometers*. 2011.

[194] Paul Mulvaney. Surface Plasmon Spectroscopy of Nanosized Metal Particles. *Langmuir*, 12(3):788–800, 1996.

[195] K. Lance Kelly, Eduardo Coronado, Lin Lin Zhao, and George C. Schatz. The Optical Properties of Metal Nanoparticles: The Influence of Size, Shape, and Dielectric Environment. *The Journal of Physical Chemistry B*, 107(3):668–677, 2003.

[196] Satyabrata Mohapatra. Tunable surface plasmon resonance of silver nanoclusters in ion exchanged soda lime glass. *Journal of Alloys and Compounds*, 598:11–15, 2014.

[197] Ji-Fei Wang, Hong-Jian Li, Zi-You Zhou, Xue-Yong Li, Ju Liu, and Hai-Yan Yang. Tunable surface-plasmon-resonance wavelength of silver island films. *Chin. Phys. B*, 19(11):117310, 2010.

[198] Klaus B. Mogensen and Katrin Kneipp. Size-dependent shifts of plasmon resonance in silver nanoparticle films using controlled dissolution: Monitoring the onset of surface screening effects. *Journal of Physical Chemistry C*, 118(48):28075–28083, 2014.

[199] S. Link and M. a. El-Sayed. Size and Temperature Dependence of the Plasmon Absorption of Colloidal Gold Nanoparticles. *The Journal of Physical Chemistry B*, 103(21):4212, 1999.

[200] R Asahi, T Morikawa, T Ohwaki, K Aoki, and Y Taga. Visible-light photocatalysis in nitrogen doped titanium oxides. *Science*, 293(5528):269–271, 2001.

[201] Jie Zheng, Philip R Nicovich, and Robert M Dickson. Highly fluorescent noble-metal quantum dots. *Annual review of physical chemistry*, 58:409–431, 2007.

[202] Mathias Schubert. Another century of ellipsometry. *Ann. Phys. (Leipzig)*, 15(7-8):480–497, 2006.

[203] L. Vegard. The Auroral Spectrum and the Upper Atmosphere. *Nature*, 113:716 – 717, 1924.

[204] Zohar Ophir. Photoemission from doped solid rare gases. *The Journal of Chemical Physics*, 62(2):650, 1975.

[205] J. C. McLennan and G. M. Shrum. On the luminescence of nitrogen, Argon, and Other condensed Gases at Very Low Temperatures. *Proc. R. soc. Lond. A*, 106:138–149, 1924.

[206] E. Morikawa, R. Reininger, P. Gurtler, V. Saile, and P. Laporte. Argon, krypton, and xenon excimer luminescence: From the dilute gas to the condensed phase. *The Journal of Chemical Physics*, 91(3):1469, 1989.

[207] K Thomas Waldeer and H M Urbassek. keV -Atom Bombardment of condensed Rare Gases: Molecular Dynamics Simulation. *Nuclear Instruments and Methods in Physics Research Section B*, 73(1):14–28, 1993.

[208] S. Fedrigo, W. Harbich, and J. Buttet. Collective dipole oscillations in small silver clusters embedded in rare-gas matrices. *Physical Review B*, 47(16):10706–10715, 1993.

[209] L Konig, I Rabin, W Schulze, and G Ertl. Chemiluminescence in the Agglomeration of Metal Clusters. *Science*, 274:1353–1354, 1996.

[210] P. Klaeboe and C. J. Nielsen. Recent Advances in Infrared Matrix-Isolation Spectroscopy - Invited Lecture. *Analyst*, 117(3):335–341, 1992.

[211] Vladimir E. Bondybey, Alice M. Smith, and Jürgen Agreiter. New Developments in Matrix Isolation Spectroscopy. *Chemical reviews*, 96(6):2113–2134, 1996.

[212] A. J. Barnes. Matrix isolation vibrational spectroscopy as a tool for studying conformational isomerism. *Journal of Molecular Structure*, 113(1):161–174, 1984.

[213] Venable. J. A. Klein, M. L. *Rare Gas Solids*. Academic Press (London) ltd., 1976.

[214] Herbert M Urbassek. Molecular-dynamics simulation of sputtering. *Nucl. Intr. and Meth. in Phys. Res. B*, 122:427–441, 1997.

[215] RE Johnson and WL Brown. Electronic Mechanisms for sputtering of condensed-gas solids by energetic ions. *Nuclear Instruments and Methods*, 198:103–118, 1982.

[216] W. L. Brown, C.T. Reimann, and E. R. Johnson. Energy transfer in solid argon during ion bombardment. *Nucl. Intr. and Meth. in Phys. Res. B*, 19(201):9–15, 1987.

[217] CT Reimann, WL Brown, and RE Johnson. electronically stimulated sputtering and luminescence from solid argon. *Physical Review B*, 37(4), 1988.

[218] N Schwentner. *Electronic Excitations in Condensed Rare Gases*. Springer Tracts In Modern Physics, 1985.

[219] Karsten Bromann, Christian Felix, Harald Brune, Wolfgang Harbich, Rene Monot, Jean Buttet, and Klaus Kern. Controlled Deposition of Size-Selected Silver Nanoclusters. *Science*, 274(November):956–958, 1996.

[220] Wolfgang Harbich, Christoph Sieber, Karl-Heinz Meiwes-Broer, and Christian Félix. Electronic excitations induced by the impact of coinage metal ions

and clusters on a rare gas matrix: Neutralization and luminescence. *Physical Review B*, 76(10):1–10, sep 2007.

[221] S. Fedrigo, W. Harbich, and J. Buttet. Optical response of Ag2, Ag3, Au2, and Au3 in argon matrices. *The Journal of Chemical Physics*, 99(8):5712, 1993.

[222] D. H. Waldeck, A. P. Alivisatos, and C. B. Harris. Nonradiative damping of molecular electronic excited states by metal surfaces. *Surface Science*, 158:103–125, 1985.

[223] R. R. Chance. Lifetime of an emitting molecule near a partially reflecting surface. *The Journal of Chemical Physics*, 60(7):2744, 1974.

[224] Mario Jakas and Eduardo Bringa. Thermal-spike theory of sputtering: The influence of elastic waves in a one-dimensional cylindrical spike. *Physical Review B*, 62(2):824–830, 2000.

[225] L Gabła, W Soszka, J Budzioch, and S Kwaśny. Emission of excited atoms from solid argon under ion bombardment. *Physics Letters A*, 187(April):259–263, 1994.

[226] A. B. Treshchalov and A. A. Lissovski. VUV - VIS spectroscopic diagnostics of a pulsed high-pressure discharge in argon. *Journal of Physics D: Applied Physics*, 42(24):245203, dec 2009.

[227] N. Merlemis, E. Reppa, and T. Efthimiopoulos. Narrowband emission of argon dimers in a dc discharge with supersonic expansion. *Applied Physics B*, 91(1):183–188, feb 2008.

[228] Alexander A Lissovski and Alexey B Treshchalov. Kinetics of VUV- VIS spontaneous emission of high-current pulsed volume discharge in argon. *Proc. of SPIE*, 6263(62630H):1–10, 2006.

[229] Aleksandr Lissovski. *Spectroscopic diagnostics of pulsed discharge in high pressure rare gas mixtures*. PhD thesis, 2004.

[230] D. Grosjean, R. Vidal, R. Baragiola, and W. Brown. Absolute luminescence efficiency of ion-bombarded solid argon. *Physical Review B*, 56(11):6975–6981, sep 1997.

[231] C. T Reinmann, W.L. Brown, and R.E. Johnson. Electronically stimulated sputtering and luminescence from solid argon. *Phys Rev B*, 37(4):1455–1473, 1988.

[232] Kh. A. Amirov, O. V. Korshunov, and V. F. Chinnov. Continua of uv radiation and kinetics of slightly ionized noble gases. *J.Phys B: At. Mol. Opt. Phys*, 27:1753–1771, 1994.

[233] C. Cachoncinlle, J. M. Pouvesle, F. Davanloo, J. J. Coogan, and C. B. Collins. Third continuum of argon in high pressure plasmas excited by dielectric controlled discharge. *Optics Communications*, 79(1-2):41–44, 1990.

[234] HJ Jodl and R Bruno. Luminescence Spectra of nitrogen in Solid Argon I. Experiment. *Phys. Stat. Sol. (b)*, 67:191–197, 1975.

[235] M. Famá, M.J. Loeffler, U. Raut, and R.a. Baragiola. Radiation-induced amorphization of crystalline ice. *Icarus*, 207(1):314–319, may 2010.

[236] a.J.H. McGaughey and M. Kaviany. Thermal conductivity decomposition and analysis using molecular dynamics simulations. *International Journal of Heat and Mass Transfer*, 47(8-9):1799–1816, apr 2004.

[237] Lars-enk Berg, Peter Lindblom, Torbjorn Olsson, Kimmo Aho, Ulf Haellsten, and Olof Solin. Excitation of oxygen and nitrogen in solid krypton and xenon using ion beam irradiation. *J. Phys. B: At. Mol. Opt. Phys*, 27:5241–5250, 1994.

[238] R Scullman, S Wallin, F Laubersheimer, and O Rehm. Luminescence from matrices of nitrogen and argon excited by α-particles. *Physica Scripta*, 52(2):172–177, 1995.

[239] R. Friedl and U. Fantz. Spectral intensity of the N 2 emission in argon low-pressure arc discharges for lighting purposes. *New Journal of Physics*, 14, 2012.

[240] a.G. Belov, I.Ya. Fugol, E.M. Yurtaeva, and O.V. Bazhan. Luminescence of oxygen-rare gas exciplex compounds in rare gas matrices. *Journal of Luminescence*, 91(1-2):107–120, sep 2000.

[241] M. Peyron and H. P. Broida. Spectra Emitted from Solid Nitrogen Condensed at Very Low Temperatures from a Gas Discharge. *The Journal of Chemical Physics*, 30(1):139, 1959.

[242] Christoph Sieber, Wolfgang Harbich, Karl-Heinz Meiwes-Broer, and Christian Félix. Collision-induced luminescence from the impact of ions and cluster ions on solid rare gases. *Chemical Physics Letters*, 433(1-3):32–36, dec 2006.

[243] R. R. Chance, A. Prock, and R. Silbey. Lifetime of an emitting molecule near a partially reflecting surface. *The Journal of Chemical Physics*, 60(7):2744, 1974.

[244] Tao Huang, Xiao-hong Nancy Xu, and See Tao Huang. Synthesis and characterization of tunable rainbow colored colloidal silver nanoparticles using single-nanoparticle plasmonic microscopy and spectroscopy. *Journal of Materials Chemistry*, 20(44):9867–9876, 2010.

[245] Kuang-Che Lee, Su-Jien Lin, Chih-Hong Lin, Chih-Song Tsai, and Yu-Jen Lu. Size effect of Ag nanoparticles on surface plasmon resonance. *Surface and Coatings Technology*, 202(22-23):5339–5342, 2008.

[246] V T A Oiko, T Mathieu, L Cao, J Liu, and R E Palmer. Note : Production of silver nanoclusters using a Matrix-Assembly Cluster Source with a solid CO2 matrix. *J. c*, 145:166101, 2017.

[247] Z W Wang, O Toikkanen, F Yin, Z Y Li, B M Quinn, and R E Palmer. Counting the atoms in supported, monolayer-protected gold clusters. *Journal of the American Chemical Society*, 132(9):2854–5, mar 2010.

[248] A Bruma and Z Y Li. Three-dimensional structure of Au nanoparticles supported on amorphous silica and carbon substrates. *Journal of Physics: Conference Series*, 371:012067, 2012.

[249] David B. Williams and C. Barry Carter. *Transmission Electron Microscopy*. Springer US, 2 edition, 2009.

[250] Z. W. Wang and R. E. Palmer. Direct atomic imaging and dynamical fluctuations of the tetrahedral Au20 cluster. *Nanoscale*, 4(16):4947, 2012.

[251] Z W Wang, Z Y Li, S J Park, A Abdela, D Tang, and R E Palmer. Quantitative Z-contrast imaging in the scanning transmission electron microscope with size-selected clusters. *Phys Rev B*, 84:073408, 2011.

[252] Z W Wang and Richard E. Palmer. Intensity calibration and atomic imaging of size-selected Au and Pd clusters in aberration-corrected HAADF-STEM. *Journal of Physics: Conference Series*, 371:012010, 2012.

[253] N. Young, Z. Li, Y. Chen, S. Palomba, M. Di Vece, and R. Palmer. Weighing Supported Nanoparticles: Size-Selected Clusters as Mass Standards in Nanometrology. *Physical Review Letters*, 101(24):246103, dec 2008.

Appendix A

Calculation of Matrix Thickness and Loading

The following section gives the method of calculation used for matrix thickness and loading. The based on ideal gas law the number of gas atoms impinging on a surface can be determined by the pressure of the gas. The impingement rate can be written as;

$$\Gamma = \frac{P}{(2\pi mkT)^{1/2}}$$

where P is the gas pressure m the gas particle mass, k the Boltzmann constant and T the temperature. Therefore an Ar pressure of 4×10^{-6} mbar would give and impingement rate of 9.6×10^{18} atoms per m^2/s. As in the MACS system dosing takes place on a cryogenic surface a sticking coefficient of 1 is assumed. Therefore the number of impinging atoms can be directly treated as the deposition rate, per unit time, per unit area. This is multiplied by dosing time to give the total number of gas atoms deposited per unit area. This is normally compared with the number of absorption sites on a surface to give monolayer values. In this case however, many

layers of solid Ar are grown the bulk density or lattice spacing can be used to convert this into a thickness. Both values give consistent answers, but for simplicity, density will be used here. The number of atoms per volume is given by;

$$N = \frac{\rho}{m} N_A$$

if ρ is density in grams. For argon, the bulk density is 1.616 g/cm^3 giving 2.44×10^{22} atoms per cm^3. By dividing the total deposited atoms per area by the atoms per volume, you get the thickness for the pressure presented above, a dosing time of 10 minutes would give a thickness of 0.24 μm.

The metal deposition rate is measured directly in thickness per unit time by QCM (based on frequency change). As such, this can be directly added to the thickness calculated for argon dosing to give matrix thickness.

The matrix concentration is given in terms of the number of atoms. As such;

$$Concentration = \frac{N_m}{N_m + N_{ar}}$$

where N_m is the number of metal atoms deposited and N_{ar} the number of argon atoms deposited. The number of argon atoms is known from the previous calculation. The number of metal atoms is calculated from the deposited thickness measured by QCM, and the bulk density by the reverse of the process shown above. The thickness is known so the number of atoms can be calculated.

Appendix B

HAADF Analysis

Scanning Transmission Electron Microscopy (STEM), or to be more accurate aberration corrected High Angle Annular Dark Field (HAADF) STEM, has been employed as the primary analysis tool for the nanoclusters produced in this thesis. This technique was chosen as it provides access to the size, shape and cluster density information.[14,90,247,248] In terms of MACS, this provides an effective way to measure both the flux and size of neutral and charged clusters alike. HAADF mode collects the highly scattered electrons that have overcome the coulomb barrier and scattered with the nucleus. Due to this fact, images show a Z contrast useful for imaging high mass groups of atoms on light support surfaces such as metal clusters. Bright field images are also taken simultaneously with the dark field images although not used for quantitative analysis.

The measurements presented in this thesis have been taken with a Jeol 2100F microscope including a spherical aberration corrector (CEOS). A full explanation of the workings of the STEM can be found else where,[249] but a brief overview of how data is collected and processed is given here.

B.0.1 Typical Resolution

Figure B.1 shows an image of a silver cluster in high magnification (twenty million times). The line profile inserts show the change in intensity across the atomic columns and gaps, the lower image covers a smaller distance to provide a clearer view of the distance from the peak to the background intensity (resolution). Here, the distance is 0.12 nm demonstrating the typical resolution of the microscope with a well aligned and focused beam. When observing small particles acquisition time has to be reduced somewhat to avoid modification of the cluster due to beam interaction effects (e.g. heating) and as such resolution and signal to noise ratio are also slightly reduced. To date the smallest cluster where geometrical structure has been resolved using the microscope at the Unviersity of Birmingham is 20 atoms.[250] So far all smaller structures have proved to be too unstable under the beam to permit conclusive statistical structural identification.

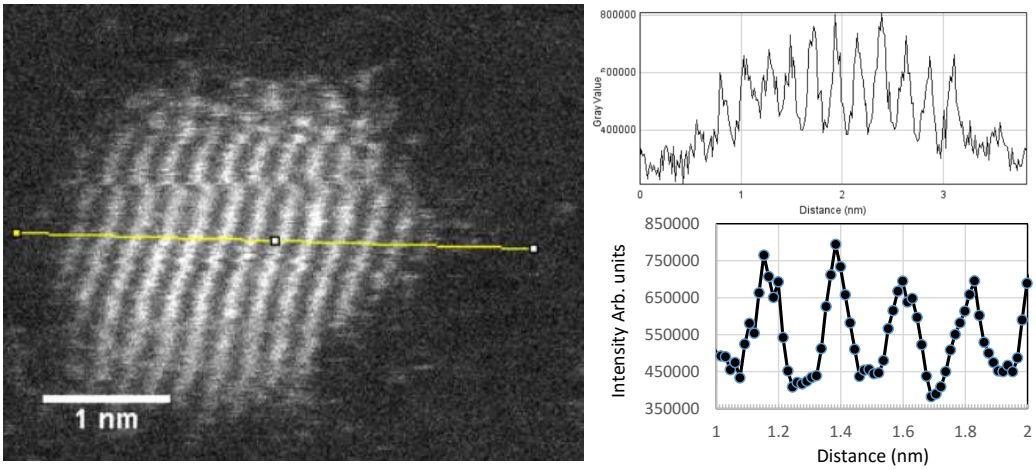

Figure B.1: The left hand image is a silver cluster imaged at high magnification (20 million times). The typical resolution is given by the distance from peak signal to background. It can be measured by taking a line profile across the lattice (top right). A zoomed in version of the central peaks is given bottom right for clear view. In this case the peak to background distance and therefore resolution is 0.12 nm

B.0.2 Weighing Clusters

In order to interpret the images produced, the origin of the signal must first be understood. As stated above, the signal comes from the very high velocity electrons that overcome the Coulomb barrier and scatter with the nucleus, it is clear then that, the more protons there are to scatter the incident electron, the more likely there is to be high angle scattering (i.e. HAADF signal). This process is described by Rutherford scattering. As such the signal is governed by atomic number and samples thickness, in essence the chance of scattering at a high angle and the number of opportunities to scatter. Considering this, the intensity of two different objects (1 and 2) can be described as follows.

$$\frac{I_1}{I_2} = \frac{N_1}{N_2}(\frac{Z_1}{Z_2})^n$$

I represents the intensity, N the number of atoms, and n a parameter of the microscope. The linearity of cluster intensity with size and the value of n has been validated for this instrument by Wang et at, giving a value of 1.46 for n.[251,252] Essentially the linearity holds when samples are very thin, as the chance of scattering is low, such that the contribution from multiple scattering is minimal and electrons that have scattered would have been unlikely to interact with the media that was on it's original trajectory. While in the linear region identification of materials with different chemical composition can be made by intensity. In the case of this thesis, all samples are pure silver clusters and as such they can be compared directly as the atomic mass term cancels. However, when imaging single atoms and clusters, different magnification and measurement times have to be used to obtain a clear measurement. This needs to be factored in when relating the intensity of the cluster and atom. As all other parameters remain unchanged as the magnification and time used simply changes the number of electrons hitting the sample per area and

therefore is proportional to the intensity. The relationship between the intensity of the same object at two different magnifications (l and h), images sizes and exposure times can be expressed by;

$$I_h = \frac{Magnification_h}{Magnification_l} . \frac{Exposure\ Time_h}{Exposure\ Time_l} . \frac{Total\ Pixels_h}{Total\ Pixels_l} I_l$$

This method has been applied to scale between high magnification atoms measurements and lower magnification cluster survey images, which typically use the imaging parameters 12 M , 1024×1024 pixels, 19 μs and 2 M, 512×512 pixel, 38 μs respectively. Atoms are effectively used as mass standards.[247,253]

Throughout the analysis, the two circle method has been employed to calculate the intensity of particles and, by comparison with single atoms, their size. To perform this two, concentric circles are drawn around the cluster: the first just larger than the cluster area and the second significantly larger, see figure B.2. The average intensity of a background pixel is given by the intensity of the outer ring divided by the number of pixels it contains e.g. (I_1 - I_2) / Pixels in outer ring. This value is then subtracted from the pixel intensities of the cluster area to calculate the background subtracted cluster intensity. An example of this method can be seen in Figure B.2. The flatter and thinner the support film, the more stable and small the background signal is. This technique is not without difficulties. Most crucially the intensity of the calibrating object must be measured carefully to prevent large errors.

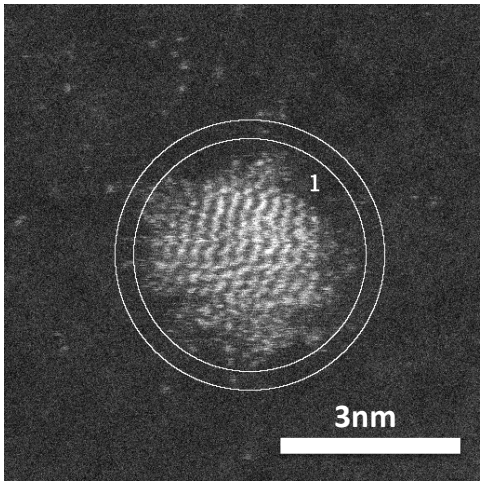

$$I_o - I_i = I_r$$

$$I_r / P_r = I_b$$

$$I_i - (I_b \times P_i) = \text{Cluster intensity}$$

I = Intensity
P = Number of pixels
I, o, r, and b are inner, outer, ring, and background respectively

	Value	Error
Average intensity of atom	$5x10^6$	$\pm 1x10^{6*}$
Cluster intensity	$4.5x10^9$	$\pm 4.5x10^8$
Atom in cluster	900	±200
Area (nm^2)	7.3	±0.7
Diameter (nm)	3.1	±0.3
Atoms	~975**	±100

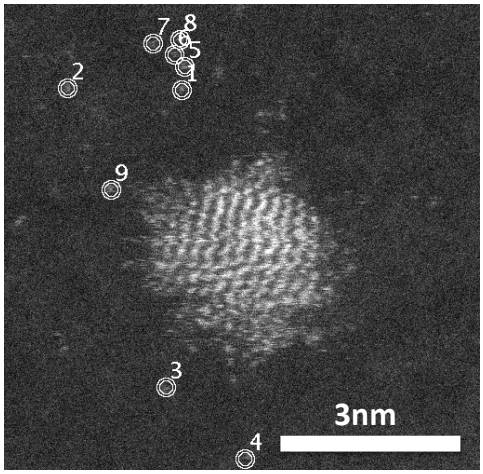

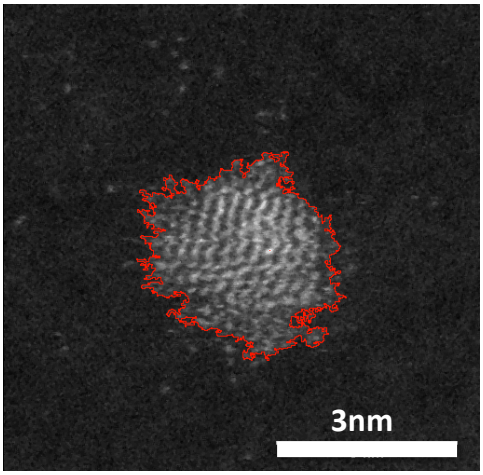

Figure B.2: An example of the two circle method used to calculate cluster size (in atoms). Top left shows the two circles used to measure the cluster, bottom left gives the analysis of single atoms to weigh the cluster. Bottom right is the boarder chosen by thresholding after noise filtering which gives the cluster area. Top right provides the calculated size of the cluster both from atom weighing and size measurement. **The large error is due to the limited number of single atoms analysed for calibration in just one image typically many images are used giving an error of ∼5-10% , **The size calculated based on cluster area is extrapolated from considering the size of particles with full geometric shells.*